EXPERIMENTAL AND NUMERICAL ANALYSES ON THE BEHAVIOR OF CIVIL AND MARINE STEEL STRUCTURES

By
LIGANG SHEN
Bachelor of Science in Civil Engineering
Shanghai Jiao Tong University
Shanghai, China
2013

Master of Engineering in Civil Engineering
Shanghai Jiao Tong University
Shanghai, China
2016

Submitted to the Faculty of the
Graduate College of the
Oklahoma State University
in partial fulfillment of
the requirements for
the Degree of
DOCTOR OF PHILOSOPHY
December 2022

EXPERIMENTAL AND NUMERICAL ANALYSES ON THE BEHAVIOR OF CIVIL AND MARINE STEEL STRUCTURES

Dissertation Approved:

Dr. Mohamed Soliman

Dissertation Adviser

Dr. Robert N. Emerson

Dr. Bruce W. Russell

Dr. Omer San

ACKNOWLEDGEMENTS

Throughout my time at Oklahoma State University, I have encountered many people that have influenced my drive to study higher education. I would like to thank my advisor professor Dr. Mohamed Soliman. Dr. Soliman has been helping me to achieve goals within my academic career and my personal development. Thank you to my committee members, Dr. Robert N. Emerson, Dr. Bruce W. Russell, and Dr. Omer San who generously agreed to serve on my doctoral committee and support the growth of this study. The professional knowledge and encouragement that they shared were truly helpful. I would also like to extend my gratitude to all my colleagues and to all the graduate and undergraduate students that helped me during my doctoral research. Lastly, thank you to my family, especially my wife, Lichun Chen, for supporting me in this journey.

I would like to acknowledge the financial supports from American Institute of Steel Construction (AISC), the Office of Naval Research (ONR), Oklahoma Center for the Advancement of Science & Technology (OCAST), and Transportation Consortium of South Central States (Tran-SET).

Name: LIGANG SHEN

Date of Degree: DECEMBER 2022

Title of Study: EXPERIMENTAL AND NUMERICAL ANALYSES ON THE BEHAVIOR OF CIVIL AND MARINE STEEL STRUCTURES

Major Field: CIVIL ENGINEERING

Abstract:

Bolts and welds in combination occur most commonly during the construction phase of a building when the design load changes, when there are unforeseen difficulties in make-up or matching of bolt holes, or in retrofit of existing structures. Due to the different load-displacement behavior of the bolts and welds, the behavior of the combination connections may change in different conditions. Pretensioned high-strength bolts and longitudinal fillet welds in combination has been studied both experimentally and numerically. Slip-dependent surface frictional and ductile fracture models have been incorporated in the numerical analysis to address the strain compatibility between bolts and welds. Effects of critical variables, e.g., bolt pattern, faying surface, weld size, weld location, and weld/bolt strength ratio have simulated and discussed.
Similarly, the fatigue behavior of stiffened panels under variable amplitude loading has been investigated. These panels are commonly found in steel structures, such as naval vessels and bridges subjected to random variable loading. An experimental fatigue test was conducted for the stiffened box girder under variable amplitude loading. An XFEM-based fatigue crack prediction approach was proposed based on the crack closure concept. Prediction were made using the proposed approach considering the loading history effect as well as stiffener effect, and residual stresses due to welding.

TABLE OF CONTENTS

Chapter Page

Chapter Page

Chapter Page

Chapter Page

LIST OF TABLES

Table Page

LIST OF FIGURES

Figure Page

Figure Page

Figure Page

Figure Page

Figure Page

Figure Page

Figure Page

Figure Page

Figure Page

Figure Page

CHAPTER I

INTRODUCTION

1.1 Introduction

Over the past several decades, research efforts have been devoted to developing a comprehensive understanding of the behavior of steel components in civil and marine structures. Oftentimes, these efforts would rely on experimental and/or numerical investigations to identify the relevant parameters affecting the behavior and develop capacity prediction models to be integrated in design specifications. Despite the sheer number of research studies dedicated to understanding behavior of steel structures, many knowledge gaps still exist. The research conducted herein utilizes experimental investigation and numerical simulations to address two of these knowledge gaps; (a) understanding the load-deformation behavior of bolted and welded combination steel connections and (b) characterizing the crack propagation behavior in stiffened panels commonly used in bridges and marine structures.

Bolts and welds are commonly used to transfer loads between structural elements in steel buildings and bridges. Only one fastening method is commonly implemented for a connection. However, it could be desirable and beneficial to combine both bolts and welds for force transfer under certain circumstances. The strength of these combination connections can be influenced by several variables, e.g., bolt size, bolt grade, pretensioning method, faying surface class, and the weld/bolt strength ratio, among others. An experimental investigation was conducted to address

these critical variables. In addition, finite element analysis was used to develop a deeper understanding of the force transfer mechanisms and investigate the behavior under different configurations of the critical variables. Several finite element models were established based on the corresponding experimental program and used to study the strain compatibility between bolts and welds and its effect on the behavior of the combination connection.

Slip-dependent surface frictional models and the weld ductile fracture model were incorporated in the finite element analysis to address the nonlinear behavior of pretensioned high-strength bolts and longitudinal fillet welds. The finite element models were validated using the experimental data and the results from the FE models showed a good agreement with the experimental tests. Numerical simulation confirmed that at low slip displacements, the capacity of the combination connection can be estimated by the summation of the resistances provided by the bolts and welds for all configurations of the critical variables at the low slip displacement. The results also indicated that the behavior of the combination connection is not sensitive with respect to the weld location as compared to the center of the bolts, as long as no eccentricity is introduced within the force transfer mechanism. Analytical models are discussed to predict the capacity of combination connections with different faying surface conditions. The effect of the weld size on the behavior of the combination connections is investigated.

A similar research routine has been applied to address the second research problem investigated in this dissertation. The second part of the dissertation is dedicated to study the fatigue crack propagation behavior in stiffened panels under variable amplitude loading. These panels are commonly found in steel structures, such as naval vessels and bridges subjected to random variable loading. During the service life of a ship, fatigue cracks could propagate up to a critical size leading to catastrophic structural failure of the hull. Extensive studies have been dedicated to developing an understanding of the crack propagation behavior in stiffened panels. Despite these efforts, fatigue cracking remains a great concern for ship structures. This is due to the large

number of factors contributing to the fatigue cracking in ship hulls. These include aggressive random loading pattern due to severe weather, complex geometry of the stiffened ship hull structure, and weld defects, among others. In addition, the residual stresses occurring due to the welding process could greatly affect the crack propagation rate in the hull structure (Dexter & Pilarski, 2000; Nussbaumer et al., 1999).

The main aim of this part of the dissertation is to put forward a framework to predict the crack propagation in stiffened box girders under random sea loading. It involves both experimental investigation and numerical simulation. The experimental investigation includes 1) middle tension, M(T), specimen (ASTM Standard E647, 2015) fatigue tests to identify fatigue parameters for the steel material used for the stiffened box girders fatigue tests, and 2) fatigue tests to characterize the fatigue behavior of the stiffened box girders and obtain necessary data for validation of the numerical models. The numerical simulations combine an analytical fatigue crack propagation model and extended finite element model (XFEM) to build a propagation prediction approach for the investigated stiffened structures. The developed approach has been validated based on the M(T) specimen fatigue tests and used for predicting of the crack growth within a stiffened box girder.

In the experimental component of the research on fatigue crack propagation conducted herein, one of the critical requitements is the ability to accurately measure the crack size and monitor the fatigue crack growth. Traditional approaches used to measure the crack size, such as the optical, compliance, and electric potential difference methods, usually require intensive labor and are difficult to automate. Other alternatives, such as infrared thermography, may require costly equipment and complex setups, in addition to the high level of training necessary to operate the equipment and interpret the results. To address these issues, this dissertation proposes an automated vision-based fatigue crack growth monitoring approach that utilizes the background subtraction algorithm. The approach treats the fatigue crack growth increment between detection

intervals as an intruding object and identifies it within a series of successive images. The narrow field of view of the utilized microscope is expanded to accommodate the large crack size by automated adjustment of the microscope location based on the identified crack tip location. The accuracy of the proposed approach was verified by fatigue tests of M(T) specimens under constant and variable amplitude fatigue loadings. The crack monitoring process was conducted automatically in a real-time manner which reduced the potential for human-induced measurement errors. The experimental data resulting from the tests were obtained through this proposed crack monitoring approach.

1.2 Research Objectives

The objectives of the dissertation are:

- Develop a comprehensive understanding of the behavior of bolted and welded combination connections considering using numerical models that are validated based on corresponding experimental data.
- Investigate the effect of different input parameters on the behavior of the combination connections using the numerical models, e.g., bolt pattern, weld size, weld location.
- Develop an automated imaging-based fatigue crack growth monitoring approach using background subtraction and other image processing algorithms. The accuracy and feasibility of the proposed approach are evaluated using fatigue tests conducted under different loading conditions.
- Develop a fatigue crack growth prediction model suitable for structures subjected to variable amplitude loading considering the load history effect. The accuracy of the approach is evaluated by testing middle tension fatigue specimens under both constant and variable amplitude loadings.
- Characterize experimentally the fatigue crack propagation in stiffened panels under realistic sea loading where the stress and the stress ratio (positive or negative) may vary randomly from cycle to cycle.

- Apply the developed crack growth prediction approach to predict fatigue crack growth for the stiffened box girder under random sea loading.

Dissertation Layout

Chapter I is the introduction of the dissertation which provides a brief description of the conducted work. It also covers the research objectives and technical contributions of the dissertation.

Chapter II is dedicated to evaluating the behavior of combination connections made with pretensioned high-strength bolts and longitudinal fillet welds using numerical simulations. It will cover the established FE models and will numerically investigate the effects of different parameters on the behavior of the combination connection. It also presents prediction strength equations for the combination connection based on the numerical analysis.

Chapter III is dedicated to the proposed automated vision-based fatigue crack growth monitoring approach. The system setup and related algorithms are illustrated and explained. The accuracy and feasibility of the proposed approach is discussed with examples of conducted fatigue tests.

Chapter IV focuses on the proposed fatigue crack growth prediction approach under variable amplitude loading. It discusses the XFEM application and crack closure effect. Experimental tests have been conducted under different loading conditions. The prediction of the proposed approach is compared to the test data and the results are discussed.

Chapter V is dedicated to studying the fatigue crack growth in stiffened panels under realistic sea loading. It incorporates experimental and numerical investigation to develop a deep understanding of the fatigue crack growth in stiffened box girders.

Chapter VI summarizes the conclusions obtained from the conducted work. It also provides suggestions for future research.

1.3 Technical Contributions of the Research

The following contributions have been achieved in the dissertation:

- This dissertation developed a new finite element model for evaluating the load-slip behavior of combination connections constructed with pretensioned high-strength bolts and fillet welds. Slip-dependent surface frictional models were incorporated for the slip resistance provided by the bolts and a ductile fracture model was used for the fillet welds. Compared to other models in literature with assume constant frictional coefficient and elastic-plastic stress-strain curve for welds, the developed model is capable of addressing the strain compatibility between capacities provided by the bolts and welds. An accurate capacity prediction model is developed and compared with experimental results of more than 70 combination connections.
- Based on the experimental and simulation results, this dissertation proposed a slip-dependent frictional coefficient model for bolted connections with Class A faying surface. The model has also been formulated to provide the slip behavior of faying surfaces if the nominal frictional coefficient defined based on RCSC (2020) is provided or obtained from tests.
- A capacity prediction was proposed for the combination connections with different faying surfaces considering the strain compatibility between bolts and welds. The model has been discussed in the publication Waite et al. (2022) along with discussion that covers strain compatibility considerations based on the experimental outcomes. In this dissertation, numerical prediction of the behavior considering strain compatibility was conducted as well.
- The application of the background subtraction algorithm for fatigue crack size measurement represented a main contribution of this dissertation. This approach provides a more accurate and cost-effective alternative to traditional fatigue crack growth measurement approaches.

- This dissertation proposed an XFEM-based fatigue crack growth prediction approach under variable amplitude loading. It can accurately predict the fatigue crack growth for middle tension specimens and stiffened panels under variable amplitude loadings. Utilizing XFEM enabled a computationally efficient method for considering loading history effect and tracking crack-opening SIF.
- A stiffened box girder specimen was tested under fatigue variable amplitude loading condition in this dissertation. The applied loading stresses varied from positive and negative and was generated based on wave-induced load spectrum. Most research in literature utilized constant or positive variable amplitude loadings, which does not reflect realistic loading conditions that ships encounter. The conducted tests provided important data to evaluate the fatigue behavior of stiffened panels in ships.

CHAPTER II

NUMERICAL INVESTIGATION OF THE BEHAVIOR OF COMBINATION CONNECTIONS WITH PRETENSIONED HIGH-STRENGTH BOLTS AND LONGITUDINAL FILLET WELDS

2.1 Introduction

Bolts or welds are commonly used to transfer loads between structural elements in steel structures. In many situations, it may be desirable to combine bolts and welds for force transfer on a common faying surface to increase the capacity of a connection. To achieve the full potential of a combination connection, different connecting elements should achieve their ultimate capacity at comparable deformation levels. Ensuring that this condition is met requires a full understanding of the load-deformation characteristics of various types of connecting elements.

Fisher (1964) defined a continuous model to represent the load-deformation behavior of bolts under the shear condition. The model utilized an exponential function with three regression parameters to simulate the shear behavior of the bolted connection taking into consideration the type of the steel plates, bolt type, and the thickness of the gripped material. Using the same model with different fitting parameters, Crawford and Kulak (1968) developed a theoretical method to predict the ultimate load on eccentrically loaded bolted connections. The model was verified by an extensive testing program and provided reasonable predictions of the ultimate capacity of the

tested connections. For representing the behavior of connections with pretensioned high-strength bolts, most research in literature adopts a rigid-perfectly plastic model with a constant friction coefficient (e.g., Chung & Ip, 2001; Ju et al., 2004; Liu et al., 2016). However, research by Soliman et al. (2021) shows that bolted connections made with pretensioned bolts can slip up to 0.5 mm (0.02-in) before the maximum slip load can be achieved. For welded connections, Lesik and Kennedy (1990) summarized previous experimental research on fillet weld behavior and derived analytical models to simulate the load-deformation behavior of fillet welds loaded at different angles (i.e., from transverse to longitudinal).

A main challenge associated with predicting the capacity of combination connections is the different load-deformation behavior of individual connecting elements. Figure 2-1 compares the estimated load-deformation behavior of different connecting elements designed to transfer the same force. The figure depicts the behavior of a bearing-type bolted double shear connection with four bolts in a 2×2 configuration made with ASTM F3125 Gr. A325 (ASTM F3125, 2021) bolts installed in a snug-tight condition. The figure also shows the behavior of longitudinal fillet welded connections designed to carry the same ultimate capacity of the bolted connection. A connection with transverse welds is also included in Figure 2-1. As shown, the ultimate capacity of these connecting elements occurs at different deformation levels. For instance, the ultimate load occurs at the deformation of 1.2 mm (0.05-in) for longitudinal fillet welds and 0.5 mm (0.02-in) of transverse fillet welds. From the figure, it seems that welds would fail at a deformation level significantly lower than that of a bearing-type bolted connection. As a result, formulating a mechanistic model to predict the capacity of a combination connection can be quite challenging.

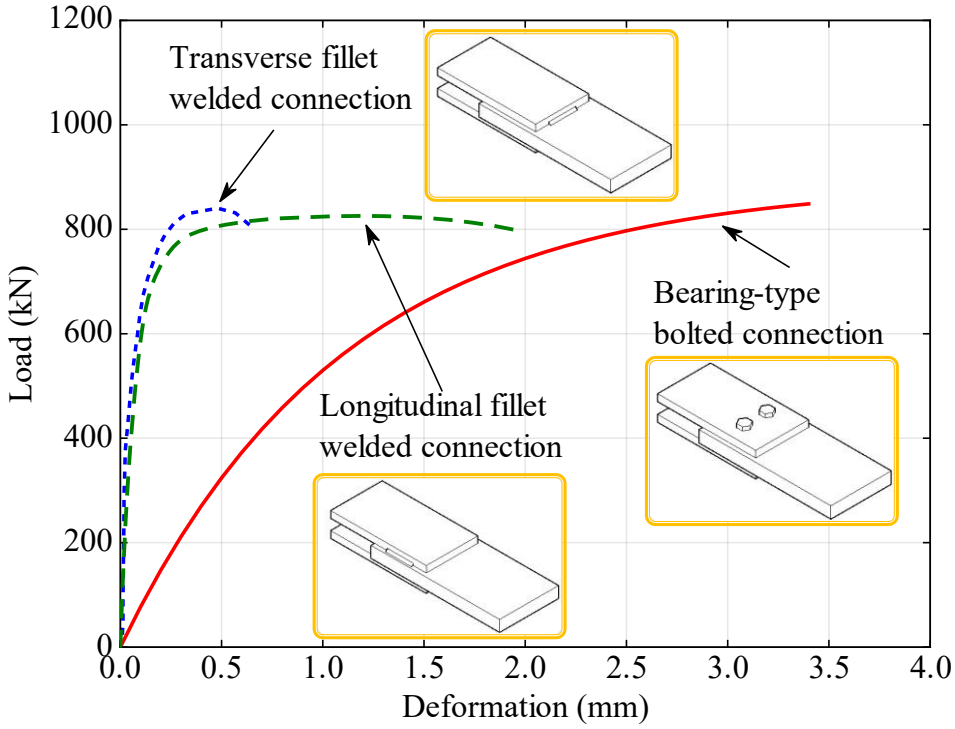

Figure 2-1. Comparison of the load-deformation behavior of double shear splice connections designed to transfer the force using four F3125 Gr. A325 bolts installed to a snug-tight condition (Fisher, 1964), four longitudinal filet welds (Lesik & Kennedy, 1990), and two transverse fillet welds (Lesik & Kennedy, 1990).

Research on this topic started in North America in the 1970s. Holtz and Kulak (1970) investigated the strength of combination connections made with high-strength bolts and longitudinal or transverse fillet welds under tensile and compressive conditions. They concluded that longitudinal fillet welds were more preferred in a combination connection than transverse welds since they can accommodate higher deformation levels before failure (see Figure 2-1). They also indicated that the existence of clearance between the bolts and hole edges, which will dictate the bearing condition, could lower the ultimate capacity of a combination connections. Jarosch and Bowman (1986) performed similar experiments and highlighted the large difference between the load-deformation behavior of connections with transverse welds and bolts. Manuel and Kulak (2000) conducted another study on tension splices that focused on the influence of bolt

pretension and bearing condition. Manuel and Kulak (2000) proposed a strength prediction equation that includes partial contribution from bolt-induced friction, bolt bearing/shear, and fillet welds capacities towards the capacity of the combination connection. Their prediction model allows for the use of longitudinal, transverse, or both types of welds.

Further research in literature (Kulak & Grondin, 2003; Shi et al., 2011a, 2011b) showed that the slip capacity provided by properly pretensioned bolts can be reliably combined with the capacity of longitudinal welds. Shi et al. (Shi et al., 2011a, 2011b) established numerical models validated using the results of two experimental tests to establish a prediction model for the capacity of combination connections with high-strength bolts and fillet welds. They also suggested that the weld/bolt strength ratio can influence the combined strength of these connections. To further investigate the effect of various input parameters on the behavior of combination connections, Soliman et al. (2021) conducted a series of experiments on double shear tension splice connections with four or six bolts and different faying surface conditions. The results indicated that the slip resistance of a bolted connection can indeed be combined with the resistance of longitudinal fillet welds resulting in a connection with higher capacity and ductility.

Figure 2-2 shows the behavior connection similar to those discussed in Figure 2-1 but made with properly pretensioned bolts. The figure compares two extreme cases, where the connection starts in positive or negative bearing conditions. The connection in negative bearing slips gradually until bolts initiate their bearing conditions and the shear/bearing failure would occur. In practical situations, the bearing condition of connections is random and can be in between these two extreme cases. The figure also shows the behavior of the connection with the longitudinal fillet weld discussed above. As seen, although the bearing failure is expected to occur at a deformation level well beyond that associated with fillet weld failure, the loss in fillet weld resistance and slip event on the faying surface of bolted connections occur at comparable deformation levels.

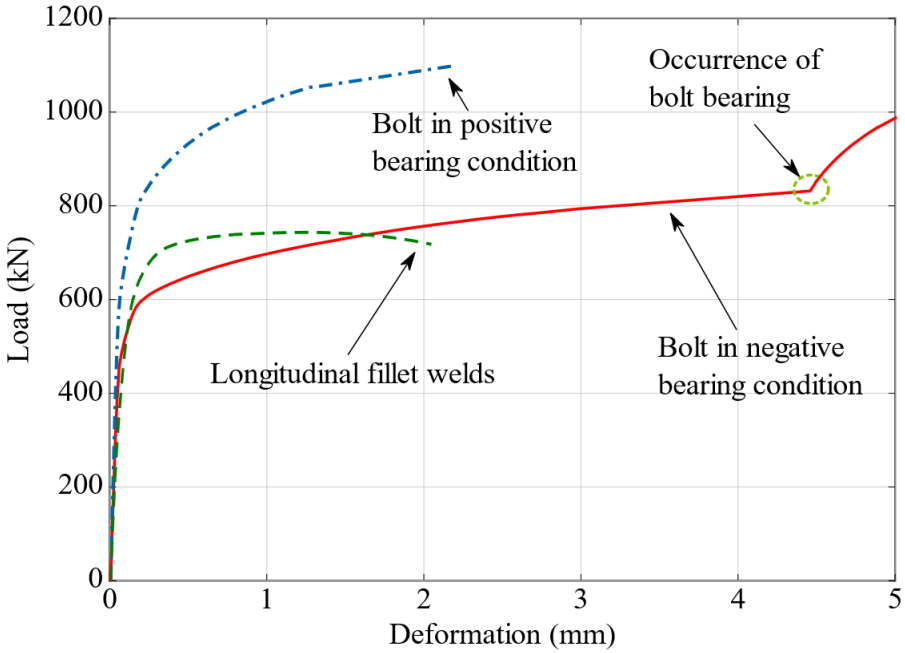

Figure 2-2. Comparison of the load-deformation behavior of double shear splice connections designed to transfer the force using four F3125 Gr. A325 pretensioned bolts in positive bearing condition (based on Kim and Lee (2020)), four F3125 Gr. A325 pretensioned bolts in negative bearing condition (based on Soliman et al. (2021)), and four longitudinal fillet welds (Lesik & Kennedy, 1990).

The experimental and analytical investigations in Soliman et al. (2021) quantified the behavior of combination connections with pretensioned high-strength bolts and longitudinal fillet welds. It covered the effect of bolt diameter, faying surface conditions, weld length, and tightening techniques. However, numerical models are still needed to develop a deeper understanding of the behavior and quantify the stresses in weld lines and the plates. Limited research on the numerical analysis of combination connections exists in literature. Shi et al. (2011a) established finite element (FE) models for the combination connections considering bolts, longitudinal and transverse welds. The FE model included two high-strength bolts, four longitudinal and two transverse welds. Limited experimental data was provided and compared to the numerical results.

Liu et al. (2016) analyzed the failure mode and weld size effect of the combined connection through a similar FE model. They indicated that the weld strength in a combination connection remains similar to that of a welded-only connection while the load carried by bolts varies with respect to the weld/bolt strength ratio. Tao et al. (2019) evaluated the behavior of combination connections constructed with two, three, and four bolts using FE models, and concluded that the strength of the combination connection was slightly lower than that provided by the addition of bolt and weld capacities while the displacement ductility improved slightly compared to welded connection.

Reviewing these numerical studies in literature shows that several assumptions that may affect the drawn conclusions were made. For instance, a constant surface frictional coefficient value was adopted in the FE models of the bolted connection. However, results in Soliman et al. (2021) indicated that the friction force carried by the connection is slip-dependent. In addition, a limited number of experimental tests were used to validate the FE models in these studies in literature. Furthermore, connections with only two bolts and a relatively short weld length were considered in these previous numerical studies. Accordingly, more research is needed to develop a deeper understanding of the load sharing mechanisms and the influence of different input parameters on the strength of these connections.

In this chapter, numerical analysis is implemented to investigate the behavior of combination connections with pretensioned high-strength bolts and fillet welds under shear loading covering different configurations of the critical variables. Strain compatibility between bolts and welds is addressed by developing an experimentally derived frictional model for the bolted connection and implementing a weld ductile fracture model. Further, the numerical analysis expands the range of input parameters beyond what was investigated experimentally. Larger connections with more bolts and longer welds are also included in the numerical simulations. Weld location and

dimension effect are also discussed in the analysis. The capacity, ductility, as well as the influence of critical variables on the behavior of combination connections, are discussed.

2.2 Experimental Program

An experimental testing program was conducted at the Bert Cooper Engineering Laboratory (BCEL) at Oklahoma State University, to investigate the behavior of these combination connections (Soliman et al., 2021). Figure 2-3 shows the direct tension test frame used to conduct the experiments with one of the specimens installed. The test program included 75 specimens with 23 different connection configurations covering bolt size, bolt grade, pretensioning method, faying surface class, and the weld/bolt strength ratio. Two main specimen layouts with 2×2 and 2×3 bolt configurations and varying weld lengths, leading to different weld/bolt strength ratios, were considered in the experimental program. Table 2-1 shows the test matrix. The tests are designated as follows BX_1-X_2-WX_3-RX_4, where B = bolt; W = weld; R = weld/bolt strength ratio; X_1 = bolt pattern (i.e., 22 or 23 for 2×2 or 2×3, respectively); X_2 = faying surface condition following the AISC (AISC, 2017) standards (i.e., A or B for Class A or Class B, respectively); X_3 = weld length (mm); X_4 = value of the weld/bolt strength ratio. For example, test B22-A-W32-R0.67 represents the combination of the 2×2 Class A connection and four 32 mm (1.25-in) longitudinal fillet welds with a value of weld/bolt strength ratio of 0.67.

Figure 2-4 shows the layout of the connections along with the instrumentation layout. Four Sensotec 060-3587-03 high accuracy linear variable displacement transducers (i.e., AC-LVDTs) were used at the bottom of the splice plates to measure the slip displacement within the connection. These AC-LVDTs had a stroke of 5 mm (0.2-in) with an output sensitivity of 4 mV/V/0.001 in. An amplifier (RDP DR7AC) is connected to the AC-LVDT to transform the AC signal into DC output. Two additional LVDTs (i.e., DC-LVDTs) with larger strokes were installed between the main plates to measure the global displacement between the top and bottom connections. These were RDP DCTH1000 with +/- 1 in of stroke. The bolt pretension force was

measured using washer-type bolt load cells. The specimens were tested under a displacement control protocol with a rate of 0.5 mm/min (0.02 in/min) leading to the generation of the load-deformation curves shown in Figure 2-5 for tests B22-A, W51, and B23-A-W102-R1.33. Soliman et al. (2021) and Waite et al. (2022) present more details on the experimental component of this research. The experimental testing results were utilized to validate the corresponding numerical models.

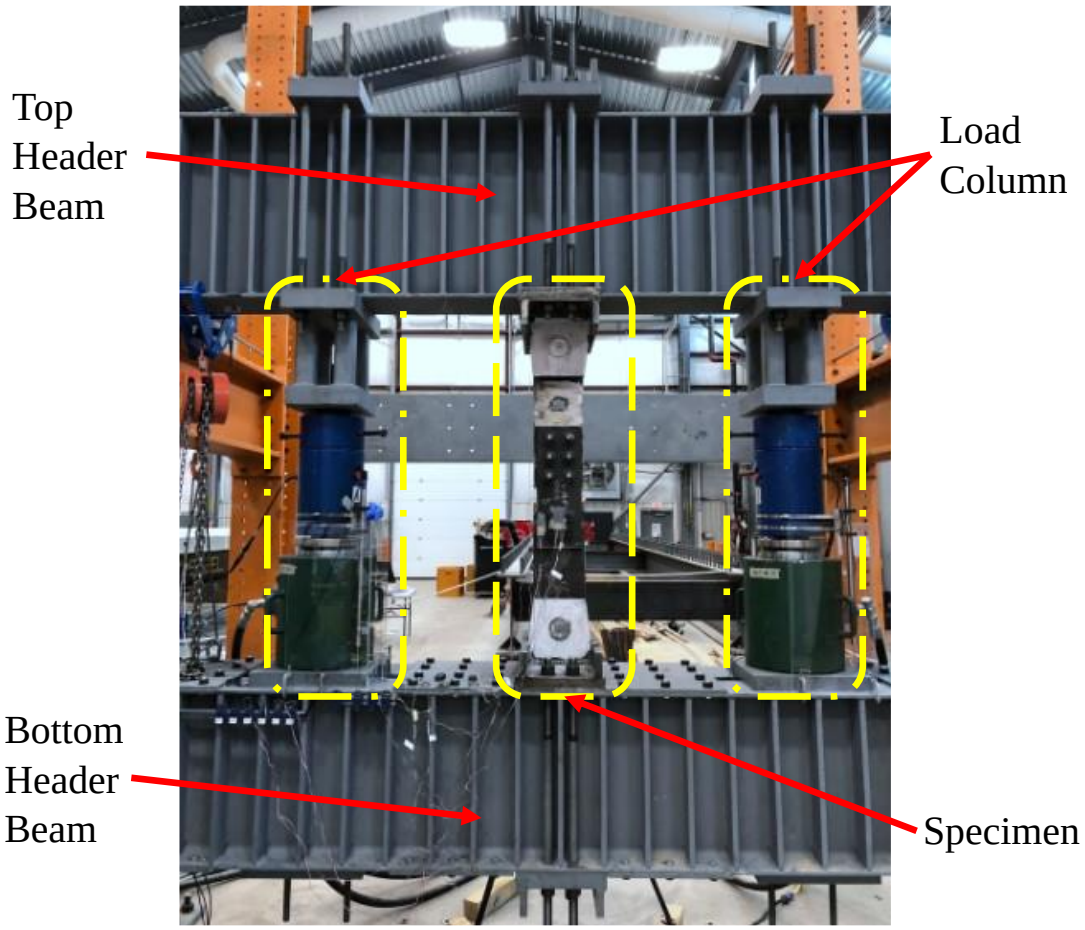

Figure 2-3. The test frame with the specimen installed in the corresponding experimental program.

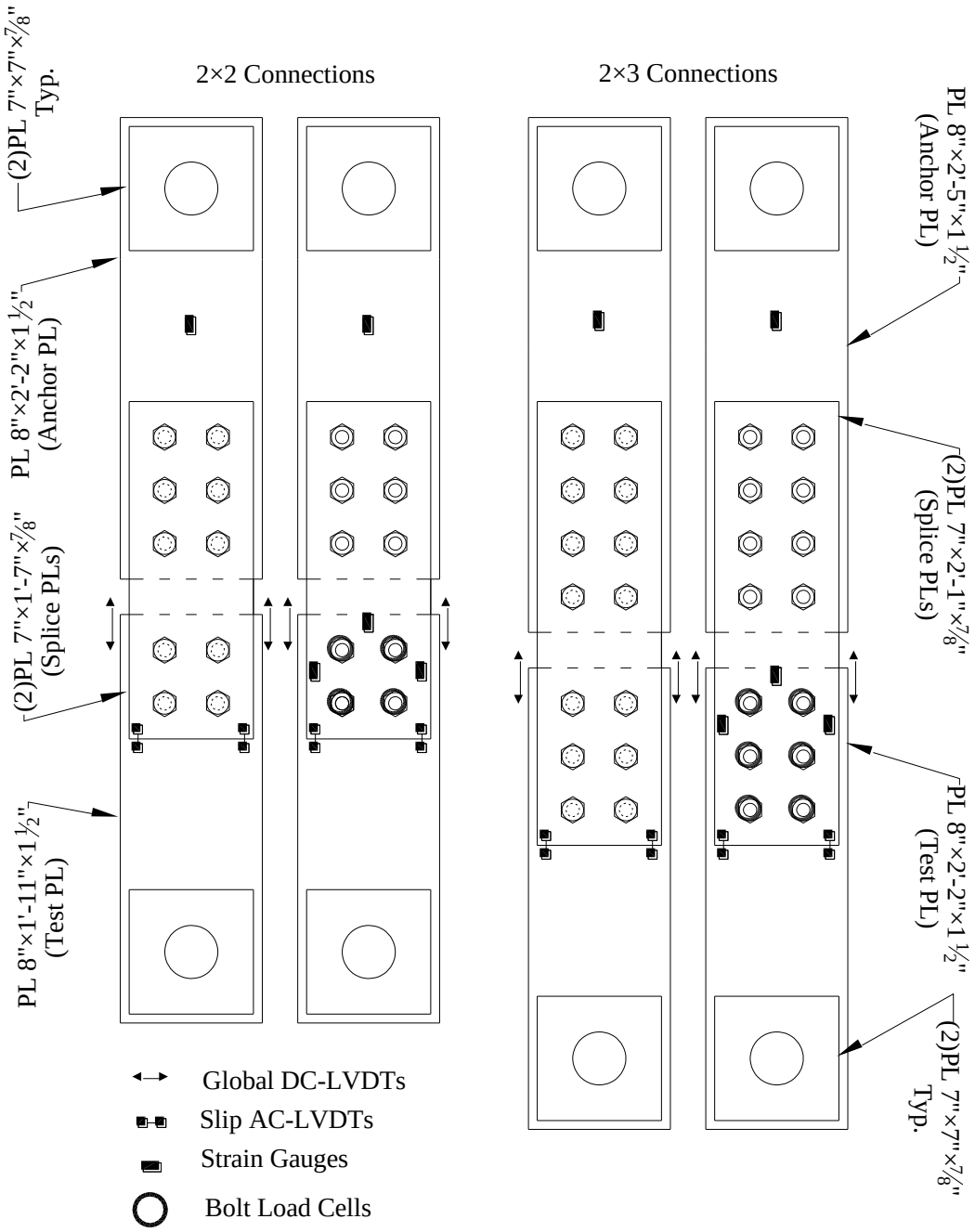

Figure 2-4. Details and instrumentation layout of 2×2 and 2×3 specimens.

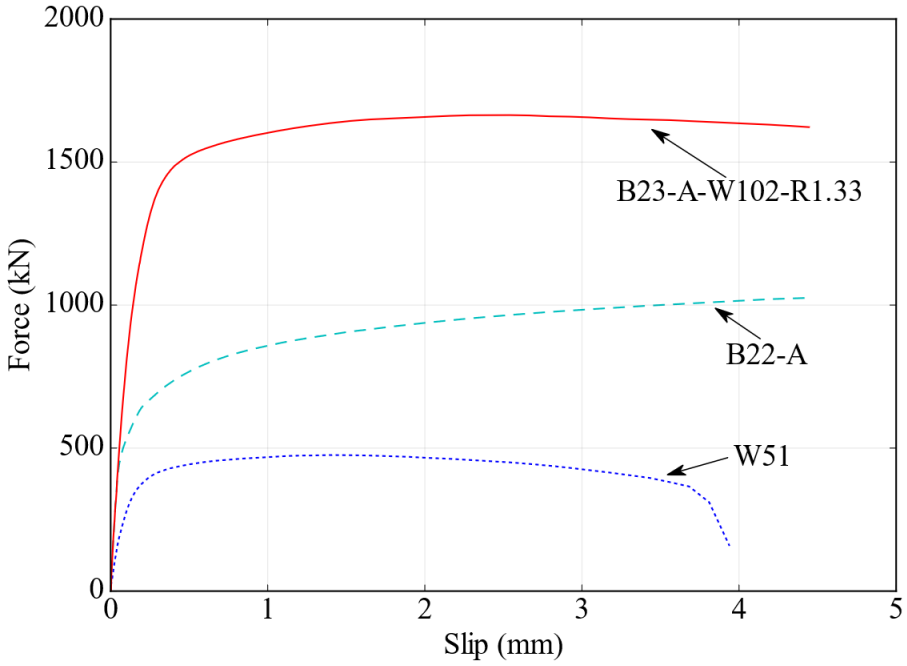

Figure 2-5. Load-deformation curves for specimens Test B22-A, Test W51, and Test B23-A-W102-R1.33.

Table 2-1. Experimental test matrix.

Configuration ID	Name	Bolt Grade	Bolt Pretensioning Method	No. of Samples
1	B22-B	A325	ToN	5
2	B22-A	A325	ToN	3
3	B22-B	A490	ToN	3
4	B22-A	A325	TC	3
5	B22-A	A490	ToN	3
6	W76	-	-	3
7	B22-B-W127-R1.5	A325	ToN	3
8	B22-B-W57-R0.67	A325	ToN	3
9	B22-B-W89-R1.0	A325	ToN	3
10	B22-B-W57-R0.67	A325	TC	3
11	B22-B-W70-R0.67	A490	ToN	3
12	B22-A-W32-R0.67	A325	ToN	3
13	B22-A-W51-R1.0	A325	ToN	3
14	B22-A-W76-R1.5	A325	ToN	3
15*	B22-A-W89-R1.0	A325	ToN	3
16	B23-A	A325	ToN	5
17-2	W51	-	-	3
17-4	W102	-	-	2
18	B23-A-W51-R0.67	A325	ToN	3
19	B23-A-W76-R1.0	A325	ToN	3
20	B23-A-W102-R1.33	A325	ToN	3
21	B23-A-W159-R2.0	A325	ToN	3
22	B23-A-W76-R1.0	A325	TC	3
23	B23-A-W51-R0.50	A490	ToN	3

NOTE: All bolts are 3/4-in. diameter (oversized holes) unless noted otherwise.
TC = Tension control bolt; ToN = Turn of nut method
* Bolts are 1-in. diameter A325 in oversized holes.

2.3 Numerical Analysis

Numerical simulations are utilized herein to better characterize the behavior of the combination connections with pretensioned high-strength bolts and longitudinal fillet welds. Abaqus/Explicit 2020 (Dassault Systemes, 2021) is chosen to establish all the FE models considering its versatility and applicability in modeling the underlying phenomena (i.e., surface friction and ductile failure).

The FE models are discussed next including details on element types, material properties, weld failure model, and surface frictional model.

All the FE models have four equal-length welds and can be categorized as 2×2, 2×3, and 4×6 bolt patterns. The FE models with 2×2 and 2×3 bolt patterns are identical to those analyzed in the experimental program (Figure 2-4) while the FE models with the 4×6 bolt pattern are aimed to simulate larger connections. The diameter of the bolts is 19 mm (3/4-in), and the size of the fillet welds is 8 mm (5/16-in). Parameters of FE models were established using data from the experimental 2×2 and 2×3 tests. The same parameters were applied to the 4×6 models to predict the behavior of larger combination connections.

The FE model of the connections includes three components: center and splice steel plates, welds, and bolts. Only the specimen area is included in the FE model as presented in Figure 2-6. All components are meshed with linear hexahedral solid elements with 8 nodes (ABAQUS C3D8R element). The mesh size of steel plates is 7.6 mm (0.3-in) while a seed size of 5.1 mm (0.2-in) is defined for the contact regions (i.e., around the bolt holes and the weld region). Welds are meshed with a seed size of 2.5 mm (0.1-in) to accurately investigate stress and strain fields and enable the implementation of the weld fracture model. The meshed FE model of the combination connection with 2×2 high-strength pretensioned bolts and four 76 mm (3-in) longitudinal fillet welds is shown in Figure 2-6. The boundary conditions of the model were defined, as shown in Figure 2-6, in accordance with the experimental test setup, i.e., hinged support at the end surfaces of two splice plates whereas the load is applied at the right free surface of the center plate.

The weld lines were connected to steel plates through a TIE constraint. The interaction between plates was defined as surface-to-surface contact. The frictional force between the steel plates, induced by the pretensioned bolts, was established by utilizing the subroutine VFRIC provided in Abaqus/Explicit. The loading process in the FE model comprises two steps. The first step is

generating the pretensioning force of the bolts by applying pressure on the head surface of the bolts in the FE model. The magnitude of the pretension force in the bolts was estimated based on data collected during the experimental program (Soliman et al., 2021). The second step is to apply the tensile load to the center steel plate in a displacement control process.

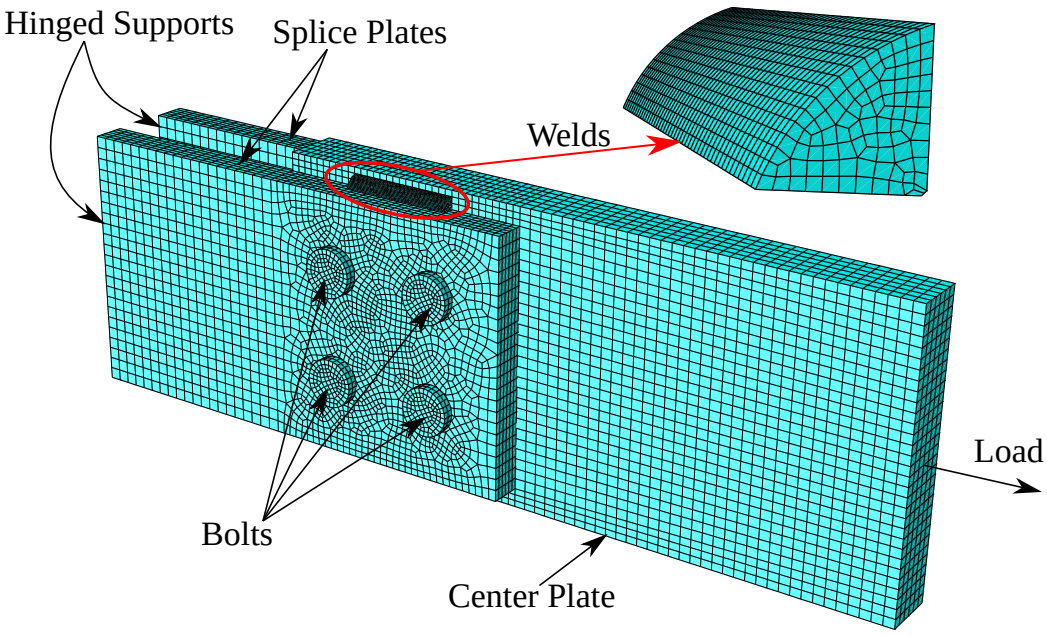

Figure 2-6. Finite element model with 2×2 slip-critical bolts and four 76 mm (3-in) longitudinal fillet welds.

2.3.1 Material Properties

Three materials are employed in the FE models, which are assigned to the steel plate, weld filler metal, and bolts. The steel plates tested in the experimental program are classified as ASTM A572 Gr. 50 (ASTM A572, 2021). A hardening stress-strain curve (Kaufmann et al., 2001; Sajid & Kiran, 2018) was adopted for modeling the steel plates with a yield strength of 374 MPa (54 ksi). The characteristics of the high-strength bolts are based on the minimum requirements of the ASTM F3125 Grade A325 specification (AISC, 2017). The stress-strain behavior of the bolt

material was assumed to follow an isotropic elastic perfectly plastic behavior with the yield strength of 634 MPa (92 ksi).

Since the weld lines play a key role in the force transfer mechanism of combination connections, it is crucial to quantify the mechanical properties of the weld material to simulate the actual behavior of these connections. Accordingly, a material test was conducted for the weld material used in the experimental program. Three tensile testing weld coupons were fabricated and tested following AWS B4 Specifications (2016). Due to the occurrence of hardening and necking in the test, the strain and stress obtained from the test after necking cannot represent the true strain and stress of the weld material (Oh et al., 2007). Thus, the Swift hardening model is utilized in the coupon FE model to represent the true stress-strain relationship for the weld material. This model can be written as (Swift, 1952)

$$\sigma = \omega\left(\varepsilon_y + \varepsilon_p\right)^n \qquad \text{Equation 2-1}$$

where σ is the stress (ksi); ε_y is the yield strain; ε_p is the plastic strain; ω, n are material parameters, which were fitted as 827 MPa (120 ksi) and 0.12, respectively. The stress-strain curves for the weld material, along with the steel plates and bolts, are shown in Figure 2-7.

The tested weld coupons are shown in Figure 2-8 along with the corresponding FE model and numerical stress results. The stress-strain curves from the coupons and the corresponding FE behavior are plotted in Figure 2-9. As shown, the adopted Swift hardening model with the fitting parameters can accurately predict the ultimate strength and deformation of the tested weld coupons.

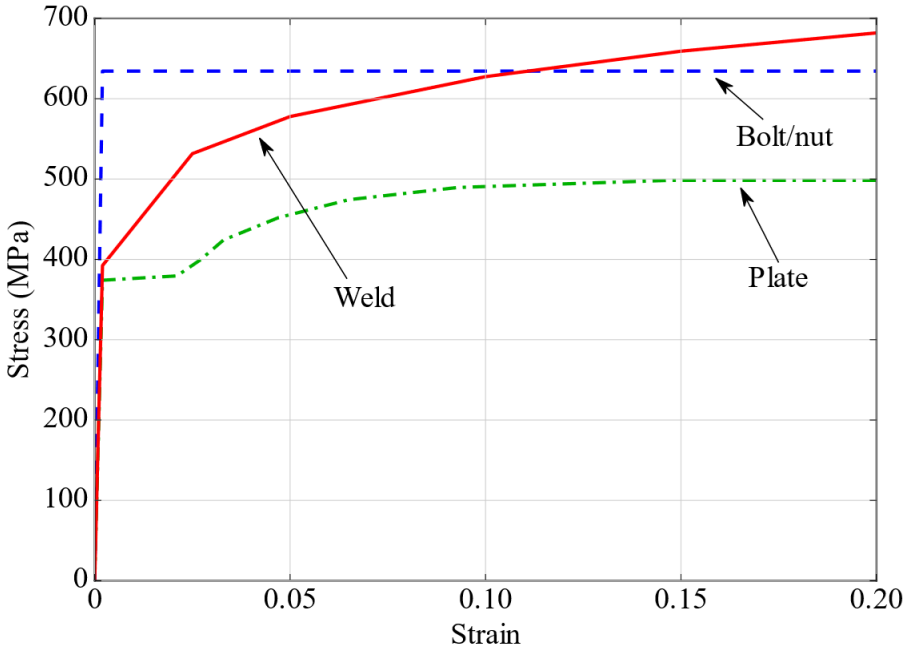

Figure 2-7. True stress-strain relationships of steel plate, bolt/nut, and weld used in FE models.

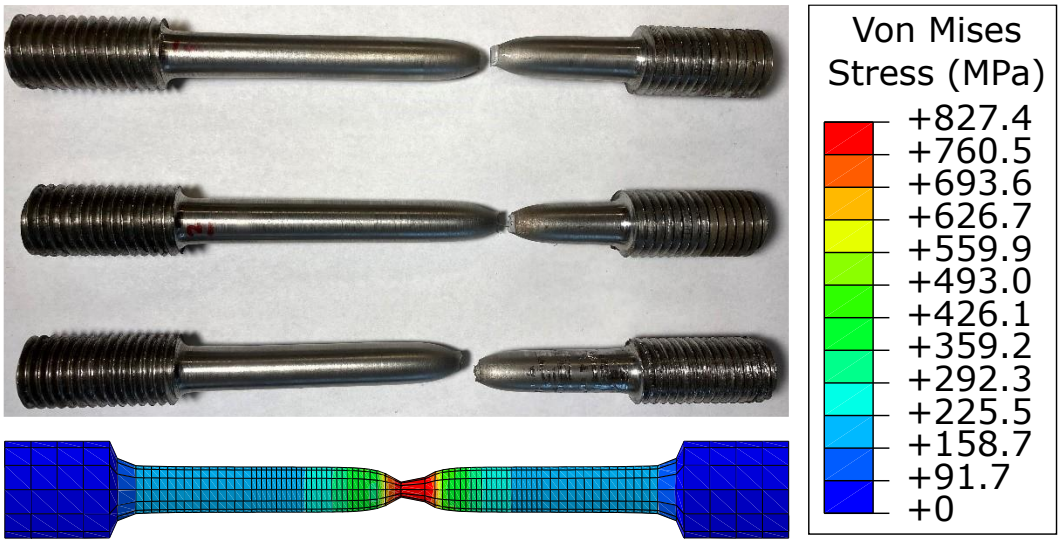

Figure 2-8. Weld coupon tests and corresponding FE stress result.

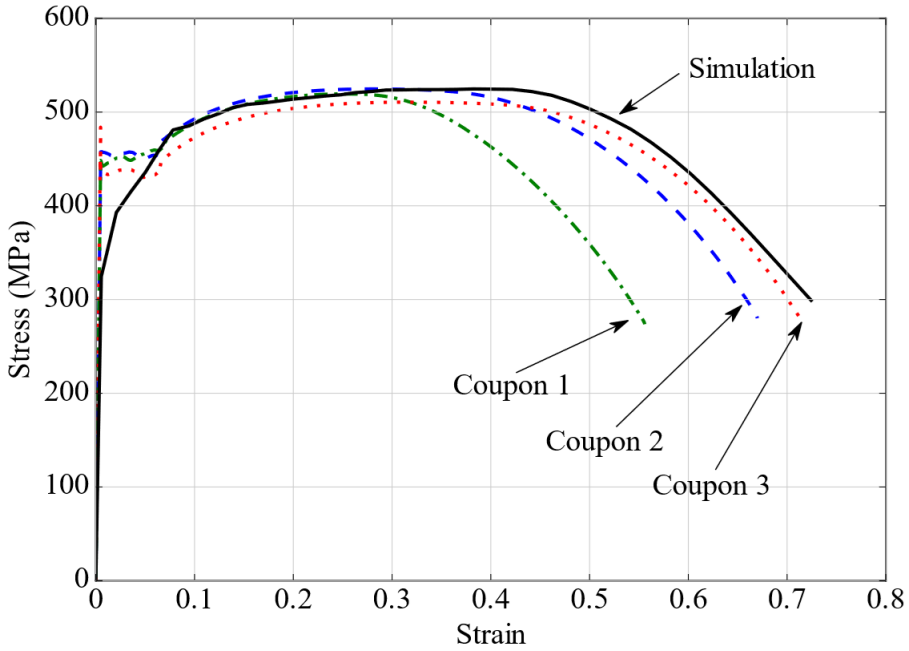

Figure 2-9. Comparison of stress-strain curves from weld coupon tests and corresponding FE model.

2.3.2 Weld Ductile Fracture

A ductile fracture model is incorporated herein to simulate the load-displacement behavior of the welds in the FE models (Kang et al., 2015). Two aspects are included in this model: damage initiation and damage evolution. Figure 2-10 shows conceptually the adopted ductile fracture model. The damage initiation criterion is defined based on the equivalent plastic strain at fracture which is a function of stress triaxiality. The equivalent plastic strain at fracture is calculated as (Rice & Tracey, 1969)

$$\varepsilon_{eq\_0}(\eta) = \alpha\, exp(-1.5\eta) \qquad \text{Equation 2-2}$$

where α is a material parameter; η is stress triaxiality, defined as σ_m/σ_{eq}; σ_m, σ_{eq} are the mean normal (hydrostatic) and equivalent stresses, respectively (Oh et al., 2007). The damage initiation criterion is activated once the following condition is satisfied

$$DI = \int_0^{\varepsilon_{eq\_0}} \frac{d\varepsilon_{eq}}{\varepsilon_{eq\_0}(\eta)} = 1 \qquad \text{Equation 2-3}$$

where *DI* is the damage indicator ranging from 0 to 1; ε_{eq} is the equivalent plastic strain.

Once the damage initiation criterion is reached, the element starts to degrade and accumulate damage. The damage evolution describes the degradation rate of elements during this damage accumulation process. The stiffness of the element will be reduced in order to reflect the damage level of the element. As the equivalent plastic displacement of an element increases due to loading, adjustment of stiffness in the numerical model is achieved by modifying the elastic modulus as follows

$$E' = \left(1 - d\left(u_{eq}\right)\right) E \qquad \text{Equation 2-4}$$

$$u_{eq} = L_e \varepsilon_{eq} \qquad \text{Equation 2-5}$$

where $d\left(u_{eq}\right)$ is the overall damage function of equivalent plastic displacement; u_{eq} is equivalent plastic displacement (mm); L_e is the characteristic length of the element.

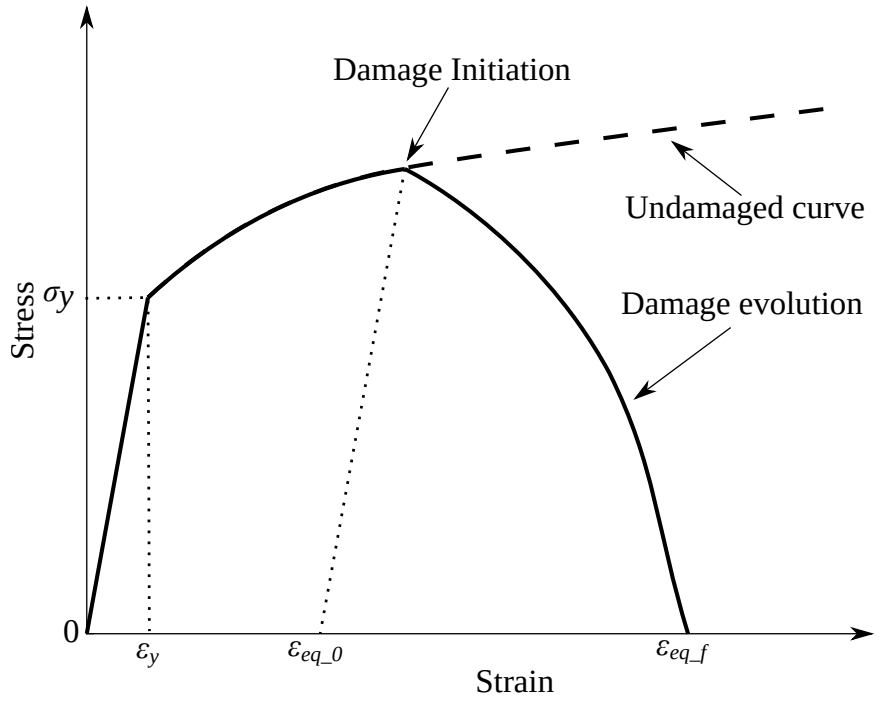

Figure 2-10. Sketch of weld ductile fracture model.

2.3.3 Surface Friction

Two faying surface conditions, i.e., Class A and Class B, were tested in the experimental program. Class A represents the AISC designation (AISC, 2017) of the faying surface with clean mill scale condition, while Class B refers to SSPC-SP6 commercial blast cleaned faying surfaces that at least two-thirds of the surface area is free of all visible residues. Note that the Eurocode (EN 1090-2, 2018) classifies the clean mill scale faying surface as Class C while the blast cleaned surfaces as Class A. However, the discussion in this dissertation uses the AISC (2017) faying surface designation. The load-displacement curves of a bolted connection with Class A and Class B faying surfaces from the experimental data are plotted in Figure 2-11. The resistance of the connections with Class A surfaces increases with the growth in the slip distance while the connection with the Class B surface reaches the ultimate capacity at a low slip level and experiences a decrease in resistance with a higher slip distance. The figure also includes two types of load-displacement curves discussed in RCSC (2020), i.e., Type (a) and Type (c). From this comparison, it seems that the behavior of bolted connections with Class A faying surface

tends to follow Type (c) trend, while the behavior of Class B resembles Type (a) profile. Accordingly, two different friction models are considered herein to account for the different slip behavior under Class A and Class B faying surface conditions. The friction model presented by Dahl (1968) was adopted for bolted connection with Class A faying surface while an exponential decay friction model was utilized for the ones with Class B surfaces.

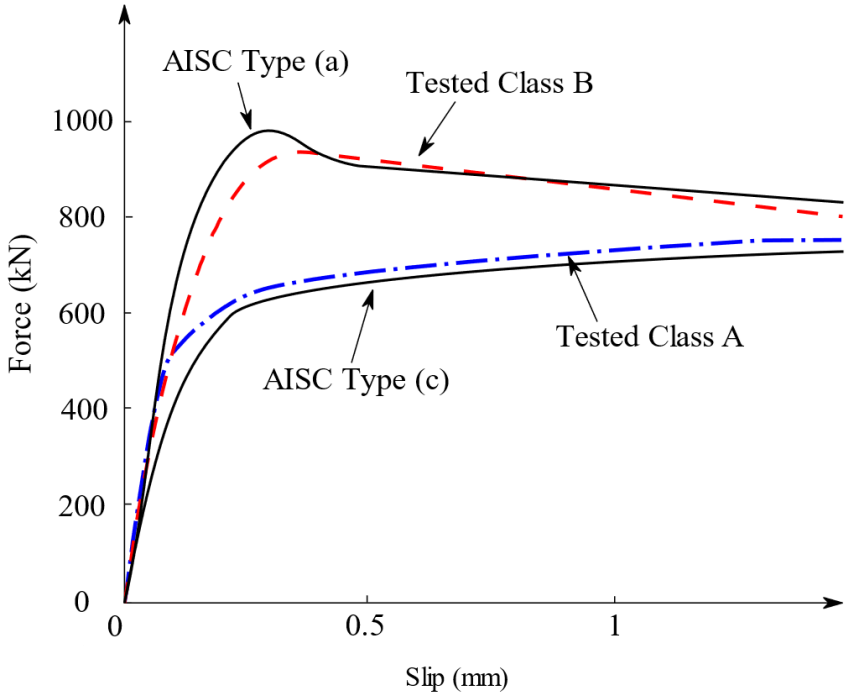

Figure 2-11. Comparison of load-slip curves defined by AISC and obtained from tested faying surface Class A and Class B.

Dahl (1968) introduced a friction model to represent sliding friction while simulating dynamic systems. This model can accurately depict the frictional behavior commonly modeled as the combination of static friction and Coulomb friction. However, in contrast to Coulomb friction which assumes a constant frictional coefficient, Dahl's model correlates the frictional coefficient to the slip displacement to account for nonlinear load-displacement relationships. The frictional coefficient $\mu(x)$ can be calculated as (Dahl, 1968)

$$\mu(x) = a \times \left(1 - (1 - b \times x)^{1/(1-k)}\right) \quad \text{Equation 2-6}$$

where *a*, *b*, *k*, are fitting parameters determined by experimental data, *k* is integer; *x* is the slip displacement.

An exponential decay friction model is adopted to represent the frictional behavior of connections with Class B faying surface. In this model, the friction coefficient is expressed as (Oden & Martins, 1985)

$$\mu(x) = \mu_k + (\mu_s - \mu_k)\, exp(-d_c x) \quad \text{Equation 2-7}$$

where μ_k is kinetic friction coefficient; μ_s is the static friction coefficient; d_c is a fitting decay parameter. Experimental data are also used to estimate these parameters for the FE simulations.

2.4 Analysis Results

The experimental program in Soliman et al. (2021) included connections with four (i.e., 2×2) and six bolts (i.e., 2×3), and longitudinal fillet welds with length ranging from 32 mm (1.25-in) to 159 mm (6.25-in) and size of 8 mm (5/16-in). These weld dimensions covered a nominal weld/bolt strength ratio ranging from 0.67 to 2.0. Data from tests using ASTM F3125 Grade A325 bolts pretensioned with turn-of-nut method (ToN) are considered herein. FE models were established consistent with these experimental tests and an additional bolt pattern of 4×6 (i.e., 24 bolts) and weld length to 432 mm are also included to examine the combinational behavior of larger connections. Welds with different sizes were also included in the FE models to investigate the effect of weld size on the combination connections. The established FE models can be categorized into three types: (1) bolted-only model, (2) welded-only model and (3) combined model. These FE models will assist in understanding the effect of critical variables on the

behavior. These variables include surface faying condition, bolt pattern, weld dimension, and weld/bolt strength ratio.

2.4.1 Load-Displacement Behavior

Strain compatibility between the behavior of bolts and welds is necessary to improve the efficiency and capacity of a combination connection. Accordingly, it is crucial for the FE models to properly capture the experimental load-displacement curves. The bolted-only and welded-only experimental results were used to calibrate the parameters of the bolt-induced frictional resistance model and weld ductile fracture model, respectively. The experimental data of bolt-only tests indicated that the faying surface characteristics of the plates used to fabricate the 2×2 connections are different than those of the plates used for the 2×3 connections. This was attributed to the natural variability between the surface properties of the two sets of plates. Consequently, two fitting frictional curves are generated in this chapter for the Class A 2×2 and Class A 2×3 connections while only one fitting curve was created for the Class B faying surface as shown in Figure 2-12. The parameters of the surface frictional models are obtained based on the test data using the least square fitting method (Leon et al., 2006). For the adopted Dahl's model, the conducted fitting procedure showed the optimal value of the parameter k is 5.7 +/- 0.8. Since k needs to be an integer, k was set as 6 for the Class A surface. With $k = 6$, the values of parameters a and b are determined for the Class A 2×2 and 2×3 surfaces, as shown in Table 2-2, resulting in a coefficient of variation of 2% and 10%, respectively, for a and b. The fitting curve of the frictional coefficient for Class A 2×2 surface along with the test data are plotted in Figure 2-13. The nominal friction coefficient for Class A faying surfaces used in the 2×2 and 2×3 connections were estimated as 0.457 and 0.339, respectively in Soliman et al. (2021). Accordingly, the obtained parameters a, b, and k in Table 2-2 can be correlated with the nominal friction coefficient, and the Equation 2-6 is modified as below to represent the frictional coefficient for Class A faying surface

$$\mu(x) = (1.16\mu_n + 0.28) \times \left(1 - \left(1 - \frac{(-8452\mu_n + 914)x}{25.4}\right)^{-1/5}\right) \qquad \text{Equation 2-8}$$

where μ_n is the nominal frictional coefficient defined based on RCSC (2020); x is the slip displacement in millimeters. For Class B plates, the same least square fitting method was applied, and the values of the corresponding parameters are $\mu_k = 0.38$, $\mu_s = 0.56$, $d_c = 20$.

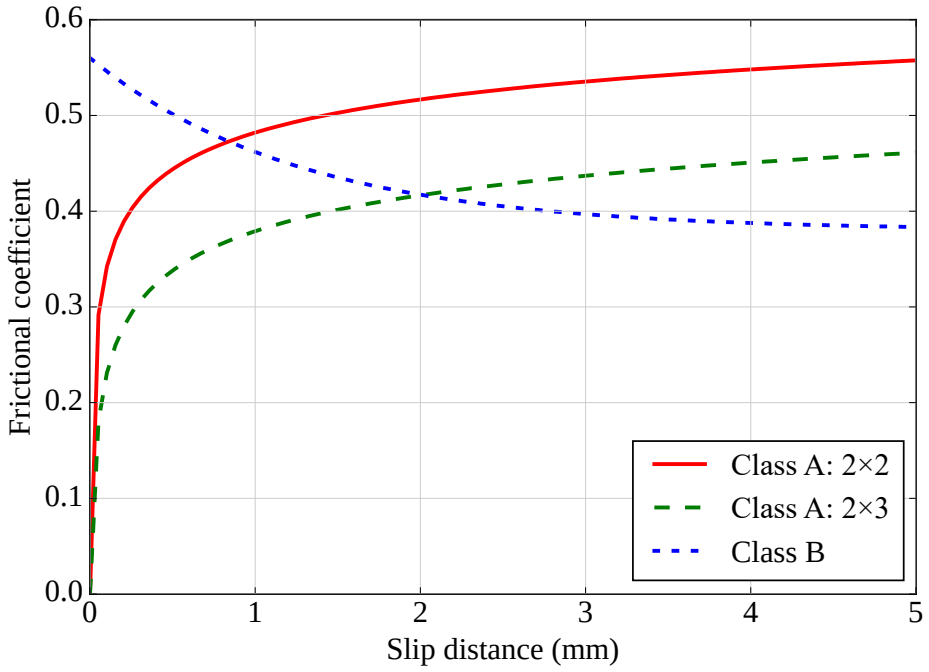

Figure 2-12. Fitted friction profiles for Class A and B faying surfaces.

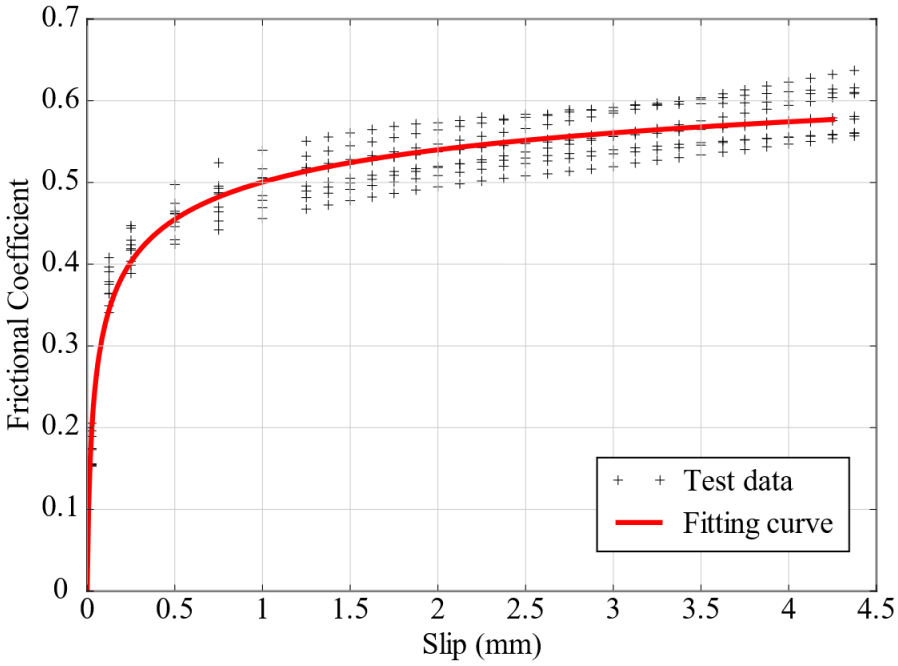

Figure 2-13. Fitting curve and test data for the Class A 2×2 surface.

Table 2-2. Parameters of the adopted friction model for Class A faying surface.

Faying surface	*a*	*b*	*k*
Class A 2×2	0.81	-2949	6
Class A 2×3	0.67	-1952	6

The load-displacement curves obtained from the FE models and the corresponding experimental results for bolted-only connections are plotted in Figure 2-14. For both faying surfaces, the FE models predicted the stiffness of the connection with less than 10% error. The difference between the FE behavior and the experimental one in terms of the force carried by the connection at higher slip loads is minor, which indicates a good ability to capture the slip behavior of bolted connections. One thing that was observed in Soliman et al. (2021) is the high variability in the slip behavior of Class A connections with the 2×3 bolt pattern and Class B bolted-only

connections. It is attributed to the natural variability associated with the surface conditions of these plates, which is not considered in the numerical analysis.

For modeling the weld behavior, the average slip level associated with fracture initiation and final failure were obtained from the experimental results of welded-only tests, which are 1.27 mm (0.05 in) and 3.05 mm (0.12 in), respectively. Next, a FE model of the welded-only connections is established without implementing ductile fracture model to obtain the history of equivalent plastic strain and stress triaxiality. By substituting the obtained history of equivalent plastic strain and stress triaxiality into the Equation 2-2, the parameter α can be calculated for the welded-only FE model as shown in Table 2-2. A linear weld damage evolution model for the welded-only connections was adopted and the equivalent plastic displacement at failure was taken as the difference between the slip level associated with weld fracture initiation and final failure, i.e., 1.78 mm (0.07 in).

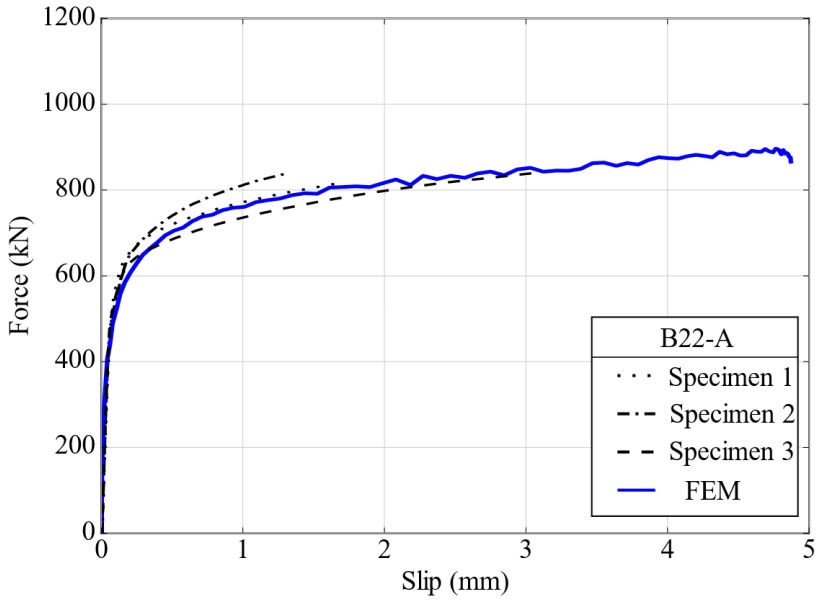
1200
1000
800
600
400
200
0
Force (kN)
0
1
2
3
4
5
Slip (mm)
B22-A
Specimen 1
Specimen 2
Specimen 3
FEM

(a)

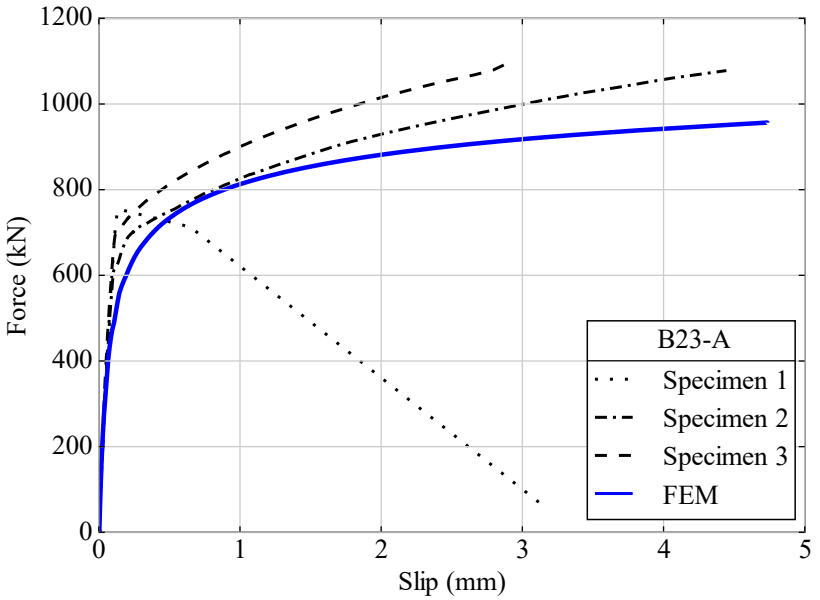
1200
1000
800
600
400
200
0
Force (kN)
0
1
2
3
4
5
Slip (mm)
B23-A
Specimen 1
Specimen 2
Specimen 3
FEM

(b)

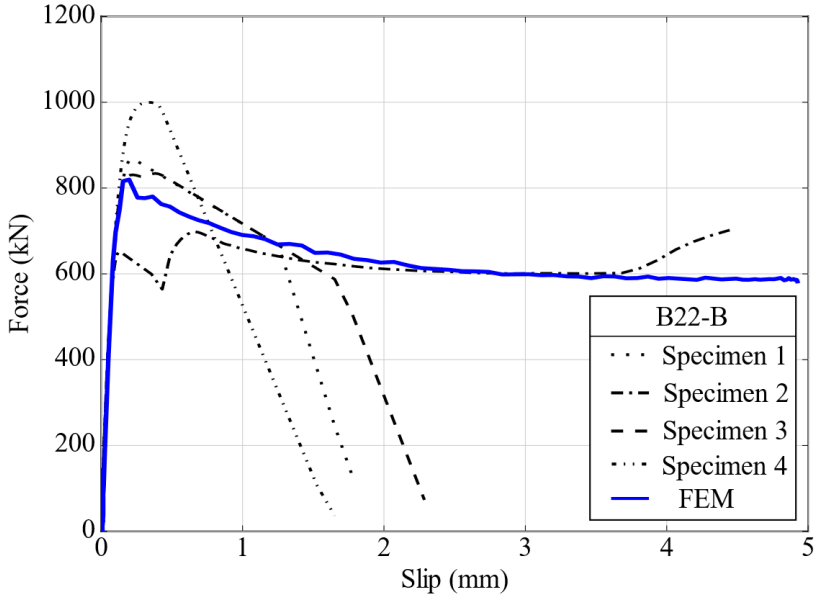

(c)

Figure 2-14. Comparison of load-displacement curves from FE models and bolted-only tests for (a) Class A 2×2, (b) Class A 2×3, and (c) Class B connections.

Figure 2-15 compares the load-deformation behavior of welded-only connection obtained from the FE model to the experimental one. As shown, the stiffness and ultimate strength obtained from the welded-only FE model were within 5% from those obtained experimentally. A noticeable difference between the FE-obtained and experimental load-displacement curves can be seen for the samples with 102 mm (4-in) welds. After examining the as built-test data, it was found that the average weld throat area of the specimen with a high capacity was 6% higher than the other specimen. If the weld size increases as the actual size in the FE model, a higher capacity from the numerical simulation can be reached.

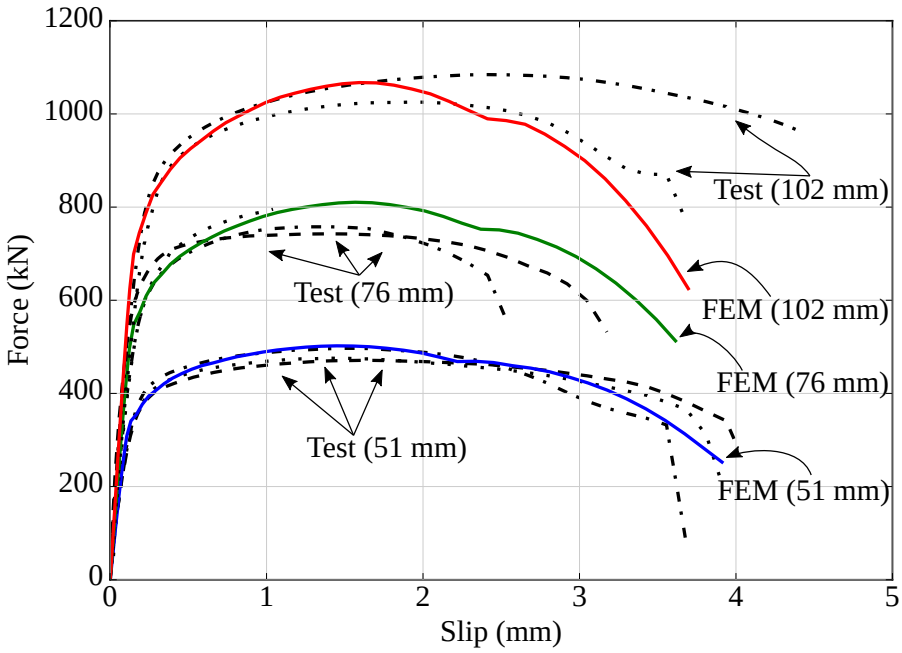

Figure 2-15. Comparison of load -displacement curves from FE models and welded-only tests.

To study the impact of bolt pretensioning on the strength and ductility of the welds, two additional experiments were conducted. In these additional experiments, grease was applied to the faying surfaces to minimize the contribution of friction force to the overall connection behavior. The results of these two tests are shown in Figure 2-16. The first additional test involved a 2×2 bolted-only specimen with greased surfaces (i.e., profile [b] in Figure 2-16) and the second one used the same plates and bolt configuration, but with four lines of 76 mm (3-in) fillet welds (i.e., profile [a] in Figure 2-16). The figure also shows the load-displacement profile resulting from subtracting the bolted-only profile from the one obtained from testing the combination connection with greased surfaces (i.e., profile [c] in Figure 2-16). The results obtained from welded-only connections with 76-mm fillet welds are also included in the figure. As shown, the ultimate capacity of the welded-only connections properly matches that of the welded-only portion of the

combination connection (see profile [c] in Figure 2-16). However, the existence of pretensioning force leads to a significant improvement in the weld ductility.

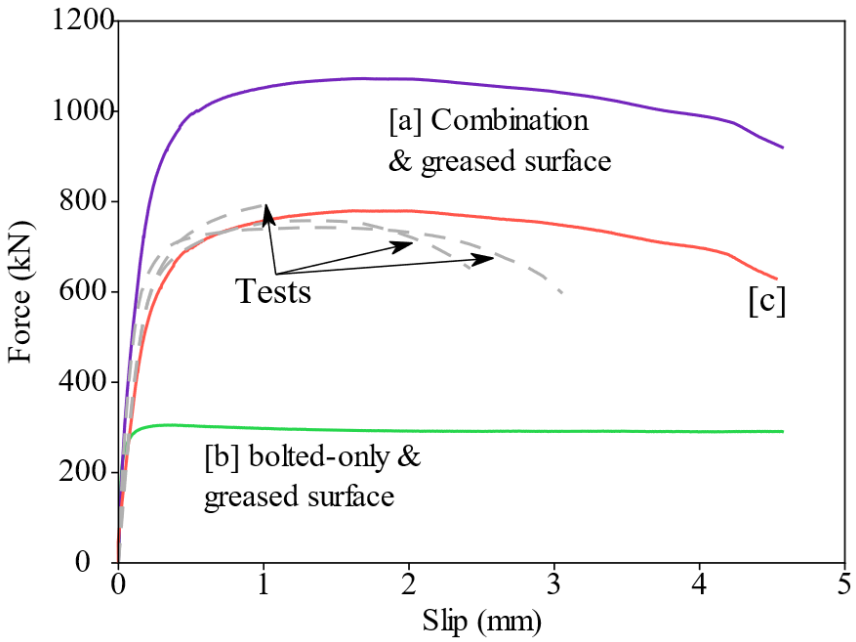

Figure 2-16. Ductility difference between welded-only and combination connections.

Videos were recorded during these tests to capture the fracture process, and the fracture initiation and final failure of connections W102 and B22-B-W89-R1.0 are shown in Figure 2-17. The crack initiation for the welded-only and combination connections occurred around the same slip level. Figure 2-17 shows the typical crack initiation of the weld lines. After crack initiation, the crack in the welded-only connection propagated rapidly resulting in a sudden failure of the specimen. However, as captured by the video, the weld crack in the combination connection experienced stable, gradual growth until a full crack is reached at approximately 89 mm (3.5-in). The rate of the failure of the welded-only connection is much faster and similar to an impact load. The existence of the bolts in the combination connections helps to reduce the failure rate of the welds, which is close to a quasi-static testing. Grimsmo et al. (2017) conducted impact and quasi-static tests for fillet welds with longitudinal and transverse directions. The ductility of the longitudinal welds under the impact loading was reported only half compared to those under the quasi-static

loading; the strength didn't change significant due to the different load rates. It is consistent with the results from the weld-only and combination connections.

The FE models for the combination connections with 2×2 and 2×3 bolt patterns were established based on the calibrated parameters from bolted-only and welded-only FE models and the load-displacement curves were also compared to the corresponding experimental tests. To account for the improvement in ductility of the combination connections as discussed above. The linear damage evolution relationship used in the welded-only connection is modified and added a horizontal part, as shown in Figure 2-18. The horizontal part represents the improved ductility of the combination connection. The length of the horizontal part is 1.2 mm (0.05-in) which is the difference of the slip distance at fracture between welded-only and combination connections. The other parameters of the weld damage evolution model from the welded-only FE model were utilized in the combined FE models, as shown in Table 2-3.

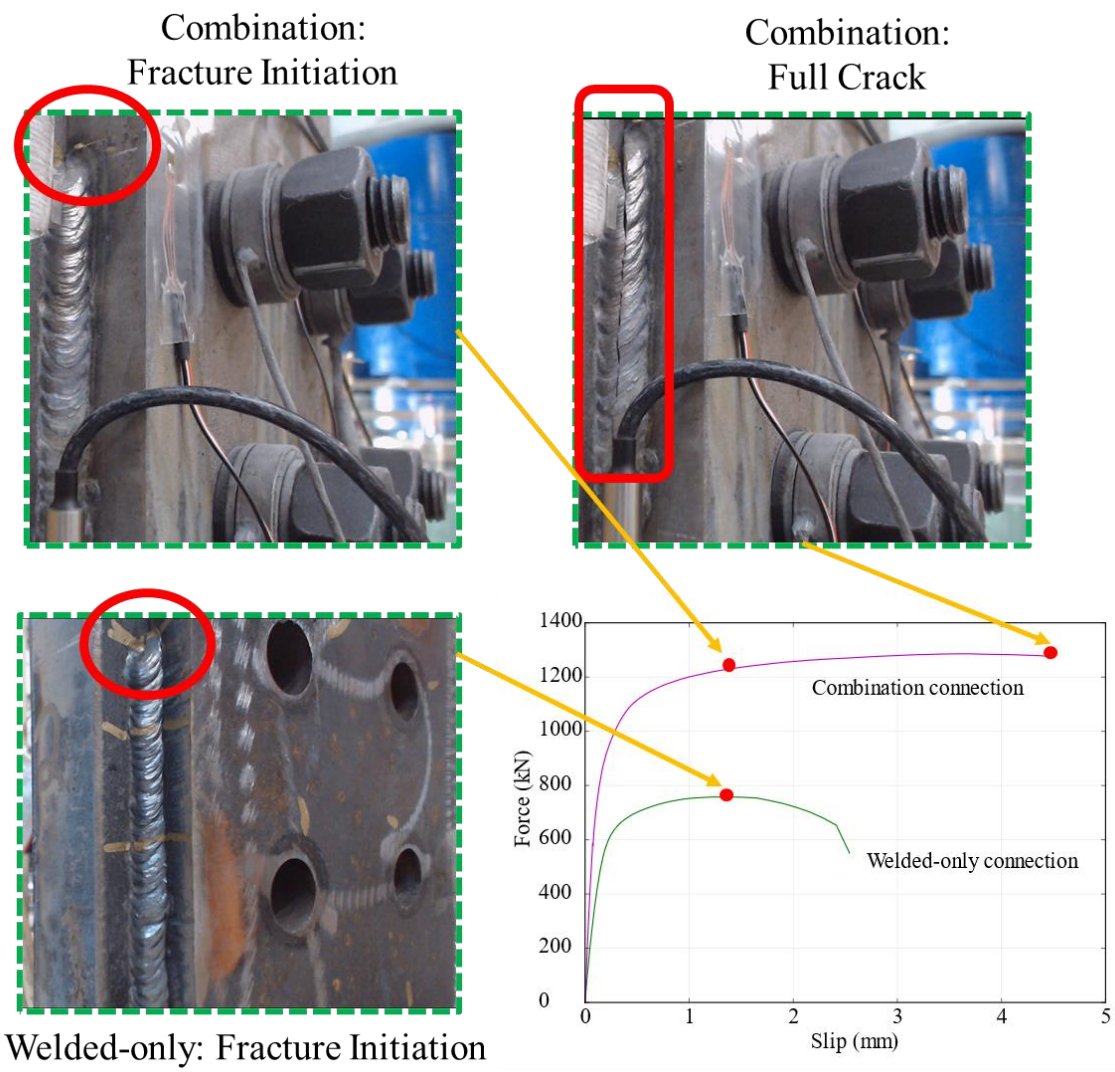

Figure 2-17. Fracture comparison of welds in the welded-only and combination connections.

Table 2-3. Parameters for weld ductile fracture model.

Connection type	α	u_{eq_f}	d_1	u_{eq_1}	u_{eq_2}
Welded-only	0.1	1.8 mm	-	-	-
Combination	0.1	3.0 mm	0.286	0.5 mm	1.8 mm

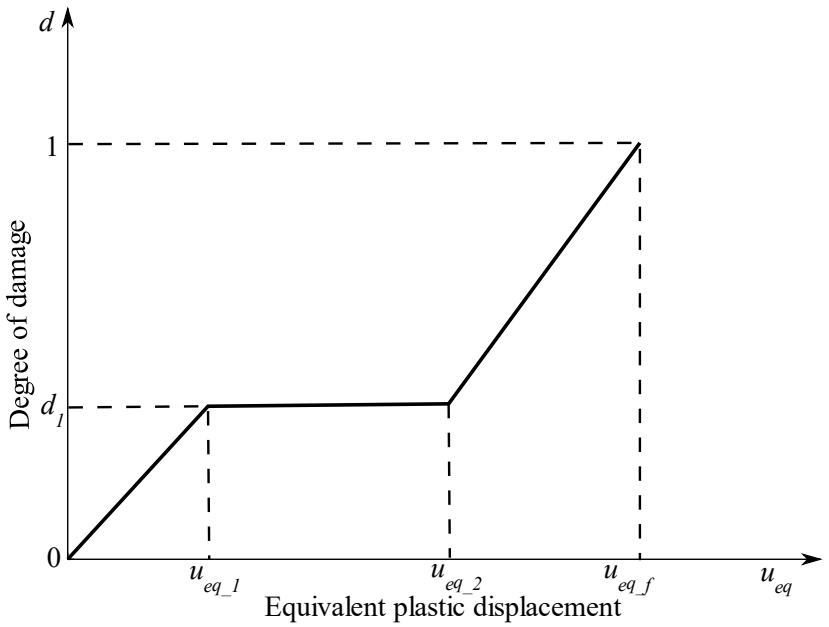

Figure 2-18. Weld damage evolution of the combination connection.

The load-displacement curves of the welded-bolted FE models for Class A with 2×2 bolts and four 51 mm welds, Class A with 2×3 bolts and four 76 mm welds, and Class B with 2×2 bolts and 89 mm welds are plotted in Figure 2-19 along with corresponding experimental data to illustrate the ability of the FE model to predict the behavior. For Class A 2×2 and Class A 2×3 connections, the load-displacement curves of the FE models closely follow the experimental behavior with respect to stiffness, strength, and ductility. For Class B 2×2 connections, the numerically obtained ultimate load follows that of the lower two samples, while the stiffness and ductility still follow the trend in the experimental tests. This can be attributed to the high variability in the friction characteristics of the Class B faying surfaces which propagated to the combination connections.

Overall, the numerical simulations utilizing the adopted surface friction and weld ductile damage fracture models were capable of predicting the load-displacement behavior of the combination connections with high-strength pretensioned bolts and longitudinal fillet welds under shear loading.

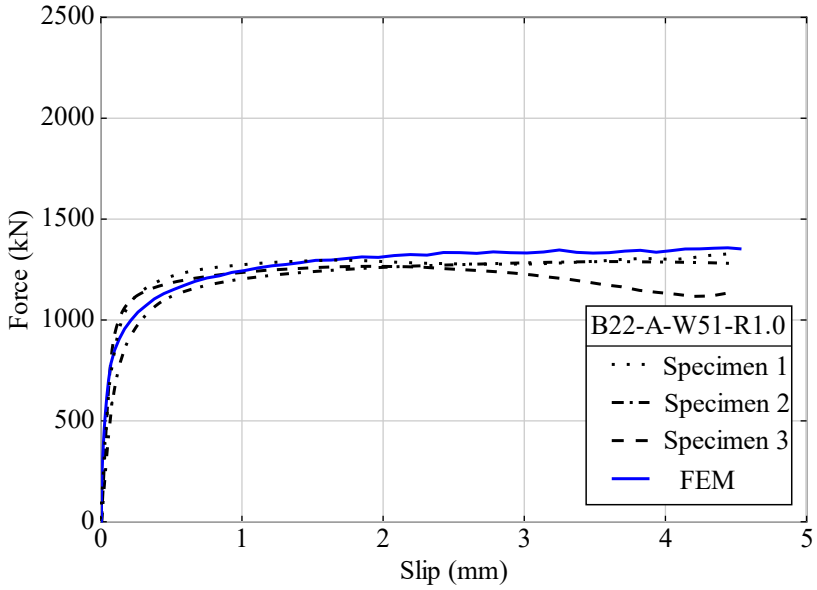
2500
2000
1500
1000
500
0
Force (kN)
0
1
2
3
4
5
Slip (mm)
B22-A-W51-R1.0
Specimen 1
Specimen 2
Specimen 3
FEM

(a)

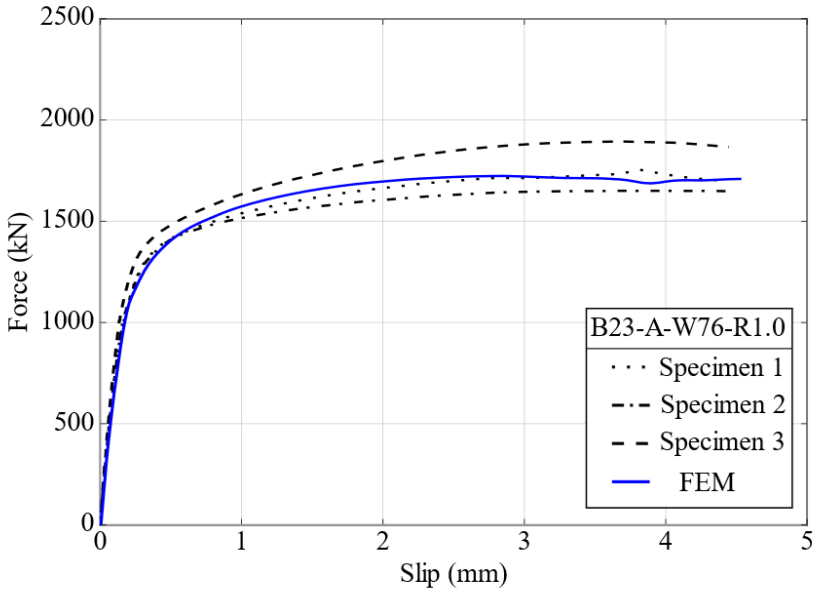
2500
2000
1500
1000
500
0
Force (kN)
0
1
2
3
4
5
Slip (mm)
B23-A-W76-R1.0
Specimen 1
Specimen 2
Specimen 3
FEM

(b)

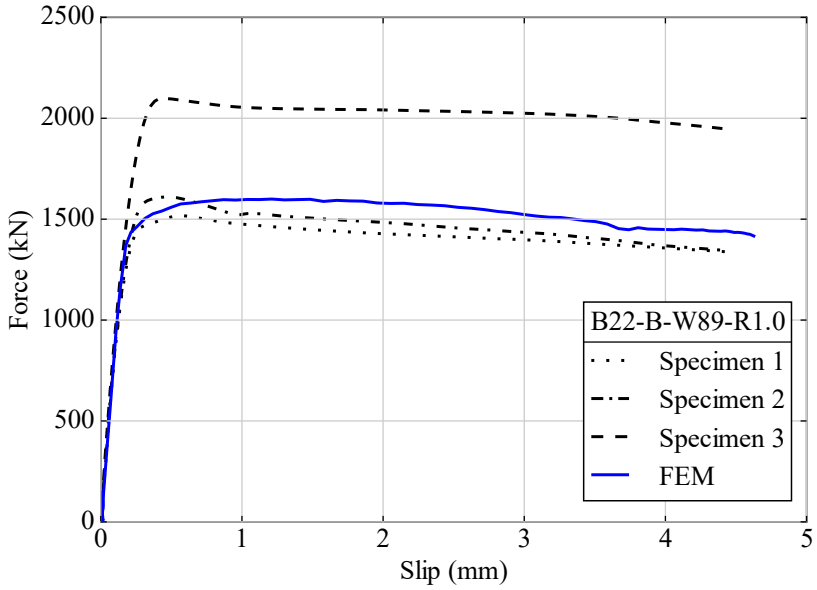

(c)

Figure 2-19. Comparison of load -displacement curves from FE models and combined tests for (a) Class A 2×2, (b) Class A 2×3, and (c) Class B connections.

2.5 Discussion

The validated numerical simulation is next used to explore different configurations of critical variables, e.g., connection size, weld location, weld size, and to investigate the impact of combination on stress distribution within connected plates.

2.5.1 Behavior of Large Combination Connections

The numerical simulation is conducted for large combination connections with 4×6 bolt pattern and four 8 mm (5/16-in) fillet welds with length of 432 mm (17-in). The material parameters adopted for the 2×2 and 2×3 models are also utilized in this model. To ensure that the same observations apply to large combination connections, the load-displacement curves of bolted-only and welded-only connections from the FE models are added, and the curves are compared to the results of the large combination connections. The comparison of the load-displacement curves is plotted in Figure 2-20. As shown in the figure, the summation curve matches the behavior at low

displacement levels. This indicates that at low slip levels (e.g., 0.5 mm), the force in the combination connection can be reliably estimated by adding the resistance of the corresponding bolted-only and welded-only connections. At higher slip levels, the behavior is significantly different due to the impact of the pretensioning-induced slip resistance on the weld ductility.

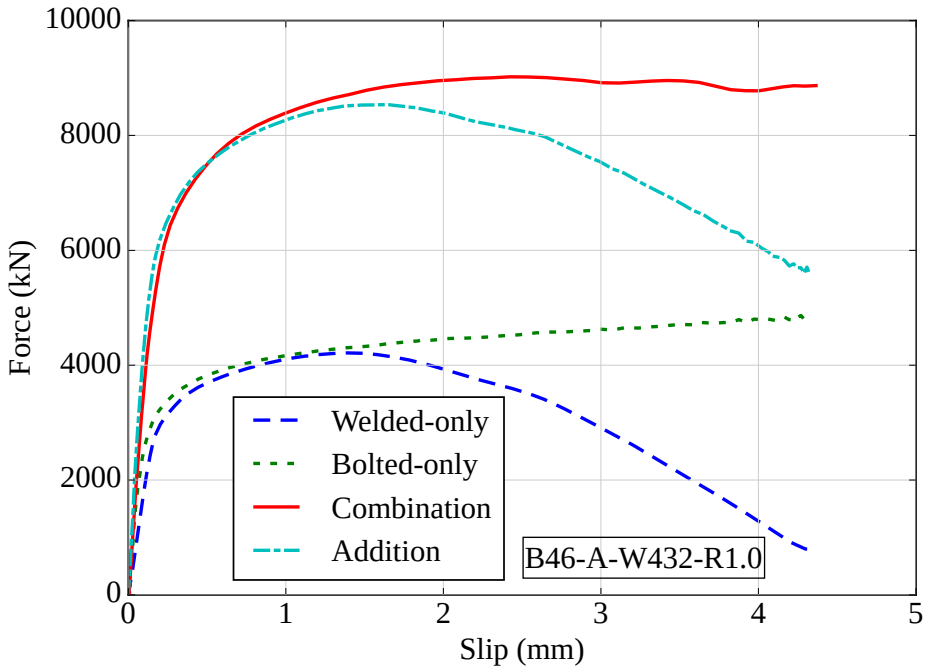

Figure 2-20. Comparison of load-displacement curves from FE models for Class A 4×6 connections.

2.5.2 Stress Distribution within the Steel Plates

The steel plates in the bolted-only and welded-only connections are normally designed against several possible failure limit states (e.g., fracture and block shear). The combination of welds and bolts improves the capacity of the connections and can influence the stress distribution in the steel plates. This can affect the resistance of the steel plates with respect to different failure limit states. Figure 2-21 and Figure 2-22 show a comparison of the stress distribution within the splice plates of Class A 2×3 and 4×6 connections for three cases: (a) the welded-only model at its ultimate

load capacity, (b) the combination model at the ultimate load capacity of the corresponding welded-only model, and (c) the combination model at its ultimate capacity. From Figure 2-21 (a) and Figure 2-22 (a), it can be noticed that the plasticity within the splice plate of the welded-only model is mainly concentrated around the welding area of the welds, while the stresses at the center of the plate are significantly lower. As shown in Figure 2-21 (b) and Figure 2-22 (b), for the combination connection at the same load level, this plastic zone disappeared, and stress increased around the inner bolts. This indicates that the pretensioning-induced friction causes stress redistribution and actively assists the welds in the force transfer.

It can also be seen from Figure 2-22 that the combination of bolts and welds can significantly increase the stress level along the cross-section of the inner bolts. Figure 2-21 (c) and Figure 2-22 (c) show the increase in the stress level at the ultimate capacity of the combined model compared to the welded-only model. A yield trend forms at the whole section of the inner bolts area which indicates a potential failure of the splice plate. Accordingly, the combination of bolts and welds could help distribute the stress evenly in the steel plates; however, with the improvement in connection capacity, it is essential to ensure that the steel plates will not experience other failure modes (e.g., tensile yielding or rupture failure). Note that for the tested 2×3 connections, the nominal yield and rupture failure loads (AISC, 2016) are estimated as 1882.8 kN (423.3 kips) and 2039.8 kN (458.6 kips), respectively, which are lower than the maximum load of 2255.1 kN (507.0 kips) applied during the testing program.

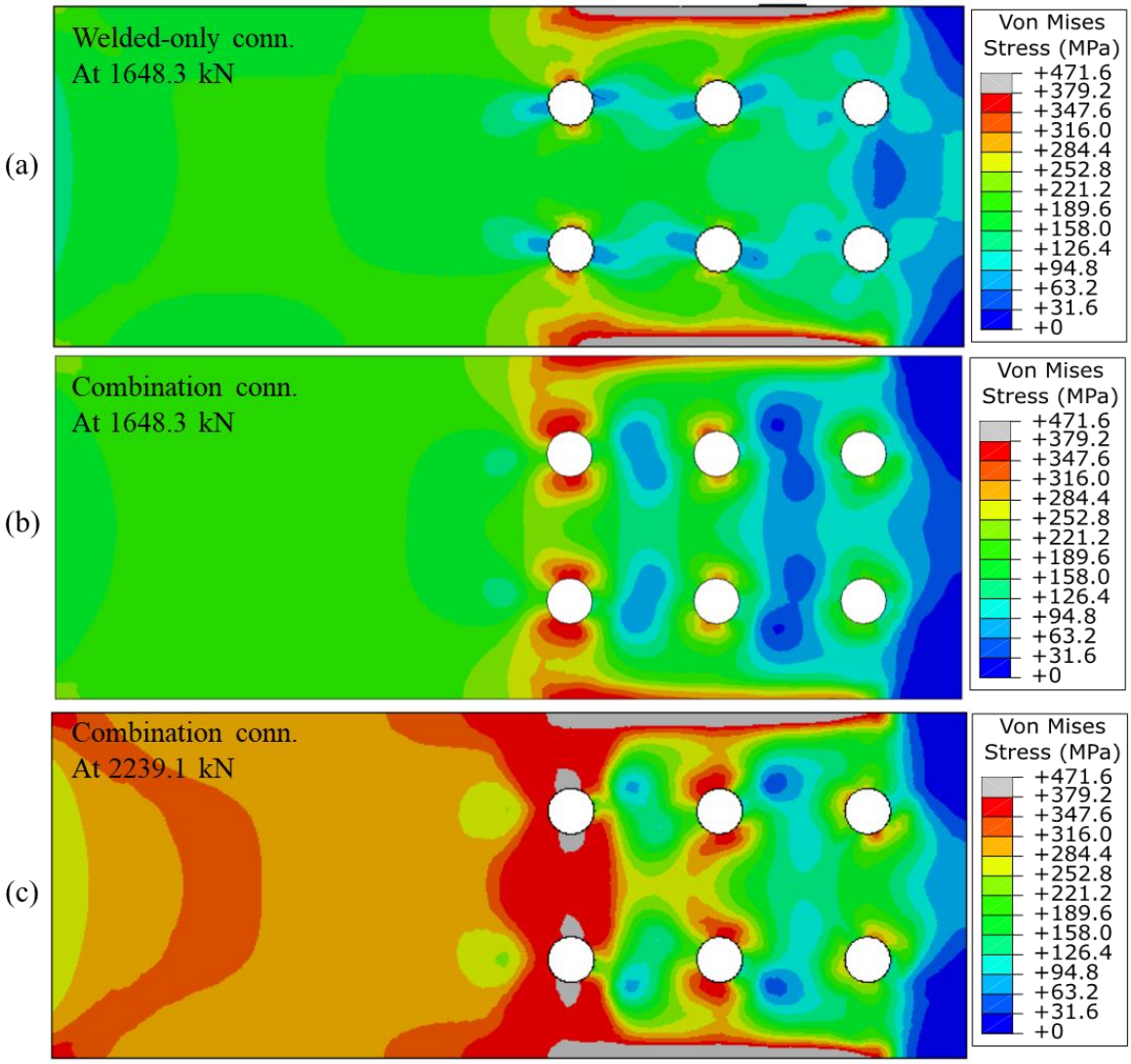

Figure 2-21. Comparison of the stress distribution within the splice plates of Class A 2×3 for three cases: (a) the welded-only model at its ultimate load capacity, (b) the combination model at the ultimate load capacity of the corresponding welded-only model, and (c) the combination model at its ultimate capacity.

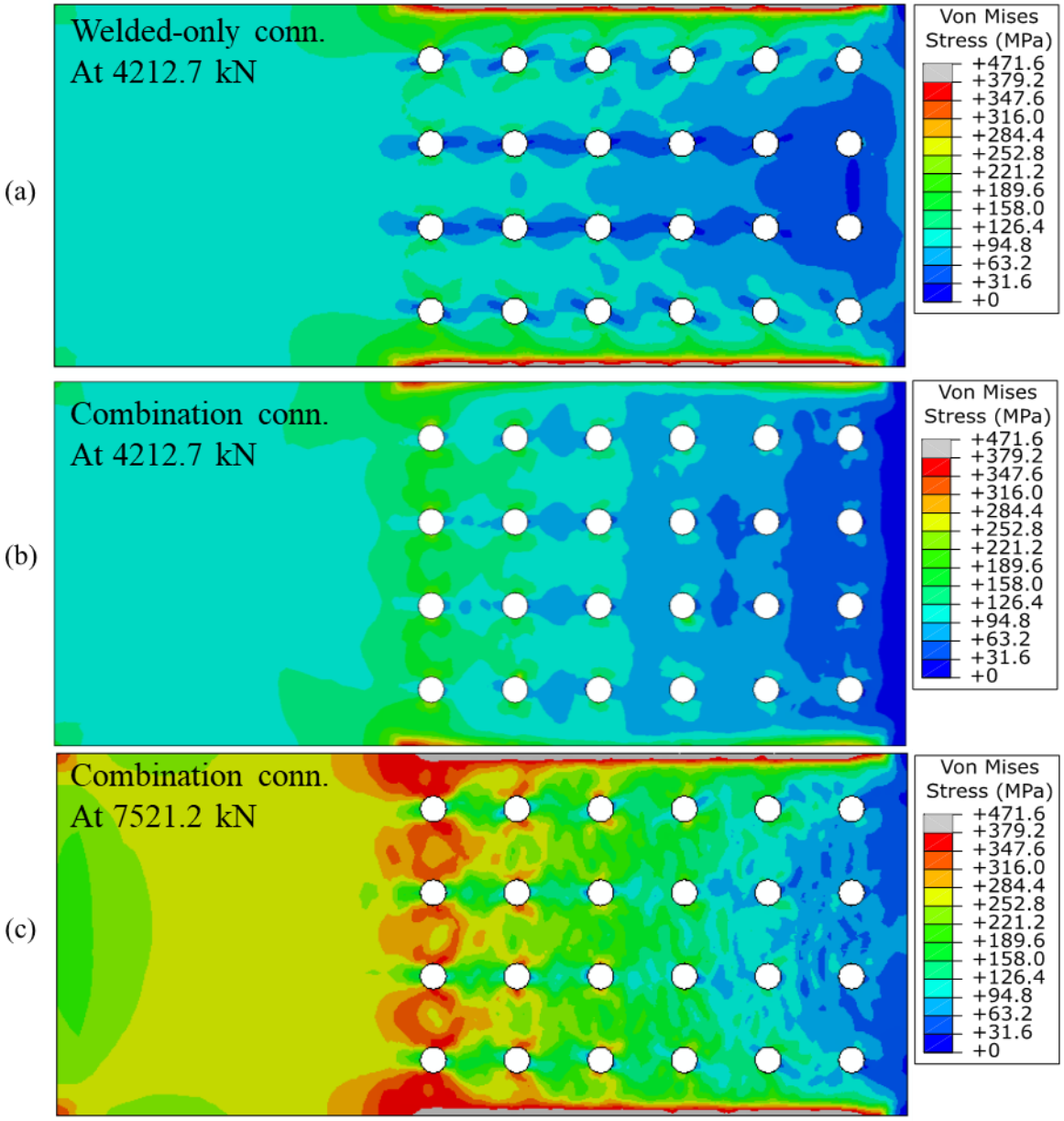

Figure 2-22. Comparison of the stress distribution within the splice plates of Class A 4×6 for three cases: (a) the welded-only model at its ultimate load capacity, (b) the combination model at the ultimate load capacity of the corresponding welded-only model, and (c) the combination model at its ultimate capacity.

2.5.3 Weld Location

Throughout the experimental program, the weld lines were always located at the center of the bolt group as shown in Figure 2-6. To investigate the effect of weld location on the behavior, three identical models based on B23-A-W76-R1.0 are established with three different weld locations. In Case *i*, the center of the welds aligns with the inner bolts, Case *ii* has the center of the welds aligning with the middle bolts, and Case *iii* has the center of the welds aligning with the outer bolts. The stress distribution of the splice plate for these three locations at the ultimate capacities is plotted in Figure 2-23. As expected, the weld location will affect the stress distribution within the plates. The Case *ii* and *iii* reveal a larger stress concentration around bolt holes compared to Case *i*. Based on previous discuss, the section along the inner bolts was the most vulnerable area in the splice plate. The stress through the weld contact area in Case *ii* and *iii* could be fully transferred to the section along the inner bolts, while only partial stress can go through the section in Case *i*. For the center plate, however, the outer bolts are the most vulnerable area; the center of the welds should align with the outer bolts to reduce the stress concentration if the center plate is weaker than the splice plates. The load-displacement curves of the three models are compared in Figure 2-24. As shown, the three models display a similar load-displacement behavior. This implies that the weld location has low influence on the capacity of the connections as long as the plates are properly designed to transfer the maximum expected connection force. The results indicate that the welds can help to reduce stress concentration if the welds are added to the weak locations of the steel plates.

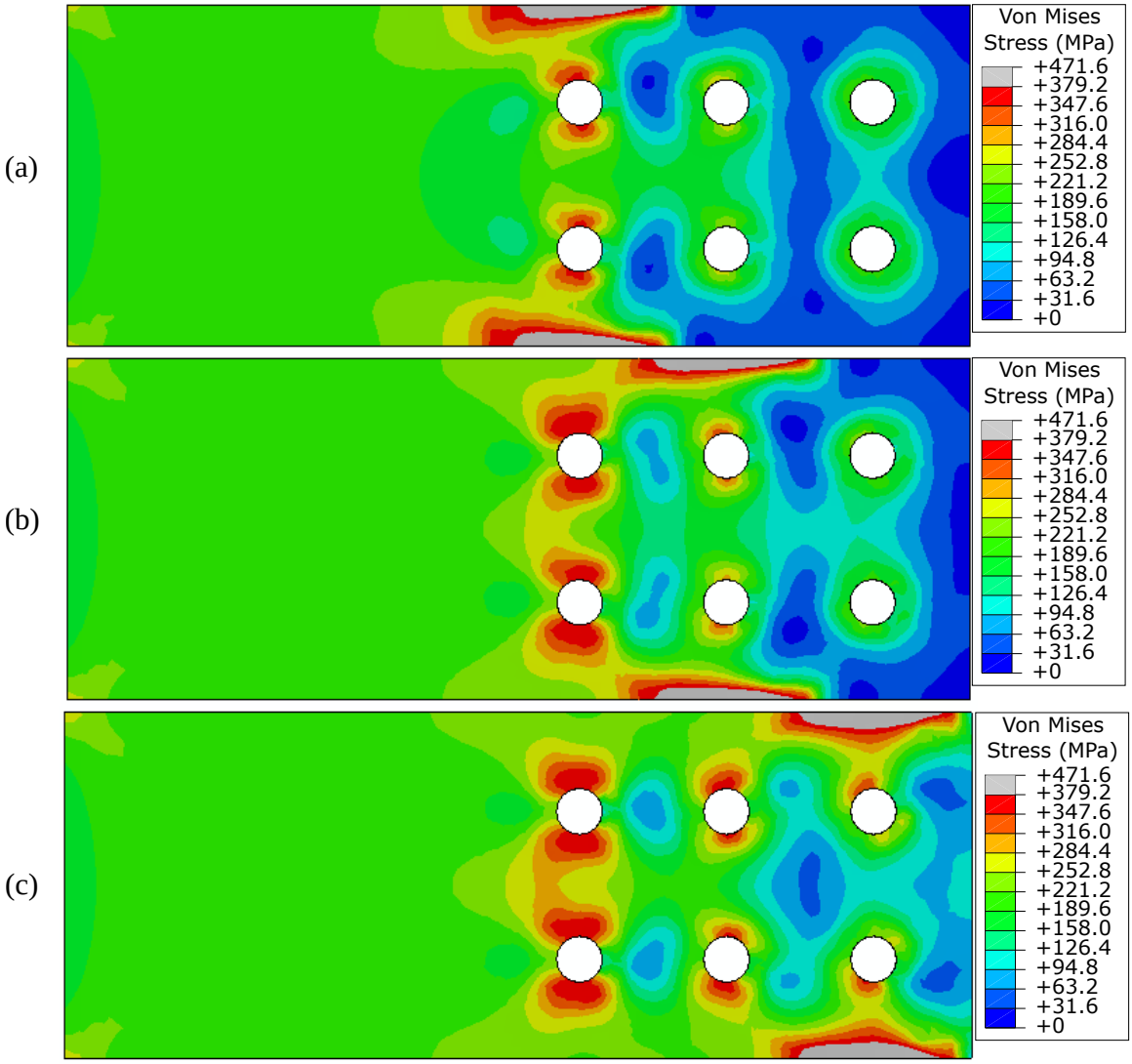

Figure 2-23. Stress distribution of the splice plate at ultimate capacities in Class A 2×3 connections when the center of the welds aligns with (a) the inner bolts, (b) the middle bolts, and (c) the outer bolts.

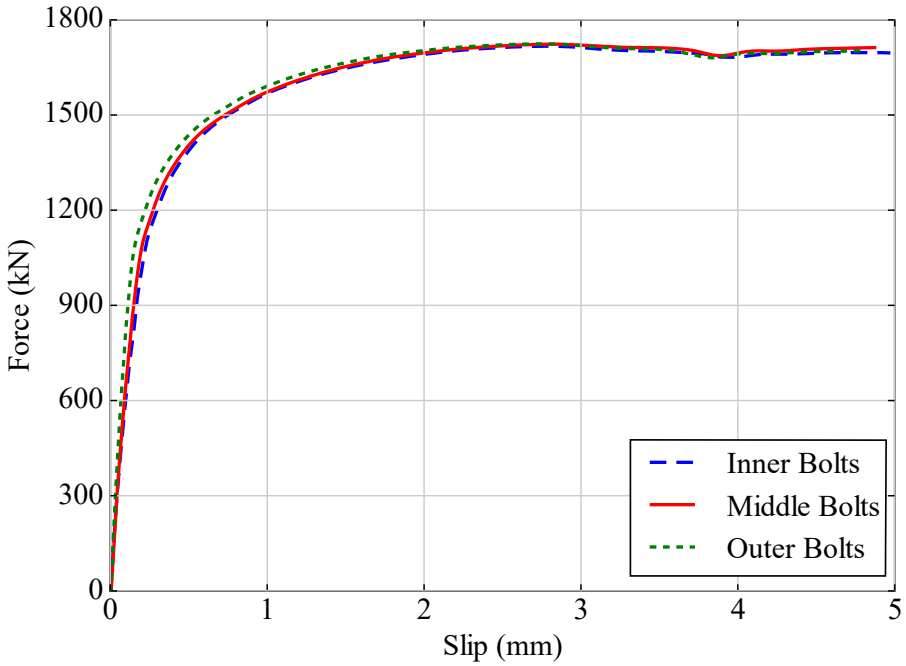

Figure 2-24. Weld location effect on the load-displacement relationship for Class A 2×3 combination connections.

2.5.4 Weld Size

FE models of combination connections with different weld sizes other than 8 mm (5/16-in), i.e., 6 mm (1/4-in), 13 mm (1/2-in), 19 mm (3/4-in), and 25 mm (1-in) are established. The corresponding bolted-only and welded-only connections are also simulated. The same parameters used in the previous analysis are utilized in these models. The load-displacement curves from the FE models with the weld size of 13 mm (1/2-in) are plotted in Figure 2-25 as an example to evaluate the weld size effect on the behavior of the combination connections. As shown in the figure, the summation curve matches the behavior at low displacement levels. This indicates that at low slip levels (e.g., 0.5 mm), the force in the combination connection can be reliably estimated by adding the resistance of the corresponding bolted-only and welded-only connections. At higher slip levels, a similar ductility increase is observed for the combination connections compared to the addition curve.

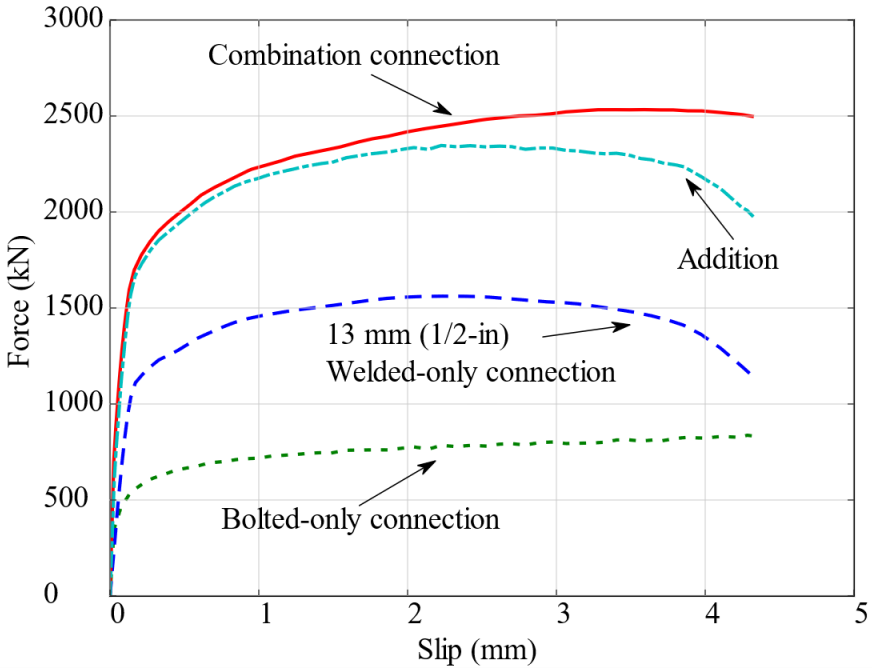

Figure 2-25. Comparison of load-displacement curves from FE models for combination connections with 12.7 mm (1/2-in) weld size.

2.5.5 Predicting the Behavior and Capacity of Combination Connection

Per AISC (2016), the nominal strength of the combination connection is calculated as the summation of the separate nominal slip resistance of bolts and weld ultimate capacity. However, based on the discussion above, the nominal strength for different connecting elements does not occur at the same deformation levels. Accordingly, the direct summation of these two capacities may not properly consider strain compatibility within connecting elements. This is highlighted in Figure 2-26 which shows typical load-displacement profiles of different connecting elements investigated in this dissertation. As seen, the ultimate capacity of the welds occurs at higher deformation level compared to bolted connections; especially those utilizing blast cleaned surfaces. To maintain strain compatibility, Waite et al. (2022) proposed computing the capacity of combination connections as

$$R_n = R_b + C_w R_w \quad \text{Equation 2-9}$$

where R_b is the capacity of the pretensioned high-strength bolts; R_w is the capacity of the longitudinal fillet welds; C_w is the strain compatibility parameter to account for the actual force carried by the welds at the slip event of the connection, which is defined as the ratio of the weld shear stress at 0.5 mm (0.02-in) of slip to the ultimate weld shear strength. The value of C_w mainly depends on the weld size and can be computed analytically based on the load-displacement relationship for welded connections following the models in Lesik and Kennedy (1990) or AISC (2017). Based on Lesik and Kennedy (1990), the value of the strain compatibility parameter C_w could reach 0.65 for welds with 25 mm (1-in) size leading to significant reduction in the weld contribution to the capacity of a combination connection. However, most of experiments reported in literature and used to develop this load-deformation prediction model for welds were conducted on fillet welds that are less than 13 mm (0.5-in) in size (e.g., (Butler & Kulak, 1971; Quinn, 1991). The load-displacement behavior of welds with larger size was derived linearly from the welds with smaller size which might overestimate the effect of weld size on the load-displacement behavior of welds.

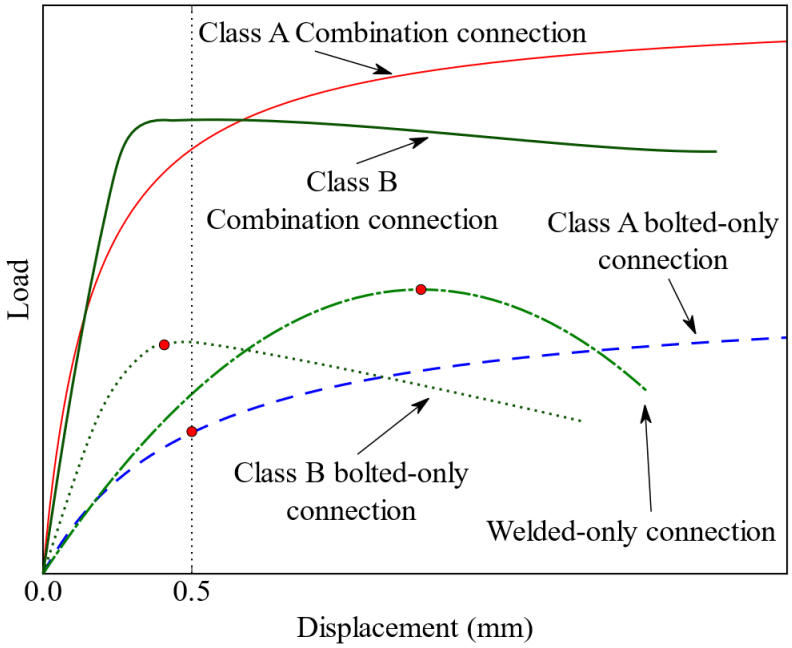

Figure 2-26. Sketch of load-displacement curves of bolted-only, welded-only, and combination connections.

A series of welded-only FE models with different weld sizes were established and the load-displacement relationships are shown in Figure 2-27. The value of C_w was obtained from the FE models as the ratio between the weld stress at 0.5 mm (0.02-in) of slip to the ultimate weld shear strength. A fitting equation of the strain compatibility parameter C_w is given as below based on the FE results

$$C_w = -0.0056w + 0.9192 \qquad \text{Equation 2-10}$$

where w is the weld size (mm).

Figure 2-28 shows the relationship of strain compatibility parameter C_w and weld size from literature Lesik and Kennedy (1990) and FE models. For smaller welded connections, the strain compatibility parameter between Lesik and Kennedy (1990) and FE models is close while the

difference becomes much larger when it comes to weld size over 13 mm. The difference could be caused by that the experimental data from Lesik and Kennedy (1990) was collected from small fillet welded connections. The inconsistency in the strain compatibility parameter indicates that more experimental work of large fillet welded connections should be investigated in future work.

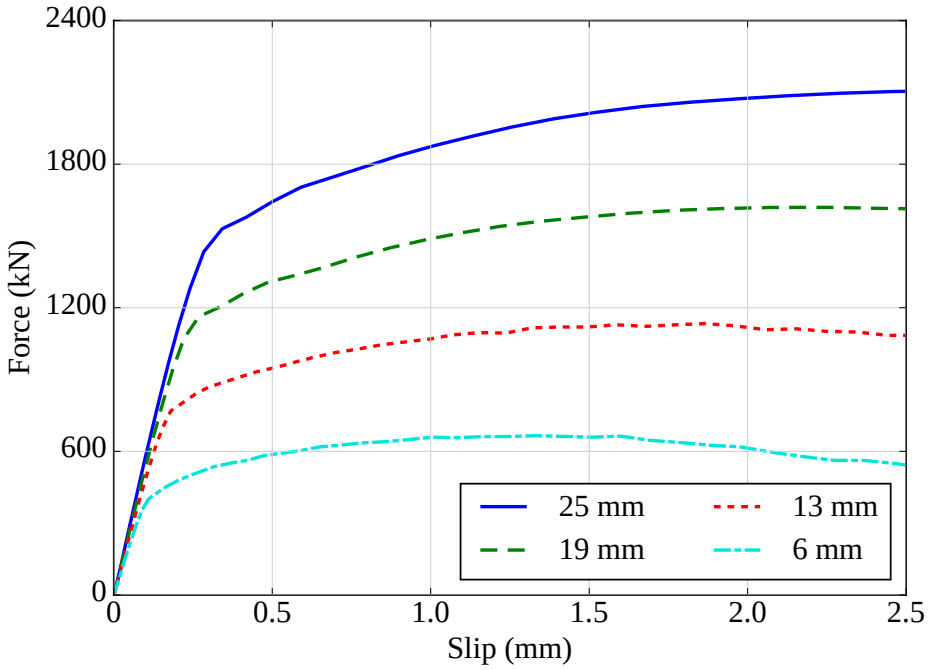

Figure 2-27. Weld size effect on the load-displacement relationship for welded-only connections.

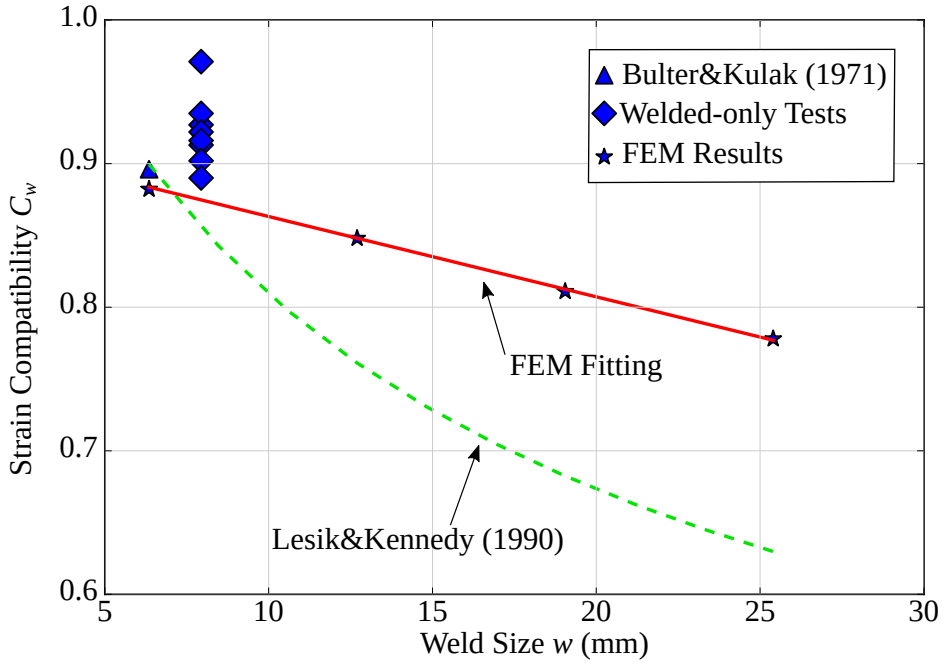

Figure 2-28. Relationship between weld size and strain compatibility.

2.6 Conclusions

This chapter presented the results of numerical analysis of combination connections with pretensioned high-strength bolts and longitudinal fillet welds. Different configuration of critical variables including connection size, weld dimensions, weld/bolt strength ratio, and faying surface condition were analyzed. The FE models were established for different configurations and were validated against the corresponding experimental results. The numerical results showed a good agreement with the experimental data. The effect of weld dimensions and location on the load-displacement behavior and stress distribution within the plates was also quantified. The following conclusions were drawn based on the previous discussions:

1. Comprehensive FE models including surface frictional model and weld ductile fracture model were established and validated for the combination connections with pretensioned high-strength bolts and longitudinal fillet welds; the behavior of the combination connections was accurately simulated using FE models.

2. The developed surface frictional models were able to properly capture the slip behavior of connections utilizing both Class A and Class B faying surfaces. These models can be integrated into numerical analysis of connections or can be used analytically to predict the connection displacements at working loads.
3. The numerical simulation results confirmed that at low slip levels, the resistance of the combination connection can be estimated as the summation of the capacities of bolts and welds for all the weld/bolt strength ratio and connection types considered.
4. The investigation results showed that, for the analyzed connections, when fillet welds are combined to a bolted connection with properly pretensioned high-strength bolts, the ultimate capacity of welds is expected to remain at the same levels of a welded-only connection; however, the deformation level at which ultimate weld fracture occurs is expected to be higher than that of a welded-only connections. This can be attributed to the sudden failure of the welds in the welded-only connections while the existence of the bolts in the combination connections helps smoothing the failure process of the welds.
5. The combination of fillet welds to a slip-resistant bolted connection causes a redistribution in the stress fields within the steel plates. Similar to a bolted connection, the plate cross-section at the inner bolt line experienced the highest stress levels. With the increase in the connection capacity, it is essential to ensure that the steel plates have enough strength to prevent failure under other limit states.
6. Numerical simulation indicates that the weld location respect to the center of the bolts has low influence on the behavior of the combination connections. The existence of welds, however, will redistribute the stress within the plates. It could help to reduce the stress concentration if the welds are added to the weak section of the steel plates.

CHAPTER III

AUTOMATED VISION-BASED FATIGUE CRACK GROWTH MONITORING BASED ON BACKGROUND SUBTRACTION

3.1 Introduction

Crack detection and measurement are critical tasks during experimental fatigue life investigations. Results from these tasks can be used to compute the fatigue crack growth rate and obtain threshold information needed to evaluate the material behavior and predict its service life. Traditional optical, compliance, and electric potential difference (EPD) methods are commonly utilized in the laboratory to measure fatigue crack size per ASTM 647 (ASTM Standard E647, 2015). Other common methods, e.g., infrared thermography and digital image correlation (DIC) are operated in both laboratory-based and in-field tests. These methods generally comply with the fatigue crack growth monitoring requirements; however, some drawbacks may also exist depending on the investigated application.

Traditional optical method normally employs a traveling microscope and can provide an accurate measurement of the crack size. However, this process can be time-consuming and may require human intervention and test interruption, in addition to the difficulties associated with its automation (Bär, 2020; Shanmugham & Liaw, 1996). Furthermore, the accuracy of optical methods is subjected to human errors despite the high resolution provided by the microscope

(Clark & Hudak, 1975). The compliance method is an alternative approach established based on the elastic relationship between the compliance of the specimen and the crack size. Donald and Schmidt (Donald & Schmidt, 1980) presented an automated test system that integrates the elastic compliance technique for a compact specimen C(T) (ASTM Standard E647, 2015). The study indicated that the required crack size measurement accuracy could be satisfied by averaging the slopes of successive load-displacement data points within the linear zone of load cycles. Nevertheless, the slope during a load-displacement cycle could change due to the crack closure effect or negative loading condition. As a result, applying the approach becomes difficult for variable amplitude loading since crack closure commonly occurs during compressive and low tensile loading. The EPD method includes direct and alternating current forms (i.e., DC and AC, respectively). The DC potential drop method (DCPDM) is an easily automated and widely used approach for determining the crack length in fatigue experiments(Bär, 2020; Funk & Bär, 2019; Johnson, 1965; Lambourg et al., 2020). However, there is a possibility of electrochemical interference near the crack tip that could lead to corrosion. Accordingly, errors may arise when calculating the stress intensity factor for cases that require an accurate identification of the crack tip location (Shanmugham & Liaw, 1996).

Thermoelastic stress analysis is another non-contact crack detection method that is based on infrared thermography. Middleton et al. (Middleton et al., 2019) developed an automated crack tracking method by combining thermoelastic stress analysis and optical flow algorithm. The process successfully detected the crack during the initiation process before it was visible. However, the error in locating the crack tip position could reach 1 mm; accordingly, this method could be more suitable for field applications. Durif et al. (Durif et al., 2012) applied DIC to measure the crack size and control load shedding during fatigue crack propagation tests. The crack length was estimated in a real-time manner with DIC, and the results were validated using the EPD method. The DIC provides a non-contact, real-time fatigue crack growth monitoring

solution that is easier to implement compared to other contact-based methods. One of the shortcomings of DIC is the high expenses associated with the required equipment and software. Furthermore, the quality of the speckle pattern applied to the surface of the specimen has a significant effect on the measurement accuracy.

On another front, computer vision (CV) algorithms have been developed over the past decades to assist in solving research problems in different fields including operation of autonomous vehicles (Janai et al., 2020), construction (Xu et al., 2021), and structural health monitoring (Feng & Feng, 2018). For FCG monitoring, the crack can be treated as an edge feature that can be detected with appropriate image processing algorithms. Yeum and Dyke (Yeum & Dyke, 2015) proposed a vision-based automated crack detection for bridge bolt inspection based on Canny edge detection (Canny, 1986) and Frangi filter (Frangi et al., 1999). The method utilized images from many different angles and prior knowledge of the typical visual characteristics of the cracks forming around bolts in bridges. Since the main research focus in Yeum and Dyke (Yeum & Dyke, 2015) was to detect cracks during field inspections, information about the crack length was not addressed.

Kong and Li (Kong & Li, 2018) established a vision-based method through video feature tracking which can be used for FCG monitoring and crack opening displacement measurement. The method tracked the surface movement under repetitive fatigue loading through a series of detected feature points on the surface. The opening and closing of the fatigue cracks led to different movement patterns on the surface, which was utilized to determine the crack length and opening displacement. Nonetheless, the crack tip location identified by this method always had an offset compared to the actual location. Sun et al. (Sun et al., 2018) proposed an automatic seed point selection method based on Hough transform (Maji & Malik, 2009) for FCG monitoring. The method can provide a level of accuracy that is comparable to traditional visual inspections. However, the error level associated with their approach makes it difficult to resolve crack

extensions of 0.1 mm as required by ASTM E647 (ASTM Standard E647, 2015). Overall, it is apparent that computer vision algorithms have the potential to provide highly accurate, automated, low-cost, and non-contact approaches for FCG monitoring.

Background subtraction is a widely used computer vision technique that can be implemented for detecting moving or intruding objects in videos recorded by static cameras (Vacavant et al., 2012). The main principle of this technique is to track the value of a given pixel among successive images. If the new value of the pixel can be well described by its established density function, then the pixel is considered to be a part of the background image; otherwise, the pixel is assumed to belong to the moving or intruding object (i.e., foreground). These density functions can become quite complex due to the differences in light conditions. One of the widely adopted algorithms for background subtraction is the Gaussian mixture model (GMM) (Rasmussen, 1999), which can accommodate complex distributions of pixel values in a camera scene. Friedman and Russell (Friedman & Russell, 2013) implemented adaptive parametric GMM with three predefined Gaussian distributions in background subtraction for vehicle detection considering illumination changes. However, their proposed approach lacked robustness when considering extreme light conditions or object intrusion/removal. Stauffer and Grimson (Stauffer & Grimson, 1999) overcame these drawbacks by modeling the value of a particular pixel as a mixture of several adaptive Gaussian distributions. Zivkovic (Zivkovic, 2004) later included an adaptive feature for the number of distributions of the mixture for each pixel, and the new algorithm shows a lower processing time and improved quality.

This chapter proposes an approach for automated fatigue crack growth monitoring through background subtraction technique. It aims at providing an accurate, real-time, non-contact, and cost-effective approach for FCG monitoring and measurement. The crack growth increment between measurement intervals is treated as an intruding object in the image. The GMM algorithm proposed by Zivkovic (Zivkovic, 2004) was adopted for background subtraction due to

its excellent performance in similar problems. In addition, a series of image processing operations (i.e., alignment and filtering) are applied in the proposed approach to enhance its feasibility and accuracy for crack size measurement. The narrow field of view (FOV) of the utilized microscope is expanded to accommodate the entire crack size by automated adjustment of its position based on the detected location of the crack tip. The feasibility of the proposed approach was verified by using middle tension (M(T)) specimens tested under constant and variable fatigue loadings following ASTM E647 (ASTM Standard E647, 2015).

3.2 Crack Monitoring Methodology

The proposed approach utilizes the background subtraction along with several other image processing algorithms to monitor the crack. A corresponding system hardware setup is also established to achieve the desired results of the FCG monitoring methodology. For typical fatigue tests, a series of images can be acquired by a microscope during the test period at fixed intervals. Although the crack growth increments among these images can be treated as intruding objects, several factors may add to the challenges in measuring these increments using the background subtraction. These factors include the low contrast between the specimen surface and crack, narrow camera scope compared to the crack length, and noise arising when images are magnified using the microscope. The following sections discuss the technical details covering the system setup and image processing algorithms designed to address these issues.

3.2.1 System setup

The system setup for the proposed FCG monitoring approach is illustrated in Figure 3-1. The desktop is used to control the crack monitoring process while the hydraulic load testing frame is operated by an MTS® FlexTest SE digital controller. The desktop and the MTS controller have a two-way communication established using a voltage output module manufactured by National Instruments (i.e., NI 9263 module) (NI, 2018) and the built-in input/output module of the MTS® FlexTest SE digital controller. The camera stand was designed such that the height of the camera

(i.e., microscope) can be adjusted manually, and the camera is installed on a slider to enable tracking the crack growth. A servo controller is used to operate a linear actuator to move the slider, along with the attached camera, such that the entire length of the crack can be viewed through the camera. The stand also provides a stable platform for image acquisition that reduces noise due to the surrounding test environment. A 50X-1000X digital microscope is used for image acquisition. A light source is installed above the microscope to induce high contrast between the crack edge and the specimen surface.

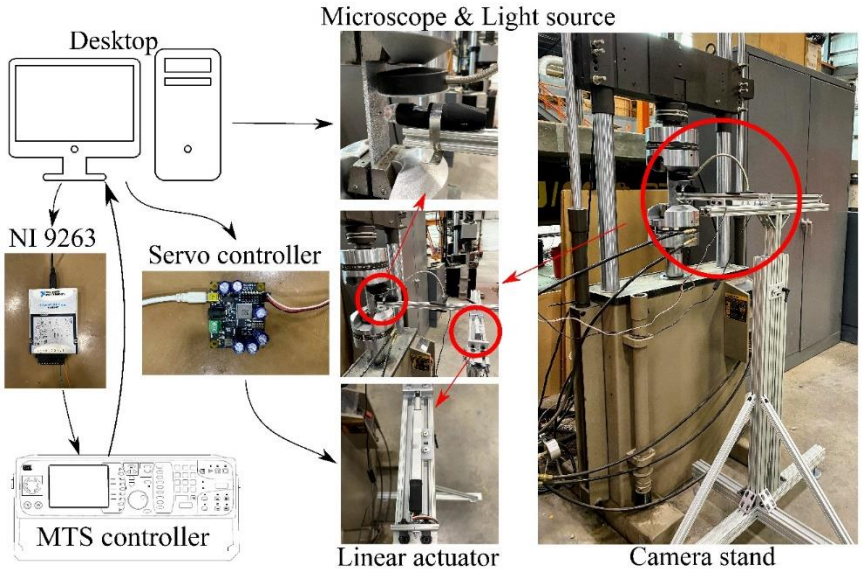

Figure 3-1. Proposed crack monitoring system setup.

3.2.2 Specimen surface preparation

Image quality could significantly affect the accuracy of the image processing algorithms applied to monitor the crack size. An image should have enough resolution to identify the crack tip and provide the contrast level needed for feature detection. For a typical metal specimen, the original surface is relatively dark and may contain contaminants including rust spots and scratches. In order to increase the contrast within the area of interest, a part of the specimen (i.e., around the notch) was polished by utilizing different grades of sandpaper and a polishing compound. The process was continued until a shiny clean surface was obtained for the area of interest. A scale

sticker was then attached to the polished surface parallel to the expected crack path. The purpose of the scale sticker is to identify the magnification level of the microscope and provide reference points to compensate for the offset occurring among successive images. This process will be explained further in the following subsections discussing the image processing algorithms. Figure 3-2 shows the steps taken for specimen surface preparation.

Figure 3-3 shows an example of the images acquired by the microscope for the prepared surface. The picture on the left shows a dashed rectangle representing the FOV of the microscope and the right picture is the corresponding magnified view captured by the microscope. The pictures acquired by microscope are all in grayscale, in which the color value ranges from 0 to 255, from black to white, respectively. As shown in Figure 3-3, despite the polishing procedure, there are still some surface defects and reflections on the specimen surface under the microscope view. These objects will be filtered in the image processing module. The distance between the markers of the scale is 1.59 mm (1/16 in) and the FOV of the camera is approximately set as 7.95 mm × 5.96 mm (5/16 in × 1/4 in). The captured image, as shown in Figure 3-3(b), is then divided into two areas: the crack area and scale area. The crack area is where the crack is expected to propagate during the fatigue test while the scale area is processed to determine the actual magnification level and provides reference points among successive images to aid in the image processing processes.

(a) (b) (c)

Figure 3-2. Specimen surface preparation steps: (a) original surface, (b) polished surface, and (c) polished surface with scale attached.

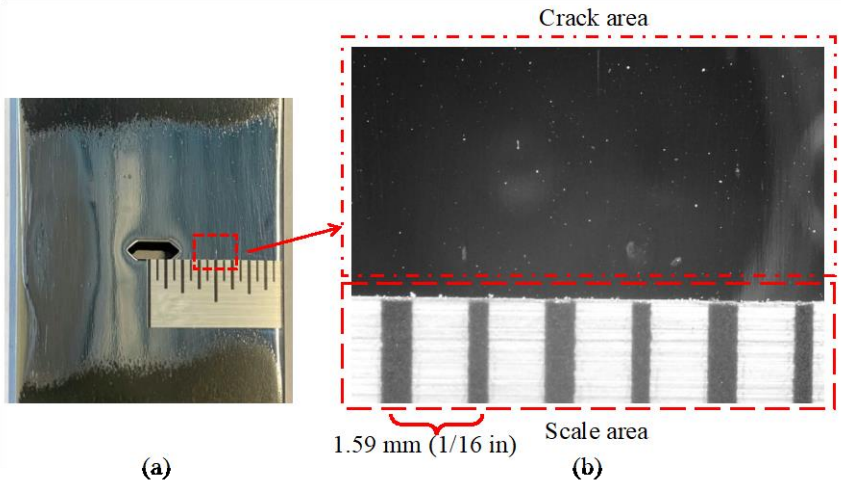

Figure 3-3. A view of the prepared specimen (a) with no magnification and (b) a magnified FOV as seen by the microscope.

3.2.3 Scale area processing

Since the gap distance between the scale markers is pre-determined, one way to calculate the magnification level of the microscope is to utilize the coordinates of the scale markers in pixels from the acquired image. As shown in Figure 3-4(a), under magnification, noise may appear on the scale area due to printing imperfections, impurities, contamination, and illumination condition. Accordingly, a two-step filtering approach was adopted herein to improve the image quality of the scale area before calculating the needed information. The first step is to apply a

bilateral blurring algorithm (Aubert et al., 2006; Tomasi & Manduchi, 1998) to the image in the scale area which will blur the area but maintain sharp boundaries. The results of this process are shown in Figure 3-4(b). As shown, compared to Figure 3-4(a), the white impurities within the black markers and the gray lines within the white areas have been minimized. The second step is to apply a threshold-based filtering algorithm (Gonzalez & Woods, 2006) to the blurred image to convert it into a purely black and white image. For each pixel, the pixel value is set to 0 (black) if it is smaller than the threshold; otherwise, the pixel value is set to 255 (white). A threshold value of 190 was chosen based on the histogram of pixel values in the blurred image as shown in Figure 3-5. This value could vary depending on the image attributes, e.g., illumination condition, specimen material, and scale sticker surface finish. The result of this two-step process is plotted in Figure 3-4(c). As shown, the markers are clearly outlined with clearly identifiable edges. This process enhances the contrast between the markers and the surrounding background and improves the accuracy of the following information retrieval algorithm (i.e., for the coordinates of the markers).

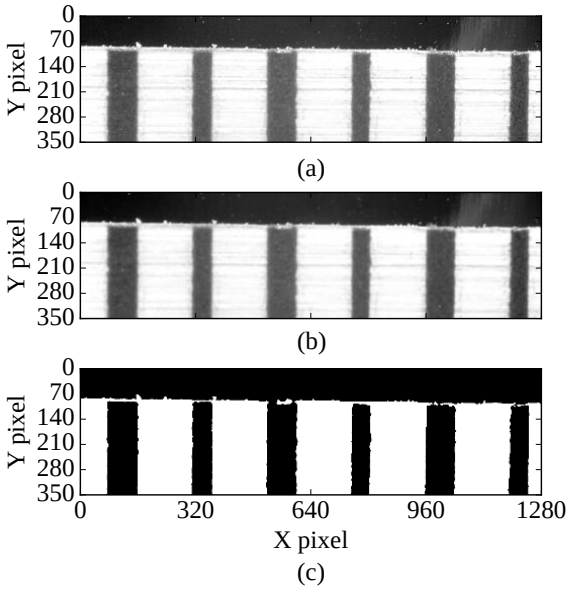

Figure 3-4. Noise filtering steps for the scale area of the specimen: (a) raw unfiltered image, (b) image after blurring filter, and (c) image after blurring and thresholding filter.

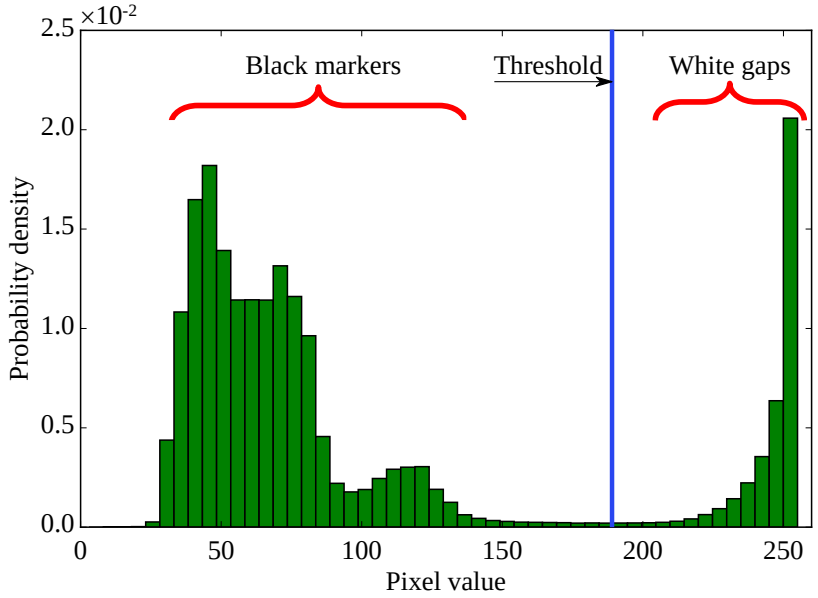

Figure 3-5. Histogram of the scale area with threshold value identified.

The filtered scale area is next processed to identify the coordinates of the black scale markers. The sums of pixel values in the horizontal and vertical directions are obtained and compared to the mean value computed for all pixels considered. An algorithm is developed to calculate the coordinates of markers in the X-direction as follows:

1) evaluate the summation of pixel values of the scale area vertically (i.e., Y-direction),

2) normalize the summation values by the maximum of the summation values, and

3) calculate the mean value of the normalized summation values.

Figure 3-6 shows the results of this process. For the filtered image shown in Figure 3-6(a), the normalized summation values, along with the mean value, are plotted in Figure 3-6(b). The high values in the summation curve in the Y-direction represent the white gap zones in the scale area, while the low values correspond to the marker regions. The mean value curve intersects with the summation curve at twelve locations that are marked with circles in Figure 3-6(b). The intersections highlighted by the circles indicate the X-direction coordinates of the left and right

edges of the markers, denoted as $X_{1,L}$, $X_{1,R}$, ... , $X_{6,L}$, $X_{6,R}$. Then the coordinates of the centers of the markers in the X-direction could be calculated as

$$X_j = (X_{j,L} + X_{j,R})/2, j = 1,2,\ldots,6 \qquad \text{Equation 3-1}$$

where j refers to the marker number; $X_{j,L}$ is the X-direction coordinate of left edge of the jth marker; $X_{j,R}$ is the X-direction coordinate of right edge of the jth marker. Similar steps can be applied to calculate the coordinates of the top edges of the markers in the Y-direction, denoted as Y_j (j = 1, 2…, 6). One difference is that for each marker, instead of using the whole scale area, only the area around the marker would be utilized since the coordinates of the marker in the X-direction have already been determined. This is represented by the dashed rectangle for the 1st marker in Figure 3-7(a). The corresponding summation curve in the X-direction, the mean value profile, and the intersection, highlighted by the circle to represent Y_1 for 1st marker, are plotted in Figure 3-7(b). Similar plots can be generated to obtain the Y-coordinates of the top edges of other markers. Consequently, the coordinates of the top centers of the markers can be determined through the two-step process discussed above.

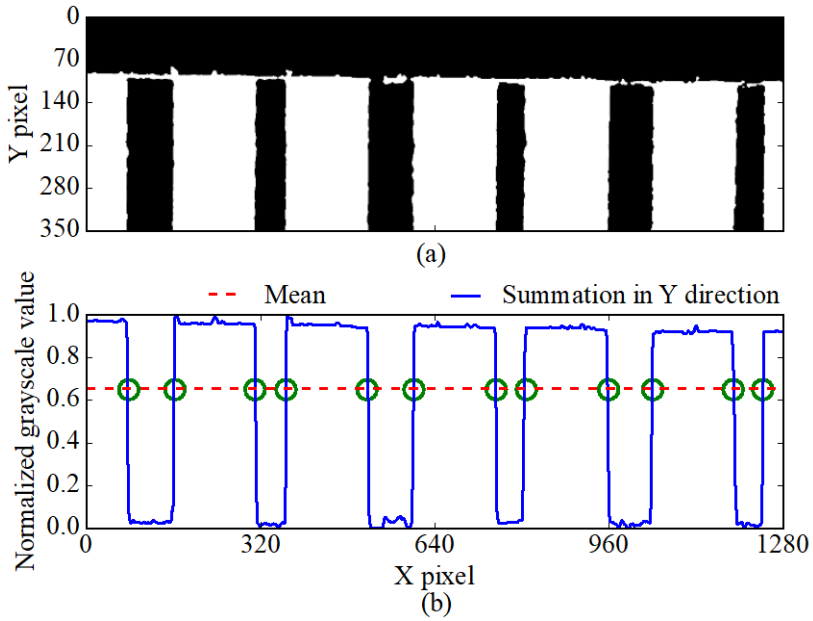

Figure 3-6. The process to determine the coordinates of markers in the X-direction: (a) filtered image and (b) summation profile of pixel values in the Y-direction.

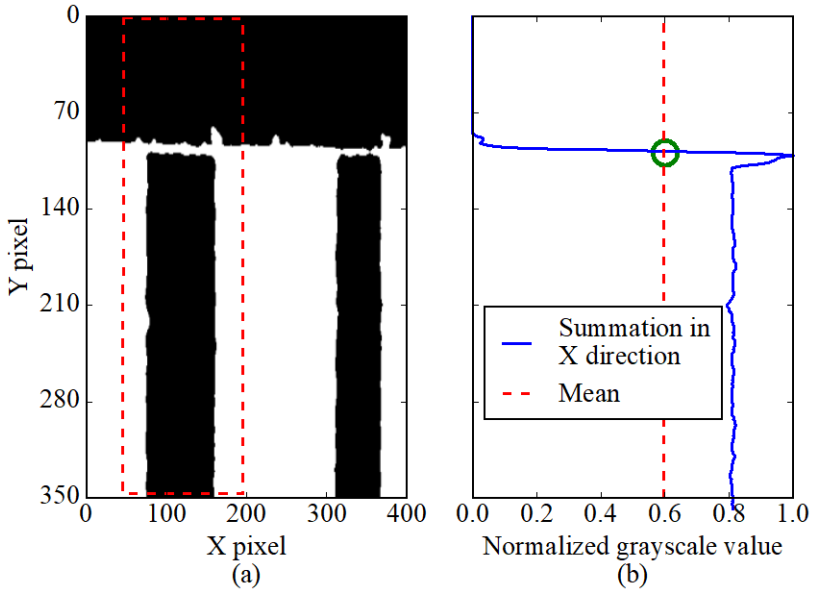

Figure 3-7. The process to determine the coordinates of markers in the Y-direction: (a) filtered image and (b) summation profile of pixel values in the X-direction.

Once the coordinates of the markers are determined, the magnification level of the microscope can be accurately estimated. A new image with reference points and region of interest (ROI) is next generated by combining the filtered scale area with the crack area as presented in Figure 3-8. The points Pt_1 and Pt_2 represent the top centers of the 1st and 2nd markers, respectively, and serve as the reference points for calculating the magnification level. The number of pixels between these points was found to be 220 pixels and since the distance between markers is 1.59 mm (1/16 in), the pixel size can be computed as 0.007 mm (0.00028 in) for this case. This pixel size will be used later for crack length calculation. The ROI, as defined in this chapter, extends from the left edge of the FOV to the midpoint between the last two markers (i.e., the 5th and 6th markers for this case) in the X-direction. In the Y-direction, the ROI extend 100 pixels above and below the crack tip location. The ROI may vary depending on the image resolution for different applications.

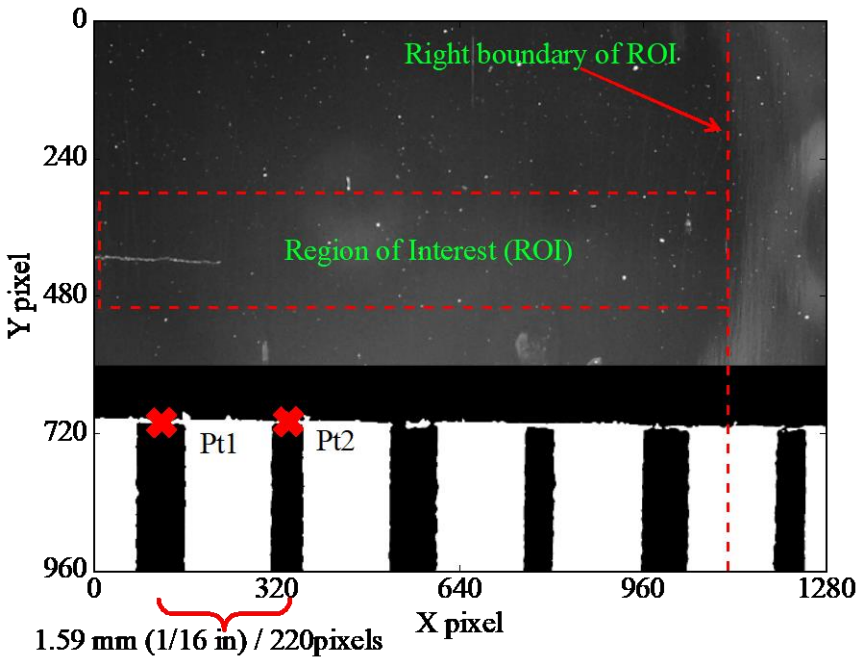

Figure 3-8. Reference points and region of interest within the specimen.

3.2.4 Alignment among images

During fatigue tests, the crack size measurement interval is adjusted based on the crack propagation rate. The images acquired at different time instances could show linear shift or rotations due to minor variations in the hydraulic grip location or ambient vibrations of the test setup or lab floor. These issues, along with other potential sources of noise, could compromise the requirement of a static camera for applying the background subtraction. Therefore, alignment among images is necessary for applying the proposed algorithm. This can be achieved by using the markers as reference points since their relative locations will not change among successive images during the test. If the coordinates of 1st and 2nd markers in the *k*th image are $X_{1,k}$, $Y_{1,k}$ and $X_{2,k}$, $Y_{2,k}$, respectively, and are respectively $X_{1,k+1}$, $Y_{1,k+1}$ and $Y_{1,k+1}$, $Y_{1,k+1}$ in the (*k*+1)th image, then the transformation matrix M_t that shifts the coordinates in the current image back to those of the previous image can be expressed as

$$M_t = \begin{bmatrix} 1 & 0 & (X_{1,k} + X_{2,k})/2 - (X_{1,k+1} + X_{2,k+1})/2 \\ 0 & 1 & (Y_{1,k} + Y_{2,k})/2 - (Y_{1,k+1} + Y_{2,k+1})/2 \end{bmatrix} \quad \text{Equation 3-2}$$

To correct for rotations between images, the rotation angle and rotation matrix M_r are

$$\theta = \tan^{-1} \frac{(Y_{2,k} - Y_{2,k+1}) - (Y_{1,k} - Y_{1,k+1})}{(X_{2,k} - X_{2,k+1}) - (X_{1,k} - X_{1,k+1})} \quad \text{Equation 3-3}$$

$$M_r = \begin{bmatrix} \cos\theta & -\sin\theta \\ \sin\theta & \cos\theta \end{bmatrix} \quad \text{Equation 3-4}$$

where θ is the angular difference between the two images. After these two operations, the ROI in previous and current images are considered to be identical except for the crack growth increment.

One restriction associated with using a microscope is the limited FOV. For the current setup, the FOV is approximately 7.95 mm× 5.96 mm (5/16 in × 4/16 in) at the desired magnification level. In most cases, the fatigue crack is expected to extend beyond this FOV. This issue is addressed in

this approach by automatically re-locating the microscope, using a linear actuator, based on current crack tip position. As a result, in addition to the necessary alignment process discussed above, there is second alignment process required due to movement of the linear actuator and the microscope. The microscope will move to the next location once the right boundary of the ROI is reached by the crack tip. At this situation, two images for the same crack length are acquired at the two locations of the microscope, as shown in Figure 3-9. Given the different coordinates of the crack tip in the two images, the same transformation matrix is used to align the images to update the coordinates of the crack tip. One difference in this alignment process compared to the previous one is that the last two markers need to be treated as reference points since these two markers are the only common markers captured in both images.

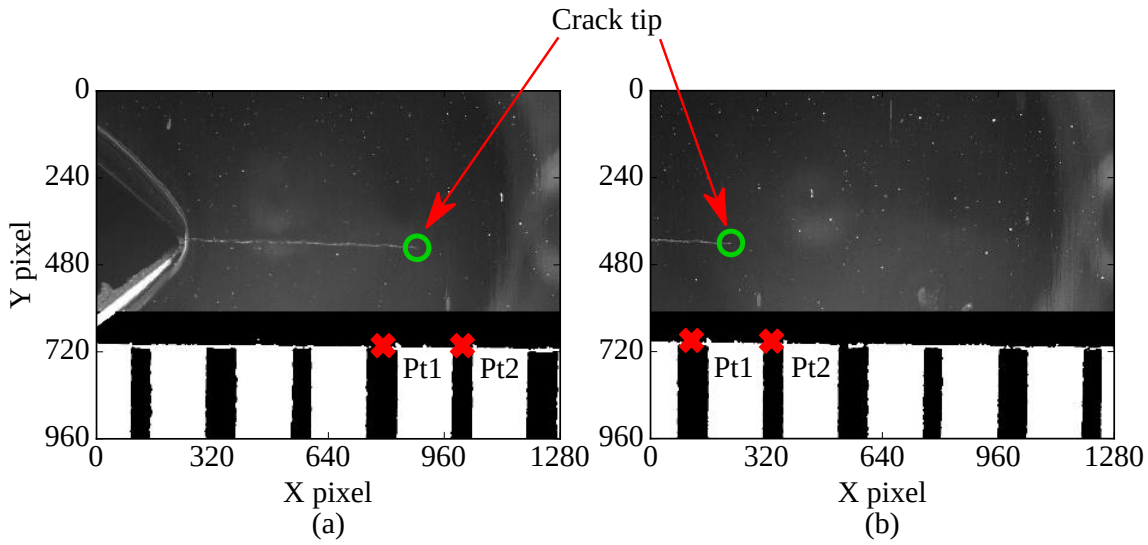

Figure 3-9. Crack tip alignment between two images acquired from different microscope locations (a) first location of the microscope and (b) second location.

3.2.5 Background subtraction

A background subtraction algorithm is applied next to measure the crack growth increment using the aligned images. In practical problems, given the difference in illumination levels over time in the FOV, the value of a particular pixel is represented as a mixture of adaptive Gaussian

distributions (Stauffer & Grimson, 1999). Denoting the recent history of the values of a specific pixel as $x_1, \ldots, x_t$ in grayscale, the probability density function that describes the value x_t of the pixel at time t is

$$p(x_t) = \sum_{i=1}^{K} \omega_{i,t} \times N(x_t; \mu_{i,t}, \sigma_{i,t}) \qquad \text{Equation 3-5}$$

where K is the number of existing components in GMM; $\omega_{i,t}$ is the weight factor that represents how much of the data belongs to the ith Gaussian distribution at time t; $\mu_{i,t}$ is the mean value of the ith Gaussian distribution at time t; $\sigma_{i,t}$ is the standard deviation value of the ith Gaussian distribution at time t; and N is the Gaussian probability density function.

The moving or intruding objects in the foreground normally will be represented by some GMM components with small weight factors. Accordingly, the background can be approximately captured by the first B largest GMM components. If these K distributions are ordered based on the value of $\omega_{i,t}$, the first B largest GMM components that represent the background at time t is

$$B = \arg\min_b \left(\sum_{i=1}^{b} \omega_{i,t} > T \right) \qquad \text{Equation 3-6}$$

where T is a threshold of the minimum portion of the data that should be accounted for by the background.

Considering the computational cost associated with modeling each pixel in the image, an online K-means approximation algorithm is implemented to check the current value of the pixel against the existing K Gaussian distributions until a match is found (Dempster et al., 1977). A match is defined when the current pixel value is within 2.5 standard deviations of the distribution (Dempster et al., 1977). New distribution would be added if no match distribution could be found. The new distribution is set with a mean value of the current pixel value, an initially high variance, and a low weight factor. The adopted GMM algorithm (Zivkovic, 2004) starts with only one

distribution centered at the first sample and more distributions are added as needed. Once the weight factor of a specific distribution is negative, the distribution is discarded. The adaptive parameters for the specific pixel at time (t+1) can be iteratively updated as follow (Zivkovic, 2004)

$$\omega_{i,t+1} = (1-\alpha)\omega_{i,t} + \alpha M_{i,t+1} - \alpha c_T \quad \text{Equation 3-7}$$

$$\mu_{i,t+1} = \mu_{i,t} + \alpha M_{i,t+1} / \omega_{i,t+1} (x_{t+1} - \mu_{i,t}) \quad \text{Equation 3-8}$$

$$\sigma^2_{i,t+1} = \sigma^2_{i,t} + \alpha M_{i,t+1} / \omega_{i,t+1} ((x_{t+1} - \mu_{i,t+1})^2 - \sigma^2_{i,t}) \quad \text{Equation 3-9}$$

where α is learning rate (Stauffer & Grimson, 1999); $M_{i,t+1}$ is 1 if the pixel value at time (t+1) matches the ith Gaussian distribution and 0 if not matching; and C_T is bias factor (Zivkovic, 2004).

An example of applying the background subtraction after alignment for FCG monitoring is plotted in Figure 3-10. Figure 3-10(a)-(c) show, respectively, the previous image, current image, and the foreground generated from background subtraction. As seen in Figure 3-10(c), most of the bright dots due to light reflection were detected and treated as objects on the background, which were removed in the foreground image. The enlarged view around the crack tip clearly indicates that the background subtraction successfully captures the crack growth increment with a clear view of the crack tip. However, noticeable noise, especially along the crack path, can also be seen in the foreground image. This is expected due to the unpredictable light reflections given the uneven surfaces along the crack path. To address this issue, several filtering steps are required after the background subtraction process to identify the correct crack growth increment.

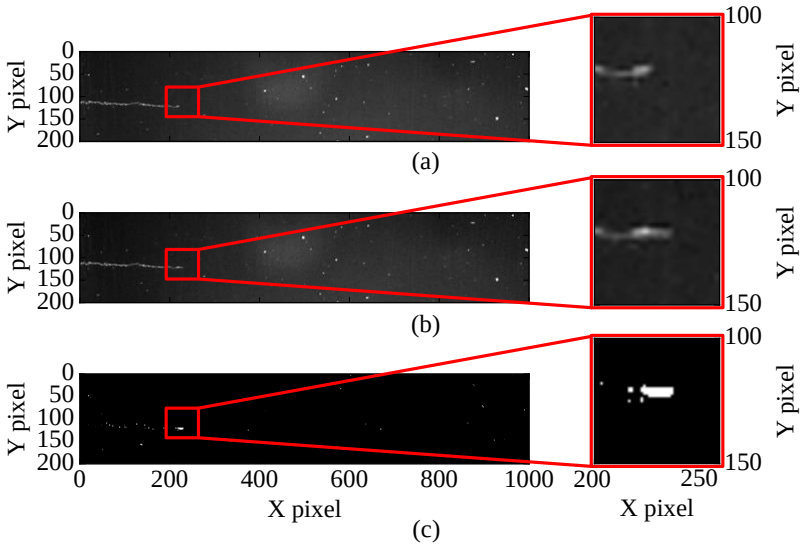

Figure 3-10. Example of crack tip identification using background subtraction: (a) previous image, (b) current image, and (c) foreground.

3.2.6 Filtering for proper identification of crack growth increment

A contour detection algorithm (Suzuki, 1985) is adopted herein to analyze the foreground image (i.e., Figure 3-10(c)) with the aim of identifying the boundaries of all objects within the foreground image. A comparison between the detected objects and the identified contours of the crack tip area is shown in Figure 3-11. Based on the detected contours, the coordinates of extreme points (marked by the stars in Figure 3-11(b)) and the area enclosed by these contours can be retrieved.

The next step is to apply the area limitation filter for all detected contours. This process aims at filtering out small contours that do not represent crack growth increment. These small contours were found to be mostly located along the crack path and cover no more than two pixels. Accordingly, an area value of two pixel^2 is selected as the threshold value. This value was found to provide an optimum balance between the resolution and accuracy of the proposed approach. A higher value can be used but it will increase the minimum crack growth increment that the

proposed approach can detect. The results of this process are shown in Figure 3-12. Figure 3-12(a) shows the detected contours in the raw unfiltered FOV while the filtered contours are plotted in Figure 3-12(b). Compared to Figure 3-12(a), most of the small contours along the crack path were removed. However, some large contours that do not belong to the crack growth increment can also be seen in Figure 3-12(b). These were found to be located at large distances from the crack tip and can be filtered out based on their distance from the detected crack tip.

Based on the filtered foreground, the extreme points of all detected contours are compared to the current crack tip location. If the current crack tip location falls within a pre-specified distance from the detected contours, this contour is next analyzed to determine the crack growth increment and update the crack tip location. This pre-specified distance is considered herein as 5 pixels. It was found that if smaller values are used, the algorithm may fail to detect the growth increment in some images, whereas a larger value would increase the noise level in the detection process. This process is shown in Figure 3-12(c) in which only the main contour including the crack tip remains in the foreground

Based on the detected contour and the established pixel size, the crack propagation length in the specific interval can be calculated using the pixel difference between the current crack tip and right extreme point of the detected contour. If the crack growth increment in a given interval is smaller than two pixels, no crack growth increment will be found with the proposed filtering approach. In this case, the crack tip location and crack length will remain the same values found in the previous image until a new image is captured.

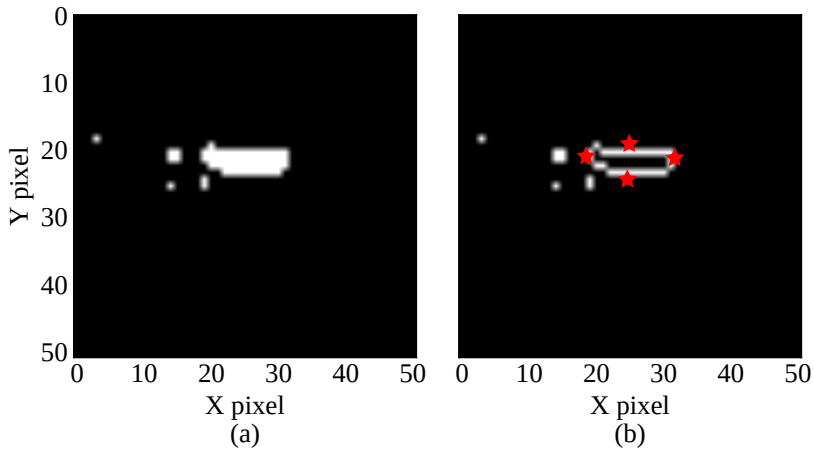

Figure 3-11. Contour detection in the foreground image, a) objects detected through background subtraction, b) contours with extreme points.

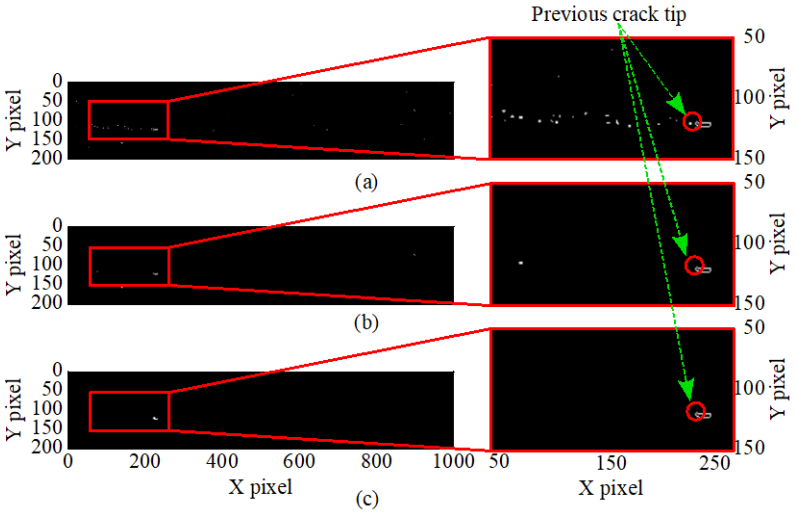

Figure 3-12. Filtering of detected contours for identifying the crack growth increment: (a) raw unfiltered contours, (b) applying the area filter, and (c) identifying the crack growth and new crack tip location.

3.2.7 Framework for automated vision-based fatigue crack growth monitoring

The proposed automated vision-based crack size monitoring framework is illustrated in Figure 3-13. It starts with the system hardware setup including the desktop computer, microscope, linear actuator, test frame (i.e., hydraulic system) setup, and specimen preparation. Once the system

setup is complete, an initial image is captured as the first background for the entire process. The initial crack tip coordinates and initial crack length are calculated manually based on this image. Then the test, as well as the crack monitoring process, will start. Once the number of load cycles reaches a predefined value, the hydraulic system will hold the load on the specimen and sends a signal to the desktop computer to call the crack monitoring algorithm. Next, the desktop will control the microscope to capture a new image, and the image processing algorithms discussed previously will be applied as follows:

1) The scale area processing algorithm is applied to establish necessary information including pixel size, ROI, and the marker coordinates
2) Alignment is next applied between successive images
3) Background subtraction is applied to the aligned images to generate the potential crack growth increment for this measurement interval
4) The proposed contour filtering is implemented to identify the correct crack growth increment
5) If a crack growth increment is identified in Step 4, the crack length and the new crack tip coordinates are updated. Furthermore, the background image is replaced by the current image. If no crack growth increment is identified, none of these updates will occur and the same background image is used for the next measurement.

The current crack length is compared to the limitation on maximum crack size for the analyzed specimen, if the value is larger than the limitation, the test is concluded and the loading system and detection algorithm will stop, otherwise the crack size is compared to the ROI. If the crack size is within the ROI, the desktop will send a signal to the MTS controller to resume the hydraulic test operation; however, if the crack tip is located outside the ROI, the desktop will control the linear actuator to move the microscope to the next location and the test is then resumed. A new image will be captured at the new location and the coordinates of the current

crack tip will be updated by the alignment algorithm. The load holding procedure should not affect the validity of the fatigue test according to ASTM E647 (ASTM Standard E647, 2015) since the crack measurement process takes less than 10 seconds. This image processing and test control framework, including all related programming codes are constructed in Python coding environment (i.e., Python 3). The OpenCV (Bradski & Kaehler, 2008) image processing library is utilized in this framework.

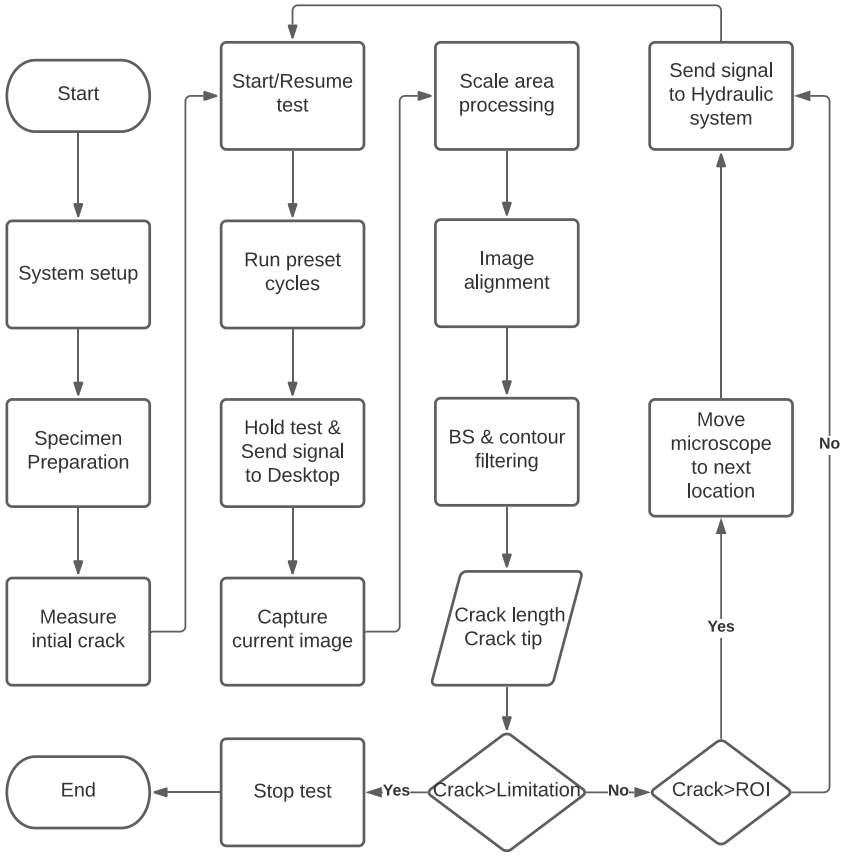

Figure 3-13. Flowchart of automated vision-based fatigue crack growth monitoring approach.

3.3 Experimental Validation

A series of middle tension, M(T), fatigue tests was conducted to quantify the feasibility and accuracy of proposed approach. The M(T) specimen is a center-notched plate that can be loaded

under either tension-tension or tension-compression conditions. The next subsections provide specifics of the test setup and discuss the results obtained from the proposed approach.

3.3.1 Test configuration

The M(T) specimen, fabricated using A572-Grade 50 steel, was designed based on ASTM E647 (ASTM Standard E647, 2015), and the detailed dimensions are shown in Figure 3-14. Two specimens were tested under different load patterns, i.e., constant amplitude loading (CAL) and variable amplitude loading (VAL), to examine the feasibility of the proposed approach under different loading conditions. The CAL had minimum and maximum amplitudes of 11.6 kN (2.6 kips) and 38.2 kN (8.6 kips), respectively. The VAL was generated to simulate wave loading conditions based on Tomita et al. (Tomita et al., 1995) and Li et al. (Li et al., 2016) resulting in a load signal with minimum and maximum amplitudes of -53.4 kN (-12 kips) and 53.5 kN (12 kips), respectively. Figure 3-15 shows realization of the CAL and VAL loads applied to the specimens. The loading frequency was set as 20 Hz for the two tests. A pre-cracking procedure was conducted to initiate the crack up to 7.6 mm (0.3 in) in length before applying the test load patterns. This crack size refers to half of the total crack length. The system setup shown in Figure 3-1 was used to conduct these fatigue tests and the framework in Figure 3-13 was followed to automatically monitor the fatigue crack growth during the tests. The time interval for crack monitoring was set as 120 seconds, which included 110 seconds for loading (2,200 cycles) and a 10 seconds load holding for image acquisition and processing.

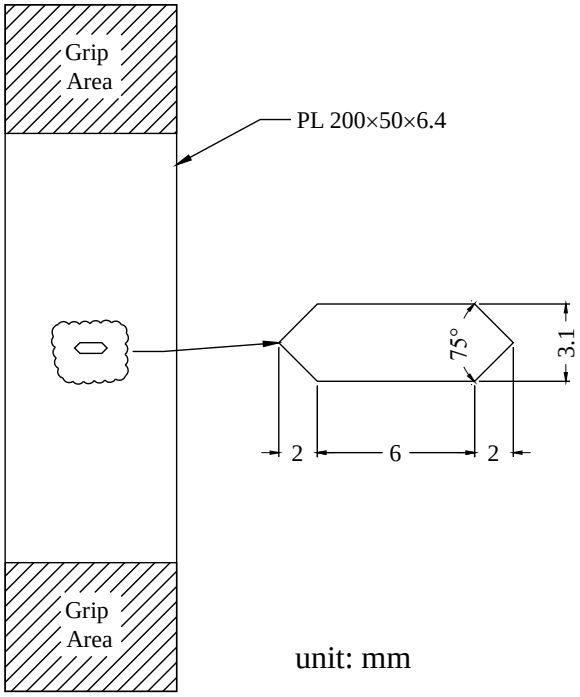

Figure 3-14. Dimensions of the tested M(T) specimens.

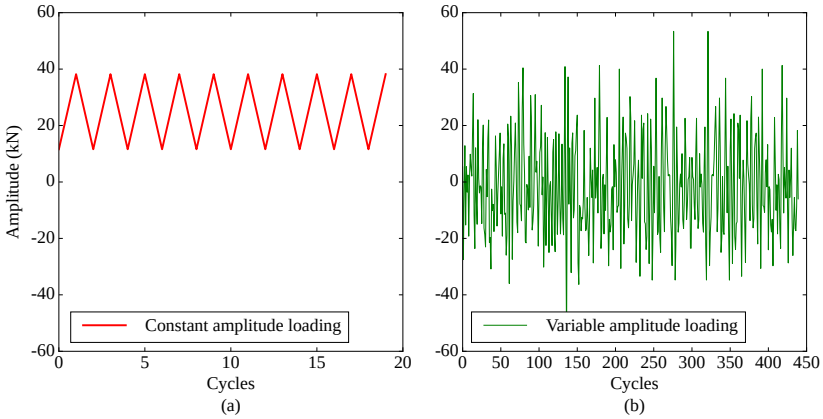

Figure 3-15. Load patterns for fatigue tests under (a) constant and (b) variable amplitude loadings.

3.3.2 Crack propagation results

A series images taken at intermediate stages of crack propagation in the CAL specimen are plotted in Figure 3-16. In the figure, rows from (a) to (e) demonstrate the successive intervals of crack growth measurement made by the proposed approach. As shown, each column (i.e.,

columns 1 to 5) has four images, in which the first and second images are the raw images acquired at the start and end of a particular measurement intervals. The third image shows the filtered contour resulting from applying the proposed approach on the two images. This filtered contour represents the detected crack growth increment for this measurement interval. The fourth image is the accumulated detected crack growth increments at the end of each interval. The colors of the third and fourth images in each column (i.e., rows c and d) were reversed to better highlight the detected crack growth increment compared to previous figures. The detected crack contours in all five images clearly captured the crack growth increment and matched the crack growth increment computed manually from the successive images. From the figures, it can be seen that the crack tip location could be clearly detected using the proposed algorithm and the accumulated detected crack growth increments represented the actual crack path in the specimen. Identifying the crack tip location and crack size can be next used for calculating key fatigue-related parameters and material properties, including the range of stress intensity factor and C and M material parameters (Paris & Erdogan, 1963).

A full view of the cracks in the specimen with constant amplitude loading is plotted in Figure 3-17. It includes the profiles captured at two locations of the microscope with the corresponding detected crack sizes of 9.46 mm and 15.84 mm. Figure 3-17(a) shows the raw image at the first microscope location captured at a crack size of 9.46 mm, while Figure 3-17(b) shows the raw image at the second location captured at crack size of 15.84 mm. Figure 3-17(c) and Figure 3-17 (d), respectively show the total detected crack growth increment at the first and second locations of the microscope. As shown, the proposed approach succeeded in capturing the crack profile through the entire length. The crack size and corresponding load cycles are plotted in Figure 3-18 for both CAL and VAL specimens. As seen, no data outliers were noticed in the profiles, and the transition between the two microscope locations was unnoticeable. This indicates that the proposed microscope transitioning strategy does not affect the feasibility of the proposed

approach. The narrow scope of the microscope can be expanded using the proposed approach to accommodate fatigue tests with long crack sizes. It was found that the proposed approach is capable of capturing the entire crack propagation process despite surrounding noise in the background.

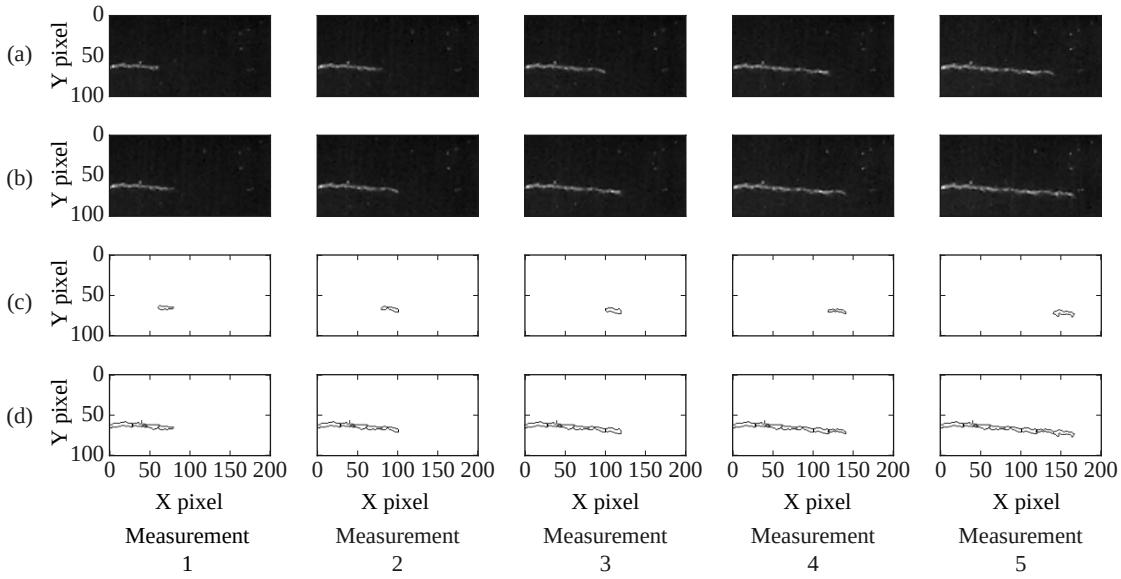

Figure 3-16. Results of five consecutive crack detection measurements: (a) previous raw image, (b) current raw image, (c) detected crack growth increment for current interval, and (d) cumulative detected crack growth increment at each interval.

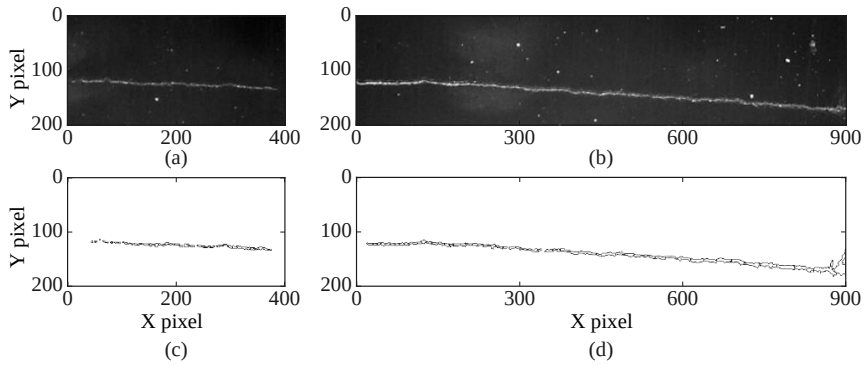

Figure 3-17. View of the crack in the constant amplitude loading specimen at two locations of the microscope: (a) raw image at the first location, (b) raw image at the second location,

(c) total crack growth increment at the first location, and (d) total crack growth increment at the second location.

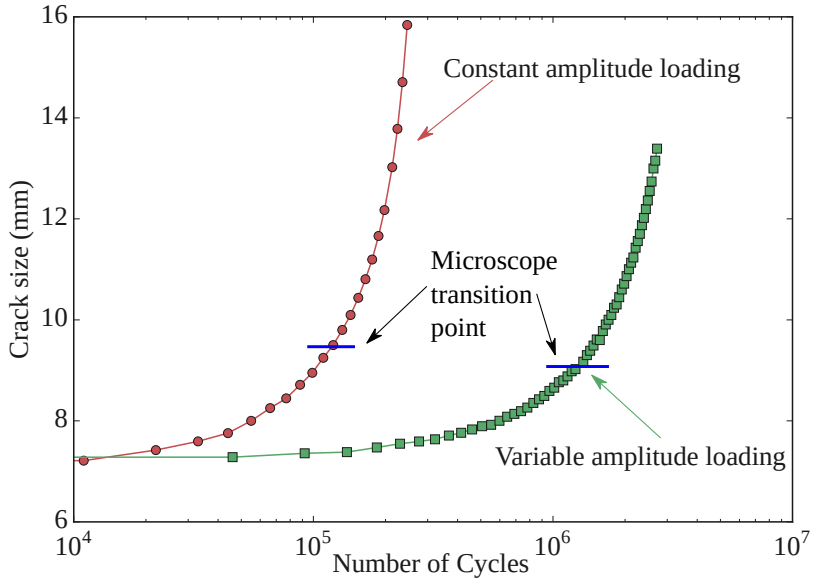

Figure 3-18. Crack size versus load cycles for the tested specimens under constant and variable amplitude loadings.

3.4 Conclusions

The chapter presented an automated imaging-based fatigue crack growth monitoring approach based on the background subtraction technique. The crack growth increments in the successive images are treated as intruding objects which can be detected by the background subtraction algorithm. Filtering and alignment algorithms are applied to the scale area to provide critical information for the crack growth monitoring process. Afterwards, the background subtraction and contour filtering are conducted on the successive images to identify the crack growth increment and crack tip location as the crack grows. A linear actuator is utilized to adjust the location of the microscope to (a) enable the automated tracking of the crack tip and (b) expand the measurement FOV such that the entire crack length can be observed. Two M(T) fatigue tests were conducted to

evaluate the feasibility of the proposed approach. The two tests covered constant and variable amplitude loading conditions.

The area limitation in the contour filtering was set to two pixel^2 while the actual size of each pixel was found to be 0.007 mm (0.00028 in) at the adopted magnification level. Accordingly, the minimum crack growth increment that the proposed approach can detect is 0.014 mm (0.00056 in) and the precision of the proposed approach can reach 0.007 mm (0.00028 in) in the current setup. In the fatigue tests, the ability to resolve crack extensions of 0.1 mm (0.004 in) is needed by ASTM E647. Accordingly, the proposed approach can provide the crack size measurement accuracy required in fatigue crack propagation tests. Although the approach is illustrated on the M(T) steel specimens, it can be applied to other materials or sample configurations tested under constant amplitude or variable amplitude loading conditions. The cost of the utilized crack monitoring equipment including the microscope, a linear actuator, and camera stand, was approximately $300. Overall, the proposed approach was found to provide an automated, cost-effective, and accurate alternative to other non-contact real-time crack measuring approaches.

CHAPTER IV

FATIGUE CRACK GROWTH PREDICTION CONSIDERING LOAD HISTORY EFFECT USING XFEM

4.1 Introduction

Modeling the crack growth in fatigue-prone structures is essential to provide accurate estimation of the service life and prevent unexpected failures. Early empirical models, e.g., Paris' law (Paris & Erdogan, 1963), provided a simple approach to predict the fatigue crack growth (FCG) and were the subject of extensive research over the following decades. Many of these early studies were based on constant amplitude loading (CAL); however, the fatigue behavior may be significantly different under variable amplitude loading (VAL) considering load history effect (Skorupa, 1998). Effects such as the stress ratio and retardation have been considered in later models (Elber, 1971; Russell, 1989). In addition, various models (Huang et al., 2008; Sander & Richard, 2006; Schijve, 2001; Skorupa, 1998; Zhu et al., 2020) have been proposed to predict FCG under VAL.

Finite element analysis (FEA) has been proven beneficial in simulating FCG under complex conditions. Traditional FEA requires continuous remeshing during the fatigue crack propagation to conform to the crack tip. Considering the singularity and discontinuity around the crack tip, it is challenging to use traditional FEA for the FCG prediction (Anderson, 2017). Extended Finite

Element Analysis (XFEM) (Belytschko & Black, 1999; Fries & Belytschko, 2010) is an alternative which utilizes enrichment functions to represent the discontinuities, and provides an asymptotic function to model the stress singularity around the crack tip. Several studies have implemented XFEM to solve fatigue related problems in different applications such as crack growth modelling in thick wall cylinders (Lee & Martin, 2016), fatigue propagation of a cracks subjected to stress gradients (Bergara et al., 2017). However, XFEM approaches in literature did not consider load history effects for fatigue crack growth prediction. Accordingly, an approach based on XFEM is needed to enable the load history consideration for FCG prediction under VAL.

This chapter addresses this need by proposing an XFEM-based approach to predict FCG under VAL. The stress singularity around the crack tip is simulated through XFEM and the load history effect is considered by tracking the residual stress/strain during crack growth. It couples XFEM with the crack closure concept (Elber, 1971) to consider the load history effect. Eliminating the need for remeshing introduced by using XFEM reduces the computational time while providing accurate information of the stress singularity around the crack tip. The proposed model is calibrated and verified using data from fatigue tests conducted on middle tension (M(T)) specimens.

4.2 Background

4.2.1 Variable Amplitude Loading and Load History Effect

Structures such as bridges, ship hulls, and airplane frames generally experience a spectrum of variable amplitude stress cycles along their lifespan. Predicting the crack growth using Paris' law (Paris & Erdogan, 1963) or the damage accumulation using Miner's rule (Miner, 1945) are perhaps the most popular methods for assessing fatigue damage in structures. Paris' law (Paris & Erdogan, 1963) characterizes crack growth by correlating the crack growth rate, da/dN, and the stress intensity factor range, ΔK, in a power-law form. The stress ratio , R, defined as minimum

stress / maximum stress within the cycle, was later incorporated into the Paris' law expressed as (Forman et al., 1967)

$$\frac{da}{dN} = \frac{C(\Delta K)^m}{(1-R)K_c - \Delta K} \quad \text{Equation 4-1}$$

where *C*, *m* are fitting parameters; K_c is the fracture toughness.

Miner's rule defines a damage accumulation index denoted as C_{Miner}, which considers damage contributions from cycles with different stress amplitudes. Once the value of the index exceeds 1, the fatigue life of the specimen is reached. The equation to calculate the damage accumulation index can be written as

$$C_{Miner} = \sum_{i=1}^{k} \frac{n_i}{N_i} \quad \text{Equation 4-2}$$

where *k* refers to the total number of bins in stress range histogram; n_i is the actual number of cycles applied at stress range S_i and N_i is the number of cycles to failure for the specific S_i.

The assumption for these models is that the sequence of different load cycles in a stress spectrum does not affect the fatigue damage (Miner, 1945). This assumption can be applicable in some cases such as structures subjected to high stress ratio *R* loading. Highway bridges, for example, have high dead loads due to the self-weight of reinforced concrete deck and pavement leading to a high stress ratio *R* (Anderson, 2017; Fisher et al., 1998). In this condition, the crack will remain open all the time during the service life, and the load history will have low effect on the FCG rate. As a result, the CAL and/or Miner's rule assumption could be suitable for highway bridge application (Soliman et al., 2013).

However, Miner's rule assumption is not always valid (Shigley & Mischke, 1989; Stephens et al., 2001), especially under overloading and compressive loads. The load interaction among the overloading and compressive loads could greatly affect the following fatigue crack growth rate

(FCGR) (Goel & Chand, 1994). In addition, experimental results in literature have shown that failure does not always occur when Miner's damage accumulation index reaches 1. Tveiten (1999) conducted several variable amplitude fatigue tests on butt welded aluminum connections; in those tests, the mean and coefficient of variation (CoV) of Miner's damage accumulation index at failure for the 12 tested specimens were reported as 1.87 and 0.25, respectively. The high mean value of the critical accumulation damage index and the high CoV indicate that the prediction results from Miner's rule may lack accuracy predicting damage under VAL conditions. This can be primarily attributed to load history effects that generally affect crack growth under VAL.

Furthermore, it was observed in literature (Matsuoka et al., 1976; Matsuoka & Tanaka, 1978; Pantelakis et al., 1995) that the load history can affect the FCGR by introducing crack retardation or acceleration due to load interactions. For instance, as shown conceptually Figure 4-1, the application of an overload within a CAL pattern leads to a delayed retardation of FCGR after the overload (Anderson, 2017). The rate increases first due to the overload and as the crack grows, the rate decreases before it recovers to the previous level. Experimental results by Fleck (1985) and Field et al. (2022) show also that when an underload is introduced, crack acceleration may occur. Neglecting the effect of these load interactions could lead to incorrect fatigue crack prediction.

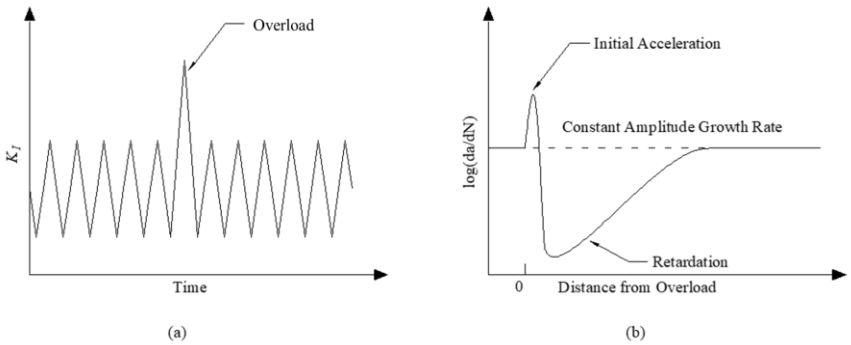

Figure 4-1. Demonstration of retardation due to overload (adopted from Anderson (2017)): (a) constant load pattern with an overload, (b) the corresponding change in crack growth rate.

Numerous experiments in literature have highlighted the effect of load interaction on fatigue crack propagation (Aïd et al., 2011; Huang et al., 2008; Lu & Liu, 2010; Mikheevskiy & Glinka, 2009). Figure 4-2 shows the experimental loading condition and the corresponding crack propagation results reported in (Skorupa, 1998) as an example. The load patterns in curves (b) and (c) would be treated similarly under Miner's rule; however, the fatigue crack propagation curves show a significant difference. The reason is that the load history in loading condition (b) generated a large amount of crack growth rate retardation; however, for loading condition (c), the underload after the overload mitigated the retardation effect due to the overload.

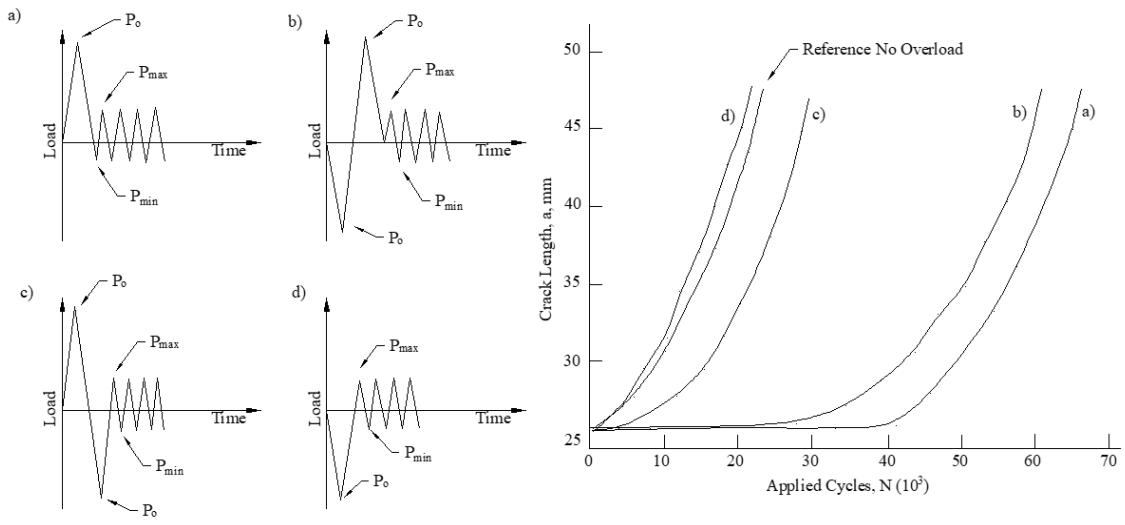

Figure 4-2. An example of load interaction on fatigue crack propagation (adopted from Skorupa (1998)).

4.2.2 Crack Closure under Fatigue

One of the major theories to explain the load history effect is the crack closure concept proposed firstly by Elber (1971). The crack closure refers to the behavior in which the crack tip remains closed even under certain levels of tensile loading. The crack closure involves various mechanisms; of those, plasticity-induced closure is considered the major mechanism (Schijve, 1988). Under the presence of a crack, a plastic zone forms at the crack tip. When the crack propagates through this area, a plastic zone remains along the crack path as shown in Figure 4-3. This plastic zone (i.e., in the wake of the crack) will keep the two surfaces of the crack closed under remote tensile stress. The crack closure affects the FCGR since the crack surfaces must be open first before it can propagate further. McEvily & Ishihara (2002) removed the plastic wake after an overload, by machining the specimen, for a load pattern similar to that shown in Figure 4-2 (a). The FCGR immediately reverted back to the normal rate before the overload as captured in Figure 4-4. This clearly proved that the crack closure due to the plastic wake was the reason of the load history effect, especially under VAL. A new term, crack-opening stress intensity factor

K_{op}, is introduced accordingly (Newman, 1981). The crack propagation relationship can be modified as $f(K, K_{op}, da/dN, R)$ where the value of K_{op} is determined from the analysis of the applied loading history. When the stress ratio R is high (such as in bridges), the high tensile stresses arising from the dead load would cause the crack to open under low additional stresses, and the effect of crack closure becomes insignificant.

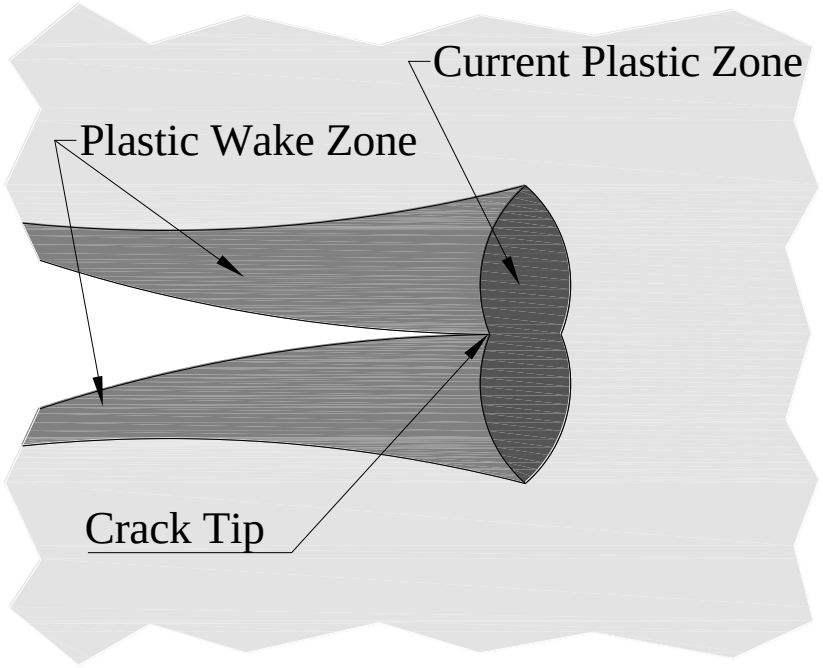

Figure 4-3. Plastic zone along the crack path (adopted from Anderson (2017)).

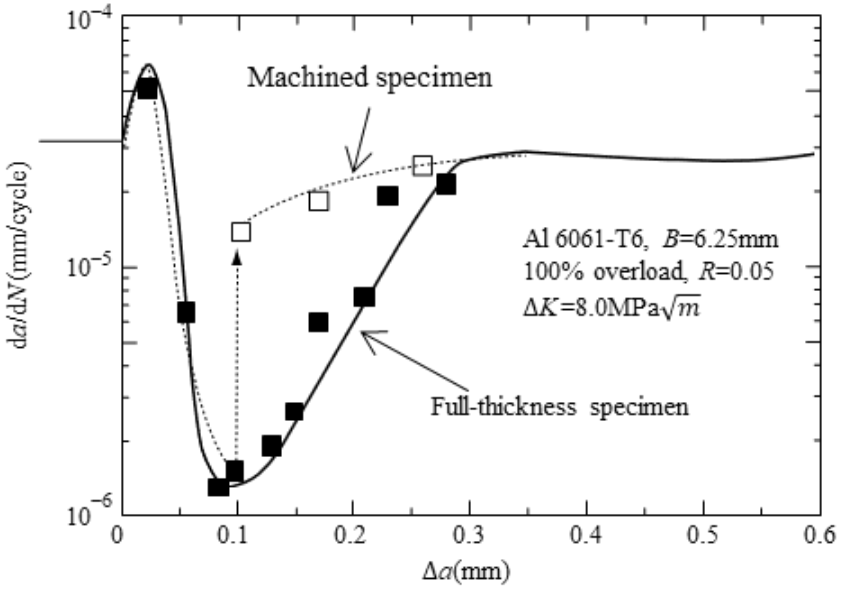

Figure 4-4. Variation in FCGR following an overload with and without plastic wake machined away (adopted from McEvily and Ishihara (2002)).

4.2.3 Crack Propagation Prediction under Variable Amplitude Loading

Various models have been proposed in literature to predict fatigue crack growth under VAL e.g., Huang et al., 2008; Sander & Richard, 2006; Schijve, 2001; Skorupa, 1998; Zhu et al., 2020. One group of these prediction models, developed first by Wheeler (1972), is based on the premise that plastic stresses in front of the crack tip influence the growth rate. These include the studies by Khan et al., 2010; Mehrzadi & Taheri, 2013; Yuen & Taheri, 2006. Another major category follows the concept of crack closure discussed above (e.g., Elber, 1971; Minakawa et al., 1983; Newman, 1981). Other models in literature include the two-parameter model proposed by Noroozi et al. (2007) to account for the residual stress and stress ratio effect. The model in Noroozi et al. (2007) considered the crack driving force as a combination of the maximum stress intensity factor and stress intensity range. The model was verified using data from fatigue tests on aluminum alloys under different load ratios. The small time scale fatigue crack growth model introduced in Lu & Liu (2010) also addresses this problem by adopting a reverse plastic zone concept. It considered FCG at any time instant within a cycle such that the stress ratio effect is

intrinsically considered to eliminate the need for cyclic counting needed in traditional approaches. Overall, all these models have made attempts to provide an accurate estimation of the FCG under VAL; however, no model has been universally recognized as the optimal solution and research efforts on this topic are still ongoing.

Most analytical models for predicting the crack propagation (e.g., Equation 4-1) rely on the concept of the SIF. This quantity was first defined by Irwin in 1957 to express the stresses around a crack. Three independent cracking modes have been identified due to different loading conditions , i.e., opening (tensile) mode, sliding (in-plane shear) mode, and tearing (out-of-plane shear) mode. Although closed-form solutions are available to estimate the SIF for different geometric conditions, it may still be difficult to estimate the SIF for complex geometries, such as those found in welded structures. To address this issue, many studies have utilized FEA to assist in predicting the fatigue crack propagation (Alshoaibi & Fageehi, 2020; Baptista et al., 2017; Fleck, 1986; Keui & Kiyotsugu, 1977; McClung et al., 1991; McClung & Sehitoglu, 1989; Newman, 1976; Park & Song, 1999; Pippan & Hohenwarter, 2017; K. Solanki et al., 2004; Wu & Ellyin, 1996; Yue et al., 2018). One of the early efforts was conducted by Newman (1976) which established two-dimensional, non-linear FE models to predict crack closure and crack-opening stress during the crack growth process under CAL. The simulated results were consistent with the experimental ones. The FE models treated the boundary condition along the crack path as springs. The stiffness of the springs would change from an extremely large value to zero to simulate the crack advancement under fatigue loadings. The crack tip location would be updated continuously as the crack propagated and a mesh refinement was needed to conform to the geometry.

Remadi et al. (2019) implemented elastic-plastic FEA to predict FCG in aluminum alloys under block loadings with periodic overloads. The residual stress distribution ahead of the crack tip was predicted using FEA and the load history effect was considered by tracking the stress distribution while updating the crack length in the FEA. The simulated results showed a better prediction

compared to AFGROW model (Harter, 1999). The mesh in FE models was updated continuously to model the crack propagation. This mesh refinement process used in traditional FEA has been shown to be challenging considering the small mesh size required around the crack tip and step-wise mesh updating (Anderson, 2017).

Other numerical simulation methods have also been developed to solve the fatigue crack propagation problem. These include the extended finite element method (XFEM) (Belytschko & Black, 1999; Moës et al., 1999), Boundary Element Method (BEM) (Mi & Aliabadi, 1994), Scaled Boundary Finite Element Method (SBFEM) (Yang, 2006), and meshless methods (Bordas et al., 2008). Among these methods, the XFEM has been widely used to assist in predicting crack growth. The XFEM can model discontinuities, e.g., holes, or cracks, without requiring mesh refinement to conform to these discontinuities. It was first introduced in Belytschko and Black (1999). For modeling cracks using XFEM, a standard displacement-based approximation was enriched near the crack by incorporating both a discontinuous jump function and a near tip asymptotic functions through a partition of unity (PU) method (Moës et al., 1999).

The mesh-independent property of the XFEM allows crack modeling through the introduction of enrichment functions. These enrichment functions typically consist of a near-tip asymptotic function that captures the singularity around the crack tip and a discontinuous function that characterizes the jump in displacement across the crack surfaces. The displacement vector function $\boldsymbol{u}$ can be approximated, using the partition of unity enrichment, as (Moës et al., 1999)

$$\boldsymbol{u} = \sum_{i=1}^{n} \boldsymbol{N_i(x)} \left[\boldsymbol{u_i} + \boldsymbol{H(x)a_i} + \sum_{\alpha=1}^{4} \boldsymbol{F_\alpha(x)b_i^\alpha} \right] \qquad \text{Equation 4-3}$$

where $\boldsymbol{N_i(x)}$ are the traditional nodal shape functions; $\boldsymbol{u_i}$ is the traditional nodal displacement vector associated with the continuous part of the finite element solution; $\boldsymbol{H(x)}$ is the discontinuous jump function across the crack surfaces; $\boldsymbol{a_i}$ is the nodal enriched degree of freedom

vector; $\boldsymbol{F_\alpha(x)}$ represents the associated asymptotic crack-tip functions; $\boldsymbol{b_i^\alpha}$ is the nodal enriched degree of freedom vector. The introduction of enrichment functions allows to represent a crack arbitrarily aligned within the mesh without remeshing. The stress intensity factors (SIF) calculated using XFEM showed excellent agreement with the analytical solution (Moës et al., 1999).

Since the introduction of XFEM, it has been widely implemented to different problems related to FCG (G. Shi et al., 2008; Giner et al., 2009; Fries & Belytschko, 2010; Bayesteh & Mohammadi, 2011; Feulvarch et al., 2013; Hedayati & Vahedi, 2014; S. Kumar et al., 2015; Lee & Martin, 2016; Bergara et al., 2017; Rege & Lemu, 2017; Dirik & Yalçinkaya, 2018). Kumar et al. (2015) performed elastic plastic XFEM simulations to evaluate the fatigue life of plane crack problems in the presence of various defects. The fatigue life obtained by linear elastic analysis was found close to prediction results assuming small plastic strains based on the Hutchinson-Rice-Rosengren (HRR) model (Hutchinson, 1968; Rice & Rosengren, 1968). The obtained crack-opening stresses, however, were lower than values reported by other researchers (Newman, 1984; Solanki, 2002). Lee and Martin (2016) applied XFEM to simulate stationary cracks and fatigue crack growth in a thick wall cylinder. The accuracy of the XFEM simulations were compared to the conventional contour integral method (Miyazaki et al., 1993) and experimental data. It was found that the crack front shape and the fatigue life can be accurately estimated with a finer mesh in XFEM. Dirik and Yalçinkaya (2016) proposed an algorithm to analyze 3D crack propagation under VAL through XFEM and a modified generalized Willenborg retardation model. The prediction results showed good agreement compared to both experimental FCG test data on 7075-T6 aluminum alloy and prediction from NASGRO crack propagation software (Mettu et al., 1999).

Accordingly, XFEM has shown its capability to address the FCG problems without the remeshing of the crack tip area continuously as crack grows. For the FCG under VAL, the load history effect

could be related to the residual stress strain field around the crack tip (Remadi et al., 2019) as well as the crack closure (Elber, 1971). Instead of using traditional FE models as described in Remadi et al. (2019), XFEM could be an alternative to provide an approximate estimation of the field around the crack tip. Coupled with the prediction model, e.g., crack closure model, a fatigue cracking prediction model considering the load history effect could be reached.

4.3 Proposed Numerical Simulation Approach for FCG under Variable Amplitude Loading

The approach proposed in this dissertation is based on numerical simulation using XFEM and the effective SIF concept considering crack closure. The load history effect of the VAL is estimated using a combination of (a) the residual plastic strain around the crack tip obtained from XFEM simulations and (b) the crack-opening SIF based on crack closure concept. A Python script is implemented to automatically update the crack length in the XFEM simulations and to keep track of the residual plastic stresses and strains during the crack propagation.

4.3.1 Fatigue Crack Growth Rate Model

The model proposed by Elber (1971) introduced an effective SIF to account for the crack closure induced by the plastic zone around the crack tip. Since the equation is essentially based on Paris' law, it cannot account for the behavior when the FCGR is close to the FCG threshold or fracture toughness. To consider these situations, Newman (1981) modified Elber's equation as

$$\frac{da}{dN} = C\left(\Delta K_{eff}\right)^m \frac{1-\left(\frac{\Delta K_{th}}{\Delta K_{eff}}\right)^2}{1-\left(\frac{K_{max}}{C_2}\right)^2} \quad \text{Equation 4-4}$$

$$\Delta K_{eff} = K_{max} - \max\left(K_{min}, K_{op}\right) \quad \text{Equation 4-5}$$

where C and m are the same coefficients used in Paris' law but with different fitting values to account for the effective SIF concept used; ΔK_{eff} is the effective SIF range; ΔK_{th} is the threshold

stress intensity factor range, taken as 2.29 $ksi\sqrt{in}$ (Ghahremani, 2015); K_{max}, K_{min}, K_{op} are the maximum SIF, minimum SIF, and crack-opening SIF, respectively.

For the structures addressed in this dissertation, such as ship hulls, the stress levels and the SIF remain relatively low compared to the material toughness for the majority of crack propagation period. Accordingly, the equation presented by Newman (1981) is modified as

$$\frac{da}{dN} = C\left(\Delta K_{eff}\right)^m \left(1 - \left(\frac{\Delta K_{th}}{\Delta K_{eff}}\right)^2\right) \qquad \text{Equation 4-6}$$

4.3.2 Crack-Opening SIF for Variable Amplitude Loading

The crack-opening SIF (i.e., K_{op}) in Equation 4-5 is estimated herein by combining the crack closure concept and results from XFEM for predicting crack growth under VAL. Newman (1981) and Solanki (2002) studied the relationship between the crack-opening stress and stress ratio under CAL and plane stress condition. Based on detailed FEA, it was found that the crack-opening stress decreased as the value of stress ratio varied from high positive to negative as shown in Figure 4-5. In this figure, S_0/S_{max} represents the crack-opening stress normalized by the maximum applied stress, and S_{max}/σ_0 refers to the maximum stress to flow stress ratio. The flow stress is defined as average of the yield and ultimate stress.

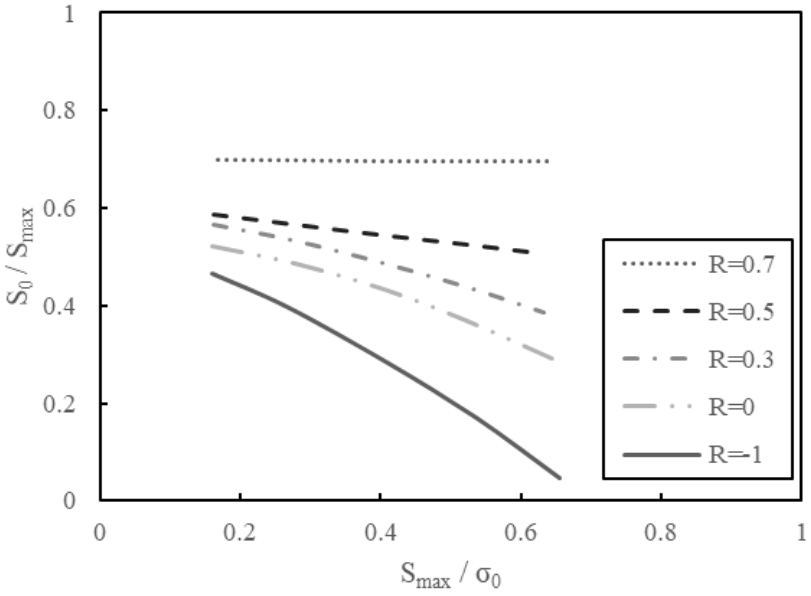

Figure 4-5. Normalized crack-opening stresses versus stress level for different stress ratios (adopted from Newman (1981)).

For middle tension, M(T), specimen, the SIF range can be calculated as (ASTM Standard E647, 2015)

$$\Delta K = \frac{\Delta P}{B}\sqrt{\frac{\pi a}{W^2}} sec\frac{\pi a}{W} \qquad \text{Equation 4-7}$$

where ΔP is the applied load range; a is the crack size (referring to half of the whole crack size for M(T) specimen); B and W are the thickness and width of the specimen. Using Equation 4-7 and the results from Newman (1981) given in Figure 1-4, a fitting surface capturing the relationship between the applied SIF, stress ratio, and crack-opening SIF K_{op} was generated using the least square fitting method (Leon et al., 2006) as shown in Figure 4-6. The obtained equation to calculate crack-opening SIF is

$$K_{op} = -0.009 \times K^2 + 3.523 \times R^2 + 0.414 \times K \times R + 0.661K - 1.816R - 1.609, \qquad -1 \le R \le 1 \qquad \text{Equation 4-8}$$

where K_{op} is crack-opening SIF; K is the applied maximum SIF; and R is the stress ratio.

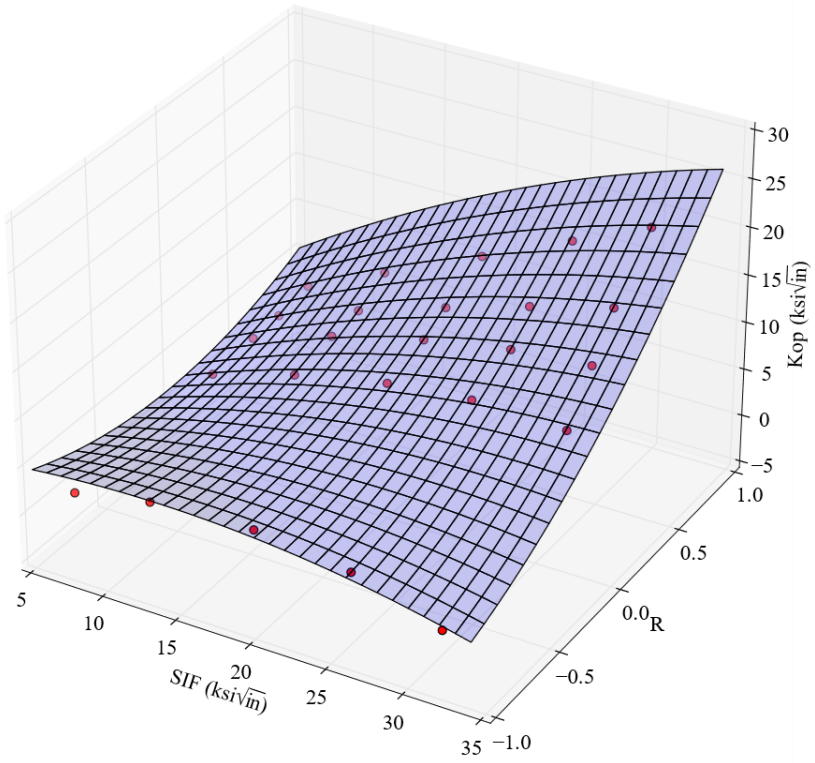

Figure 4-6. The fitting surface of the relationship between applied maximum SIF, stress ratio *R*, and crack-opening SIF K_{op}.

The stress ratio in CAL, along with the K_{max}, determines the properties of the plastic zone around the crack tip. For fatigue crack propagation under VAL, no constant stress ratio can be utilized directly. The attributes of the local plastic zone (e.g., plastic zone size and strain distribution) around the crack tip under VAL mainly depends on the load history applied. Accordingly, if similar plastic strain conditions existed under VAL and CAL at the same K_{max}, the stress ratio under the CAL can be treated as an *equivalent* stress ratio for the VAL case. In order to utilize Figure 4-6 to calculate the crack-opening SIF under VAL, this equivalent stress ratio for a specific VAL will be obtained through XFEM analysis later in this chapter. The plastic strain

information around the crack tip reflects the degree of plasticity, accordingly, it will be used as a parameter to be correlated with the load history to evaluate this equivalent stress ratio for VAL.

An example of the residual plastic strain evaluation process under VAL using XFEM is shown in Figure 4-7. The model represents half of a M(T) specimen and is updated continuously with longer crack size through a Python script. During the updating process, the residual stress and strain information are tracked. For the *i*th model, the residual stress and strain fields will be treated as the initial conditions of the next (*i*+1)th model as shown in Figure 4-7. As shown in the figure, as the crack grows and a larger SIF is applied to the model, the plastic zone around the crack tip, as well as the strain value increase. Since the residual stress and strain due to previous loads are considered, not only the current load but also the load history contributes to the formation of the current plastic zone.

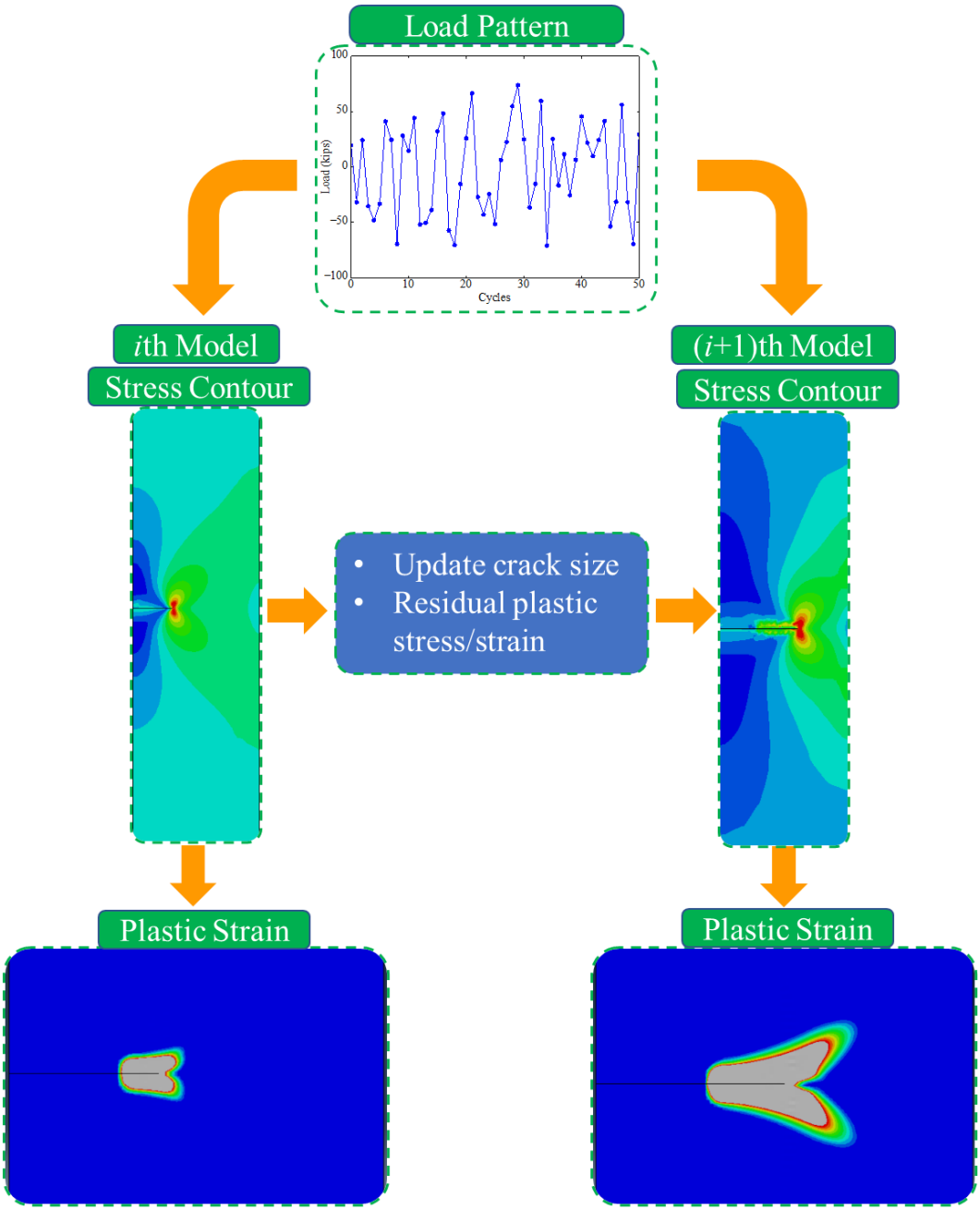

Figure 4-7. Example of residual plastic strain evaluation as crack grows under VAL using XFEM.

Retardation and/or acceleration in the FCGR may occur due to overloads and underloads (Fleck, 1985). As show in Figure 4-4, the retardation due to an overload is delayed by a certain crack extension. Accordingly, the crack needs to advance a certain distance before the load history

effect (i.e., retardation) could take place. This small crack extension, defined here as a_c, can be taken as a fraction (e.g., 10%) of the theoretical plastic zone size obtained using elastic-plastic corrections as indicated in (Irwin, 1960). Other researchers such as Newman (1981) used 0.1 mm (0.005-in) for this small crack extension. In this dissertation, this value is considered 0.01 in which was found to provide a good agreement with experimental crack growth tests. After this crack extension, retardation will take place. This delay in retardation allows to discretize the crack growth into small increments (e.g., 0.005-in in length); the growth in each of these increments will depend on the load history effects (i.e., K_{op}) obtained from the crack growth in the previous increment. Furthermore, the load applied in the current crack growth increment will not affect the opening SIF in this particular increment, rather, it will affect the K_{op} in later increment(s). Accordingly, only the load history applied before the current crack growth stage should be considered for characterizing the load history effects in the current crack growth segment.

Figure 4-8 shows a VAL load pattern and illustrates further the approach used to compute K_{op} at different crack growth increments. As shown, the maximum and minimum load values within a segment of loading are obtained. In XFEM, these loading values will be applied to the model to determine the residual plastic strain around the crack tip while the other loading cycles with lower amplitudes are assumed to have a negligible effect. The plastic strain information for an interval of the VAL is estimated and will be used to obtain the K_{op} for the next crack growth increment. Once the plastic strain is estimated through XFEM, the relationship between the plastic strain around the crack tip, ε_{pl} and the applied SIF are used to compute the equivalent stress ratio *R*. This relationship is denoted $f(R, K, \varepsilon_{pl})$. The parameters in this equation (see Equation 4-9 below) will be established using the fatigue testing data under CAL and results from corresponding XFEM. The equation is discussed in the following section since it is heavily based

on experimental and numerical results. The equivalent R value calculated from $f(R, K, \varepsilon_{pl})$ equation can be used with Equation 4-8, to obtain the crack-opening SIF for VAL condition.

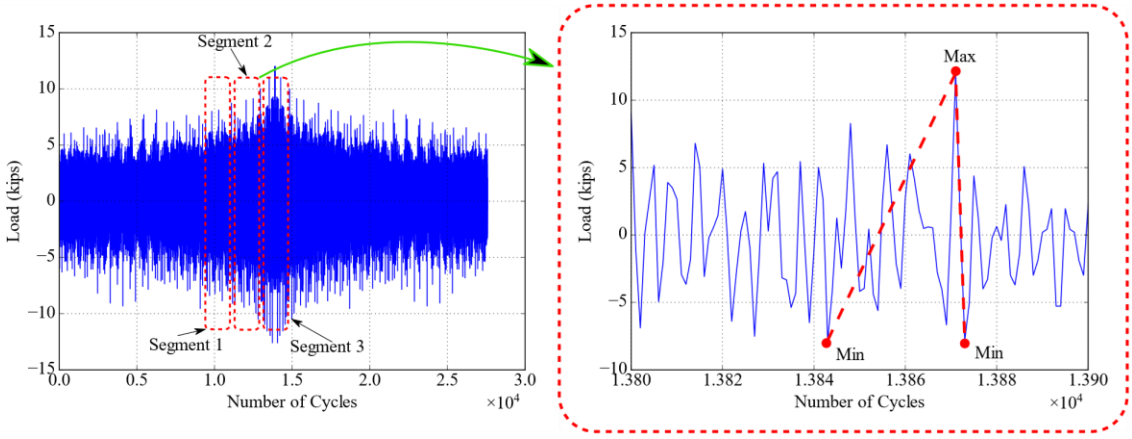

Figure 4-8. Maximum and minimum values of VAL for XFEM.

4.3.3 FCG Prediction Procedure

The procedure to predict the FCG under VAL follows the flowchart described in Figure 4-9. The information about the specimen or model is defined in the first step including material properties, dimensions, crack size, and FCG fitting parameters (i.e., C and m). Next, for a given VAL pattern, the following steps need are executed:

1. Initiate the XFEM model with the initial or updated crack size.
2. A segment of the load history is selected and examined to obtain the maximum and minimum load values within this segment. The length of the segment is chosen randomly.
3. The obtained max/min loads are then applied to the established XFEM model.
4. Information including residual stress/strain, SIF, and plastic strain around the crack tip are retrieved from the analysis results.
5. The crack-opening SIF K_{op} is evaluated with the plastic strain around the crack tip and Equation 4-8 and Equation 4-9.

6. The crack growth for the applied VAL pattern is then calculated using Equation 4-5 and Equation 4-6.
7. The obtained crack growth is compared to the crack extension unit a_c, defined herein as 0.01 in. If the difference is larger than a certain tolerance (defined herein as 0.00001 in), then the length of the load segment needs to be adjusted, either with longer or shorter loading time.
8. Repeat step 2 to 7 until the difference falls within the tolerance.
9. Once the above steps are done, the crack propagates by one unit of the crack extension (i.e., a_c) and initial conditions are generated based on the residual stress/strain in the current XFEM model
10. Repeat step 1 to 9 if the crack size is less than the size limit a_f ; otherwise, the analysis is done.

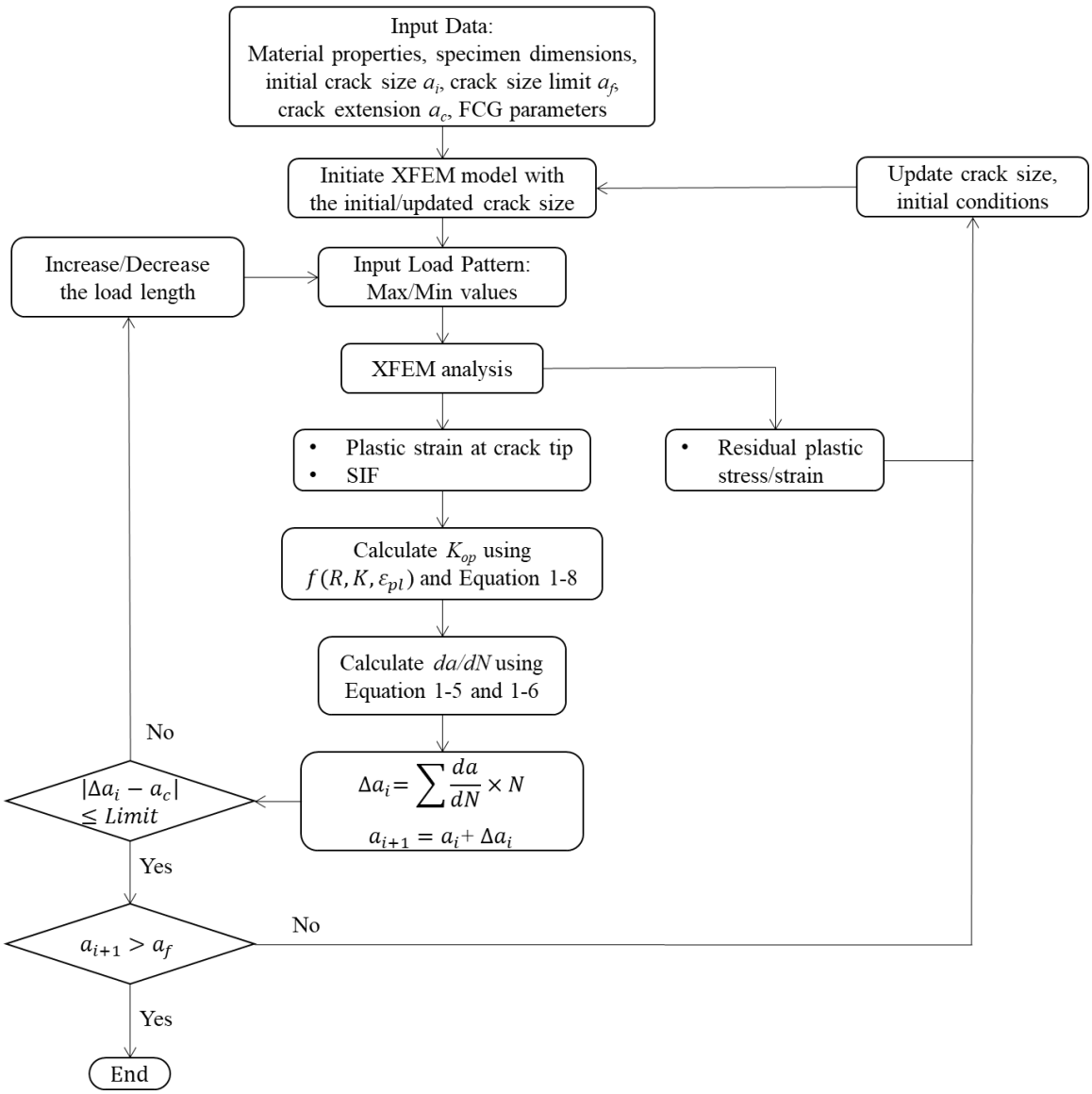

Figure 4-9. Flowchart of the proposed FCG prediction approach.

4.4 Middle Tension Fatigue Test Details

To verify the proposed numerical procedure, a series of fatigue tests were conducted on middle tension M(T) specimens under (a) constant amplitude loadings (CALs) with different stress ratios and (b) variable amplitude loadings (VALs). The M(T) specimens were designed according to the ASTM E647 specifications (ASTM Standard E647, 2015). The specimens were fabricated from A572 Gr. 50 steel plates, which is the same material used for the large-scale fatigue test discussed later in this dissertation. The details of the designed M(T) specimen are shown in Figure 4-10.

The notch width is 0.4-in, and precracking procedure was implemented until the initial crack size of 0.3-in in each direction was reached. Per ASTM E647 (ASTM Standard E647, 2015) the amplitude of the loads applied during the precracking phase is equal or less than the amplitude of the loading applied during the fatigue tests. An MTS 880 load frame with 22 kips actuator capacity was utilized for the fatigue testing. The automated vision-based fatigue crack growth monitoring system introduced in the previous chapter was used herein to monitor the crack growth and measure the crack size. The same system setup shown in Figure 3-1 in Chapter III was used to conduct these fatigue tests.

Five tests in total have been conducted on the M(T) fatigue specimens. Three specimens were tested under CALs with stress ratios -0.3, 0.1, and 0.3. The details of the CALs are presented in Table 4-1. Two additional M(T) specimens were tested under VAL patterns. The load histories used in the VAL are shown in Figure 4-11. The variable loading spectrum applied to Test 4 has maximum and minimum load amplitudes of 11 kips and -4.9 kips, respectively, while Test 5 had, respectively, 12 kips and -12 kips as the maximum and minimum load amplitudes. Although the load spectrum applied in Test 5 has a higher maximum amplitude, the first pattern (i.e., used in Test 4) has higher number of positive load cycles compared to the second pattern as shown in Figure 4-12. The first variable loading pattern was scaled based on wave-induced load history recorded during structural health monitoring operations of a ship hull operating in the North Atlantic. The second variable loading pattern was generated to simulate wave loading conditions based on Tomita et al. (1995) and Li et al. (2016), which will be discussed in more depth later in this dissertation. The load application frequency adopted in Test 4 is 6 Hz while a frequency of 20 Hz was adopted in all other tests.

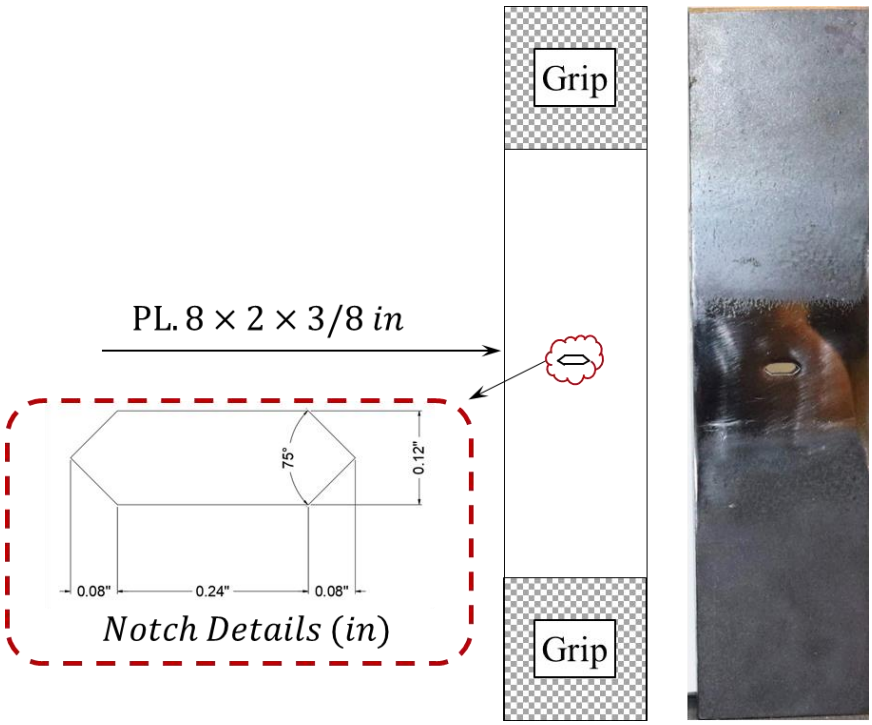

Figure 4-10. Details of the middle tension specimen.

Table 4-1. Fatigue coupons tested under constant amplitude loadings with different stress ratios.

	Stress Ratio, R	Max Force (kips)	Min Force (kips)	Max Stress (ksi)	Min Stress (ksi)
Test 1	-0.3	8.6	-2.6	17.2	-5.2
Test 2	0.1	8.9	0.9	17.8	1.8
Test 3	0.3	8.6	2.6	17.2	5.2
Test 4	Variable	11.0	-4.9	22.0	-9.8
Test 5	Variable	12.0	12.0	24	-24

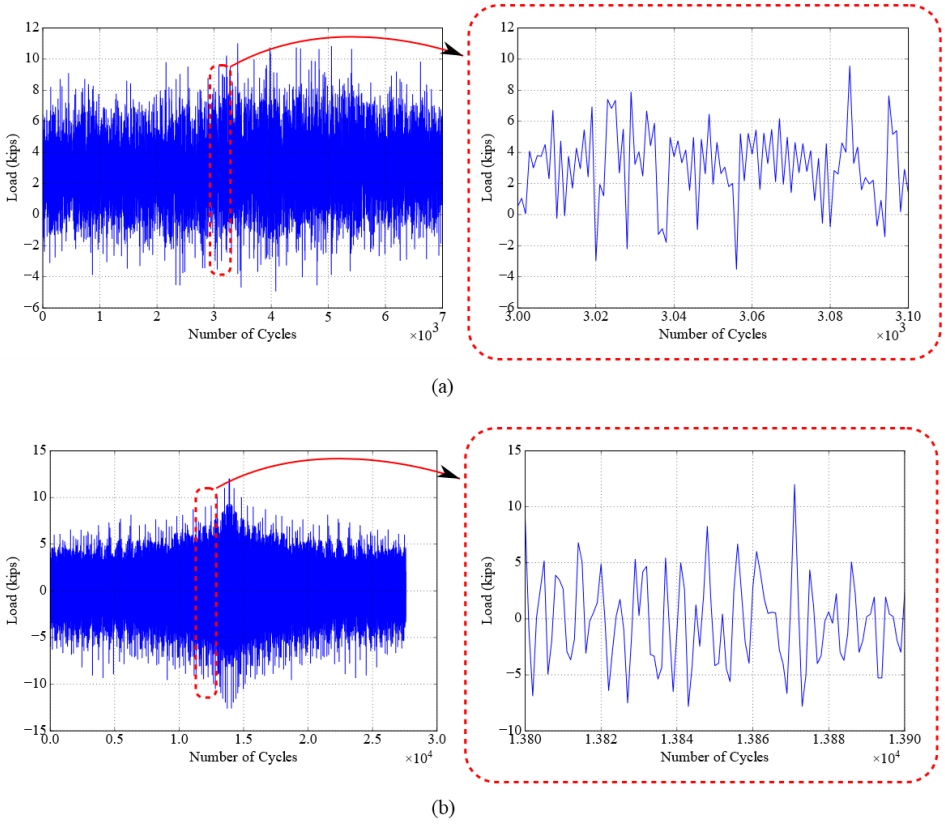

Figure 4-11. Variable amplitude loading profile applied in (a) Test 4 and (b) Test 5

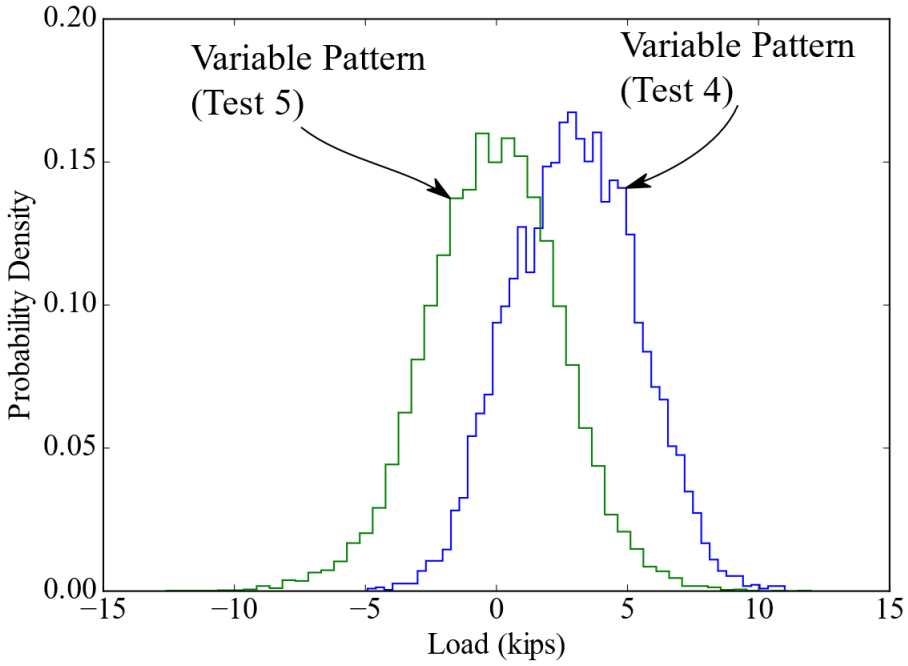

Figure 4-12. Probability density of the force amplitudes in the two variable amplitude loading spectra.

4.5 XFEM-Based FCG Modeling

An XFEM-based model was constructed in Abaqus environment (Dassault Systemes, 2021) based on the M(T) fatigue test specimens. The dimensions of the FE model are 8-in, 1-in, and 1/4-in in length, width, and thickness, respectively. Only half the width of the specimen is constructed with solid elements due to the symmetry of the M(T) specimen. Nodes along the left surface of the FE model (i.e., axis of symmetry) are restricted in terms of X- and Z-axis displacements and rotations around the Z-axis. The bottom surface is fixed by coupling constraints, and the load is applied to the top surface. The crack is defined using XFEM (Fries & Belytschko, 2010) with an initial crack size of 0.3-in. The size of the mesh around the crack is set as 0.01-in. The crack extension for this model is set as 0.01-in accordingly. The material is assumed as elastic perfectly plastic with a yield strength of 50 ksi. Figure 4-13 shows a view of the FE model, the implemented constraints, and a close up view of the crack region.

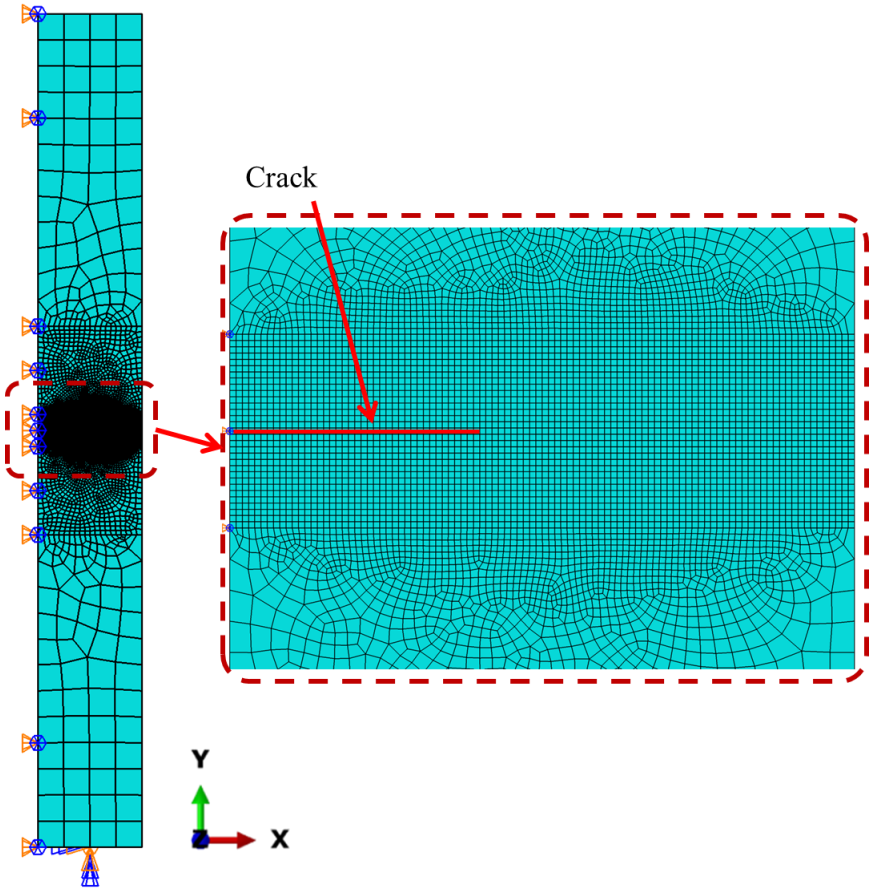

Figure 4-13. The FE model of the analyzed M(T) specimen and meshing details.

The SIF obtained from the XFEM model is compared in Figure 4-14 to the analytical SIF solution using Equation 4-7. As also reported in literature (e.g., Bayesteh and Mohammadi (2011)), the figure clearly confirms that the XFEM can estimate the SIF with reasonable accuracy.

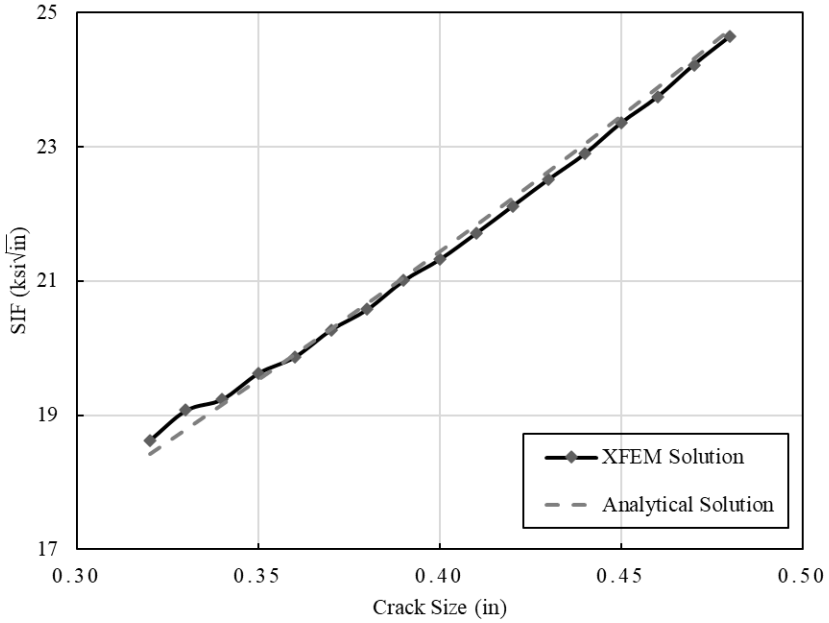

Figure 4-14. Comparison between the SIF obtained from the XFEM model and the analytical solution from ASTM E647 (ASTM Standard E647, 2015).

To develop the relationship between the plastic strain around the crack tip ε_{pl} , applied SIF *K*, and equivalent stress ratio *R*, five CALs with stress ratios of -1, -0.3, 0.1, 0.3, and 0.7 are applied to the FE models. The positive amplitudes of the five loadings are all set as 8.6 kips which is the same amplitude of the Test 1 and 3. The value of the plastic strain around the crack tip was obtained from the first element after the crack tip. An example of the plastic strain around the crack tip versus the applied load is plotted in Figure 4-15 (a). The figure shows the load vs time and plastic strain vs time obtained after the application of the maximum and minimum loads as described in the flowchart above. The figure also shows the corresponding residual plastic strain distribution at different load times.

The same process is repeated at different crack sizes for each of the five generated stress ratios. The results are combined and the best fit surface is obtained based on the least square fitting method (Leon et al., 2006) and shown in Figure 4-16. The best fit surface is used to obtain the equivalent R by means of the following equation $f(R, K, \varepsilon_{pl})$

$$R = -5.14 \times 10^{-4} \times K^2 - 1.17 \times 10^5 \times \varepsilon_{pl}^2 + 2.12 \times K \times \varepsilon_{pl} - 0.65K + 1270\varepsilon_{pl} - 1.28$$

Equation 4-9

where R is the equivalent stress ratio for the applied VAL; K is the applied maximum SIF; ε_{pl} is the residual plastic strain value obtained from the first element after the crack tip.

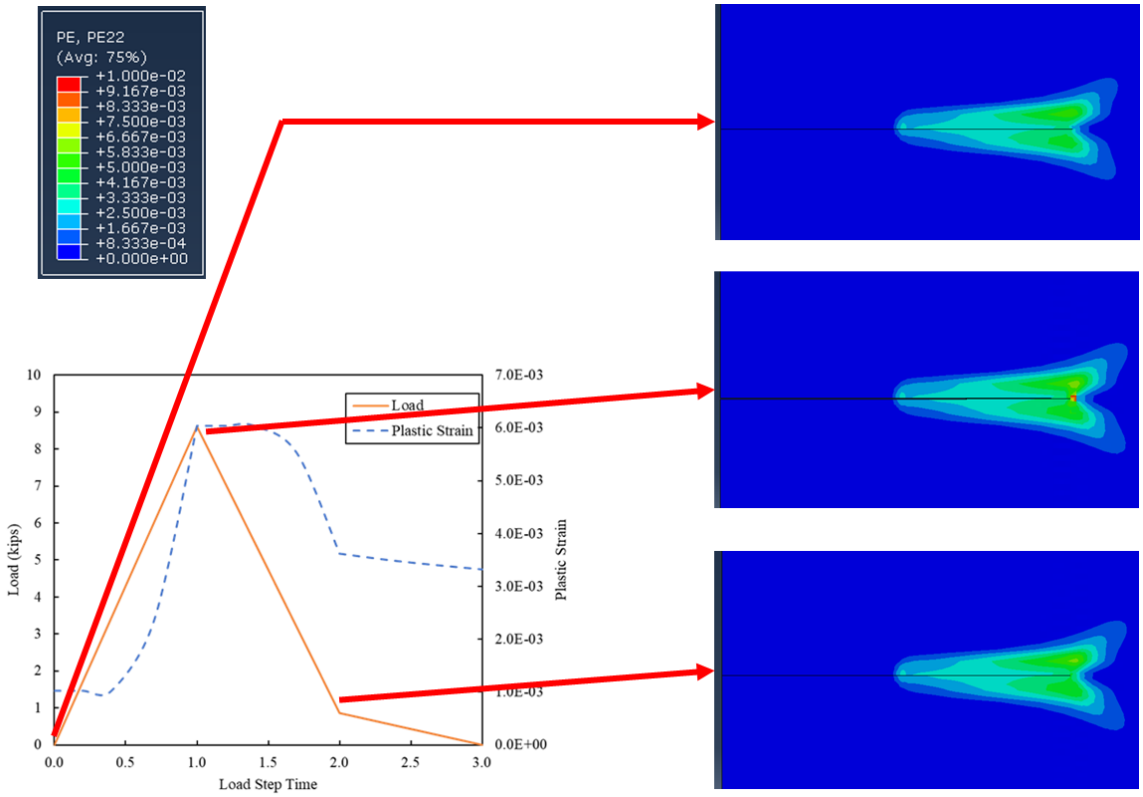

Figure 4-15. Example of plastic strain fields around the crack tip: (a) load versus time and plastic strain versus time.

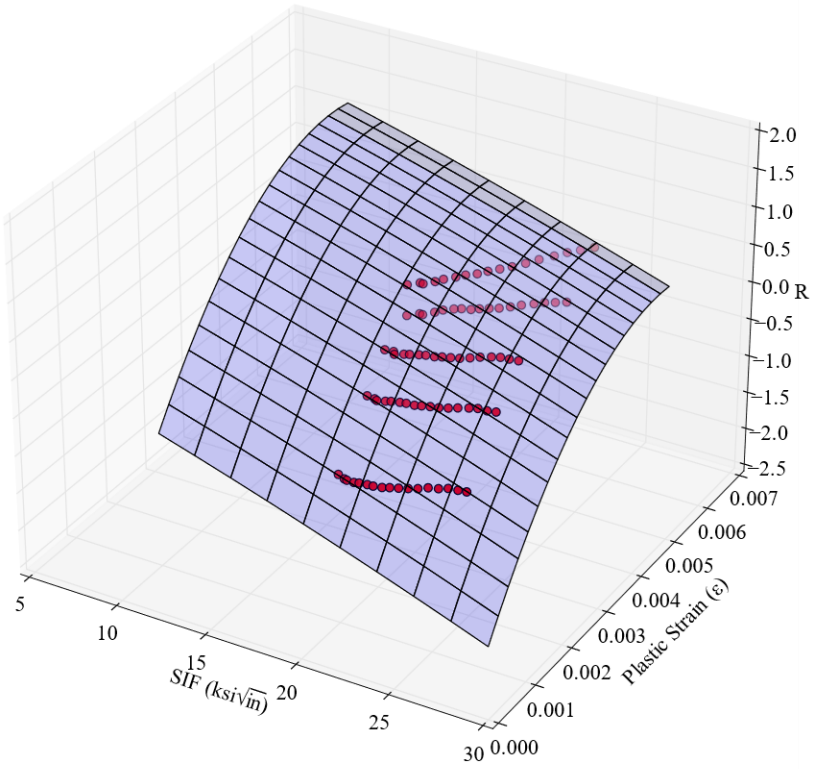

Figure 4-16. The fitting surface of the relationship between SIF, crack tip plastic strain, and stress ratio *R*.

4.6 Crack Growth Prediction Results

For the three conducted specimens with CALs, the corresponding FE models are established as discussed above. The history of the plastic strains around the crack tip is tracked for different crack sizes under different stress ratios. The equivalent R is calculated using Equation 4-9 for each crack increment and the crack-opening SIF associated to be used for the next increment is calculated using the obtained equivalent R and Equation 4-8. Combining the calculated crack-opening SIF and the experimental data from the three tests, the parameters in Equation 4-6 were calibrated in customary units as follows: $C = 2.03\times10^{-9}$, $m = 2.82$. The fitting curve is plotted in Figure 4-17. The fitting process resulted in a coefficient of determination of 0.958. The comparison between the crack growth prediction results using Equation 4-6 and crack growth test

data is shown in Figure 4-18. For different stress ratios, the prediction model was capable of predicting the crack growth under CAL with an error of 8%.

The proposed prediction numerical procedure is used next for crack growth prediction for the two specimens tested under VALs. The comparison of the results is depicted in Figure 4-19. FCG prediction using Paris' law for the two conducted tests under VALs is also included in the figure. The parameters in Paris' law are estimated based on the conducted fatigue tests under constant amplitude loading, i.e., C=1.24$\times 10^{-10}$, m=3.14 fitted using of ksi for stress and inches for the crack length. For different load histories, neglecting the load history effects can over-or under-estimate the actual crack growth profile. For Test 4, the prediction using Paris' law is led to slower crack propagation rate than the actual test while it predicted a faster growth rate for Test 5. On the other hand, for the proposed approach considering load history effects, the prediction results show good agreement with the experimental data. This suggests that the load history effect in VAL is accounted for properly using the proposed prediction model. Accordingly, for structures under VAL, the proposed fatigue crack growth prediction model can account for the load history effect and accurately predict the crack growth. The same model and fitting parameter values will be used to predict the crack propagation behavior under VAL in large-scale welded stiffener panels.

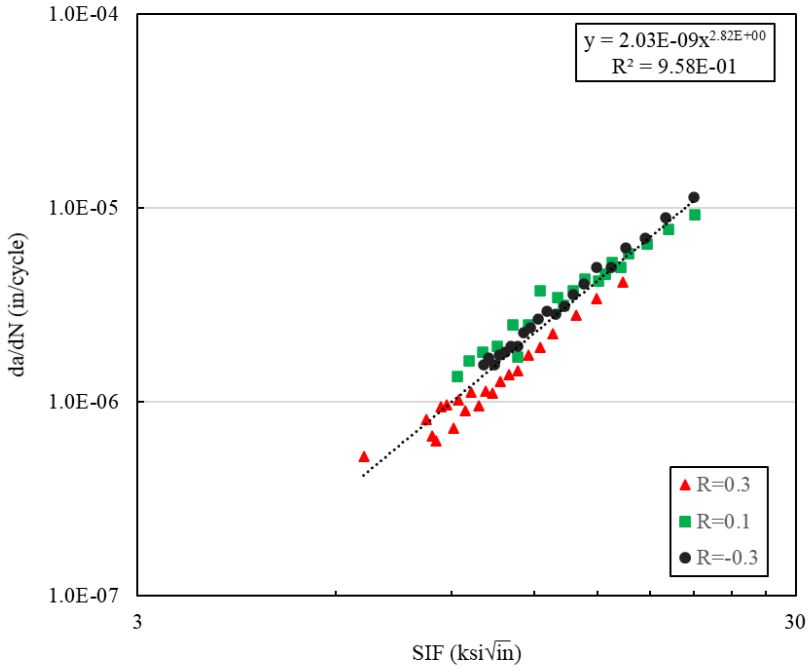

Figure 4-17. FCG fitting using the data from the conducted M(T) tests.

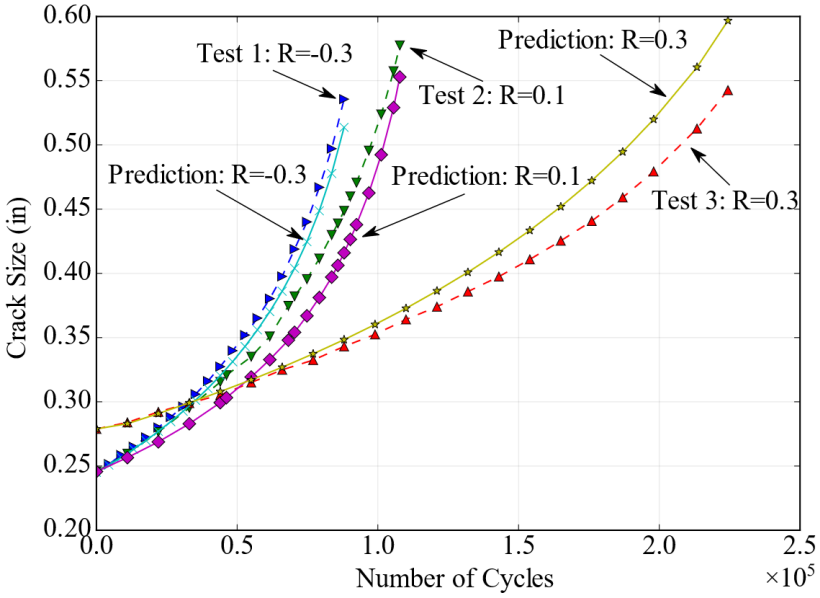

Figure 4-18. Results comparison between prediction and tests under constant amplitude loading profiles with different stress ratios.

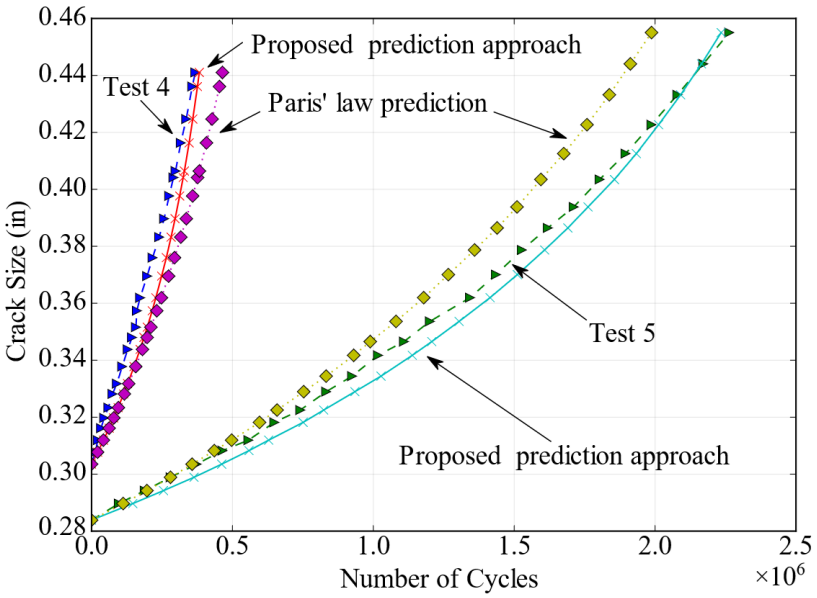

Figure 4-19. Results comparison between tests and prediction under variable amplitude loadings.

4.7 Conclusions

This chapter presents an approach for predicting FCG under VAL. XFEM was used to model the fatigue crack and obtain the stress/strains fields around the crack tip. The continuous tracking of residual stress/strain, as well as the applied initial conditions, enables the XFEM to retain memory of the previous analysis results and integrate the load history effect. The plastic strain around the crack tip was used to calculate an equivalent stress ratio under the VAL. This ratio was next used to compute the crack-opening SIF based on the crack closure concept. An analytical crack advancement rule was used to track the crack propagation. Middle tension fatigue tests were conducted to provide essential experimental data for validating the prediction model. The following conclusions can be drawn:

1. The proposed FCG prediction framework can predict the crack growth profiles under both constant and variable amplitude loadings. For the majority of considered cases, the predicted crack growth profile was within 8% of the experimental results.

2. Utilizing XFEM to account for crack closure effects provides a computationally efficient approach for tracking the crack-opening SIF under variable amplitude loading condition. The proposed approach allows computing the crack-opening SIF over larger crack length segments, rather than on a cycle-by-cycle basis, leading to a significant reduction of the computational cost of the analysis.
3. Neglecting the effect of crack closure and load history effect can overestimate or underestimate the fatigue life under variable amplitude loading.
4. The developed relationship that can compute the crack-opening SIF as a function of the plastic strain around the crack tip, applied maximum SIF, and the equivalent stress ratio, resulted in accurate crack growth prediction results. It is recommended to use this approach for studying crack growth under different geometric and/or loading conditions.

CHAPTER V

EXPERIMENTAL AND NUMERICAL INVESTIGATION OF THE FATIGUE CRACK GROWTH OF STIFFENED PANELS UNDER RANDOM SEA LOADINGS

5.1 Introduction

Fatigue cracking commonly occurs in ships due to the wave-induced variable amplitude loading encountered throughout the service life. Fatigue cracks in ship hulls are inevitable due to the large number of welded connections. These cracks can propagate to a critical length which could lead to a catastrophic failure of the ship hull. Steel grades with higher toughness have been used in modern ship construction to mitigate the fatigue cracking. Welded stiffened panels are typically adopted in ship hull structure design to improve the structural performance and increase the capacity with respect to plate buckling failures. The presence of multiple stiffeners that are generally subjected to low stress at service load levels creates mechanisms for load transfer from a cracked element to adjacent elements. Due to the high redundancy of these hull structure, cracks can reach a relatively large length before unstable failure occurs (Fricke, 2017). However, these long cracks can still cause the sudden failure of the hull along with the significant consequences associated with this failure event.

Hull cracks represent a safety hazard and must be monitored and repaired in a timely manner to prevent catastrophic failures. Developing methodologies that can predict the hull reliability under

the presence of cracks is essential for properly planning maintenance and repair actions. Accordingly, it is crucial to establish an accurate prediction model for the fatigue crack growth (FCG) and the remaining service life for the welded stiffened panels subjected to fatigue cracking.

The presence of the stiffeners and the existence of residual stresses due to the welding process have significant effects on the crack propagation behavior in welded stiffened panels (Nussbaumer, 1994). Several studies focused on developing FCG models that account for these factors (Dexter & Pilarski, 2000; Faulkner, 1975; Mahmoud & Dexter, 2005; Mathummal, 1983; Nussbaumer, 1994; Nussbaumer et al., 1999). However, most research results are based on testing specimens under constant amplitude loading with positive stress ratio. This is in contrast to actual wave-induced variable amplitude loading that ship hulls encounter during normal operation. In this situation, the fatigue crack growth rate (FCGR) highly depends on load history effects and may experience retardation and/or acceleration due to the interaction between overloads and underloads (Skorupa, 1998). As a result, FCG prediction based on constant amplitude loading that neglects load history may fail to accurately reflect the actual crack growth in ship hulls.

To address this research need, this chapter presents the results of an experimental investigation on FCG of stiffened box girders under variable amplitude loadings. The XFEM-based FCG prediction model proposed in the previous chapter and an analytical model have been used here to predict the fatigue behavior considering the load history effect. The same parameters from the small-scale fatigue tests have been used in the proposed framework. The predicted results are compared to the experimental ones to demonstrate the feasibility of the proposed approach.

5.2 Background

5.2.1 Crack Propagation in Welded Stiffened Panels

Early research aiming at characterizing fatigue crack propagation in stiffened panels started in the 1960s. Poe (Poe, 1971; Poe Jr, 1969) studied the FCG behavior of aluminum alloy stiffened panels constructed with riveted and integral stiffeners. Fatigue tests under constant amplitude fatigue loading were conducted on both unstiffened and stiffened panels with different stiffener parameters including spacing and dimensions. Experiment results indicated that the presence of riveted stiffeners significantly reduced the FCGR compared to unstiffened panels; however, integral ones had less effect on the FCGR. The reason was that bolted stiffeners remained mostly intact when the crack propagated through the main plate past the stiffeners, while integral stiffeners would also experience crack propagation and could be severely damaged as the crack grew. An analytical model was proposed by (Poe Jr, 1969) to calculate the stress intensity factor (SIF) range for cracks propagating through stiffened panels. The FCG predictions based on the analytical model showed good agreements with to the test results. It should be noted that residual stresses were not considered in the analytical model since it was indicated that no significant residual stress existed in the tested extruded stiffened panels (Poe, 1971).

For welded stiffened panels, the welding process generally causes considerable residual stresses around the stiffeners due to differential thermal expansion and contraction of the weld metal and parent material. This process generally creates high tensile stresses close to the stiffeners and compressive stresses between the stiffeners (Radaj, 2012). These residual stress fields will affect the FCG behavior in the welded stiffened panels (Nussbaumer et al., 1999). Based on Poe's work, the effect of residual stress was considered in a modified analytical model for predicting the SIF range in welded stiffened panels in Nussbaumer (1994) and Nussbaumer et al. (1999). Nussbaumer et al. (1999) designed three-flanged welded box beams with one stiffener, as a representation of double hull ship construction, and tested them under constant amplitude loading.

The test results indicated that this type of box beam construction can sustain long fatigue cracks before unstable crack propagation is reached. The residual stresses due to welding used in the finite element analysis (FEA), showed a good agreement with the measured result using the standardized strain-gauge hole-drilling method. The investigation results revealed that the residual stress field can greatly affect the SIF range as well as the FCGR. FCG predictions were made through the modified analytical formulations and the FEA, and both exhibited good agreements with the experimental results.

Dexter and Pilarski (Dexter & Pilarski, 2000) continued the research using the newly designed stiffened box beam specimens with multiple stiffeners. The fatigue crack resistance and structural redundancy of the box beam specimens were confirmed by all the tested specimens. A significant shear lag effect was noticed in the specimens due to the limited height of the box web plates. This led to nonuniform stress distribution across the stiffened panels. The SIF range was evaluated in the FEA using the gap elements along the crack faces. The gap element prevents the faces from overlapping in regions of compressive stress and estimates the resultant contact forces. However, it could be time-consuming compared to analytical modeling. The residual stress distribution model proposed in (Faulkner, 1975) was used in conjunction with the analytical model developed in (Nussbaumer, 1994) and verified by measuring the residual stress field within the tested specimens. Mahmoud and Dexter (Mahmoud & Dexter, 2005) performed a series of fatigue tests, under direct tensile loading, on multiple stiffened panels to investigate the effect of stiffener types, stiffener spacing, plate thickness, and heat input on the FCG characteristics. The same analytical and FEA procedures presented in (Dexter & Pilarski, 2000) were used to evaluate the SIF range and the predicted FCG in the tested specimens was, in general, close to the test results.

Most of these studies have tested specimens under constant positive amplitude loadings. However, for the welded stiffened panels used in ship structures, the wave-induced stresses are variable in amplitude. Furthermore, these variable amplitude loads encountered by ship hulls can

vary, in stress ratio, from positive to negative between cycles. As discussed in Chapter IV of this dissertation, it is essential to consider load history effects in predicting FCG under variable amplitude loading (Aïd et al., 2011; Geary, 1992; Skorupa, 1998; Sonsino, 2007). In addition, the effects of plasticity, e.g., crack closure, was not considered in the analytical and finite element (FE) models developed to study FCG in stiffened panels. The main reason for neglecting crack closure in (Dexter & Pilarski, 2000) was to obtain more conservative crack growth estimates by neglecting crack growth retardation. However, underloads can cause FCGR acceleration and, as in the case of ship hull loading, neglecting the effect of plasticity can lead to unconservative estimates of the fatigue life. Ships encounter random sea loadings during their service life which include tensile and compressive stress cycles with variable amplitudes. As a result, crack closure, as well as crack growth rate retardation and acceleration, could play a role in the fatigue crack growth process.

In literature, many studies utilized constant tensile cyclic loading in experimental work aiming at characterizing crack propagation in ships; however, as discussed above, many of the fatigue damage and crack growth prediction approaches are unable to consider the load history effect. The generalized crack prediction models based on the results of these experiments cannot be directly used to predict FCG under variable amplitude loading. Hence, experimental data for crack growth in welded stiffened panels under wave-induced variable amplitude loading is necessary to provide a clear picture of the realistic crack growth behavior in ship hulls. A fatigue cracking prediction model considering load history effects is also needed to estimate the fatigue life of welded stiffened panels. Data from the experimental work can be used to validate the developed prediction models.

5.2.2 SIF Analytical Model for Stiffened Panels

The analytical model (Dexter & Pilarski, 2000; Nussbaumer, 1994; Poe, 1971) is adopted herein to estimate the SIF range in stiffened panels. This model has shown high accuracy compared to

the results of FE modeling. The analytical model is based on the superposition principle considering the effects of stiffener restraint, stiffener separation, and residual stresses.

The effect of stiffener restraint accounts for the restraint provided by a stiffener before the crack reaches it. It was first studied by Greif and Sanders Jr (1965) and Isida (1973) for a non-symmetric crack approaching a stiffener in an infinite plate and a symmetric crack in a stiffened plate with finite width, respectively. Nussbaumer (1994) modified Isida's work to provide a solution for panels with multiple stiffeners. The effect of stiffener restraint f_1 on the SIF range is computed as (Nussbaumer, 1994)

$$f_1 = \Sigma f_{1,i} \qquad \text{Equation 5-1}$$

$$f_{1,i} = \left(1 - \frac{1}{f_{k,i}}\right)\left(\frac{1}{1+\beta_i}\right)^{\alpha_1} + \frac{1}{f_{k,i}} + \frac{0.3\chi_i^2}{f_{k,i}}\left(\frac{4}{\beta_i^2-2\beta_i+4} - 1\right) - 1 - \alpha_2\left(\frac{\chi_i^{10}+\chi_i^{30}+\chi_i^{50}}{f_{k,i}}\right)\left(\frac{4}{\beta_i^2-2\beta+4} + 1\right),\ for\ \chi_i \le 1 \qquad \text{Equation 5-2}$$

$$f_{k,i} = \frac{1 - 0.5\chi_i + 0.326\chi_i^2}{\sqrt{1-\chi_i}} \qquad \text{Equation 5-3}$$

where a is half the crack size; $\chi_i = \frac{a}{x_i}$, $\beta_i = \frac{A_{st,i}}{t_{pl}x_i}$, x_i is the distance from the center of the crack to the *i*th stiffener, $A_{st,i}$ is the cross-sectional area of the *i*th stiffener, t_{pl} is the plate thickness; α_1 and α_2 are constants to compensate the overestimated restraining effect, Nussbaumer suggested $\alpha_1 = 1$, $\alpha_2 = 0.1$ after comparing with the results reported in Poe (1971).

Once the crack has passes through the stiffeners, the effect of stiffener restraint will disappear and the effect of stiffener separation takes place. Wedge forces are generated by the severed stiffeners and applied as point forces to the crack face. The effect of stiffener separation f_2 is computed as (Nussbaumer, 1994)

$$f_2 = \Sigma f_{2,i} \qquad \text{Equation 5-4}$$

$$f_{2,i} = \frac{2\mu}{\pi(1-\mu)} \cdot \frac{{}^{2s}/_{x_i}}{\sqrt{\chi_i^2 - 1}},\ for\, \chi_i > 1 \qquad \text{Equation 5-5}$$

where $\mu = \frac{A_{st}}{A_{st}+A_{pl}}$; A_{st} is the area of the stiffener and A_{pl} is the area of the plate between two stiffeners; *s* is the half of the distance between two stiffeners. Combining the effects of stiffener restrain and separation yields the stiffened panel coefficient, which can be calculated as

$$f_{st} = 1 + \Sigma f_{1,i} + \Sigma f_{2,i} \qquad \text{Equation 5-6}$$

The SIF arising from the residual stresses due to welding can be expressed as (Rooke & Cartwright, 1976)

$$K_{res} = \sqrt{\pi a}\frac{2}{\pi}\int_0^a \frac{\sigma_{res}(x)}{\sqrt{a^2 - x^2}}dx \qquad \text{Equation 5-7}$$

This model is based on Green's function (Duffy, 2015), integrating the solution for a pair of splitting forces acting at the crack faces. The model proposed by Faulkner (1975) is adopted herein to represent the residual stress distribution across welded panels due to welding. This model was validated based on Fisher et al. (1992) and Dexter and Pilarski (2000). Figure 5-1 shows an example of the calculated residual stress field across the stiffened panel studied experimentally in this dissertation. As seen in the figure, the area around the stiffeners is subjected to triangular residual tensile stress while the area between stiffeners experiences constant residual compressive stress. The largest width of the area subjected to tensile stresses is considered to be 3.5 times of plate thickness as suggested by Dexter and Pilarski (2000). A yield strength of 59 ksi is also considered based on the auxiliary tests conducted as part of this chapter.

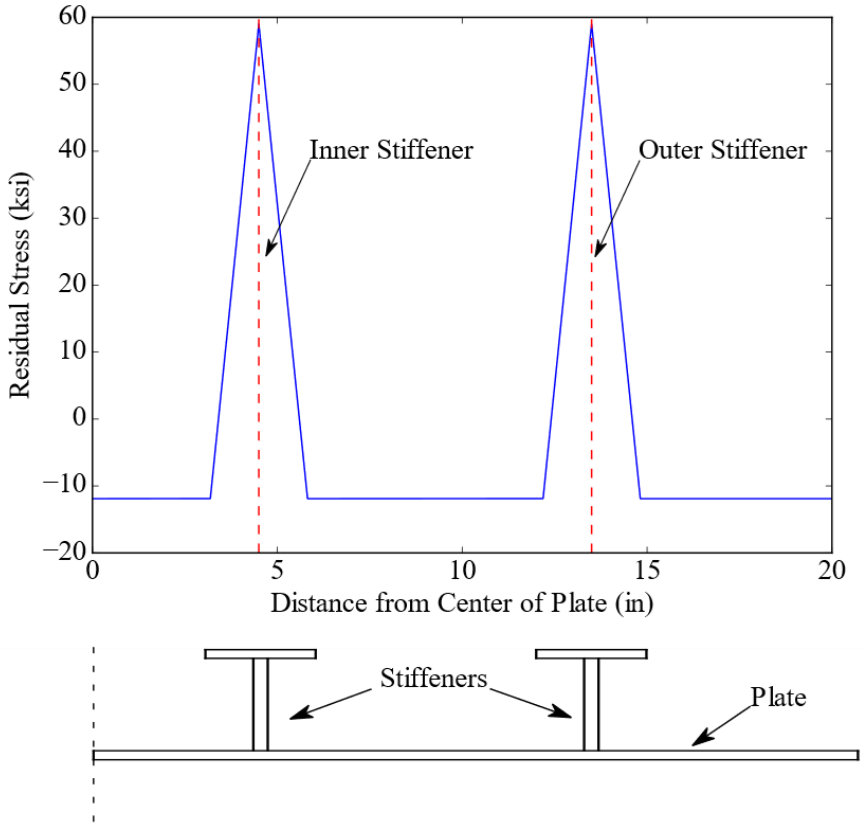

Figure 5-1. Residual stress field of Specimen S1 using Faulkner's model.

Accordingly, the SIF for the stiffened panel can be evaluated as

$$K = K_{st} + K_{res} \qquad \text{Equation 5-8}$$

$$K_{st} = f_{\sigma} f_{st} \sigma \sqrt{\pi a} \qquad \text{Equation 5-9}$$

$$f_{\sigma} = \frac{I_0 c(a)}{I(a) c_0} \qquad \text{Equation 5-10}$$

where f_{σ} is the net section coefficient to account for the finite width effect presented by Nussbaumer(1994); a is the crack size in the stiffened panels including cracks in plate and stiffeners; I_0 is the original moment of inertia of the uncracked stiffened panel; $I(a)$ is the moment of inertia of the cracked net section which is related to the crack size; c_0 is the original centroid of

the uncrack stiffened panel; *c(a)* is the centroid of the cracked stiffened panel in terms of crack size.

5.3 Stiffened Box Girder Fatigue Test Details

A series of fatigue tests on stiffened box girders are designed to characterize the actual FCG behavior in stiffened box girders and obtaining the necessary data for validating the developed prediction model. This dissertation discusses the specimen design, test matrix, and instrumentation plan, as well as the results of the first test specimen. Four stiffened specimens have been designed with different parameters, i.e., the stiffener type, the distance between stiffeners, and main flange plate thickness. Till the time of preparing this dissertation, only the first specimen from the proposed specimen matrix has been tested considering the lengthy fatigue test time. The other three specimens have been already fabricated and tests are ongoing to evaluate their fatigue behavior. A 220-kips custom loading frame is designed for the conducted test. Instrumentation devices including LVDT, strain gauge, and load cell have been utilized in the data acquisition system to monitor the behavior of the specimen during the test. The FCGR and crack length are also supervised with microscopes. This section discusses the details of the experimental investigation on the stiffened box girder.

5.3.1 Specimen Design and Matrix

The designed specimens consist of three stiffened box segments that are connected with a series of ASTM F3125 Grade A490 pretensioned bolts to form the box girder. The goal behind this modular design is to reduce the test cost by reusing the two side box segments for all fatigue tests, as a result, only the center box segment is considered as the specimen in this chapter. Figure 5-2 shows the designed stiffened box girder. In Figure 5-2 (a), the 3D model of the box girder with two side boxes and specimen in the middle is rendered. The box segments are connected with the pretensioned bolts and a side view of the assembled bolted connection is captured in Figure 5-2 (b). Figure 5-2 (c) shows a 3D view of the inner surface of the bottom flange with the welded

stiffeners. For the first specimen, four T-shaped stiffeners with a spacing of 9-in are welded to the flanges of the middle box segment. In Figure 5-2 (a) two holes with diameter 11 ¾-in are cut into the two web plates of the box specimen to allow access for inspection and instrumentation devices. The overall length of the entire box girder is 202-in, width is 42-in, and height is 24-inThe center segment has a length of 81-in. Detailed dimensions of the designed specimen can be found in Figure 5-3 and Figure 5-4. The material utilized for the specimen construction is A572 Gr.50 steel.

Four specimens with different configurations have been designed to quantify the effect of critical input parameters on the crack propagation behavior. Preliminary analysis indicated that the crack propagation behavior mainly depends on the thickness of the box flange, stiffener spacing, and stiffener type. Accordingly, the configurations of the four specimens are designed to study these parameters as shown in Table 5-1. The first specimen as discussed above, namely Specimen S1, is investigated in this dissertation.

Table 5-1. Stiffened box girder experimental test matrix.

Specimen ID	Plate Thickness (in)	Stiffener Type	Stiffener Spacing (in)	Stiffener Height (in)	Stiffener Thickness (in)
S1 (control)	3/8	T	9	4	3/8
S2	3/8	**Flat bar***	9	5-1/4	1/2
S3	**1/2***	T	9	4	3/8
S4	3/8	T	**11***	4	3/8

Note: ***** indicated the difference between specimens.

For Specimen S1, the bottom flange is 3/8-in in thickness. An 8-in cut is introduced using a reciprocating saw at the center of the bottom flange of the middle box along the transverse direction. A pre-cracking procedure was applied afterwards to remove the effect of the reciprocating saw per ASTM E647 (ASTM Standard E647, 2015). A CAL with minimum force of 5 kips and maximum of 80 kips was utilized in the precracking stage. As the fatigue crack path is expected to be propagated along the pre-cracking direction, the surface of the potential crack

area is polished as shown in Figure 5-5 to facilitate the crack length measuring procedure. This process enhances the visibility of the crack and makes it easier to identify the crack tip during measurement. A sticky ruler is attached parallel to the polished surface to calculate the actual magnification ratio of microscopes and measure the crack size. The unit used on the ruler is inches.

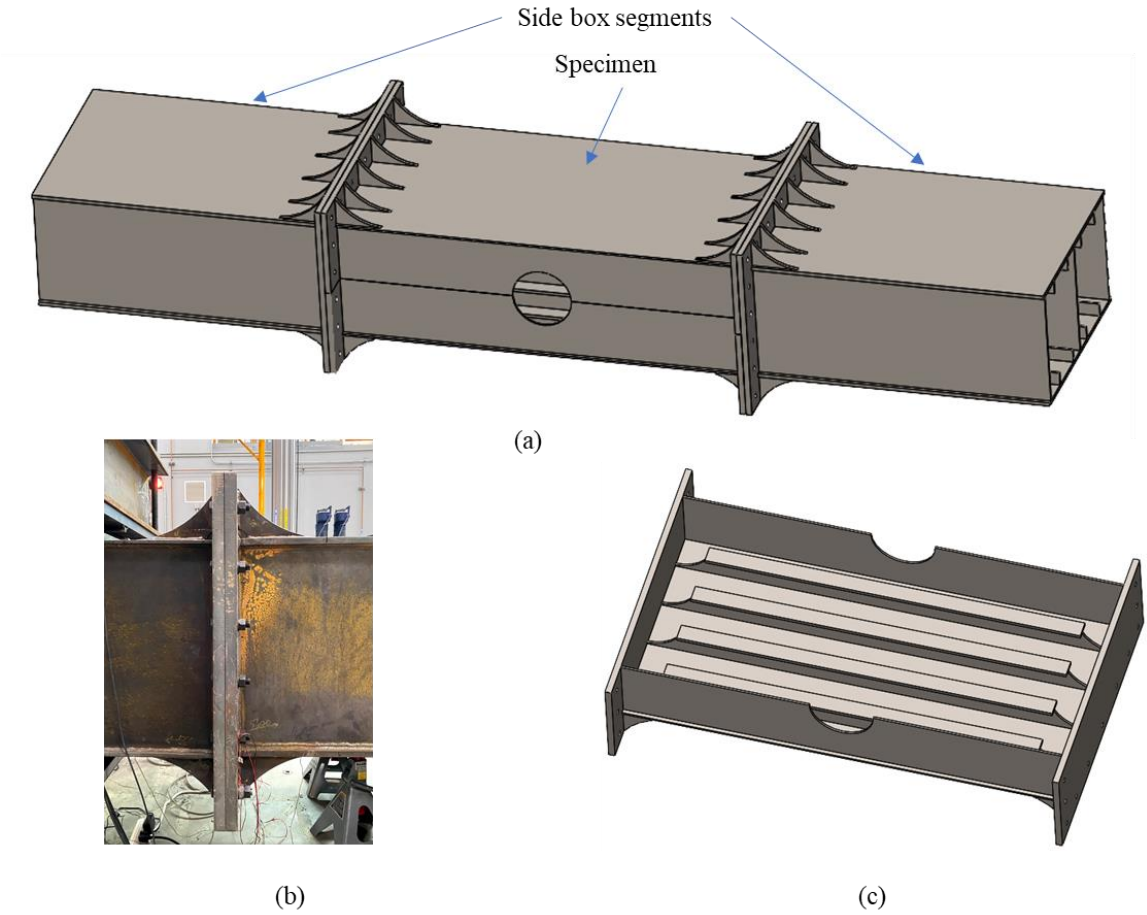

Figure 5-2. Details of the stiffened box girder (a) 3D rendering of the entire box girder (b) side view of the intermediate bolted connection, and (c) bottom flange with the four stiffeners.

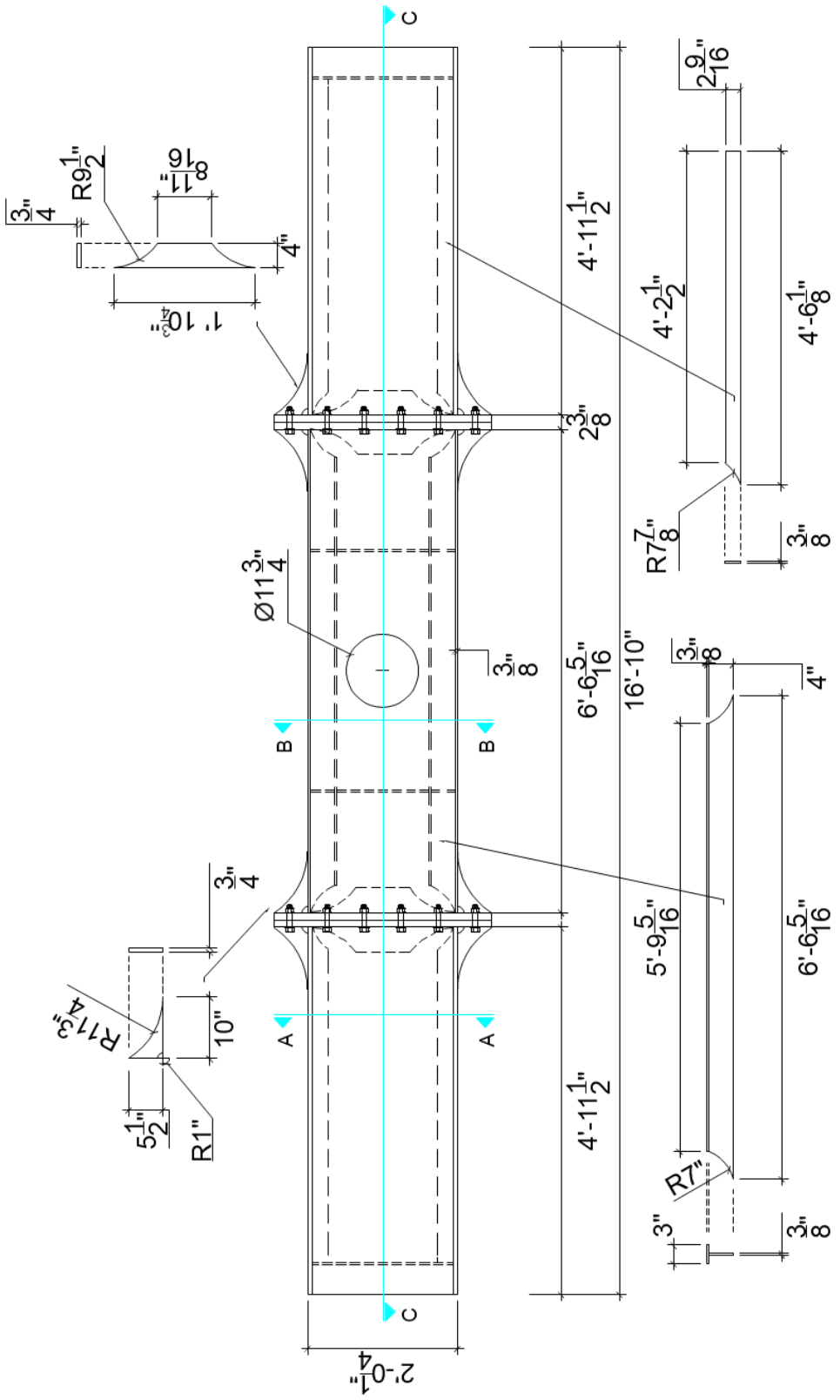

Figure 5-3. Elevation view of the first specimen with stiffener details.

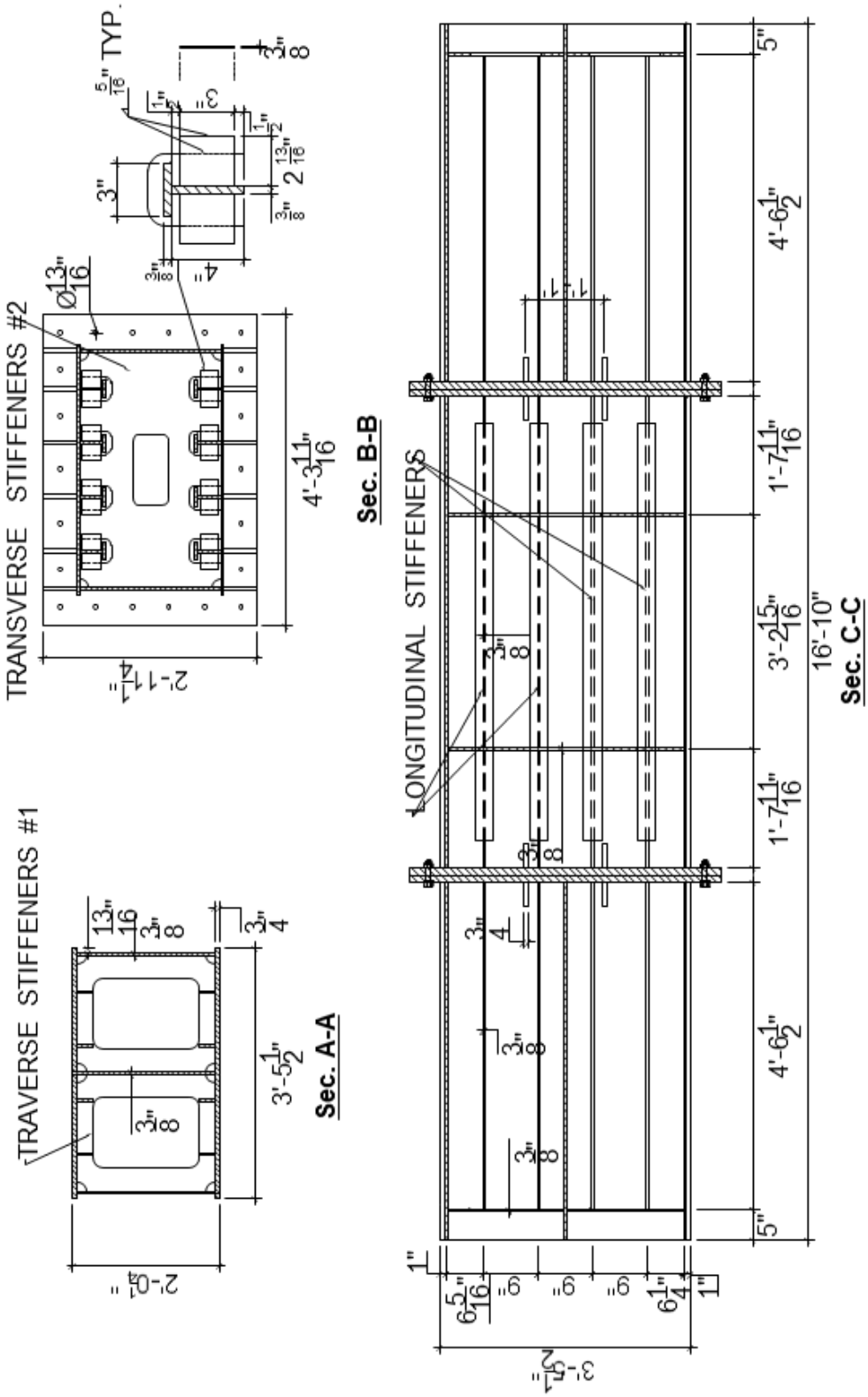

Figure 5-4. Cross-sectional views of the first specimen.

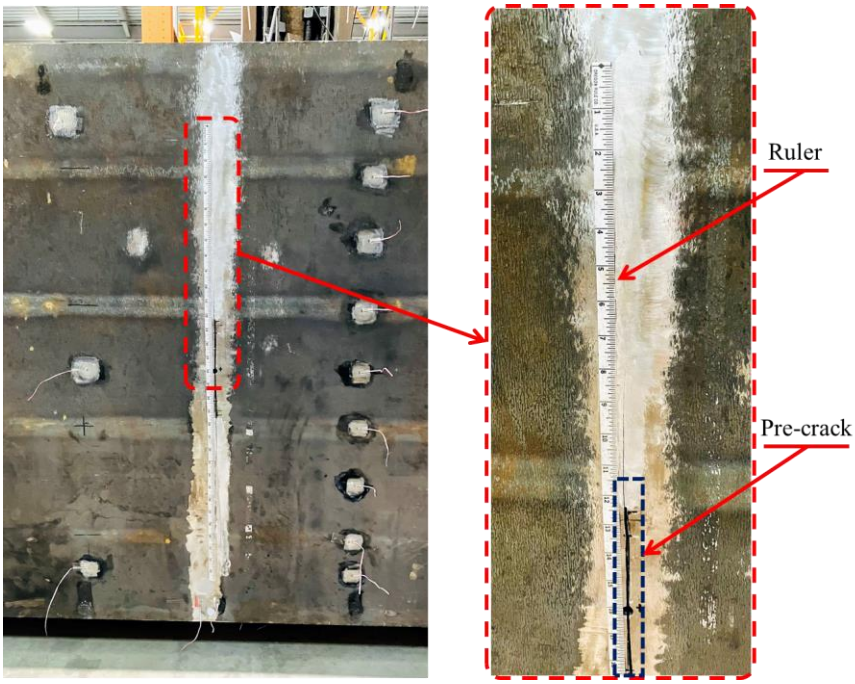

Figure 5-5. The pre-crack, surface polishing, and sticky ruler of Specimen S1.

5.3.2 Auxiliary Material Dog-Bone Tensile Test

An auxiliary tensile test was conducted for the A572 Gr.50 steel used to fabricate Specimen S1. This test provided accurate information about the material properties to be used for the prediction model. The tested dog-bone specimen was designed based on ASTM E8 (ASTM Standard E8, 2021) and shown in Figure 5-6. The scale of the dog-bone specimen is designed to accommodate the available test frame.

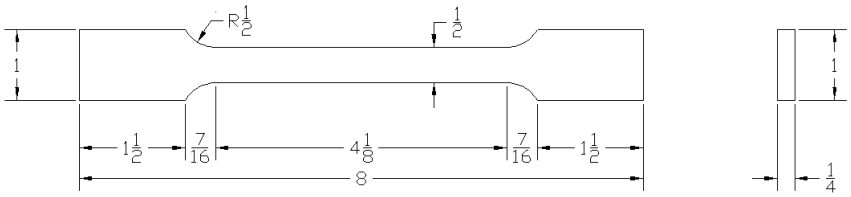

Figure 5-6. Dimensions of the dog-bone specimen obtained from the steel used to fabricate Specimen S1

5.3.3 Test Frame Setup

A custom loading frame is designed and constructed to test the stiffened box girders under fatigue loading. Figure 5-7 shows the 3D rendering of the loading frame. As shown in the figure, two braced columns are bolted to the strong floor in the lab. The flanges of the beams are coped and connected to the columns with 7/8-in diameter high-strength pretensioned bolts. A220-kips MTS actuator is mounted to the bottom of the reaction beams and the other end is attached to the loading mechanism of assembled box girder. The orientation of the loading frame is also indicated in the figure. The applied fatigue loading spectrum includes both tensile and compressive loads to represent the actual wave loading encountered by ship hulls. The loading frame is designed to be able to apply both tensile and compressive loads. A custom loading/reaction mechanism is designed to accommodate the upward and downward displacements and rotations while preventing specimen uplift during tensile loads. Four load/reaction connections are mounted on the designed specimen to form a four-point bending loading condition as shown in Figure 5-8. The two external connections, representing the reaction points, are bolted to the strong floor, while the two interior ones transfer loads from the actuator to the specimen with a spreader beam. The loading mechanism consists of a W16×89 spreader beam that transfers the load to two W16×89 beams that distribute the force transversally across the upper flange of the specimen. A full height transverse stiffener is located within the center box segment under each load point as shown in Section B-B of Figure 5-4. The assembled load/reaction connections are also included in the figure.

The details of the load/reaction connections are depicted in Figure 5-9. Each load/reaction point consists of four steel plates which are connected using with four 1 1/2-in diameter threaded rods. Two steel plates are used above and below the specimen with one 3-in diameter steel rod placed in between the two plates as shown in Figure 5-8. The plates directly above and below the specimen have long slotted holes to enable the rotation of the girder. The load/reaction

connections are designed with one hinge and a roller supports to allow horizontal displacement of the specimen during the bending tests. The west side reaction connection is designed as a hinged support and the east side is designed as the roller support as shown in Figure 5-8. Steel blocks are welded onto the inner sided of the reaction plates to control the horizontal displacement of the 3-in steel pin. This horizontal displacement is restricted by these blocks for the hinged support. For the roller support, the steel bars are welded 1-in away from the steel pin to allow the horizontal displacement. A close view of the assembled hinge and roller supports is depicted in Figure 5-10.

The constructed loading frame along with the Specimen S1 is depicted in Figure 5-11. The central MTS SilentFlo 90-GPM pump at the Bert Cooper Engineering Laboratory (BCEL) is used to provide hydraulic power throughout the laboratory. The 220-kips actuator is connected to an MTS hydraulic service manifold (HSM) and load procedure for the test is controlled using an MTS FlexTest 60 controller. The tests are conducted in a load control procedure with rate of 1 Hz.

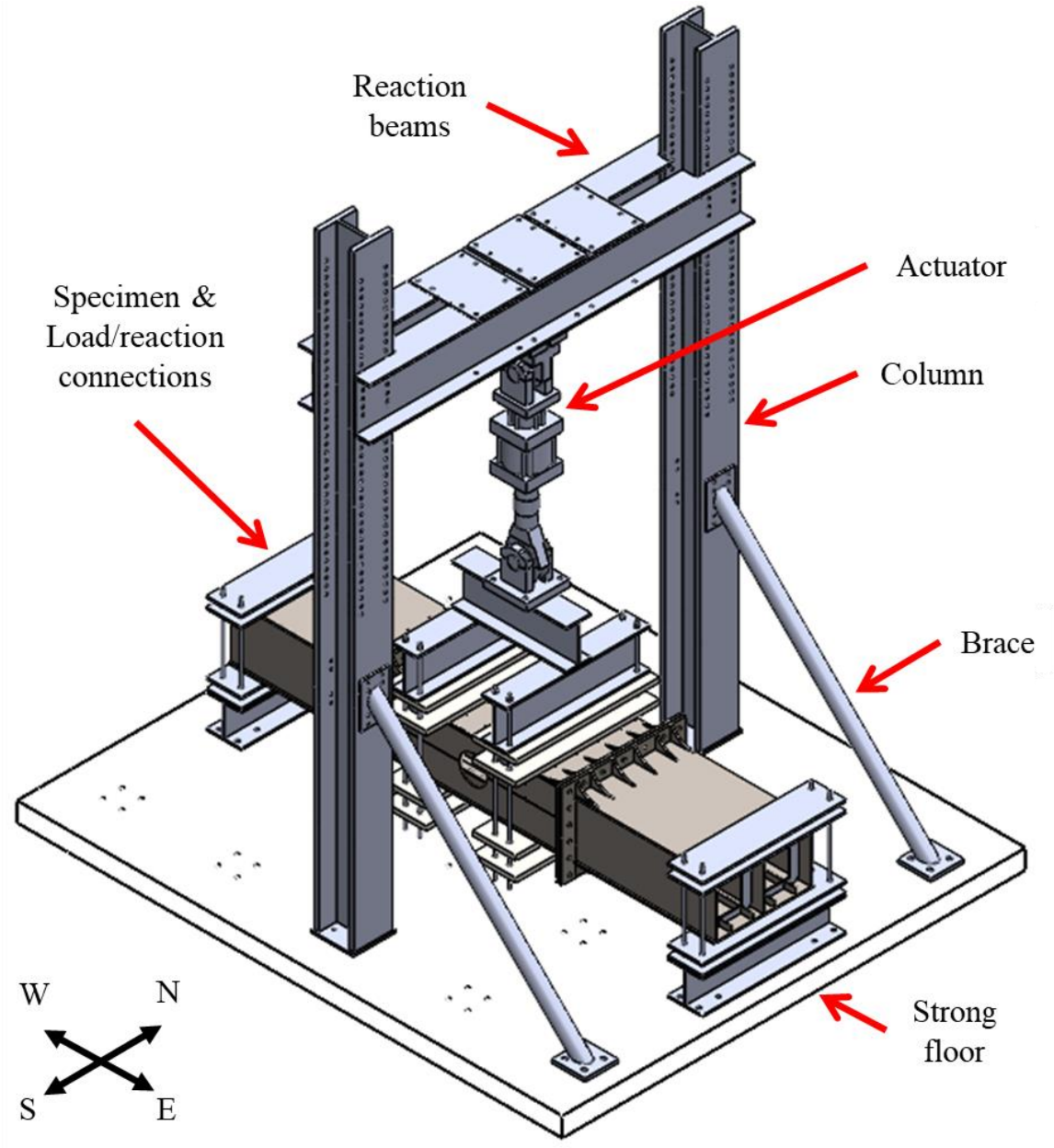

Figure 5-7. 3D rendering of the custom loading frame.

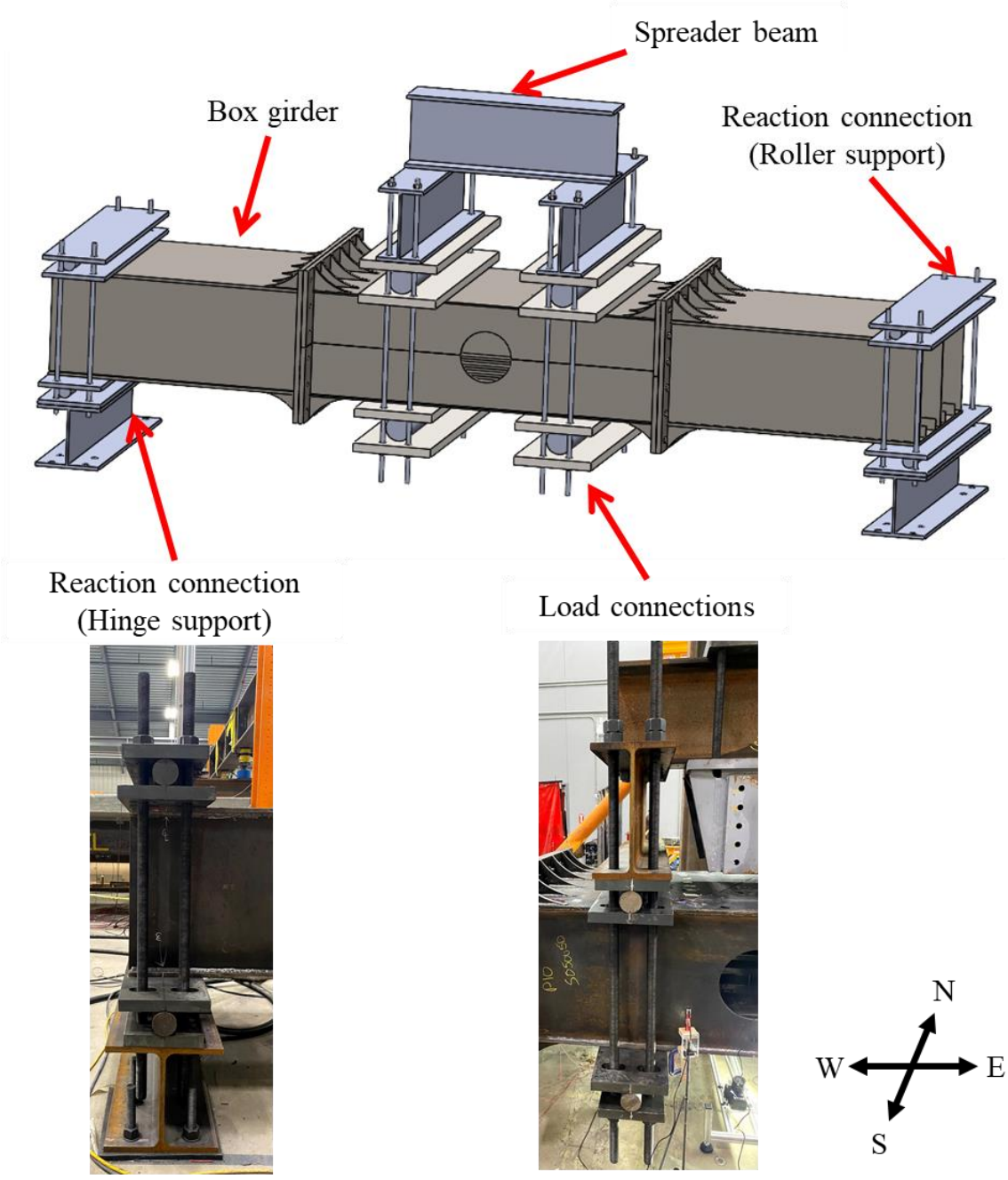

Figure 5-8. The 3D model of load/reaction connections in Specimen S1.

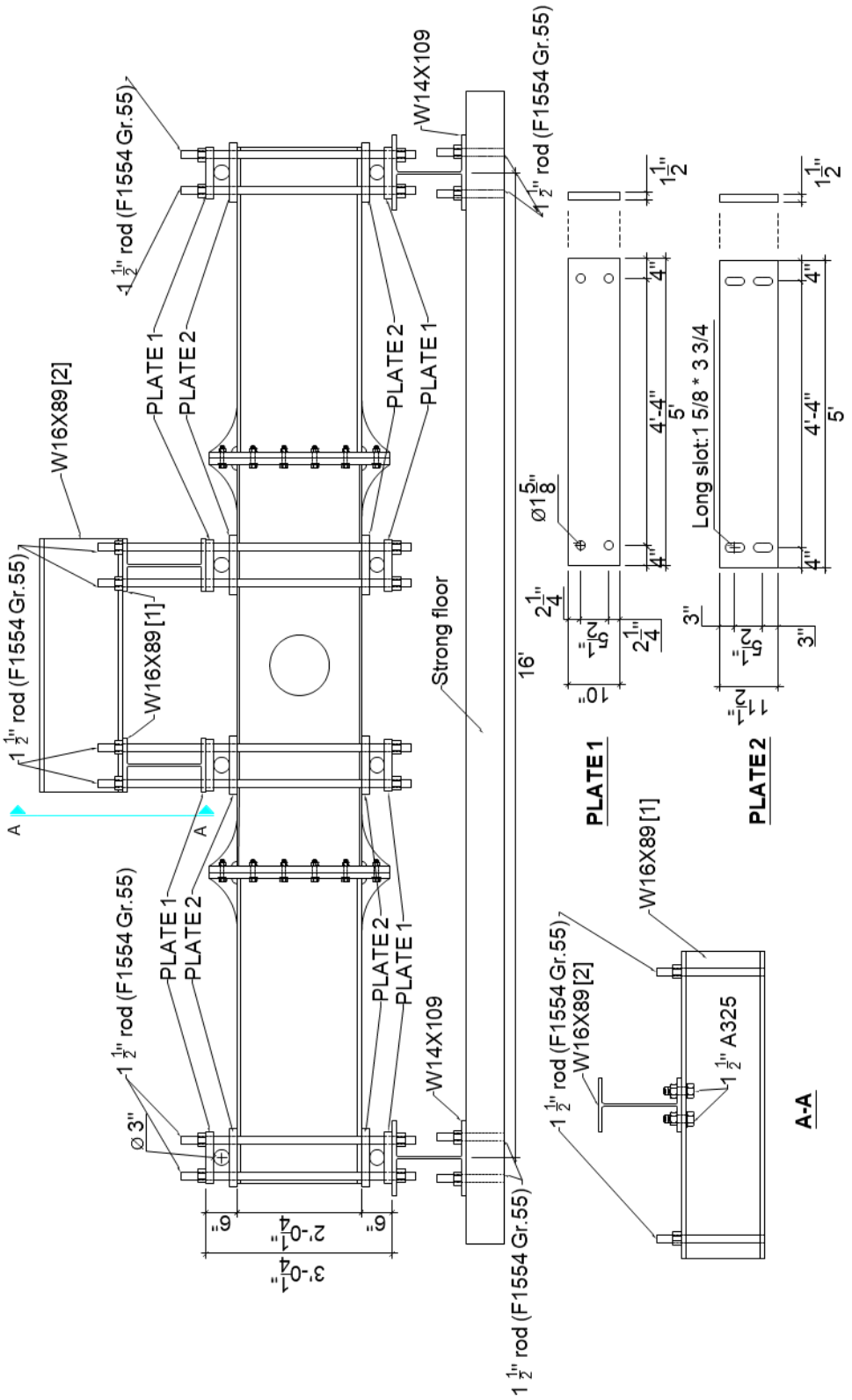

Figure 5-9. Details of the load/reaction connections in Specimen S1.

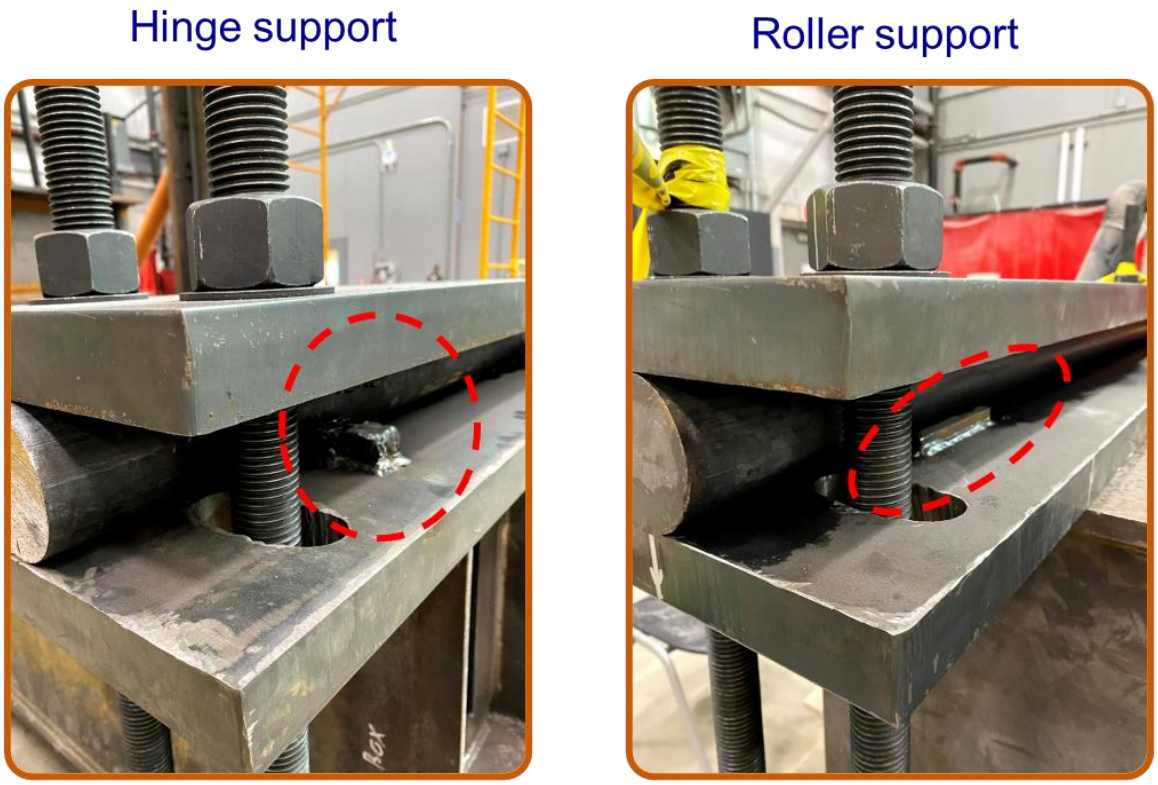

Figure 5-10. Details of hinge and roller supports in Specimen S1.

Figure 5-11. Constructed loading frame along with assembled Specimen S1.

5.3.4 Instrumentation System

To evaluate the structural behavior of the specimen under the fatigue loading, different parameters including strains, displacements, and bolt pretension force, are monitored during the stiffened box girder fatigue test. An instrumentation system is established to accommodate 28 strain gauges, 5 LVDTs, and 8 bolt load cells. Figure 5-12 (a) shows the data acquisition system

setup including a laptop, a power station, and ports for different instrumentation devices. A National Instruments cDAQ-9178 is used for data acquisition and LabVIEW NXG (NI, 2018) is used to write related data acquisition codes. Figure 5-12 (b) depicts a LVDT along with the stand used in the test; Figure 5-12 (c) shows the fabricated bolt load cell; Figure 5-12 (d) captures the installed strain gauges on the bottom flange of the specimen. Figure 5-13 shows the layout of utilized National Instruments modules for Specimen S1. It has three cDAQ-9237 and two cDAQ-9236 for strain gauges, two cDAQ-9237 for bolt load cells, and one cDAQ-9215 for LVDTs and applied load.

The detailed instrumentation layout of Specimen S1 is plotted in Figure 5-14. Strain gauges with 1/4-in gauge length and 350 Ω resistance (C4A-06-060SL-350-39P) manufactured by OMEGA™ are utilized for the strain data acquisition. Twenty-two strain gauges are located at the bottom flanges of the three boxes as shown in Figure 5-14. Strain gauges No. 1, 2, 21, and 22 are located at the two side box segments to monitor the strain values. A significant difference between the readings from these strain gauges could indicate a certain level of eccentricity or bolt loosening. Strain gauges No. 3 to 9, 13, 17 to 20 are located at the center of specimen to monitor the eccentricity of loading and the shear lag within the lower flange. Strain gauges No. 9 to 17 are placed along the crack path to monitor the change in strain resulting from crack growth. Strain gauges No. 23 to 26 are installed on the flanges of the four T-stiffeners on the bottom flange of the middle box. The stiffeners are defined as Stiffener 1, Stiffener 2, Stiffener 3, and Stiffener 4, from north to south, as shown in Figure 5-14. Strain gauges No. 27 and 28 are placed on the top flange of the middle box. These strain gauges are installed to provide information on the stress redistribution as the fatigue crack propagated during the test. Four LVDTs are placed to monitor the vertical displacements at the loading points of Specimen S1. Any loading eccentricity can also be checked by comparing the displacements from the four LVDTs. A 5th LVDT is placed to measure the horizontal displacement at the roller support of the specimen during the fatigue test.

For Specimen S1, 3/4-in diameter pretensioned high-strength bolts are used to connect the three boxes. These bolts may fracture due to the fatigue loading before the crack reaches its critical length. Additionally, any pretension loss will affect other instrumentation data, such as displacements and strains. Accordingly, it is critical to monitor the bolt pretension forces during these fatigue tests. Eight washer-type bolt load cells are fabricated and installed on selected bolts as shown in Sections A-A and B-B in Figure 5-14. These custom bolt load cells constructed using thick wall tube section with outer and inner diameters of 1-in and 3/4-in. Sections that are 1/2-in in width are cut from the tube to fabricate each load cell. Two flat surfaces are cut using saw cutter to attach the strain gages. Four 1kΩ strain gauges are attached to measure the force using the load cell. The circuit diagram details are described in Figure 5-15. The bolt load cells were calibrated using an Instron 1500 HDX-C4-G7C universal test machine located at the BCEL.

The actual test load is measured using the built-in load cell of the 220-kips actuator. The load data is sent out from the MTS FlexTest 60 controller to the NI data acquisition system simultaneously during the test.

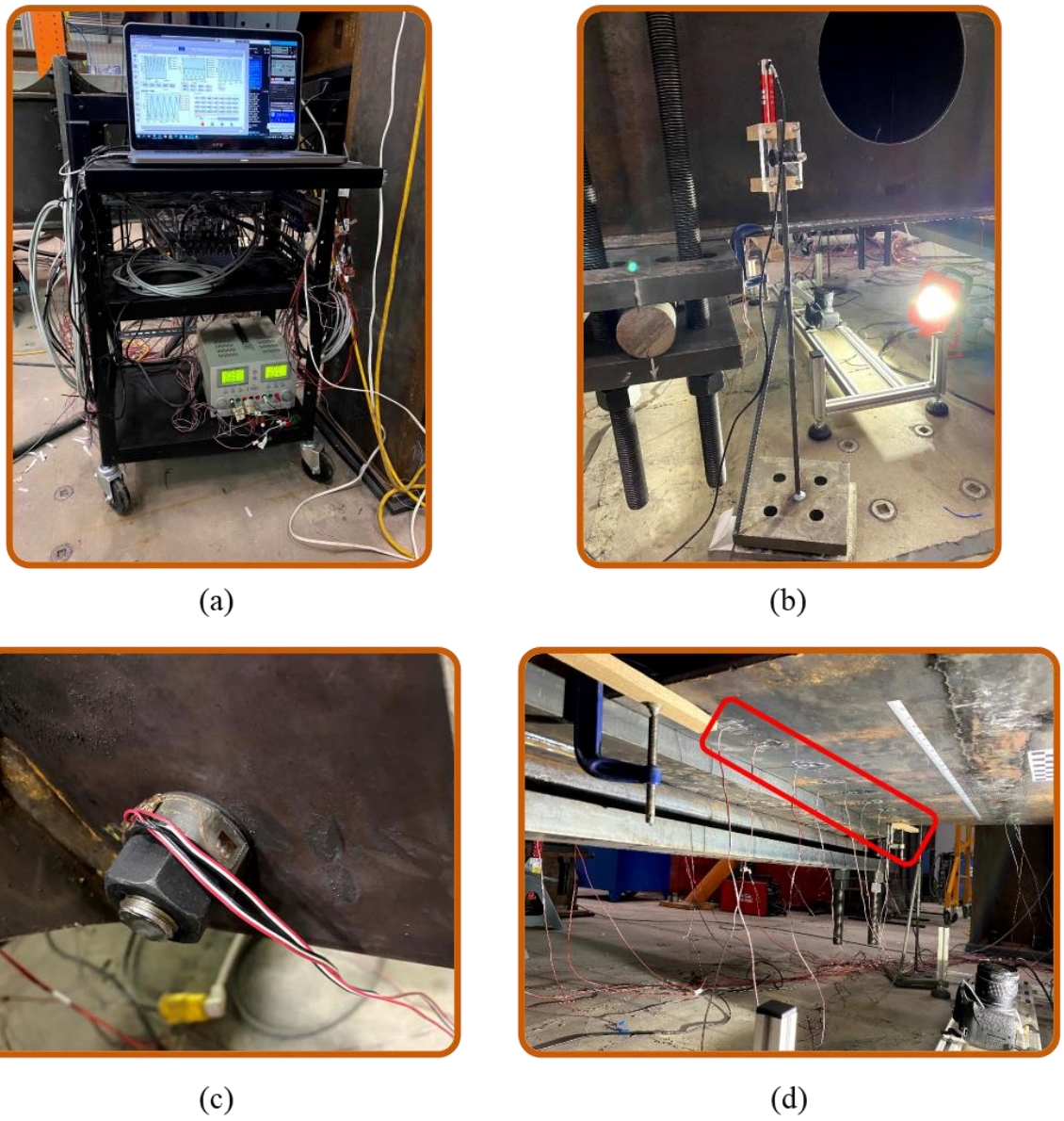

Figure 5-12. Instrumentation system for the stiffened box girder experimental test (a) data acquisition system, (b) LVDT, (c) bolt load cell, and (d) strain gauges.

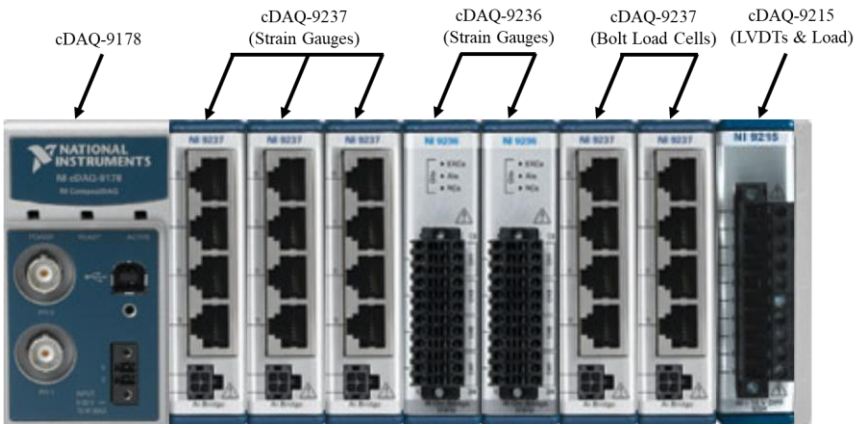

Figure 5-13. Data acquisition configuration.

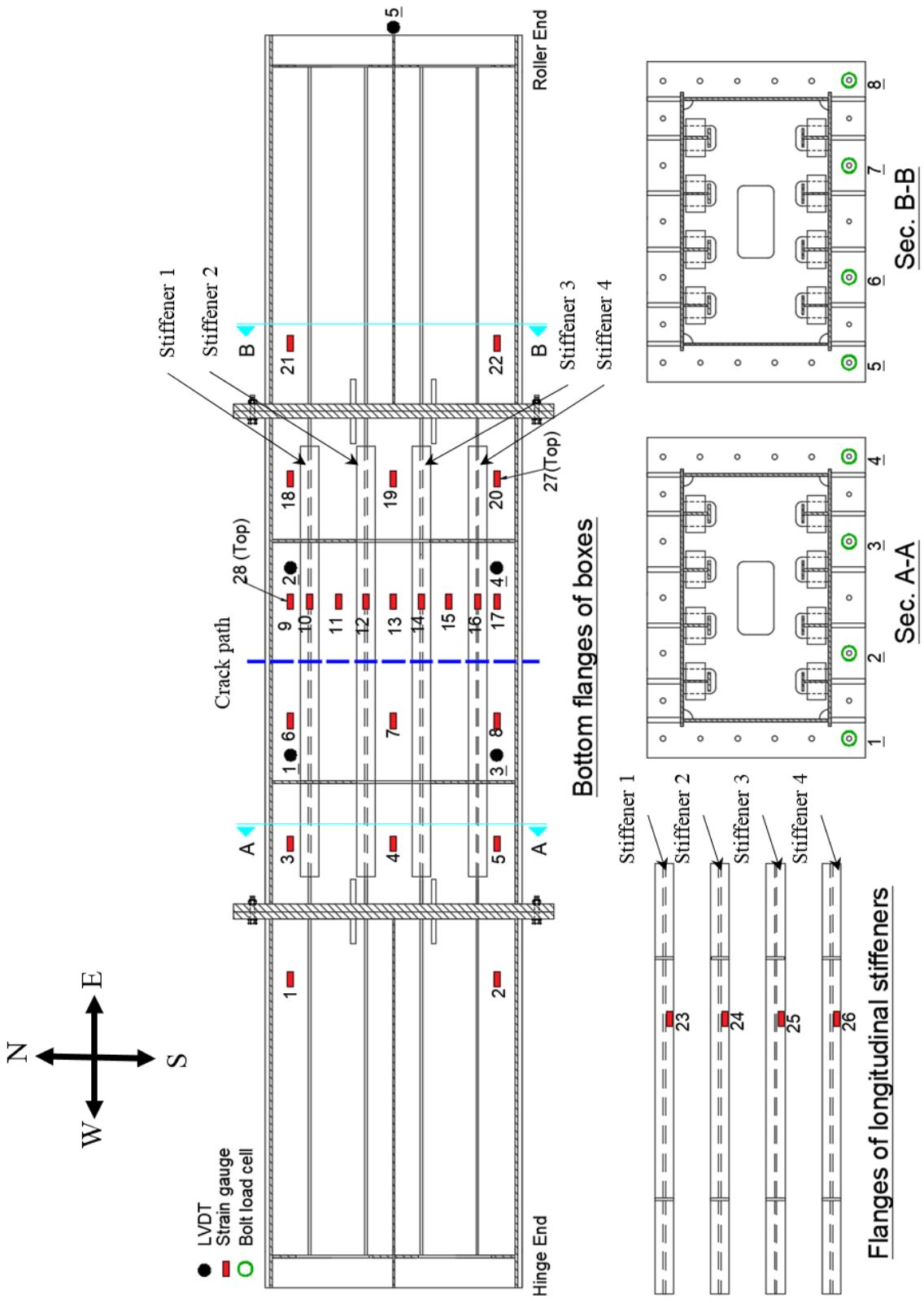

Figure 5-14. Instrumentation layout of Specimen S1.

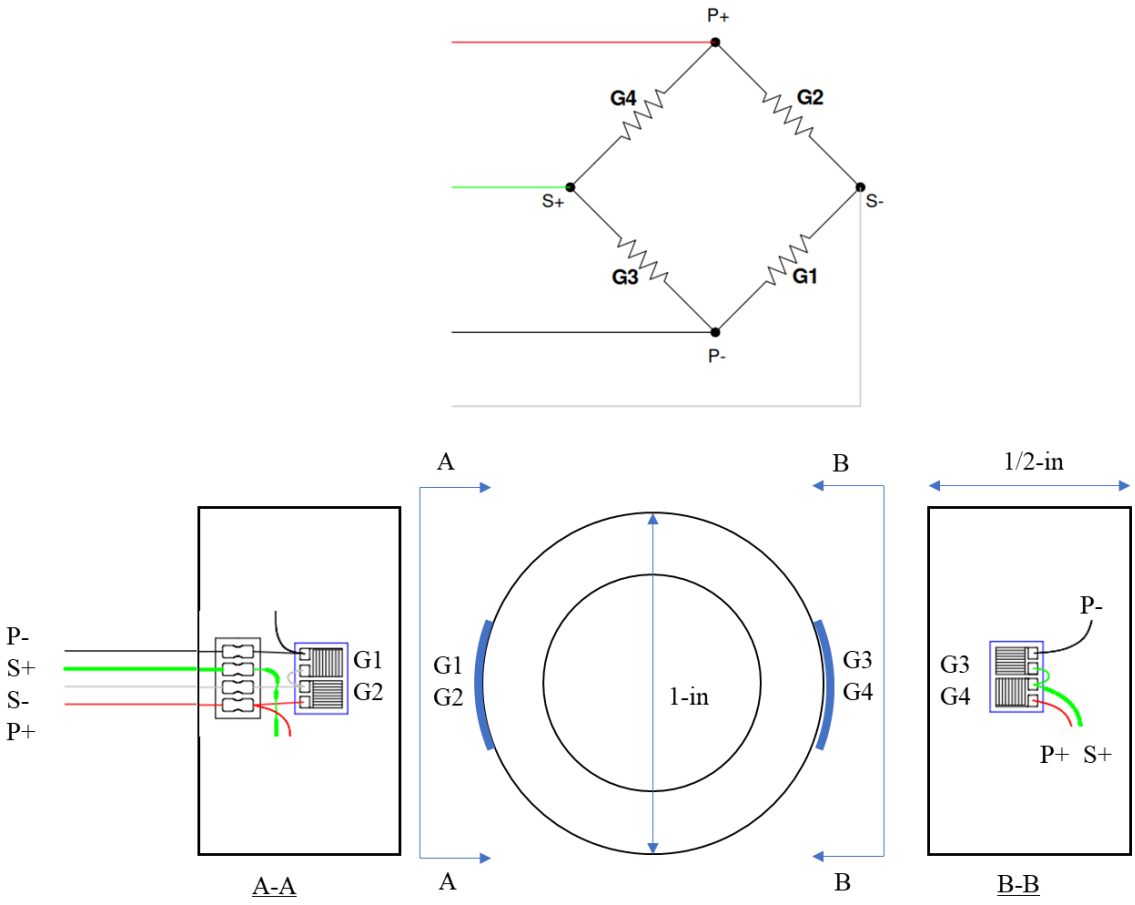

Figure 5-15. Diagram of the custom bolt load cell.

5.3.5 Crack Monitoring and Measuring System

Four microscopes are utilized to monitor the fatigue crack propagation at four locations of the Specimen S1. These are the two crack tips, namely North Crack and South Crack, located at the bottom flange of the specimen box segment as shown in Figure 5-16. Two microscopes are placed underneath the box to monitor the crack growth. Two crack tips along the webs of Stiffener 2 and Stiffener 3 inside the specimen box are also monitored as shown in Figure 5-17. These are denoted Stiffener 2 Crack (for the north side) and Stiffener 3 Crack (for the south side). The microscopes can provide a 20X~200X magnification range and are able to identify the crack tip clearly. The ruler attached along the crack path is used herein to calculate the actual magnification ratio of the microscopes used to monitor the crack size across the bottom flange.

Two additional rulers are also attached to the stiffener webs to work together with the two inside microscopes.

One drawback of microscopes is the limited field of scope. Accordingly, a microscope frame along with linear actuators are used together with the underneath microscopes as depicted in Figure 5-18. The linear actuator is mounted to the microscope frame, and the microscope is attached to the head of the linear actuator rod. A Python script is written to control the linear actuator movement as well as the microscope based on the current crack tip location during the fatigue test. It improves the accuracy of measurement by excluding manual checks. Meanwhile, it greatly relieves the crack measurement work considering the limited room underneath the specimen.

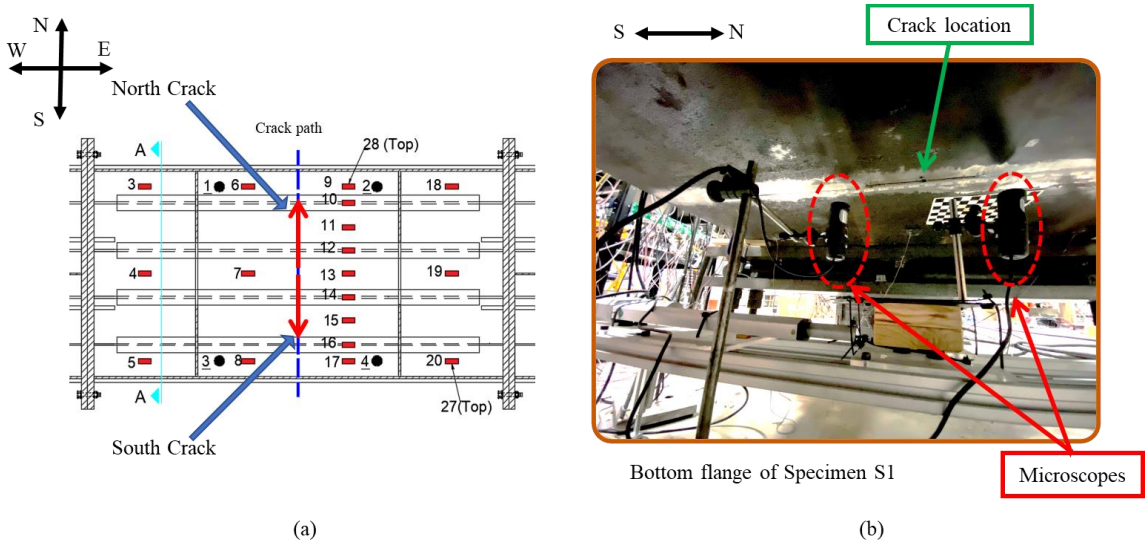

Figure 5-16. Locations of the cracks and microscopes on the bottom flange of Specimen S1 (a) North Crack and South Crack, and (b) two microscopes underneath the bottom flange.

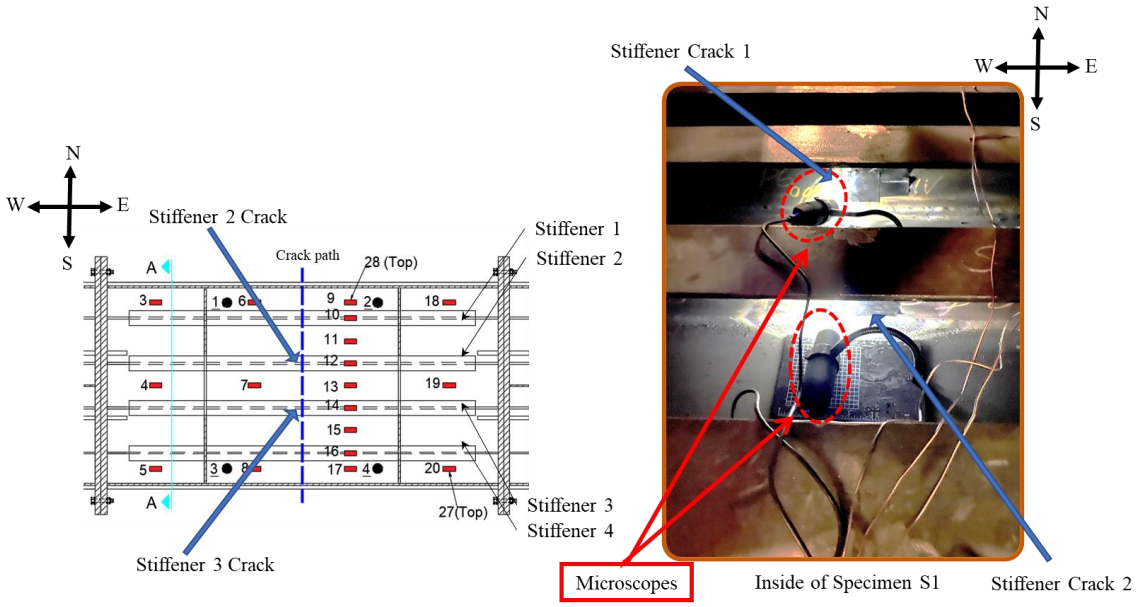

Figure 5-17. Locations of the cracks and microscopes inside the middle box of Specimen S1 (a) Stiffener Crack 1 and Stiffener Crack 2 on the webs of the inner stiffeners, and (b) two microscopes.

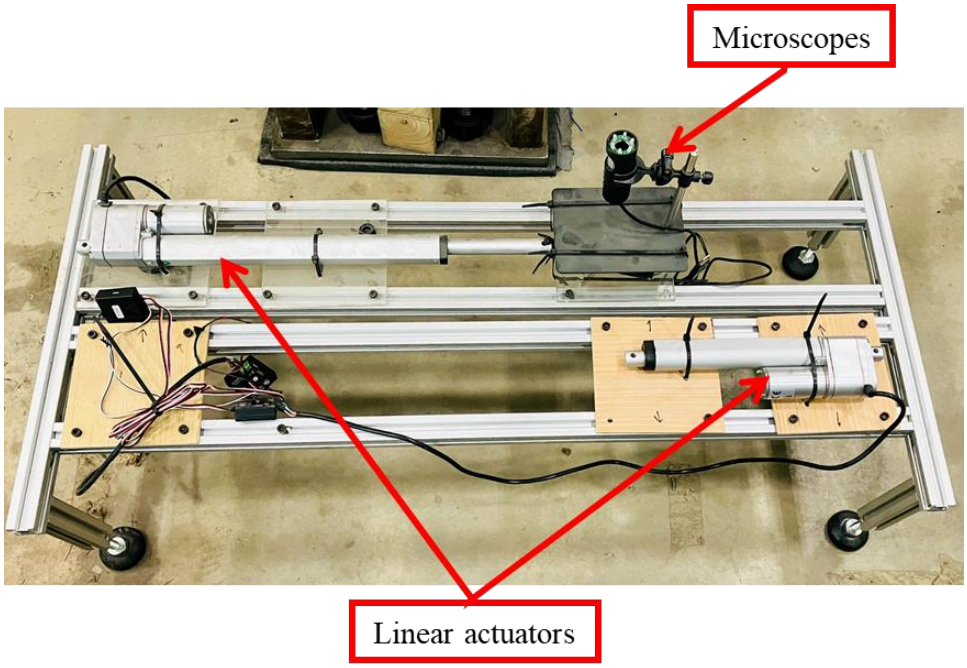

Figure 5-18. Microscope frame and linear actuators.

5.3.6 Variable Amplitude Loading Pattern

Ships are expected to experience random load spectra that include tensile and compressive conditions with variable amplitudes. As shown in Figure 4-19 in Chapter IV, the crack closure, as well as crack growth rate retardation and acceleration due to load history, may significantly affect the fatigue service life. To assess the effect of load history on the crack propagation in stiffened panels, Specimen S1 is tested under variable amplitude loading. The loading pattern is generated to simulate wave loading conditions based on Tomita et al. (Tomita et al., 1995) and Li et al. (Li et al., 2016). Under wave-induced loading conditions, the load history can be categorized into two types: calm sea and storm sea. The wave height and induced stresses in the storm sea condition are higher than those occurring in calm sea conditions. The spectrum for the wave-induced load effect $S_M(\omega_{e,U,H})$ can be calculated as (Sikora, 1998)

$$S_M(\omega_{e,U,H}) = \left|\mathrm{F}_i(\omega_{e,U,H})\right|^2 \cdot S_\omega(\omega_{e,U,H}) \qquad \text{Equation 5-11}$$

$$\omega_{e,U,H} = \left|\omega - V\frac{\omega^2}{g}\cos H\right| \qquad \text{Equation 5-12}$$

where $S_\omega(\omega_{e,U,H})$ is the input spectral density function of sea waves, $\mathrm{F}_i(\omega_{e,U,H})$ is the transfer function; and $\omega_{e,U,H}$ is the encountered wave frequency (rad/s); V is the ship speed (m/s); g is the gravitational acceleration (m/s^2); ω is the frequency (rad/s); H is the wave height (m).

The JONSWAP spectrum is utilized as the input spectral density function, which is defined as (Hasselmann et al., 1973)

$$S_\omega(\omega) = \alpha\frac{g^2}{(2\pi)^4}(T)^5\exp\left(-\frac{5}{4}(\frac{\omega_p T}{2\pi})^4\right)\gamma^{exp\left[-\frac{(\frac{2\pi}{T}-\omega_p)^2}{2\sigma^2{\omega_p}^2}\right]} \qquad \text{Equation 5-13}$$

where T is the average wave period (s); ω_p is the frequency at the spectral peak; γ is the peak enhancement factor; σ is the peak shape parameter; α is the Philips constant and it is expressed as a function of the significant wave height (SWH) as $\alpha = 4.5\,(\frac{\omega_p}{2\pi})^4 SWH^{\,2}$ (Ochi, 2003). A

simplified random loading model and the corresponding generated variable amplitude loading pattern are shown in Figure 5-19.

During the fatigue test of Specimen S1, a first loading pattern was used to represent the random storm occurrence discussed above. This load pattern had a minimum and maximum load amplitudes of -110 kips and 110 kips, respectively, and load histogram is plotted in Figure 5-20 (a). As seen in the figure, this load pattern has a relatively similar occurrence probability of positive and negative load amplitudes. The first pattern (i.e., Pattern 1) has 2.07×10^6 cycles which requires 24 days when applied at 1 Hz. After 1.45×10^7 cycles were applied, it was noted that the crack propagation rate was relatively slow. This was attributed to the presence of compressive residual stresses between the stiffeners and the low number of cycles with high load magnitude. Pattern 1 utilized the storm occurrence probability to generate the cyclic load spectrum which resulted in low number of cycles with high amplitudes. To accelerate the test, two additional load patterns with more intensive loading were applied to. Pattern 2 was generated based on a scaled time-history realization of sea elevation under calm sea condition. This resulted in a larger number of cycles with high force amplitudes. Figure 5-20 (b) shows Pattern 2. The third pattern (i.e., Pattern 3) is similar to Pattern 2 but the maximum positive loads (i.e., tensile loads on the crack side) were scaled to 150 kips. Figure 5-20 (c) shows Pattern 3. The second and third patterns both have 28,800 cycles which requires 8 hours when applied at 1 Hz. All the loading patterns were set at 1 Hz during the test. Patterns 2 and 3 were applied iteratively and the tests were stopped every 72 hours to inspect the side box segments and the loading mechanism for any undesirable fatigue damage.

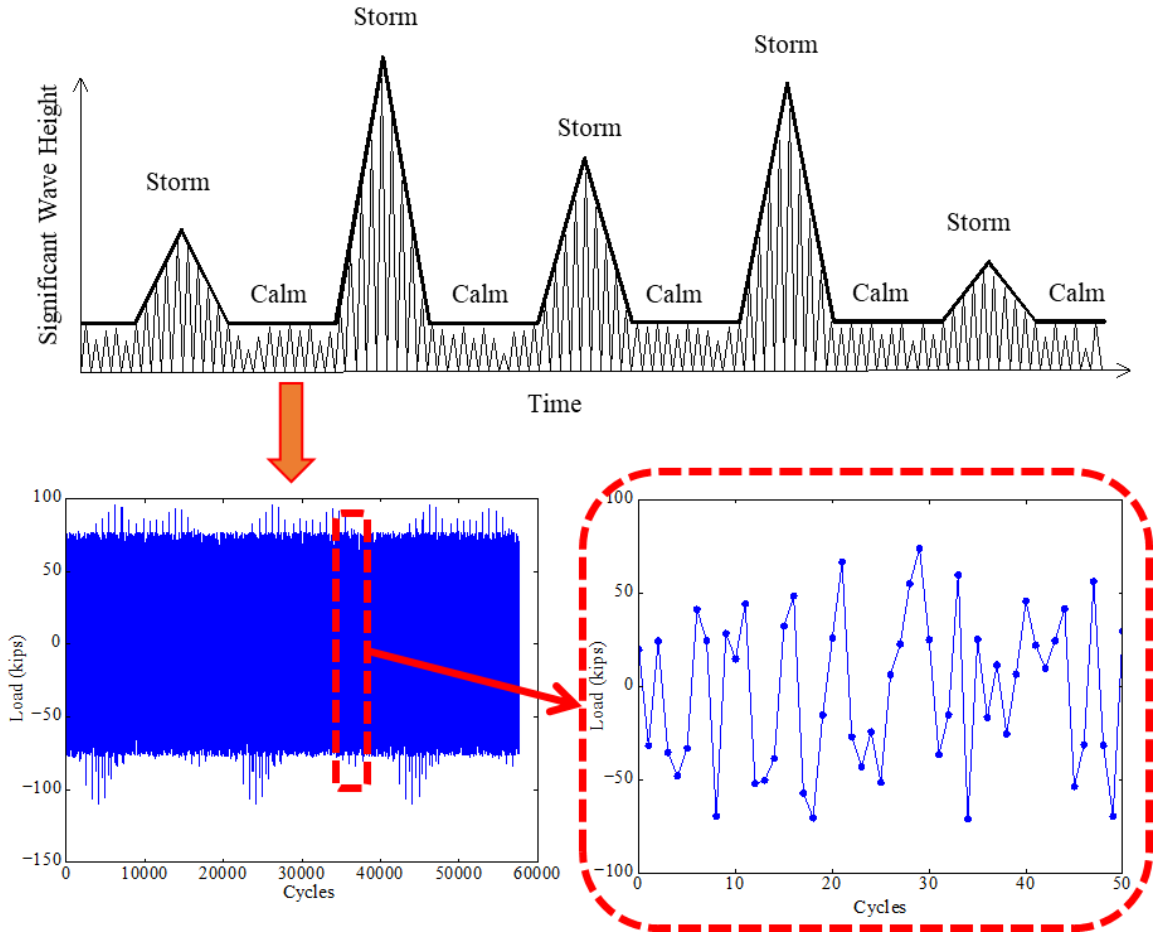

Figure 5-19. Generated wave-induced random variable amplitude loading pattern.

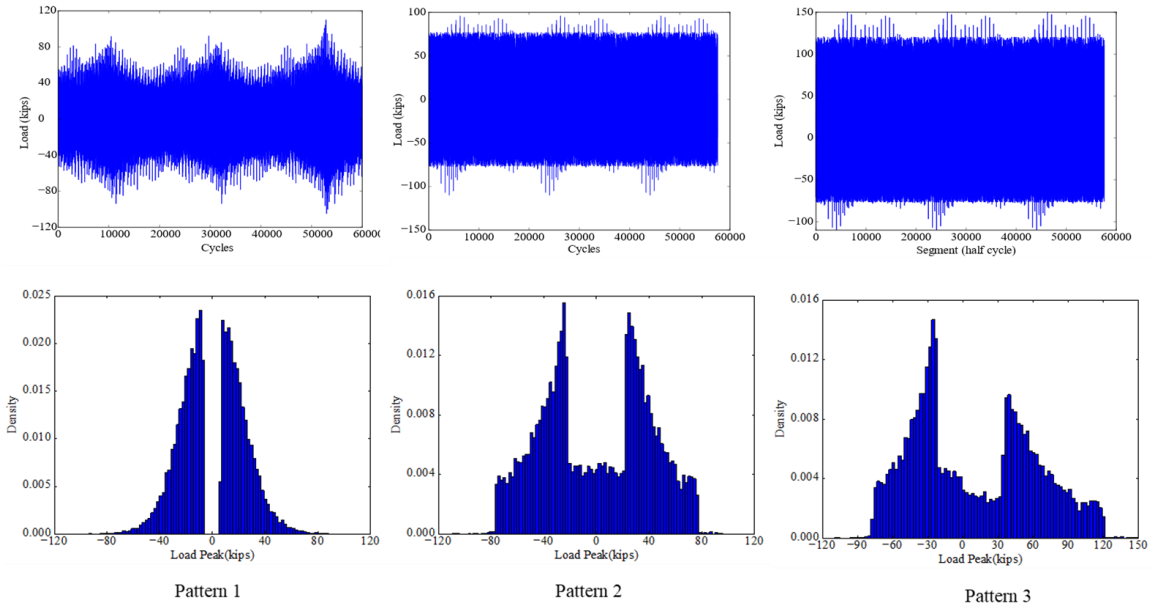

Figure 5-20. Three loading patterns used for Specimen S1.

5.4 Results and Discussions: Specimen S1

5.4.1 Auxiliary Tensile Test Results

The Three dog-bone specimens, shown in Figure 5-21, were tested under the tensile loading to determine the mechanical properties of the steel plate used to fabricate the bottom flange of the box girder. An extensometer was attached to the specimen during the test and the gage length was set at 2 in. The stress-strain curves from these three tests are plotted in Figure 5-22. Since the material did not display a clear yield point, the 0.2% offset yield strength of the material was utilized. The test results indicated that the average yield strength of the material is 58.7 ksi and the average ultimate strength is 68.1 ksi from the three tests.

Figure 5-21. Three dog-bone tested specimens.

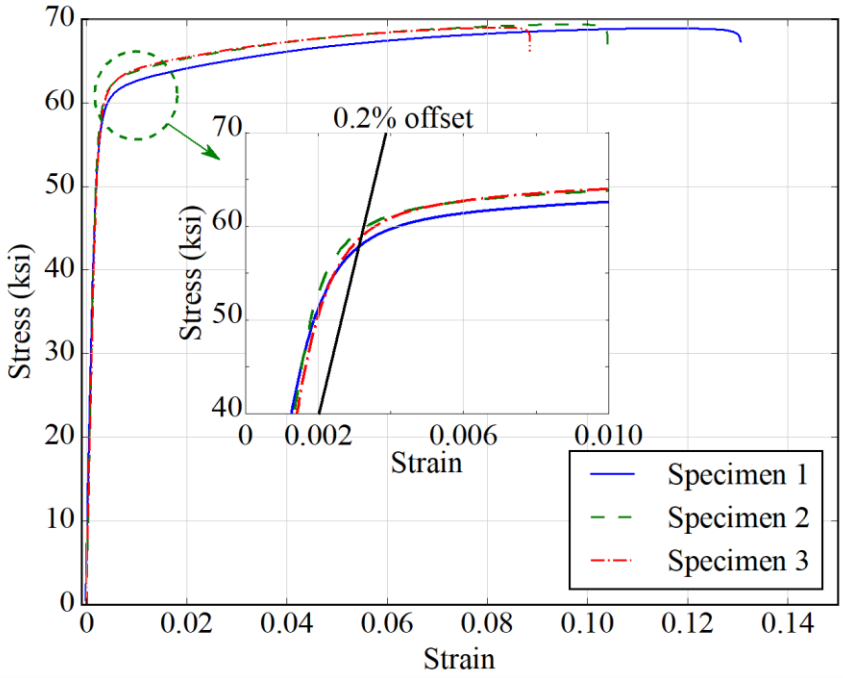

Figure 5-22. Stress-strain curve for the tested dog-bone specimens.

5.4.2 Crack Growth Results

As discussed above, only test results of Specimen S1 are reported and analyzed in this chapter. After 2.29×10^7 cycles of fatigue loading, North Crack tip reached was 2.75-in away from the north web plate of Specimen S1 and the FCGR was significantly high. Due to the significant reduction in the area of the lower flange, all the tensile stresses were transferred through the remaining flange area and the webs. This resulted in an increase in the forces in bolts 1, 4, 5, and 8 shown in Figure 5-14. These bolts started experiencing accelerated fatigue failures (i.e., within few hours of testing). Accordingly, it was decided to stop the test at this stage. As shown in Figure 5-23(a), before stopping the test, the North and South Cracks, as well as the cracks in all stiffeners except the south one were all active. The lengths of the North and South Cracks were 16.8-in and 10.2-in, respectively.

A large difference in length existed between the North and South Cracks. This was attributed to the presence of load eccentricity in the transverse direction (i.e., between the north and south sides of the specimen). This eccentricity resulted from slight misalignments and distortions in the plates that occurred during the welding process. The eccentricity was evident when the strain gage data was analyzed. Data from the strain gauges 6, 8, 9, and 17, which were installed on the bottom side of the lower flange plate of Specimen S1, are plotted in Figure 5-23(b) against the size of North crack at a load level of 50 kips. The average strain value at the north side (i.e., Strain gauges 6 and 9) has been consistently larger than the average at the south side (i.e., Strain gauges 8 and 17) throughout the test. As shown in the figure, the averages of north strains were approximately 10% higher than those recorded in the south side. This indicates that the specimen has a certain degree of eccentricity.

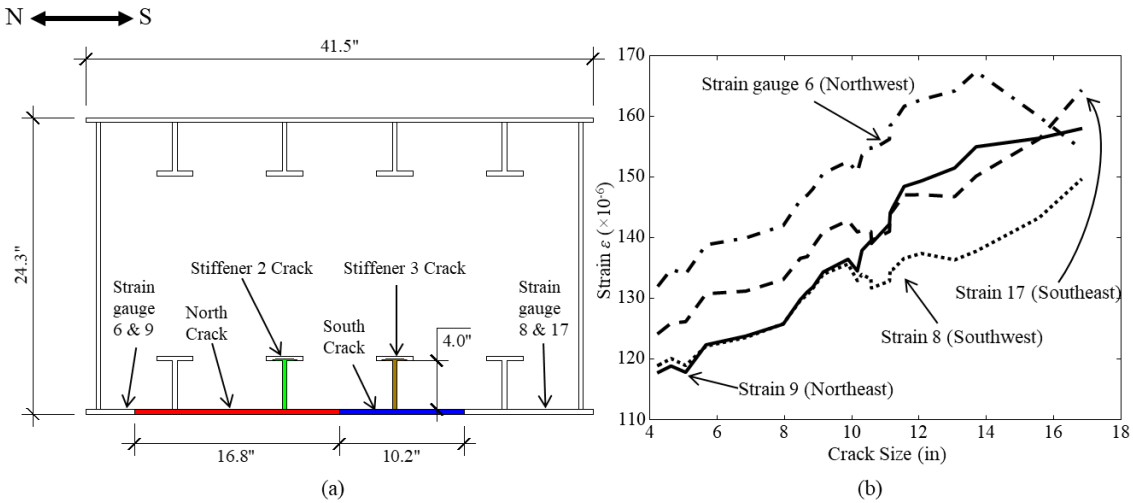

Figure 5-23. Final crack size and related strain gauge readings (a) final crack size (b) strain.

The crack size versus number of load cycles for North and South cracks are plotted in Figure 5-24 and those for cracks in the stiffeners are shown in Figure 5-25. The North and South cracks showed a similar propagation rate until approximately 7.5-in of length or 9×10^6 cycles; afterwards, the propagation rate of the two cracks started to diverge. Similar trends were also noticed for cracks of Stiffener 2 Crack and Stiffener 3 Crack.

In terms of propagation rate versus crack size for the main crack in the bottom flange, after the crack tip passed the inner stiffener, the rate started to increase. This can be attributed to the effect of welding tensile residual stresses that affect the locations adjacent to the weld lines. When the crack tip reached the middle area between the stiffeners, the propagation rate decreased. Again, this is believed to be caused by the compressive residual stresses between stiffeners. At the load cycles of 1.5×10^7, the second loading pattern was applied. The propagation rate of the four cracks increased immediately but decreased after approximately 0.5-inch. At this crack length, based on the crack prediction analysis discussed later in this chapter (see Figure 5-35), the effective stress intensity factor, representing the crack driving force, reaches a very low value due to the compressive residual stresses. After applying an additional 5.8×10^7 load cycles, the third loading pattern with the maximum load amplitude of 150 kips was applied. The propagation rate

increased immediately and continued to increase until the test was stopped when North Crack was 2.75-in away from the web plate.

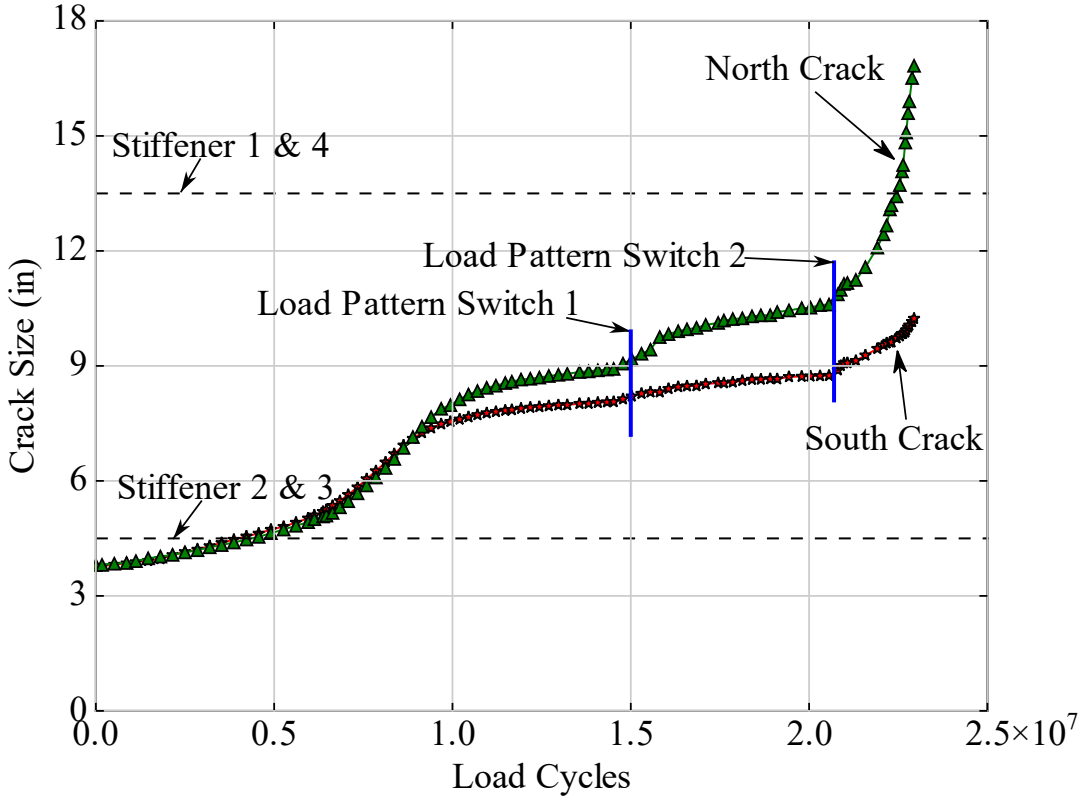

Figure 5-24. Crack size versus load cycles of cracks in the bottom flange of Specimen S1.

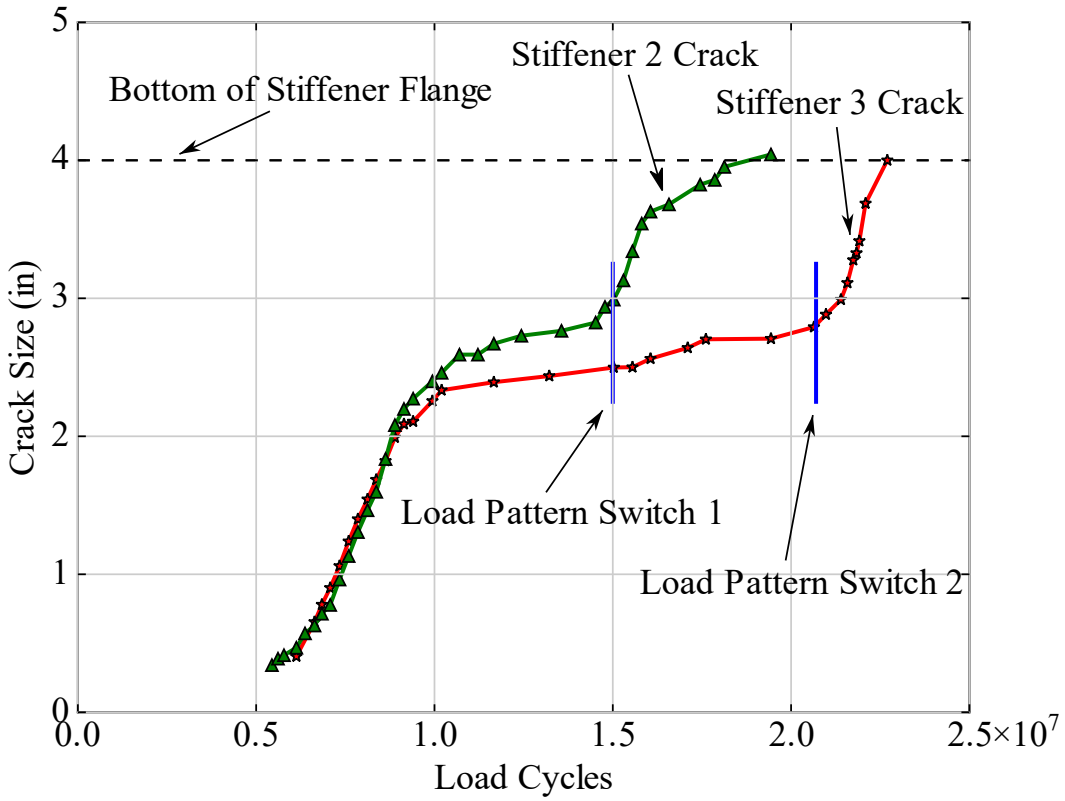

Figure 5-25. Crack size versus load cycles of cracks in the stiffeners of Specimen S1.

5.4.3 Effect of crack propagation on the strain profiles

In fatigue test on stiffened girders, shear lag can lead to significant variation in the strains across the stiffened panel. These non-uniform strains increase the difficulty of predicting the crack propagation behavior. For instance, Dexter and Pilarski (Dexter & Pilarski, 2000) indicated that a significant shear lag effect existed in their stiffened panel specimens due to the relatively shallow box used. This shear lag caused the initial applied stress at the center of the specimen to drop to 2.0-ksi. This was significantly lower than the desired stress level. The average applied stress was raised to 7.0 ksi in their tests by adding additional web plates alignment with the webs of the specimens; however, the stress still showed a high gradient along the crack propagation direction with a low value of 2.9 ksi at the center of the bottom flange. Due to this significant shear lag effect, in their tests, the interior stiffeners experienced lower stress with a value of 0.6-ksi while

the exterior ones were subjected to 5.1 ksi. In this presented work, the aspect ratio of the designed box girder was carefully selected to minimize this shear lag, after several design iterations, the height of the tested stiffened box girder was set as 24-in. In Figure 5-26, the strain readings along the crack propagation direction are plotted at different crack sizes. The figure shows these strain profiles at a load level of 100 kips with no crack, 3.5 in for the North Crack, and 4.9 in for North Crack, As shown, the strain readings across the bottom flange were very close before the cracking. The average strain is 230 $\mu\varepsilon$, which translates to 6.7 ksi of average stress. The difference in stress levels across the bottom flange was within 0.6 ksi. The strain values from the four strain gauges attached to the four stiffeners are also close.

As the crack propagated, the load applied to the specimen will be redistributed. The strain gauges near the crack, e.g., No. 12, 13, and 14, experienced a significant drop in the strain when the crack reached 4.9-in (shown in Figure 5-26). A full history of the stress redistribution due to crack propagation at the bottom flange of Specimen S1 is plotted in Figure 5-27. The strain recorded near the center of the crack almost dropped to zero when the crack length reached 16.8-in. The average strains recorded close to the web plates increased from 250 $\mu\varepsilon$ to 330 $\mu\varepsilon$ when the crack reached 16.8-in. A sharp drop in the strains existed at the crack length approximately 8.5-in. A similar increase in the strain values experienced by the stiffeners also occurred at the same crack length as shown in Figure 5-28. This indicates that the stresses were redistributed from the bottom flange to the four stiffeners as the crack propagated. In terms of stress level, the average stress experienced by the four stiffeners increased from 1.5 ksi to 3.5 ksi. The existence of the stiffeners helps support the loads as the crack propagates improving the redundancy of the entire system.

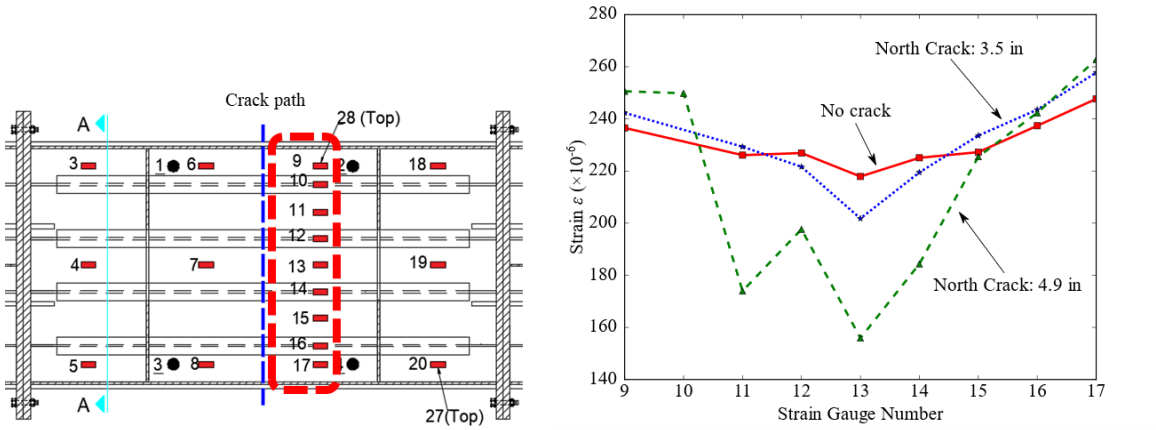

Figure 5-26. Shear lag effect along the crack path direction at the different crack sizes at a load level of 100 kips (a) locations of the strain gauges (b) curves of strain versus crack size.

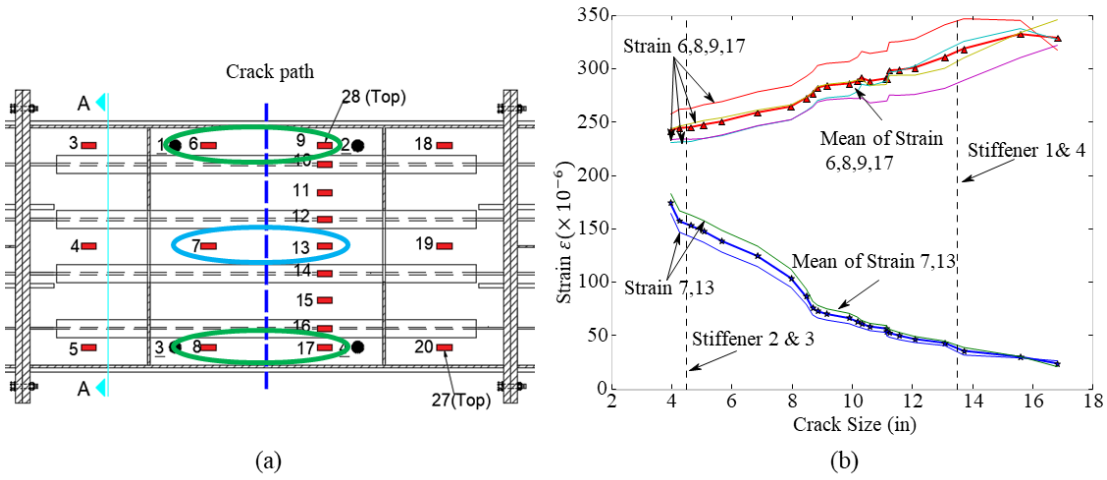

Figure 5-27. Comparison of strains at the bottom flange versus crack size at a load level of 100 kips (a) locations of the strain gauges (b) strain versus crack size.

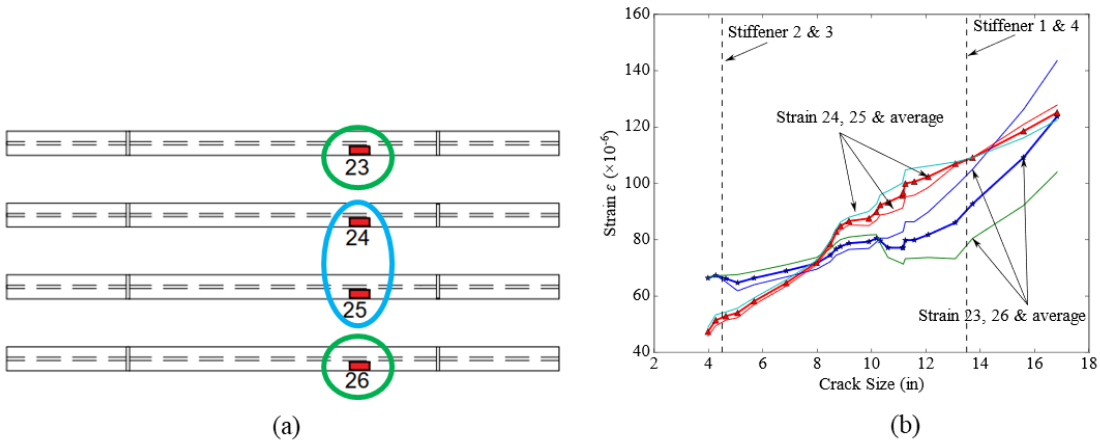

Figure 5-28. Comparison of strains at the bottom flange versus crack size at a load level of 100 kips (a) locations of the strain gauges (b) curves of strain versus crack size.

5.4.4 Specimen Stiffness

Another quantity that is worthy of evaluation is the change in the specimen stiffness change with the increase in the crack size. The specimen stiffness is evaluated using two different measured quantities. First, the vertical displacements recorded by the four LVDTs next to the load points are used to compute the stiffness, this quantity is denoted Stiff_1 herein. Next, readings from the built-in displacement sensor on the MTS actuator are used to compute the stiffness. This actuator obtained stiffness is denoted Stiff_2. In both cases, the stiffness is computed as the change in load divided by the change in displacement obtained from the increasing segment of a load cycle. The LVDTs reflect the deflection of the specimen only while the reading from the actuator includes deformations of the load frame and supporting mechanism. Figure 5-29 depicts the relationship between the computed stiffness quantities versus the crack size based on the data from LVDTs and the MTS actuator. The stiffness is normalized with respect to the values obtained from the intact specimen using the data from North Crack. The two curves are close before the crack reaches around 11 in; after that, the stiffness ratio from LVDTs is 3% lower than the one from the load actuator. Overall, the stiffness ratio drops approximately 10% compared to the intact specimen when the crack reached 16.8-in. As discussed later, several bolt failures occurred during

the test on Specimen S1. A sharp drop in the normalized stiffness obtained from the LVDTs is noticed around crack size of 13 in. This drop corresponds to one of the bolt failure events.

Compared to the intact specimen, the stiffness of the cracked specimen dropped by 10% based on the experimental data while the nominal moment of inertia dropped by 30% when the cracked areas are removed from the section. The results of this comparison are shown in Figure 5-30. This indicates the ability of the stiffened section to redistribute the load under the effect of growing cracks.

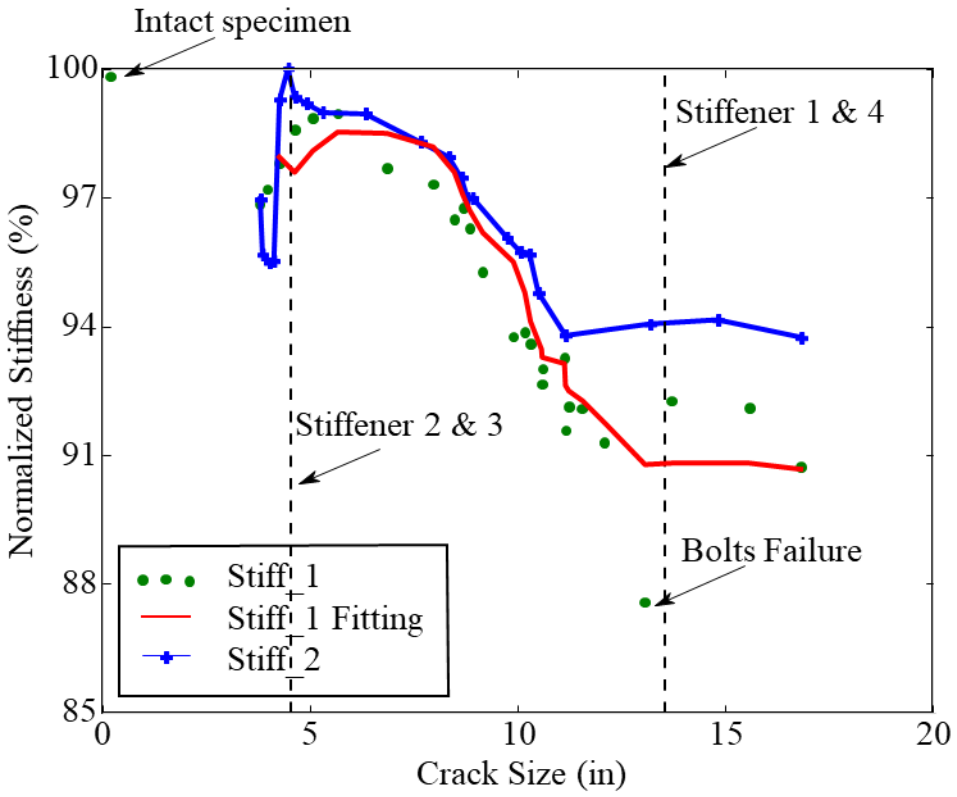

Figure 5-29. Relationship between the stiffness reduction of the specimen versus crack size.

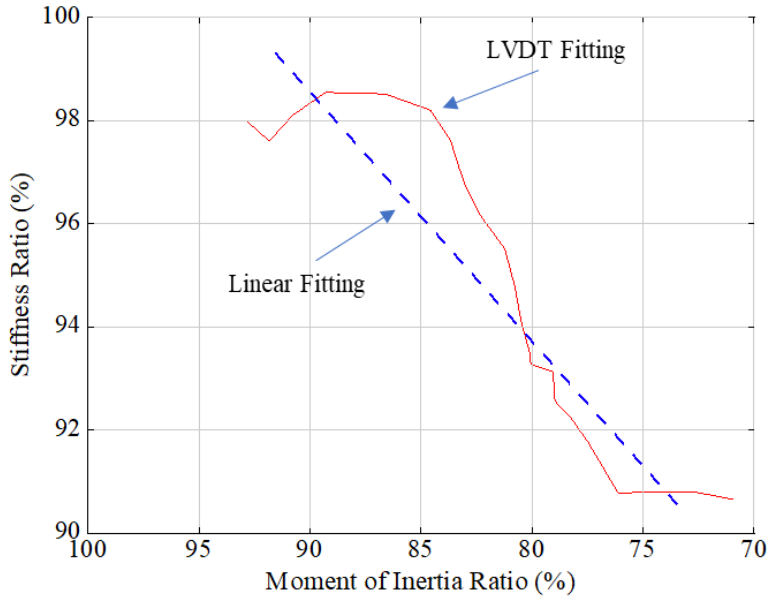

Figure 5-30. Relationship between the stiffness ratio of the specimen and the moment of inertia ratio.

5.4.5 Bolt Failure

During the test of Specimen S1, three bolt failure events occurred due to the application of fatigue loading. The details of these three bolt failure events are listed in Table 5-2. All of these failures were located at the bottom zone of the connection plates as depicted in Figure 5-31. The reason is that only the uncracked portion of the bottom flange can transfer loads. as a result, some of the bolts are forced to transfer higher loads compared to others leading to a reduced fatigue life. Two different fracture locations were found in the failed bolts: (a) fracture within the threads, and (b) fracture at the junction between the bolt head and shank (see Figure 5-32).

To assess the safety of the utilized pretensioned bolts, the failure data is compared to the S-N curve (AASHTO, 2020) and is plotted in Figure 5-33. Since these pretensioned bolts are subjected to high stress ratio with mainly tensile loading, it is appropriate to evaluate their fatigue life using traditional approaches such as the S-N approach or Miner's rule. The rainflow-counting algorithm (Amzallag et al., 1994) is used to obtain the effective load cycles and generate the

stress-range bin histogram. As seen in Figure 5-33, the bolt failure occurred at stress levels higher than those provided by the design S-N curve. To minimize these failures in the remaining specimens, the diameter of the bolts was raised to 1-in, and the hole diameters were enlarged to accommodate these larger bolts.

Table 5-2. Details of the bolt failure events for Specimen S1.

	Failed Bolt Number	Load Cycles	North Crack size (in)
First Failure	1	1.79×10^7	10.2
Second Failure	7	2.21×10^7	12.4
Third Failure	1	2.29×10^7	16.5

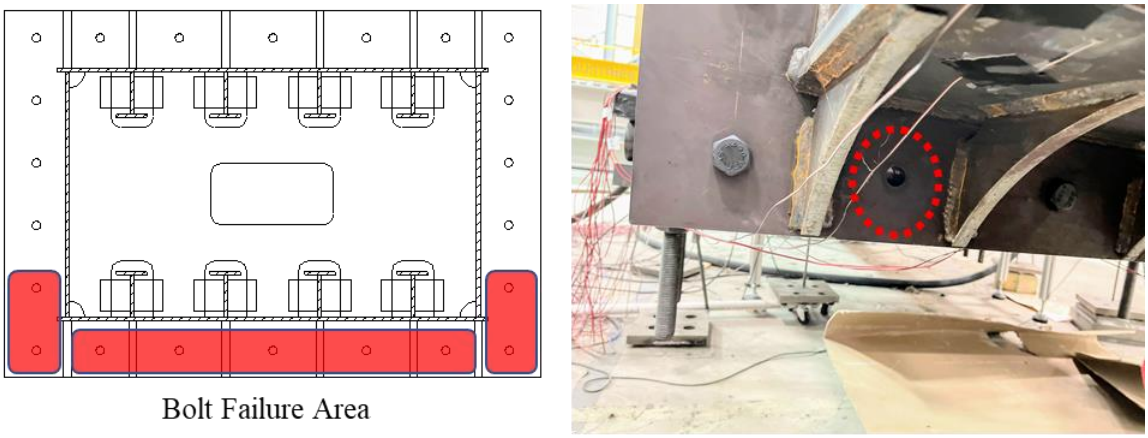

Figure 5-31. Example of the bolt failure locations.

Figure 5-32. Example of the failed bolts during Specimen S1 test (a) thread fracture (b) head fracture.

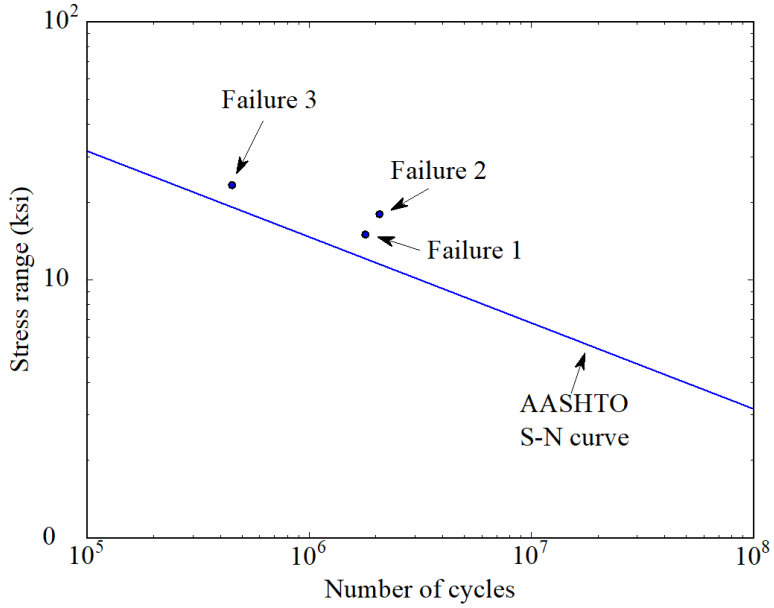

Figure 5-33. Comparison between the S-N curve and the three bolt failure events.

5.4.6 Crack Propagation Prediction Results

The proposed XFEM-based fatigue crack growth prediction model discussed in Chapter IV is used to calculate the crack-opening SIF considering load history effect. Assuming that different specimen geometries with same applied SIF will generate a similar plastic strain fields around the crack tip, the established M(T) model in Chapter IV was used to calculate the plastic strain around the crack tip for Specimen S1. Since the crack size is small in the M(T) model compared to Specimen S1, the load applied to the M(T) model was adjusted to generate the same maximum SIF as those applied to Specimen S1 during the test. For this analysis, the maximum SIF is computed under the assumption of a center crack in an infinite plate. The flowchart for this procedure is plotted in Figure 5-34. Later, the effect of stiffener restraint, stiffener separation, and residual stresses will be considered following Equation 5-1 to 5-10 along with the crack-opening SIF. Several M(T) models with different loading levels were established to represent the Specimen S1 at different crack sizes. For instance, for North Crack size at 6.09-in, the maximum stress applied to Specimen S1 is 6.0 ksi at load level of 110 kips. Under this condition, the

maximum SIF, assuming a crack in an infinite plate, is 26.1 ksi. In order to maintain the same SIF in the M(T) model, the load level is considered to be 10.5 kips at crack size of 0.4-in. Similar analysis is conducted at different crack sizes in Specimen S1.

Table 5-3 shows the maximum stress levels experienced by Specimen S1 at different crack size obtained from the strain gauge readings. The crack size in Table 5-3 represents the size of the North Cracks. The strains are the average values obtained from strain gauges No. 6, 8, 9, and 17. Table 5-4 shows the obtained crack-opening SIF for different crack sizes and K_{max} experienced by Specimen S1. The crack-opening SIF values between these crack sizes are estimated by linear interpolation. As the crack grows, the obtained crack-opening SIF gradually decreases. For crack size of 10.51-in, the crack-opening SIF diminishes.

Next, Equations 5-1 to 5-10 are used to compute the total SIF for Specimen S1 to properly account for the effect of stiffeners and residual stresses. Figure 5-35 shows the SIF at load of 110 kips versus the crack size for Specimen S1. The figure depicts the SIF arising from the stiffener restraint and separation, K_{st}, the SIF associated with the residual stress K_{res}, the total SIF K_{total}, and the effective SIF K_{total} - K_{op}. Equation 4-6 in Chapter IV is used to predict the FCG curve for Specimen S1 with $C = 2.03\times10^{-9}$, $m = 2.82$ as discussed in Chapter IV. The obtained crack propagation results are depicted in Figure 5-36 along with the test data. As shown, the prediction is in good agreement with the test curves. The prediction also was capable of capturing the change in the FCGR as the applied load pattern changed. Moreover, the figure shows the FCG prediction results using Equations 5-1 to 5-10 but without considering the crack closure or K_{op}. By neglecting the crack-opening SIF, the crack propagation parameters C and m are obtained from the Paris' law fit based on the conducted fatigue tests under constant amplitude loading in Chapter IV. The value of these parameters is $C = 1.24\times 10^{-10}$, $m = 3.14$ using ksi for stress and inches for crack length. As shown, neglecting the crack closure effects underestimated the crack

size since the value of *C* becomes much smaller and the predicted FCGR is lower compared to the one considering the load history effect.

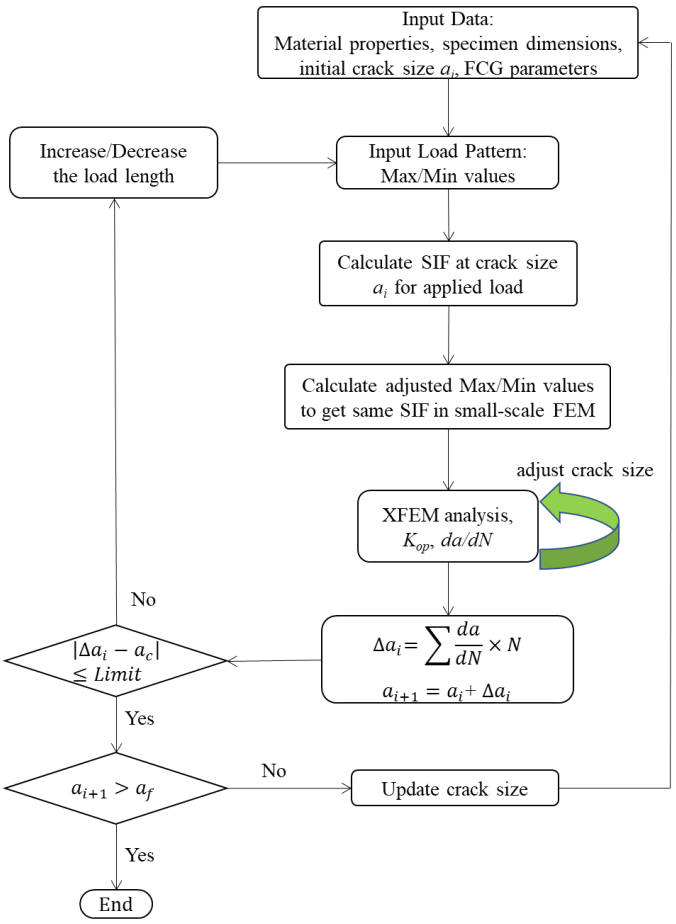

Figure 5-34. Flowchart of the proposed XFEM-based prediction approach for stiffened panels.

Table 5-3. Stress levels for different crack sizes based on strain gauges.

Number of Cycles	North Crack size (in)	Max Stress (ksi)	Max SIF ($ksi\sqrt{in}$)
0.00E+00	3.80	6.4	22.01
4.57E+06	4.54	6.3	23.97
7.85E+06	6.09	6.0	26.14
9.40E+06	7.66	6.0	29.44
1.48E+07	9.06	6.2	33.29
1.98E+07	10.51	7.2	41.16

Table 5-4. Crack-opening SIF versus crack size using XFEM-based prediction approach.

North Crack size (in)	Max SIF ($ksi\sqrt{in}$)	Equivalent R	K_{op} ($ksi\sqrt{in}$)
3.80	22.01	-0.9	4.66
4.54	23.97	-1	4.23
6.09	26.14	-1	3.74
7.66	29.44	-1	2.83
9.06	33.29	-1	1.50
10.51	41.16	-1	0

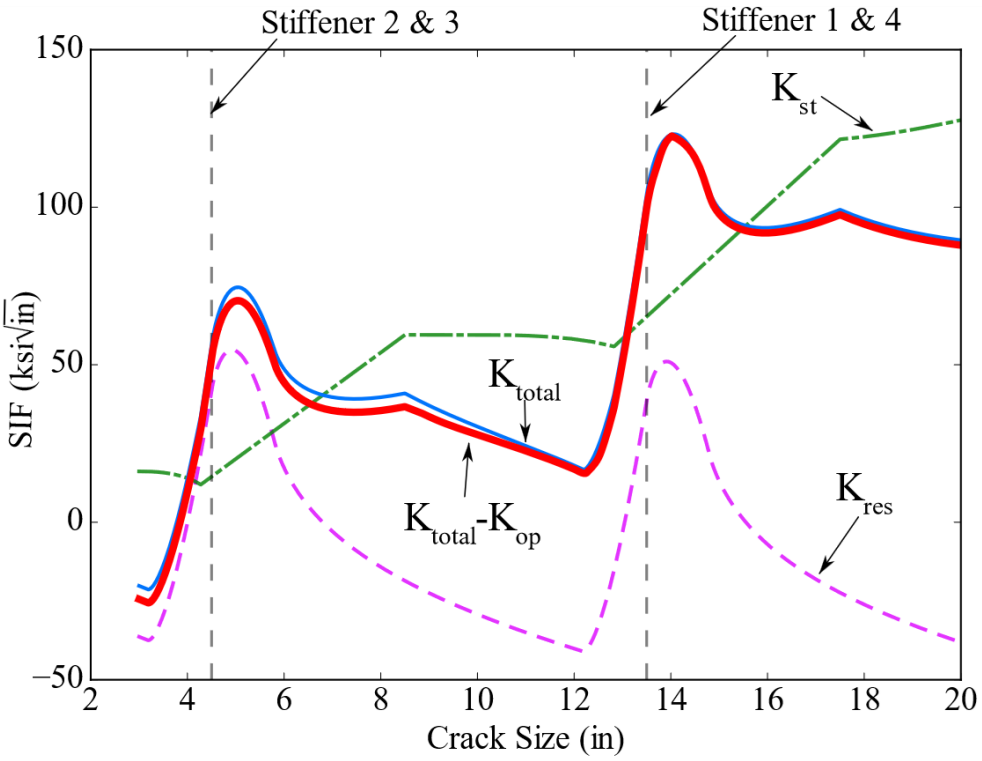

Figure 5-35. SIFs versus crack size considering stiffener, residual stress, and crack closure effects.

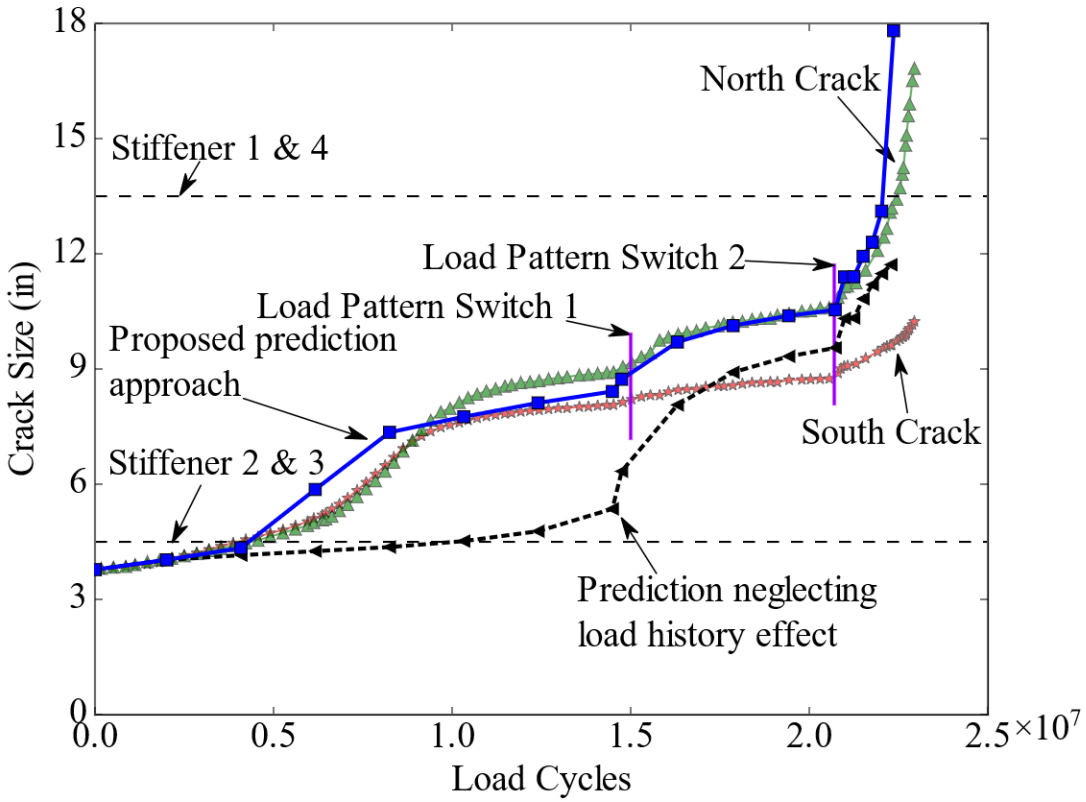

Figure 5-36. Comparison of the prediction from the XFEM-based proposed approach, prediction neglecting load history effect and test data for Specimen S1.

The S-N curve is another commonly used tool to evaluate the fatigue behavior of steel structures. It can be used for assessing details under variable amplitude loading along with a damage accumulation index. This approach has been implemented to assess the fatigue life of different types of components in bridges (Alencar et al., 2021), offshore structures (Varma et al., 2002), and aircraft frames (Kumar et al., 2013), among others. It was of interest to the author to evaluate the feasibility of its use and compare it to the results obtained from the proposed approach. Unfortunately, no dedicated detail category can be found in the design specifications or literature that is similar to the studied specimen.

5.5 Conclusions

This chapter presented the results of an experimental and numerical investigation into the crack propagation behavior under VAL in stiffened box girders. Stiffened box girders were designed, constructed, and tested under VAL in which the stress ratio changes randomly from positive to negative to replicate wave loading conditions. The specimens were instrumented with several strain gages and displacement transcoders to measure the change in the specimen behavior as the cracks grow. The size of the cracks was measured and recorded throughout the test. The crack growth profiles were compared to the results of a prediction model that account for crack closure and load history effects. The following conclusions can be drawn:

1. The adopted analytical model for computing the stress intensity factor for stiffened panels, coupled with the XFEM-based prediction of the load history effects, is capable of predicting the crack propagation in the tested stiffened box girder.
2. The fatigue crack propagation behaver in stiffened panels is heavily influenced by the existence of the stiffeners. The existence of these welded stiffeners generated residual stress fields that can induce a significant effect on the crack propagation.
3. The load history also affects the fatigue crack growth rate. Although, the crack-opening SIF was not as high compared to the total SIF, the crack growth prediction parameters obtained without considering crack closure effects can lead to incorrect prediction of the crack growth profiles.
4. The crack propagation has a considerable effect on the strain distributions within the specimen. From the conducted tests specimen, the strains around the center of the crack dropped to almost zero when the test was concluded. The remaining uncracked areas experienced 30% increase in the strains while some of the stiffeners experienced 100% increase in the strain level. This shows the high redundancy of this type of stiffened structures.

5. The tested specimens experienced a drop in stiffness as the cracks propagated. This drop reached only 10% at the end of the test. At this stage, the total crack length was 27-in while the width of the flange was 41.5-in. This actual drop in stiffness is sufficiently lower than the corresponding drop in the moment of inertia. Accordingly, it may not be possible to use the drop in stiffness as a parameter for early fatigue damage detection for this type of structures.

CHAPTER VI

CONCLUSIONS

6.1 Overview

This dissertation presents the work about the behavior of the combination connection constructed with pretensioned high-strength bolts and welds. Numerical simulation has been conducted to develop a deep understanding of the load-slip behavior of the combination connections with different configurations, e.g., bolt pattern, weld dimension, and weld/bolt strength ratio. It has been confirmed experimentally and numerically that the strength of the combination connections can be estimated using the summation of the resistances of bolts and welds at low slip levels. This dissertation also discussed the work about the application of the compute vision algorithms to fatigue crack measurement and monitoring. The proposed approach have been applied to the conducted middle tension fatigue tests and the obtained results showed a good accuracy. Meanwhile, an XFEM-based fatigue crack growth prediction was proposed in this dissertation. Experiments have been conducted on the stiffened box girder under realistic wave-induced loading. The predictions using the approach showed good results compared to the experimental data.

6.2 Numerical Investigation of the Behavior of Combination Connections with Pretensioned High-Strength Bolts and Longitudinal Fillet Welds

This chapter presented the numerical analysis of the combination connections with pretensioned high-strength bolts and longitudinal fillet welds in different configuration of critical variables including bolt pattern, weld dimension, weld/bolt strength ratio, faying surface condition. The FE models were established for different configurations and were validated with the corresponding experimental program. Following conclusions were drawn based on the previous discussions:

1. Comprehensive FE models including surface frictional model and weld ductile fracture model were established and validated for the combination connections with pretensioned high-strength bolts and longitudinal fillet welds; the behavior of the combination connections was accurately simulated using FE models.
2. The developed surface frictional models were able to properly capture the slip behavior of connections utilizing both Class A and Class B faying surfaces. These models can be integrated into numerical analysis of connections or can be used analytically to predict the connection displacements at working loads.
3. The numerical simulation results confirmed that at low slip levels, the resistance of the combination connection can be estimated as the summation of the capacities of bolts and welds for all the weld/bolt strength ratio and connection types considered.
4. The investigation results showed that, for the analyzed connections, when fillet welds are combined to a bolted connection with properly pretensioned high-strength bolts, the ultimate capacity of welds is expected to remain at the same levels of a welded-only connection; however, the deformation level at which ultimate weld fracture occurs is expected to be higher than that of a welded-only connections. This can be attributed to the sudden failure of the welds in the welded-only connections while the existence of the bolts in the combination connections helps smoothing the failure process of the welds.

5. The combination of fillet welds to a slip-resistant bolted connection causes a redistribution in the stress fields within the steel plates. Similar to a bolted connection, the plate cross-section at the inner bolt line experienced the highest stress levels. With the increase in the connection capacity, it is essential to ensure that the steel plates have enough strength to prevent failure under other limit states.
6. Numerical simulation indicates that the weld location respect to the center of the bolts has low influence on the behavior of the combination connections. The existence of welds, however, will redistribute the stress within the plates. It could help to reduce the stress concentration if the welds are added to the weak section of the steel plates.

6.3 Automated Vision-Based Fatigue Crack Growth Monitoring Based on Background Subtraction

The chapter presented an automated imaging-based fatigue crack growth monitoring approach based on the background subtraction technique. It is aimed to provide an automated and accurate alternative for crack measurement and monitoring. The background subtraction adopted can detect moving objects from a static camera. The fatigue crack growth in an interval can be treated as a moving object. A linear actuator is utilized to adjust the location of the microscope to (a) enable the automated tracking of the crack tip and (b) expand the measurement FOV such that the entire crack length can be observed. The accuracy of the proposed approach can reach 0.014 mm (0.00056 in) and has the ability to resolve crack extensions of 0.1 mm (0.004 in) needed by ASTM E647. Accordingly, the proposed approach can provide the crack size measurement accuracy required in fatigue crack propagation tests. The cost of the utilized crack monitoring equipment including the microscope, a linear actuator, and camera stand, was approximately $300. Overall, the proposed approach was found to provide an automated, cost-effective, and accurate alternative to other non-contact real-time crack measuring approaches.

6.4 Fatigue Crack Growth Prediction Considering Load History Effect Using XFEM

This chapter presents an approach for predicting FCG under VAL. XFEM was used to model the fatigue crack and obtain the stress/strains fields around the crack tip. The continuous tracking of residual stress/strain, as well as the applied initial conditions, enables the XFEM to retain memory of the previous analysis results and integrate the load history effect. The plastic strain around the crack tip was used to calculate an equivalent stress ratio under the VAL. This ratio was next used to compute the crack-opening SIF based on the crack closure concept. An analytical crack advancement rule was used to track the crack propagation. Middle tension fatigue tests were conducted to provide essential experimental data for validating the prediction model. The following conclusions can be drawn:

1. The proposed FCG prediction framework can predict the crack growth profiles under both constant and variable amplitude loadings. For the majority of considered cases, the predicted crack growth profile was within 8% of the experimental results.
2. Utilizing XFEM to account for crack closure effects provides a computationally efficient approach for tracking the crack-opening SIF under variable amplitude loading condition. The proposed approach allows computing the crack-opening SIF over larger crack length segments, rather than on a cycle-by-cycle basis, leading to a significant reduction of the computational cost of the analysis.
3. Neglecting the effect of crack closure and load history effect can overestimate or underestimate the fatigue life under variable amplitude loading.
4. The developed relationship that can compute the crack-opening SIF as a function of the plastic strain around the crack tip, applied maximum SIF, and the equivalent stress ratio, resulted in accurate crack growth prediction results. It is recommended to use this approach for studying crack growth under different geometric and/or loading conditions.

6.5 Experimental and Numerical investigation of the Fatigue crack growth of Stiffened panels under random sea loadings

This chapter presented the results of an experimental and numerical investigation into the crack propagation behavior under VAL in stiffened box girders. Stiffened box girders were designed, constructed, and tested under VAL in which the stress ratio changes randomly from positive to negative to replicate wave loading conditions. The specimens were instrumented with several strain gages and displacement transcoders to measure the change in the specimen behavior as the cracks grow. The size of the cracks was measured and recorded throughout the test. The crack growth profiles were compared to the results of a prediction model that account for crack closure and load history effects. The following conclusions can be drawn:

1. The adopted analytical model for computing the stress intensity factor for stiffened panels, coupled with the XFEM-based prediction of the load history effects, is capable of predicting the crack propagation in the tested stiffened box girder.
2. The fatigue crack propagation behaver in stiffened panels is heavily influenced by the existence of the stiffeners. The existence of these welded stiffeners generated residual stress fields that can induce a significant effect on the crack propagation.
3. The load history also affects the fatigue crack growth rate. Although, the crack-opening SIF was not as high compared to the total SIF, the crack growth prediction parameters obtained without considering crack closure effects can lead to incorrect prediction of the crack growth profiles.
4. The crack propagation has a considerable effect on the strain distributions within the specimen. From the conducted tests specimen, the strains around the center of the crack dropped to almost zero when the test was concluded. The remaining uncracked areas experienced 30% increase in the strains while some of the stiffeners experienced 100%

increase in the strain level. This shows the high redundancy of this type of stiffened structures.

5. The tested specimens experienced a drop in stiffness as the cracks propagated. This drop reached only 10% at the end of the test. At this stage, the total crack length was 27-in while the width of the flange was 41.5-in. This actual drop in stiffness is sufficiently lower than the corresponding drop in the moment of inertia. Accordingly, it may not be possible to use the drop in stiffness as a parameter for early fatigue damage detection for this type of structures.

6.6 Future Research

This dissertation provides the foundation for several topics in which future research may be needed. Ideas for future work and suggestions are list below:

1. For the investigated steel connections, the finite element analysis conducted in this dissertation resulted in load-deformation behavior for fillet welds with large size that is different than the profiles obtained using analytical models available in literature. It was found that limited experimental research have been conducted on welded connections with fillet welds exceeding ½-inch in size. It is desirable to experimentally characterize the behavior of steel connections with large fillet weld size.
2. Stress/strain field along the crack in the conducted fatigue tests were monitored with strain gauges. Due to the limitation of the number of strain gauges applied, it was difficult to provide a full image of these variables. In addition, the crack closure effect consideration has shown a great effect on the prediction. Advanced methods, e.g., digital correlation image (DIC), would be desirable to be applied to monitor all these variables.
3. The change in stiffness for the tested box girders under fatigue loading was inconsistent with the change in the moment of inertia as the cracks propagated. A similar trend was also observed in other fatigue tests conducted in literature on different structural

components. More studies are needed to develop approaches that enable quantifying the degradation in stiffness as a function of the crack size.

REFERENCES

AASHTO. (2020). *AASHTO LRFD Bridge Design Specifications* (9th ed.). American Association of State Highway and Transportation Officials.

Aïd, A., Amrouche, A., Bouiadjra, B. B., Benguediab, M., & Mesmacque, G. (2011). Fatigue life prediction under variable loading based on a new damage model. *Materials & Design*, *32*(1), 183–191.

AISC. (2016). *Specification for Structural Steel Buildings, ANSI/AISC 360-16*. American Institute of Steel Construction.

AISC. (2017). *Steel Construction Manual, 15th Edition*. American Institute of Steel Construction.

Alencar, G., Hong, J. K., de Jesus, A., da Silva, J. G. S., & Calçada, R. (2021). The Master SN curve approach for fatigue assessment of welded bridge structural details. *International Journal of Fatigue*, *152*, 106432

Alshoaibi, A. M., & Fageehi, Y. A. (2020). 2D finite element simulation of mixed mode fatigue crack propagation for CTS specimen. *Journal of Materials Research and Technology*, *9*(4), 7850–7861. https://doi.org/10.1016/j.jmrt.2020.04.083

Amzallag, C., Gerey, J. P., Robert, J. L., & Bahuaud, J. (1994). Standardization of the rainflow counting method for fatigue analysis. *International Journal of Fatigue*, *16*(4), 287–293.

Anderson, T. L. (2017). *Fracture mechanics: Fundamentals and applications* (4th ed.). CRC Press.

ASTM A572. (2021). *Standard specification for high-strength low-alloy columbium-vanadium structural steel*. ASTM International.

ASTM F3125. (2021). *Standard Specification for High Strength Structural Bolts and Assemblies, Steel and Alloy Steel, Heat Treated, Inch Dimensions 120 ksi and 150 ksi Minimum Tensile Strength, and Metric Dimensions 830 MPa and 1040 MPa Minimum Tensile Strength*. ASTM International.

ASTM Standard E8. (2021). *Standard Test Methods for Tension Testing of Metallic Materials*. ASTM International.

ASTM Standard E647. (2015). *Standard test method for measurement of fatigue crack growth rates*. ASTM International.

Aubert, G., Kornprobst, P., & Aubert, G. (2006). *Mathematical problems in image processing: Partial differential equations and the calculus of variations* (Vol. 147, p.26). Springer.

AWS B4.0:2016. (2016). *Standard Method for Mechanical Testing of Welds*. American Welding Society.

Baptista, J. B., Antunes, F. V., Correia, L., & Branco, R. (2017). A numerical study of the effect of single overloads on plasticity induced crack closure. *Theoretical and Applied Fracture Mechanics*, *88*, 51–63. https://doi.org/10.1016/j.tafmec.2016.12.001

Bär, J. (2020). Crack Detection and Crack Length Measurement with the DC Potential Drop Method–Possibilities, Challenges and New Developments. *Applied Sciences*, *10*(23), 8559.

Bayesteh, H., & Mohammadi, S. (2011). XFEM fracture analysis of shells: The effect of crack tip enrichments. *Computational Materials Science*, *50*(10), 2793–2813. https://doi.org/10.1016/j.commatsci.2011.04.034

Belytschko, T., & Black, T. (1999). Elastic crack growth in finite elements with minimal remeshing. *International Journal for Numerical Methods in Engineering*, *45*(5), 601–

620. https://doi.org/10.1002/(SICI)1097-0207(19990620)45:5<601::AID-NME598>3.0.CO;2-S

Bergara, A., Dorado, J. I., Martin-Meizoso, A., & Martínez-Esnaola, J. M. (2017). Fatigue crack propagation in complex stress fields: Experiments and numerical simulations using the Extended Finite Element Method (XFEM). *International Journal of Fatigue*, *103*, 112–121. https://doi.org/10.1016/j.ijfatigue.2017.05.026

Bordas, S., Rabczuk, T., & Zi, G. (2008). Three-dimensional crack initiation, propagation, branching and junction in non-linear materials by an extended meshfree method without asymptotic enrichment. *Engineering Fracture Mechanics*, *75*(5), 943–960.

Božić, Ž., Schmauder, S., & Wolf, H. (2018). The effect of residual stresses on fatigue crack propagation in welded stiffened panels. *Engineering Failure Analysis*, *84*, 346–357. https://doi.org/10.1016/j.engfailanal.2017.09.001

Bradski, G., & Kaehler, A. (2008). *Learning OpenCV: Computer vision with the OpenCV library*. O'Reilly Media, Inc.

Butler, L. J., & Kulak, G. L. (1971). Strength of fillet welds as a function of direction of load. *Welding Journal*, *50*(5), 231–234.

Canny, J. (1986). A computational approach to edge detection. *IEEE Transactions on Pattern Analysis and Machine Intelligence*, (6), 679-698.

Chung, K. F., & Ip, K. H. (2001). Finite element investigation on the structural behaviour of cold-formed steel bolted connections. *Engineering Structures*, *23*(9), 1115–1125.

Clark, W. G., & Hudak, S. J. (1975). Variability in Fatigue Crack Growth Rate Testing. *Journal of Testing and Evaluation*, *3*(6), 454–476. https://doi.org/10.1520/JTE11702J

Crawford, S. F., & Kulak, G. L. (1968). *Behavior of Eccentrically Loaded Bolted Connections*. Department of Civil Engineering, Nova Scotia Technical College, Halifax, Nova Scotia.

Dahl, P. R. (1968). *A solid friction model*. Aerospace Corp El Segundo Ca.

Dassault Systemes. (2021). *SIMULIA User Assistance*. http://194.167.201.93/English/DSSIMULIA_Established.htm

Dempster, A. P., Laird, N. M., & Rubin, D. B. (1977). Maximum likelihood from incomplete data via the EM algorithm. *Journal of the Royal Statistical Society: Series B (Methodological)*, *39*(1), 1–22.

Dexter, R. J., & Pilarski, P. J. (2000). Effect of welded stiffeners on crack growth rate. https://rosap.ntl.bts.gov/view/dot/42153

Dexter, R. J., & Pilarski, P. J. (2002). Crack propagation in welded stiffened panels. *Journal of Constructional Steel Research*, *58*(5), 1081–1102. https://doi.org/10.1016/S0143-974X(01)00094-3

Dirik, H., & Yalcinkaya, T. (2016). Fatigue Crack Growth Under Variable Amplitude Loading Through XFEM. *Procedia Structural Integrity*, *2*, 3073–3080.

Dirik, H., & Yalçinkaya, T. (2018). Crack path and life prediction under mixed mode cyclic variable amplitude loading through XFEM. *International Journal of Fatigue*, *114*, 34–50. https://doi.org/10.1016/j.ijfatigue.2018.04.026

Donald, J. K., & Schmidt, D. W. (1980). Computer-controlled stress intensity gradient technique for high rate fatigue crack growth testing. *Journal of Testing and Evaluation*, *8*(1), 19–24.

Duffy, D. G. (2015). *Green's functions with applications*. Chapman and Hall/CRC.

Durif, E., Réthoré, J., Combescure, A., Fregonese, M., & Chaudet, P. (2012). Controlling stress intensity factors during a fatigue crack propagation using digital image correlation and a load shedding procedure. *Experimental Mechanics*, *52*(8), 1021–1031.

Elber, W. (1971). The significance of fatigue crack closure. In *Damage tolerance in aircraft structures*. ASTM International.

EN 1090-2. (2018). *Execution of steel structures and aluminium structures—Part 2: Technical requirements for steel structures*. European Committee for Standardization (CEN).

Faulkner, D. (1975). A review of effective plating for use in the analysis of stiffened plating in bending and compression. *Journal of Ship Research*, *19*(01), 1–17.

Feng, D., & Feng, M. Q. (2018). Computer vision for SHM of civil infrastructure: From dynamic response measurement to damage detection–A review. *Engineering Structures*, *156*, 105–117.

Feulvarch, E., Fontaine, M., & Bergheau, J.-M. (2013). XFEM investigation of a crack path in residual stresses resulting from quenching. *Finite Elements in Analysis and Design*, *75*, 62–70. https://doi.org/10.1016/j.finel.2013.07.005

Field, I., Kandare, E., Dixon, B., Tian, J., & Barter, S. (2022). Effect of underloads in small fatigue crack growth. *International Journal of Fatigue*, *157*, 106706.

Fisher, J. W. (1964). *On the Behavior of Fasteners and Plates with Holes*. Fritz Engineering Laboratory, Department of Civil Engineering, Lehigh University.

Fisher, J. W., Dexter, R. J., Roberts, R., Yen, B. T., Decorges, G., Pessiki, S. P., Nussbaumer, A. C., Tarquinio, J. E., Kober, G. R., & Gentilcore, M. L. (1992). Structural failure modes for advanced double-hull fatigue and fracture failure modes. *Final Report for Cooperative Agreement*, *00014*, 91–01.

Fisher, J. W., Kulak, G. L., & Smith, I. F. (1998). *A fatigue primer for structural engineers*. National Steel Bridge Alliance, American Institute of Steel Construction.

Fleck, N. A. (1985). Fatigue crack growth due to periodic underloads and overloads. *Acta Metallurgica*, *33*(7), 1339–1354.

Fleck, N. A. (1986). Finite element analysis of plasticity-induced crack closure under plane strain conditions. *Engineering Fracture Mechanics*, *25*(4), 441–449.

Forman, R. G., Kearney, V. E., & Engle, R. M. (1967). Numerical analysis of crack propagation in cyclic-loaded structures. *Journal of Basic Engineering*, *89*(3), 459-463.

Frangi, A. F., Niessen, W. J., Hoogeveen, R. M., Van Walsum, T., & Viergever, M. A. (1999). Model-based quantitation of 3-D magnetic resonance angiographic images. *IEEE Transactions on Medical Imaging*, *18*(10), 946–956.

Fricke, W. (2017). Fatigue and fracture of ship structures. *Encyclopedia of Maritime and Offshore Engineering*, 1–12.

Friedman, N., & Russell, S. (2013). Image segmentation in video sequences: A probabilistic approach. *ArXiv Preprint ArXiv:1302.1539*.

Fries, T.-P., & Belytschko, T. (2010). The extended/generalized finite element method: An overview of the method and its applications. *International Journal for Numerical Methods in Engineering*, *84*(3), 253–304.

Funk, M., & Bär, J. (2019). DCPD based detection of the transition from short to long crack propagation in fatigue experiments on the aluminum alloy 7475 T761. *Procedia Structural Integrity*, *17*, 183–189.

Geary, W. (1992). A review of some aspects of fatigue crack growth under variable amplitude loading. *International Journal of Fatigue*, *14*(6), 377–386.

Ghahremani, K. (2015). *Fatigue assessment of repaired highway bridge welds using local approaches*. Doctoral dissertation, University of Waterloo.

Giner, E., Sukumar, N., Tarancón, J. E., & Fuenmayor, F. J. (2009). An Abaqus implementation of the extended finite element method. *Engineering Fracture Mechanics*, *76*(3), 347–368.

Goel, H. S., & Chand, S. (1994). A fatigue crack growth model for single overload tests. *Journal of Engineering Materials and Technology*, *116*(2), 168–172.

Gonzalez, R. C., & Woods, R. E. (2006). *Digital Image Processing* (3rd Edition). Prentice-Hall, Inc.

Greif, R., & Sanders Jr, J. L. (1965). The effect of a stringer on the stress in a cracked sheet. *Journal of Applied Mechanics*, *32*(1), 59-66.

Grimsmo, E. L., Clausen, A. H., Aalberg, A., & Langseth, M. (2017). Fillet welds subjected to impact loading – an experimental study. *International Journal of Impact Engineering*, *108*, 101–113. https://doi.org/10.1016/j.ijimpeng.2017.02.023

Harter, J. A. (1999). *AFGROW users guide and technical manual*. https://apps.dtic.mil/sti/citations/ADA37043.

Hasselmann, K., Barnett, T. P., Bouws, E., Carlson, H., Cartwright, D. E., Enke, K., Ewing, J. A., Gienapp, A., Hasselmann, D. E., & Kruseman, P. (1973). Measurements of wind-wave growth and swell decay during the Joint North Sea Wave Project (JONSWAP). *Ergaenzungsheft Zur Deutschen Hydrographischen Zeitschrift, Reihe A, Nr. 12*.

Hedayati, E., & Vahedi, M. (2014). Using Extended Finite Element Method for Computation of the Stress Intensity Factor, Crack Growth Simulation and Predicting Fatigue Crack Growth in a Slant-Cracked Plate of 6061-T651 Aluminum. *World Journal of Mechanics*, *4*(1), 42192. https://doi.org/10.4236/wjm.2014.41003

Holtz, N. M., & Kulak, G. L. (1970). *High-strength Bolts and Welds in Load-sharing Systems*. Department of Civil Engineering, Nova Scotia Technical College.

Huang, X., Torgeir, M., & Cui, W. (2008). An engineering model of fatigue crack growth under variable amplitude loading. *International Journal of Fatigue*, *30*(1), 2–10. https://doi.org/10.1016/j.ijfatigue.2007.03.004

Hutchinson, J. (1968). Singular behaviour at the end of a tensile crack in a hardening material. *Journal of the Mechanics and Physics of Solids*, *16*(1), 13–31.

Irwin, G. R. (1960). Plastic zone near a crack and fracture toughness. *Proceedings of the 7th Sagamore Army Materials Research Conference*, Syracuse Univ. Press, Syracuse, N.Y.

Isida, M. (1973). Analysis of stress intensity factors for the tension of a centrally cracked strip with stiffened edges. *Engineering Fracture Mechanics*, *5*(3), 647–665. https://doi.org/10.1016/0013-7944(73)90045-3

Janai, J., Güney, F., Behl, A., & Geiger, A. (2020). Computer vision for autonomous vehicles: Problems, datasets and state of the art. *Foundations and Trends® in Computer Graphics and Vision*, *12*(1–3), 1–308.

Jarosch, K. H., & Bowman, M. D. (1986). Tension butt joints with bolts and welds in combination. *Engineering Journal-American Institute of Steel Construction.*, *23*(1), 25–35.

Johnson, H. H. (1965). Calibrating the electric potential method for studying slow crack growth. *Materials Research and Standards*, *5*(1), 442–445.

Ju, S.-H., Fan, C.-Y., & Wu, G. H. (2004). Three-dimensional finite elements of steel bolted connections. *Engineering Structures*, *26*(3), 403–413.

Kang, L., Ge, H., & Kato, T. (2015). Experimental and ductile fracture model study of single-groove welded joints under monotonic loading. *Engineering Structures*, *85*, 36–51. Scopus. https://doi.org/10.1016/j.engstruct.2014.12.006

Kaufmann, E. J., Metrovich, B., & Pense, A. W. (2001). Characterization of Cyclic Inelastic Strain Behavior on Properties of A572 Gr. 50 and A913 Gr. 50 Rolled Sections (ATLSS Report No. 01-13). *Bethlehem, USA: Lehigh University*.

Keui, O., & Kiyotsugu, O. (1977). FEM analysis of crack closure and delay effect in fatigue crack growth under variable amplitude loading. *Engineering Fracture Mechanics*, *9*(2), 471–480.

Khan, S. U., Alderliesten, R. C., Rans, C. D., & Benedictus, R. (2010). Application of a modified Wheeler model to predict fatigue crack growth in Fiber Metal Laminates under variable amplitude loading. *Engineering Fracture Mechanics*, *77*(9), 1400–1416.

Kim, D.-K., & Lee, C.-H. (2020). Experimental and analytical study of combined bolted-welded lap joints including high-strength steel. *Journal of Constructional Steel Research*, *168*, 105995. https://doi.org/10.1016/j.jcsr.2020.105995

Kong, X., & Li, J. (2018). Vision-based fatigue crack detection of steel structures using video feature tracking. *Computer-Aided Civil and Infrastructure Engineering*, *33*(9), 783–799.

Kulak, G. L., & Grondin, G. Y. (2003). Strength of joints that combine bolts and welds. *Engineering Journal- American Institute of Steel Construction*, *40*(2), 89–98.

Kumar, A. R., Balakrishnan, S. R., & Balaji, S. (2013). Design of an aircraft wing structure for static analysis and fatigue life prediction. *Int. J. Eng. Res. Technol*, *2*(5), 1154–1158.

Kumar, S., Shedbale, A. S., Singh, I. V., & Mishra, B. K. (2015). Elasto-plastic fatigue crack growth analysis of plane problems in the presence of flaws using XFEM. *Frontiers of Structural and Civil Engineering*, *9*(4), 420–440. https://doi.org/10.1007/s11709-015-0305-y

Lambourg, A., Henaff, G., Nadot, Y., Gourdin, S., d'Andrebo, Q. P., & Pierret, S. (2020). Optimization of the DCPD technique for monitoring the crack propagation from notch root in localized plasticity. *International Journal of Fatigue*, *130*, 105228.

Lee, S., & Martin, D. (2016). Application of XFEM to model stationary crack and crack propagation for pressure containing subsea equipment. *Pressure Vessels and Piping Conference*, *50411*, V005T05A006.

Leon, S. J., Bica, I., & Hohn, T. (2006). *Linear algebra with applications*. Pearson Prentice Hall Upper Saddle River, NJ.

Lesik, D. F., & Kennedy, D. L. (1990). Ultimate strength of fillet welded connections loaded in plane. *Canadian Journal of Civil Engineering*, *17*(1), 55–67.

Li, S., Cui, W., & Paik, J. K. (2016). An improved procedure for generating standardised load-time histories for marine structures. *Proceedings of the Institution of Mechanical Engineers, Part M: Journal of Engineering for the Maritime Environment*, *230*(2), 281–296.

Liu, X., Bradford, M. A., Chen, Q.-J., & Ban, H. (2016). Finite element modelling of steel–concrete composite beams with high-strength friction-grip bolt shear connectors. *Finite Elements in Analysis and Design*, *108*, 54–65.

Lu, Z., & Liu, Y. (2010). Small time scale fatigue crack growth analysis. *International Journal of Fatigue*, *32*(8), 1306–1321. https://doi.org/10.1016/j.ijfatigue.2010.01.010

Mahmoud, H. N., & Dexter, R. J. (2005). Propagation rate of large cracks in stiffened panels under tension loading. *Marine Structures*, *18*(3), 265–288.

Maji, S., & Malik, J. (2009). Object detection using a max-margin hough transform. *2009 IEEE Conference on Computer Vision and Pattern Recognition*, 1038–1045.

Manuel, T. J., & Kulak, G. L. (2000). Strength of joints that combine bolts and welds. *Journal of Structural Engineering*, *126*(3), 279–287.

Mathummal, A. K. T. (1983). *Reliability of a ship hull in the fracture and fatigue modes of failure*. University of California, Berkeley.

Matsuoka, S., & Tanaka, K. (1978). Delayed retardation phenomena of fatigue crack growth in various steels and alloys. *Journal of Materials Science*, *13*(6), 1335–1353.

Matsuoka, S., Tanaka, K., & Kawahara, M. (1976). The retardation phenomenon of fatigue crack growth in HT80 steel. *Engineering Fracture Mechanics*, *8*(3), 507–523. https://doi.org/10.1016/0013-7944(76)90005-9

McClung, R. C., & Sehitoglu, H. (1989). On the finite element analysis of fatigue crack closure—1. Basic modeling issues. *Engineering Fracture Mechanics*, *33*(2), 237–252. https://doi.org/10.1016/0013-7944(89)90027-1

McClung, R. C., Thacker, B. H., & Roy, S. (1991). Finite element visualization of fatigue crack closure in plane stress and plane strain. *International Journal of Fracture*, *50*(1), 27–49.

McEvily, A. J., & Ishihara, S. (2002). On the development of crack closure at high R levels after an overload. *Fatigue & Fracture of Engineering Materials & Structures*, *25*(11), 993–998.

Mehrzadi, M., & Taheri, F. (2013). A material sensitive modified wheeler model for predicting the retardation in fatigue response of AM60B due to an overload. *International Journal of Fatigue*, *55*, 220–229. https://doi.org/10.1016/j.ijfatigue.2013.06.022

Mettu, S. R., Shivakumar, V., Beek, J. M., Yeh, F., Williams, L. C., Forman, R. G., McMahon, J. J., & Newman, J. C. (1999). NASGRO 3.0: A software for analyzing aging aircraft. *The Second Joint NASA/FAA/DoD Conference on Aging Aircraft, Pt. 2*.

Mi, Y., & Aliabadi, M. (1994). Three-dimensional crack growth simulation using BEM. *Computers & Structures*, *52*(5), 871–878.

Middleton, C. A., Gaio, A., Greene, R. J., & Patterson, E. A. (2019). Towards automated tracking of initiation and propagation of cracks in aluminium alloy coupons using thermoelastic stress analysis. *Journal of Nondestructive Evaluation*, *38*(1), 1–14.

Mikheevskiy, S., & Glinka, G. (2009). Elastic–plastic fatigue crack growth analysis under variable amplitude loading spectra. *International Journal of Fatigue*, *31*(11–12), 1828–1836.

Minakawa, K., Newman, J. C., & McEvily, A. J. (1983). A critical study of the crack closure effect on near-threshold fatigue crack growth. *Fatigue & Fracture of Engineering Materials & Structures*, *6*(4), 359–365.

Miner, M. A. (1945). Cumulative damage in fatigue. *Journal of Applied Mechanics, (12)*3, 159-164.

Miyazaki, N., Ikeda, T., Soda, T., & Munakata, T. (1993). Stress intensity factor analysis of interface crack using boundary element method—Application of contour-integral method. *Engineering Fracture Mechanics*, *45*(5), 599–610.

Moës, N., Dolbow, J., & Belytschko, T. (1999). A finite element method for crack growth without remeshing. *International Journal for Numerical Methods in Engineering*, *46*(1), 131–150.

Newman, J. C. (1976). A finite-element analysis of fatigue crack closure. *Mechanics of crack growth, ASTM STP 590,* ASTM International, 281-301.

Newman, J. C. (1981). A crack-closure model for predicting fatigue crack growth under aircraft spectrum loading. *Methods and models for predicting fatigue crack growth under random loading, ASTM STP 748,* ASTM International, 53-84.

Newman, J. C. (1984). A crack opening stress equation for fatigue crack growth. *International Journal of Fracture*, *24*(4), R131–R135.

NI. (2018). *LabVIEW NXG 3.0 User Manual*. National Instruments. https://www.ni.com/documentation/en/labview/3.0/manual/manual-overview/. Accessed 10 Dec. 2018.

Noroozi, A. H., Glinka, G., & Lambert, S. (2007). A study of the stress ratio effects on fatigue crack growth using the unified two-parameter fatigue crack growth driving force. *International Journal of Fatigue*, *29*(9), 1616–1633. https://doi.org/10.1016/j.ijfatigue.2006.12.008

Nussbaumer, A. C. (1994). *Propagation of long fatigue cracks in multi-cellular box beams.* Lehigh University.

Nussbaumer, A. C., Fisher, J. W., & Dexter, R. J. (1999). Behavior of long fatigue cracks in cellular box beam. *Journal of Structural Engineering*, *125*(11), 1232–1238.

Oden, J. T., & Martins, J. (1985). Models and computational methods for dynamic friction phenomena. *Computer Methods in Applied Mechanics and Engineering*, *52*(1–3), 527–634.

Oh, C.-K., Kim, Y.-J., Baek, J.-H., & Kim, W. (2007). Development of stress-modified fracture strain for ductile failure of API X65 steel. *International Journal of Fracture*, *143*(2), 119. https://doi.org/10.1007/s10704-006-9036-3

Pantelakis, S. G., Kermanidis, T. B., & Pavlou, D. G. (1995). Fatigue crack growth retardation assessment of 2024-T3 and 6061-T6 aluminium specimens. *Theoretical and Applied Fracture Mechanics*, *22*(1), 35–42.

Paris, P., & Erdogan, F. (1963). A critical analysis of crack propagation laws. *Journal of Basic Engineering*, *85*(4), 528–533.

Park, S.J., & Song, J.H. (1999). Simulation of fatigue crack closure behavior under variable-amplitude loading by a 2D finite element analysis based on the most appropriate mesh size concept. *ASTM STP*, *1343*, 337–350.

Pippan, R., & Hohenwarter, A. (2017). Fatigue crack closure: A review of the physical phenomena. *Fatigue & Fracture of Engineering Materials & Structures*, *40*(4), 471–495. https://doi.org/10.1111/ffe.12578

Poe, C. C. (1971). Fatigue crack propagation in stiffened panels. *Damage Tolerance in Aircraft Structures, ASTM STP 486*, ASTM International, 39-49.

Poe Jr, C. C. (1969). The effect of riveted and uniformly spaced stringers on the stress intensity factor of a cracked sheet. *Conference on fatigue and fracture of aircraft structure and materials, Miami beach, FL.*

Quinn, B. P. (1991). The effect of profile and root geometry on the strength of fillet welds. *MSCE Thesis, Purdue University*, *2*, 283–313.

Radaj, D. (2012). *Heat effects of welding: Temperature field, residual stress, distortion*. Springer Science & Business Media.

Rasmussen, C. (1999). The infinite Gaussian mixture model. *Advances in Neural Information Processing Systems*, *12*.

RCSC. (2020). *Specification for Structural Joints Using High-Strength Bolts*. Research Council on Structural Connections, Chicago, IL: American Institute of Steel Construction.

Rege, K., & Lemu, H. G. (2017). A review of fatigue crack propagation modelling techniques using FEM and XFEM. *IOP Conference Series: Materials Science and Engineering*, *276*(1).

Remadi, A., Bahloul, A., & Bouraoui, C. (2019). Prediction of fatigue crack growth life under variable-amplitude loading using finite element analysis. *Comptes Rendus Mécanique*, *347*(8), 576–587. https://doi.org/10.1016/j.crme.2019.06.008

Rice, J. R., & Rosengren, G. (1968). Plane strain deformation near a crack tip in a power-law hardening material. *Journal of the Mechanics and Physics of Solids*, *16*(1), 1–12.

Rice, J. R., & Tracey, D. M. (1969). On the ductile enlargement of voids in triaxial stress fields. *Journal of the Mechanics and Physics of Solids*, *17*(3), 201–217.

Rooke, D. P., & Cartwright, D. J. (1976). Compendium of stress intensity factors. *Procurement Executive, Ministry of Defence. H. M. S. O. 1976, 330 p(Book).*

Russell, S. G. (1989). A new model for fatigue crack growth retardation following an overload. *Engineering Fracture Mechanics*, *33*(6), 839–854.

Sajid, H. U., & Kiran, R. (2018). Influence of high stress triaxiality on mechanical strength of ASTM A36, ASTM A572 and ASTM A992 steels. *Construction and Building Materials*, *176*, 129–134.

Sander, M., & Richard, H. A. (2006). Fatigue crack growth under variable amplitude loading Part II: Analytical and numerical investigations. *Fatigue & Fracture of Engineering Materials & Structures*, *29*(4), 303–319.

Schijve, J. (1988). Fatigue crack closure: Observations and technical significance. In *Mechanics of fatigue crack closure* (Vol. 982, pp. 5–34). American Society for Testing and Materials Philadelphia, PA.

Schijve, J. (2001). *Fatigue crack growth under variable-amplitude loading*. Springer.

Shanmugham, S., & Liaw, P. K. (1996). *Detection and Monitoring of Fatigue Cracks*. *ASM Handbook*, *19*, 210-221 https://doi.org/10.31399/asm.hb.v19.a0002363

Shi, G., Shi, Y., Wang, Y., & Bradford, M. A. (2008). Numerical simulation of steel pretensioned bolted end-plate connections of different types and details. *Engineering Structures*, *30*(10), 2677–2686.

Shi, Y. J., Wang, L., Wang, Y. Q., Ma, J. S., & Bai, R. S. (2011a). Finite element analysis of the combined connection with bolts and welds. *Applied Mechanics and Materials*, *94*, 316–321. https://www.scientific.net/AMM.94-96.316

Shi, Y. J., Wang, L., Wang, Y. Q., Ma, J. S., & Bai, R. S. (2011b). Proposed Design Method of Combined Connections with Bolts and Longitudinal Welds. *Applied Mechanics and Materials*, *94*, 923–928. https://www.scientific.net/AMM.94-96.923

Shigley, J. E., & Mischke, C. R. (1989). Mechanical Engineering Design, McGraw-Hill. *Inc, Singapore*.

Sikora, J. P. (1998). Cumulative lifetime loadings for naval ships. *ASME International Mechanical Engineering Congress and Exposition*, *15892*, 299–312.

Skorupa, M. (1998). Load interaction effects during fatigue crack growth under variable amplitude loading—a literature review. Part I: Empirical trends. *Fatigue & Fracture of Engineering Materials & Structures*, *21*(8), 987–1006.

Solanki, K., Daniewicz, S. R., & Newman, J. C. (2004). Finite element analysis of plasticity-induced fatigue crack closure: An overview. *Engineering Fracture Mechanics*, *71*(2), 149–171.

Solanki, K. N. (2002). *Two and three-dimensional finite element analysis of plasticity-induced fatigue crack closure: A comprehensive parametric study*. Mississippi State University.

Soliman, M., Frangopol, D. M., & Kim, S. (2013). Probabilistic optimum inspection planning of steel bridges with multiple fatigue sensitive details. *Engineering Structures*, *49*, 996–1006.

Soliman, M., Russell, B., Waite, D., Shen, L., & Stringer, E. (2021). *Understanding the Behavior of Steel Connections with Bolts and Welds in Combination | American Institute of Steel*

Construction. https://www.aisc.org/technical-resources/research/researchlibrary/understanding-the-behavior-of-steel-connections-with-bolts-and-welds-in-combination/

Sonsino, C. M. (2007). Fatigue testing under variable amplitude loading. *International Journal of Fatigue*, *29*(6), 1080–1089.

Stauffer, C., & Grimson, W. E. L. (1999). Adaptive background mixture models for real-time tracking. *Proceedings. 1999 IEEE Computer Society Conference on Computer Vision and Pattern Recognition (Cat. No PR00149)*, *2*, 246–252.

Stephens, R. I., Fatemi, A., Stephens, R. R., & Fuchs, H. O. (2001). Metal Fatigue in Engineering, John Wiley and Sons. *Inc., New York*.

Sun, H., Liu, Q., & Fang, L. (2018). Research on Fatigue Crack Growth Detection of M (T) Specimen Based on Image Processing Technology. *Journal of Failure Analysis and Prevention*, *18*(4), 1010–1016. https://doi.org/10.1007/s11668-018-0493-6

Suzuki, S. (1985). Topological structural analysis of digitized binary images by border following. *Computer Vision, Graphics, and Image Processing*, *30*(1), 32–46.

Swift, H. (1952). Plastic instability under plane stress. *Journal of the Mechanics and Physics of Solids*, *1*(1), 1–18.

Tao, L. A. N., Jinsan, J. U., & Mengsha, L. I. U. (2019). Analysis of Ultimate Load-Carrying Capacity of Combined Connection with Bolts and Welds. *Mechanics*, *25*(6), 426–433.

Tomasi, C., & Manduchi, R. (1998). Bilateral filtering for gray and color images. *Sixth International Conference on Computer Vision (IEEE Cat. No. 98CH36271)*, 839–846.

Tomita, Y., Matobat, M., & Kawabel, H. (1995). Fatigue crack growth behavior under random loading model simulating real encountered wave condition. *Marine Structures*, *8*(4), 407–422.

Tveiten, B. W. (1999). Fatigue Assessment of Welded Aluminum Ship Detail. *Proc. 5th International Conference FAST*.

Vacavant, A., Chateau, T., Wilhelm, A., & Lequievre, L. (2012). A benchmark dataset for outdoor foreground/background extraction. *Asian Conference on Computer Vision*, 291–300.

Varma, A. H., Salecha, A. K., Wallace, B., & Russell, B. W. (2002). Flexural fatigue behavior of threaded connections for large diameter pipes. *Experimental Mechanics*, *42*(1), 1–7.

Waite, D., Shen, L., Soliman, M., & Russell, B. (2022). Experimental Investigation into the Capacity of Concentrically Loaded Steel Connections with Pretensioned High-Strength Bolts and Longitudinal Fillet Welds in Combination. *Engineering Journal-American Institute of Steel Construction*.

Wheeler, O. E. (1972). Spectrum loading and crack growth. *Journal of Basic Engineering, 94*(1), 181-186.

Wu, J., & Ellyin, F. (1996). A study of fatigue crack closure by elastic-plastic finite element analysis for constant-amplitude loading. *International Journal of Fracture*, *82*(1), 43–65.

Xu, S., Wang, J., Shou, W., Ngo, T., Sadick, A.-M., & Wang, X. (2021). Computer vision techniques in construction: A critical review. *Archives of Computational Methods in Engineering*, *28*(5), 3383–3397.

Yang, Z. (2006). Fully automatic modelling of mixed-mode crack propagation using scaled boundary finite element method. *Engineering Fracture Mechanics*, *73*(12), 1711–1731.

Yeum, C. M., & Dyke, S. J. (2015). Vision-based automated crack detection for bridge inspection. *Computer-Aided Civil and Infrastructure Engineering*, *30*(10), 759–770.

Yue, J., Dong, Y., & Guedes Soares, C. (2018). An experimental-finite element method based on beach marks to determine fatigue crack growth rate in thick plates with varying stress states. *Engineering Fracture Mechanics*, *196*, 123–141. https://doi.org/10.1016/j.engfracmech.2018.04.015

Yuen, B. K. C., & Taheri, F. (2006). Proposed modifications to the Wheeler retardation model for multiple overloading fatigue life prediction. *International Journal of Fatigue*, *28*(12), 1803–1819.

Zhu, J., Guo, W., & Guo, W. (2020). Surface fatigue crack growth under variable amplitude loading. *Engineering Fracture Mechanics*, *239*, 107317.

Zivkovic, Z. (2004). Improved adaptive Gaussian mixture model for background subtraction. *Proceedings of the 17th International Conference on Pattern Recognition, 2004. ICPR 2004.*, *2*, 28–31.

VITA

Ligang Shen

Candidate for the Degree of

Doctor of Philosophy

Dissertation: EXPERIMENTAL AND NUMERICAL ANALYSES ON THE BEHAVIOR OF CIVIL AND MARINE STEEL STRUCTURES

Major Field: Civil Engineering

Biographical:

Education:

Completed the requirements for the Doctor of Philosophy in Civil Engineering at Oklahoma State University, Stillwater, Oklahoma in December 2022.

Completed the requirements for the Master of Engineering in Civil Engineering at Shanghai Jiao Tong University, Shanghai, China in 2016.

Completed the requirements for the Bachelor of Science in Civil Engineering at Shanghai Jiao Tong University, Shanghai, China in 2013.